Design, Synthesis, and Evaluation of Manganese(I) Photoinduced CO-releasing Molecules and Water-Soluble Lanthanide Cages

A dissertation presented to

the faculty of

the College Arts and Sciences of Ohio University

In partial fulfillment

of the requirements for the degree

Doctor of Philosophy

Shabnam Pordel

December 2022

This dissertation titled

Design, Synthesis, and Evaluation of Manganese(I) Photoinduced CO-releasing Molecules and Water-Soluble Lanthanide Cages

by

SHABNAM PORDEL

has been approved for

the Department of Chemistry and Biochemistry

and the College of Arts and Sciences by

Eric Masson

Professor of Chemistry and Biochemistry

Sarah Poggione

Interim Dean, College of Arts and Sciences

Abstract

PORDEL, SHABNAM, Ph.D., December 2022, Chemistry

Design, Synthesis, and Evaluation of Manganese(I) Photoinduced CO-releasing Molecules and Water-Soluble Lanthanide Cages

Director of Dissertation: Eric Masson

Carbon monoxide (CO) is a toxic gas that has been known as the "silent killer" for decades. At high concentrations, CO reacts with hemoglobin, impairing its ability to transfer oxygen throughout the body. At low concentrations, however, CO has anti-cancer and anti-inflammatory effects. CO has also been shown to increase the sensitivity of certain types of cancer cells to the reactive oxygen species (ROS) produced by chemotherapeutics, thereby reducing drug resistance. One way to deliver CO in a controlled and safe manner is through the use of photoCORMs, or photoactivated CO releasing molecules. Transition metal-based photoCORMs are a class of molecules that release CO by breaking the M-CO bond upon exposure to light.

In Chapters 2 and 3, my research study the effect of ligand set variation (both electronically and sterically) around the Mn(I) metal center on the photophysical and photochemical properties, as well as the assignment of photochemical intermediate formation during visible light irradiation. In Chapter 4, we designed a system that combined photo-activated CO delivery and singlet oxygen ($^1O_2$). The photophysical and photochemical properties of two Mn(I)-based photoCORMs sensitized with a luminescent BODIPY, as well as their ability to generate singlet oxygen during visible light irradiation were investigated.

In Chapter 5, my focus was on water-soluble 3D supramolecular coordination cages (SCCs). The internal cavity incorporated in these structures allows them to encapsulate various guest molecules. Water-soluble Ln(III)-based SCCs are scarce, and the arrangement of water molecules inside the cavity, as well as the recognition properties of the latter, are mostly unknown. The study of such interactions would be of interest to the growing field of SCCs.

To this end, we designed and synthesized a water-soluble Eu(III)-based supramolecular coordination cage with the general formula of Eu_2L_3 and a triple-stranded helicate structure. The guest binding properties of the Eu_2L_3 cage were studied with smaller mono- and di-cationic organic guests through ^1H NMR titration in D_2O.

Dedication

I dedicate this work to my mom and dad for their endless love and support throughout my pursuit for education.

I would also like to dedicate this dissertation to my one and only sister, Shahrzad, who has always been there for me, and to my beloved niece and nephew, Armita and Kian.

Acknowledgments

I would like to express my special and deepest appreciation and thanks to my advisors Prof. Eric Masson and Prof. Jessica White for all their guidance, continuous support, and tremendous mentorship throughout my graduate study. I would like to thank them for allowing me to grow as a researcher. I would like to thank my dissertation committee members Prof. Michael Jensen, Prof. Jixin Chen, and Prof. Rebecca Snell for all their help and time during the different stages of this dissertation. I wish to sincerely thank my groupmate and my best friend, Dr. Rachael Pickens, who has always been there for me. I would like to thank her for her valuable advice, insightful suggestions, and support in the hardest of times. I want to thank her for all of the fun and adventure that we had and will have. Special thanks to my friends Mitra Rooein and Dr. Saeed Shahbazi who are always willing to help and answer random questions about setups and computational experiments. I am very thankful to the former and current faculty and staff of the Department of Chemistry and Biochemistry, especially Profs. McMills, Dr. Travis White, Prof. Rebecca Barlag, and Prof. Andrew Tangonan, for their training, assistance, support, and encouragement. I would like to thank my former and current group members for their support and help. Special thanks to Dr. Sima Saeedi, Mahsa Boraghi, and Esther Mbuna for their wonderful support. I would also like to express my sincere thanks to Adam Killmeyer, Xinyue Cheng, Fahimeh Movahedifar, Nazimuddin Md, Nathan Thompson, Ashton Smith, Dr. Hector Barbero, and Dr. Ramin Rabbani for providing insights, training, their assistance with organic synthetic procedures and ITC over the last year. Thanks should also go to my friends and colleagues Vahdat Jahed, Nazanin

Ghobadi, and Javad Shokraiyan for borrowing reagents, and all their help setting up air-sensitive reactions. I also had the great pleasure of working with some wonderful undergraduate students Adam Hering, Grace Judd, Demi Reed, and Shanan Ashton in the lab. Finally, but not least, I want to thank my parents, sister, and brother-in-law for their unparallel support, love, and profound belief in my abilities.

Table of Contents

Page

List of Tables

Page

List of Figures

Page

List of Schemes

Page

List of Abbreviations

$^1O_2$= Singlet oxygen
$^3O_2$ = triplet oxygen
BODIPY= Boron-dipyrromethenes
CBS= cystathionine β-synthase
COSY= Correlation spectroscopy
DFT= Density functional theory
DOSY= Diffusion-ordered spectroscopy
ET= Energy transfer
GSH= γ-l-glutamyl-l-cysteinyl-glycine
HOMO= Highest occupied molecular orbital
IR/NIR= Infrared/Near-infrared
ISC= Intersystem crossing
ITC= Isothermal titration calorimetry
LED = light emitting diode
Ln= Lanthanide
LUMO= Lowest unoccupied molecular orbital
m/z = Mass-to-charge ratio
MLCT= Metal to ligand charge transfer
MO= Molecular diagram
NN = bidentate diimine ligand
NOESY= Nuclear Overhauser effect spectroscopy
PDT= Photodynamic therapy
photoCORM= photo activated CO releasing molecule
PS= Photo sensitizer
QY= Quantum yield
ROS= Reactive oxygen species
rt = room temperature
S0= Ground state
S_1= Singlet excited state
SCC= Supramolecular coordination complex
SOSG= Singlet oxygen sensor green
T_1= Triplet excited state
UV= Ultraviolet
π = Pi-type interaction
σ = Sigma-type interaction

Chapter 1: Introduction

Despite the growing amount of research on developing new drugs for cancer treatment, they suffer from serious drawbacks, and the most concerning one is being harmful to healthy cells. While cisplatin has been a successful well-known chemotherapeutic drug for 40 years, its efficiency has been diminished by drug resistance and lack of selectivity. One way to address this issue is to use photosensitive drugs. In this method, light can be used as an external signal to activate the dark stable molecule at the desired time and location.

Recent studies have suggested that carbon monoxide (CO), a toxic, odorless, and colorless gas from incomplete combustion of carbon containing compounds, not only shows anticancer activity in low doses but also can sensitize some certain types of cancer cells to the produced reactive oxygen species (ROS) from some common chemotherapeutics, thus reducing drug resistance.

So far, the effect of exogenous CO in clinical and preclinical trials has been evaluated through inhalation and CO-releasing molecules.[1] However, in the case of inhalation due to the low solubility of CO in the biological fluid, high concentrations of CO must be inhaled. Moreover, CO inhalation suffers from lack of selectivity.[1] The photo-activated CO releasing molecules or "photoCORMs," however, offer more selectivity and controlled delivery of CO into a specific target. photoCORMs are dark stable molecules that release CO upon exposure to light.

Despite many reported studies, photoCORMs are still in their infancy, and more in vitro and in vivo studies are required to gain a better understanding of such compounds' photochemistry and mechanism of action.

1.1. CO in Biology

CO is a toxic and colorless gas resulting from incomplete combustion of carbon containing compounds.[2] CO poisoning is caused by CO's great affinity toward hemoglobin, as it exhibits an affinity about 200 times greater than O_2. Once CO binds to one of hemoglobin's four Fe^{2+} sites, the resulting carboxyhemoglobin (COHb) undergoes a conformational change in the three remaining sites, leading to a greater affinity for O_2 such that the bound O_2 cannot be released to the tissue.[3,4] However, as a gasotransmitter, CO is endogenously produced as a byproduct of heme's degradation to regulate proliferation, inflammation, vascular function, metabolism, and many more in the body.[1] As a result, while CO is anti-inflammatory and anti-apoptotic at physiological concentrations, it is anti-proliferative and pro-apoptotic at higher concentrations.[5] To determine the exposure time and appropriate doses of therapeutic CO for pharmaceutical purposes, COHb has been a precious tool.[5] In a placebo-controlled Phase I trial the safe dose of inhaled CO in a human body was determined to be at 3.0 mg per kg per hour dosing (daily for 10 days).[6] At this dose, the COHb levels in the blood stream were increased by 12% with no severe side effects.[6] This is equal to the COHb level of heavy smokers.[5] Figure 1 shows the dose response of CO in the human body.

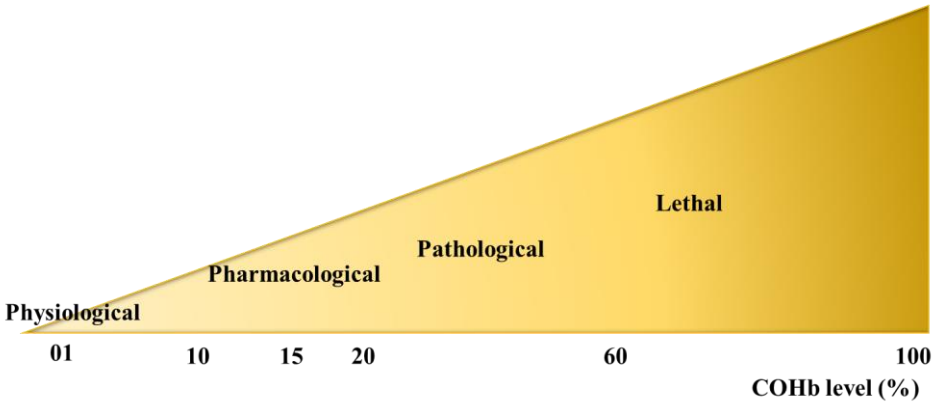

Figure 1. The dose response of CO in the human body

1.2. CO As a Therapeutic Agent

Owing to the many beneficial biological functions, including antiproliferative activity, regulation of inflammation, and modulation of blood vessel tone, CO has attracted great attention as a potential therapeutic agent.[1] Moreover, administration of exogenous CO in cancer cells inhibits cystathionine β-synthase (CBS), an enzyme known to have a cytoprotective effect.[1] CBS is a key enzyme that catalyzes the biosynthesis of cysteine, the limiting reagent in glutathione (GSH) production. Reducing the activity of CBS in the cancer cell decreases the GSH abundance in return. GSH or γ-l-glutamyl-l-cysteinyl-glycine is a major sulfur containing antioxidant in the human body, fighting against free radicals and oxidative stress.[7] As shown in Figure 2, during oxidative stress, the sulfur atom in GSH reacts with ROS and generates glutathione disulfide (GSSG). The GSH regenerates from GSSG via accepting electrons from NADPH.[8]

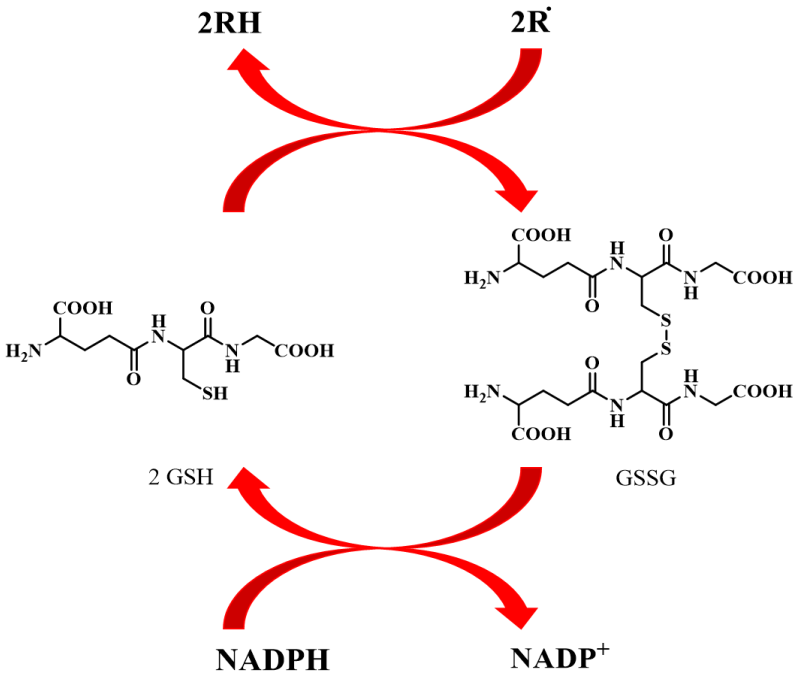

Figure 2. Role of GSH/GSSG during oxidative stress

Reducing the glutathione level increases the reactive oxygen species (ROS) production and reduces the antioxidant capacity of the cancer cell, leading to the induction of apoptosis.[9] This effect also increases the susceptibility of the cancer cells to the chemotherapy drugs.[9]

One of the mechanisms by which most chemotherapeutic such as doxorubicin or vincristine treat cancer is through the generation of excessive ROS. ROS induce apoptosis by damaging proteins, lipids, and DNA. However, the effectiveness of these chemotherapeutics is diminished by the drug resistance developed in cancer cells.[10] It has been shown that a high level of GSH caused by CBS overexpression in cancer cells is responsible for drug resistance.[11] Administration of CO to cancer cells, reduces the drug

resistance by inhibiting the CBS production and diminishing the GSH level, as a result decreasing the antioxidant capacity of cancer cells.[12]

In one study, CO was shown to mitigate chemotherapeutic resistance by sensitizing breast cancer cells to paclitaxel and doxorubicin by attenuating the GSH level through CBS inhibition.[11] In this study, exogenous CO mediated cell death by more than 40%.

Another mechanism by which the high level of GSH in cancer cells could lead to drug resistance and deactivation is through the binding of GSH through its sulfur atom to the chemotherapeutic, thus interfering with drug activity.[13] In another study, CO was demonstrated to lower the viability of ovarian cancer cells by sensitizing these cells to cisplatin by reducing GSH level.[13]

1.3. Delivery of Therapeutic CO

So far, the effect of exogenous CO in clinical and preclinical trials has been evaluated through inhalation or CO-releasing molecules.[1] However, in case of inhalation due to the low solubility of CO in the biological fluid, high concentrations of CO must be inhaled.[1] Moreover, CO inhalation suffers from lack of selectivity.[14]

The carbon monoxide releasing molecules (CORMs), however, offer more selectivity and controlled delivery of CO into a specific target. The release of CO from a series of transition metal carbonyls known as CO-RMs for therapeutic purposes was first introduced by Motterlini and co-workers in 2002.[15] CORMs release their CO ligands by either an internal or external trigger.[16] An internal trigger CORM might release the COs upon an enzymatic reaction.[16] The photo-activated CO releasing molecules or

"photoCORMs" release the CO ligands upon exposure to light, which serves as an external trigger (Figure 3). In photoCORMs the amount of released CO is a function of the incident light, allowing to determine the dosage of CO release.[16]

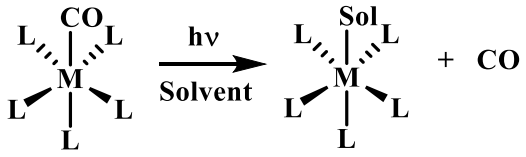

Figure 3. Photochemical CO dissociation from a photoCORM in a coordinating solvent (Solv).

photoCORMs

CO is coordinated to the metal through the C atom. Absorption of a photon causes M-C bond cleavage, and this leaves an open coordination site on the metal where a solvent molecule can coordinate. The advantage of photoCORMs is the use of light as a signal to determine the dose, time, and location of delivery.[16] An ideal photoCORM should be stable in the dark in an aqueous solution or commonly used drug delivery solvents such as DMSO as well as biological fluids such as plasma.[17] The photo-intermediates and photoproducts should be non-reactive and non-toxic.[18] Eventually, due to the poor penetration of UV light into the tissue and its deleterious effects on biological targets, an ideal photoCORM should be activated by visible or near-IR light, especially wavelengths in the phototherapeutic window (600-900 nm).[18]

Among photosensitive molecules, transition metal-based complexes offer some advantages, including structural diversity and easily tunable photophysical,

photochemical, and redox properties by ligand set variation around the metal center.[19] In addition, the kinetic and thermodynamic properties of such coordination complexes, including the rate of ligand exchange, can be easily tuned by rational ligand design.[19]

The $Mn_2(CO)_{10}$ and $Fe(CO)_5$ complexes shown in Figure 4 were the first two photoactive CORMs that were introduced by Motterlini and co-workers as pharmaceutical agents for CO delivery in 2002.[15] However, their activation under UV light, low solubility in aqueous media, and lack of tunability limited their applications and excluded them from further studies.

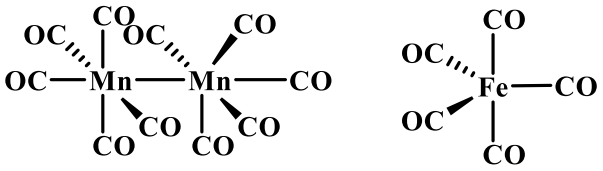

Figure 4. Early CORMs introduced by Motterlini et al.

The term "photoCORM" was first used by Ford et al. in 2010. In this study, they reported a photoactive water-soluble tungsten carbonyl complex $W(CO)_5(TPPTS)^{3-}$ (TPPTS: tris(sulphonatophenyl)phosphine) (Figure 5).

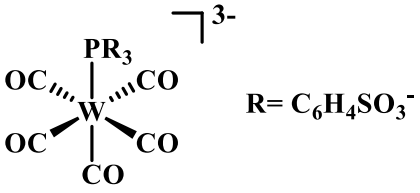

Figure 5. W-based photoCORM introduced by Ford et al.

This photoCORM was shown to release one equivalent of CO upon UV light irradiation, followed by the release of additional CO as a result of the autooxidation of the tungsten center.[20]

The water-soluble dicarbonylbis(cysteamine)iron(II) complex introduced by Westerhausen and co-workers in 2011 was the first visible light activated photoCORM (i.e., >400 nm).[21] Irradiation of this photoCORM with visible light resulted in the release of CO ligands in just a few minutes (Figure 6).

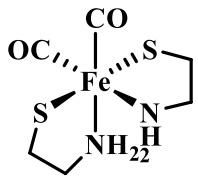

Figure 6. First visible light activated Fe-based photoCORM introduced by Westerhausen et al.

Choice of Metals in photoCORMs

The choice of metal in metal-based photoCORMs is of importance as their toxic or therapeutic response as pharmaceutical agents is dependent on their oxidation states.[22] For instance, while Cr^{+6} compounds are highly toxic, Cr^{+3} supplements can be purchased from supermarkets for their many health benefits, such as helping muscle development and lowering cholesterol.[23]

Generally, metals in groups 3,4, and 5 (Sc, Ti, and V triads) with oxygen sensitive oxidation states are avoided as they can only form metal-carbonyl bonds under reducing conditions.[24] Due to forming unsaturated 16 electrons complexes, metals from groups 9

and 10 are also avoided. A close scrutiny of the literature shows that the majority of reported metal-based photoCORMs are based on Cr, Mo, W, Mn, Re, Fe, and Ru from groups 6, 7, and 8. [25] The main drawback of the majority of these photoCORMs, however, is their activation under UV light irradiation. During the last decade, Mn(I)-tricarbonyl photoCORMs have received increasing attention owing to their ability to release CO ligands upon exposure to visible light. It is known that CO with its strong π-accepting properties can form strong bonds with low valent metal centers such as Mn(I) metal ions.[26] The *fac*-$[Mn(CO)_3]^+$ motif was among the first class of Mn-based photoCORMs to be investigated.[26] $[Mn(tpm)(CO)_3](PF_6)$ (tpm = tris(pyrazolyl)methane) was the first complex of these series reported by Schatzschneiderin in 2008.[27] This photoCORM releases 2 equivalents of CO and shows cytotoxicity against colon cancer cells upon photolysis with UV light.

CO As a Ligand

CO is a diatomic molecule, characterized by a triple bond between carbon and oxygen (C≡O) with high dissociation energy of 1070 $kJ \cdot mol^{-1}$.[28] CO is only slightly soluble in water (35 mg/L), as the protonated form of CO (HCO^+) is highly reactive in water. As mentioned previously, CO forms a strong bond with low valent metal centers. This can be further explained by the CO molecular orbital (MO) diagram.[24] The simplified MO diagram of CO is illustrated in Figure 7.

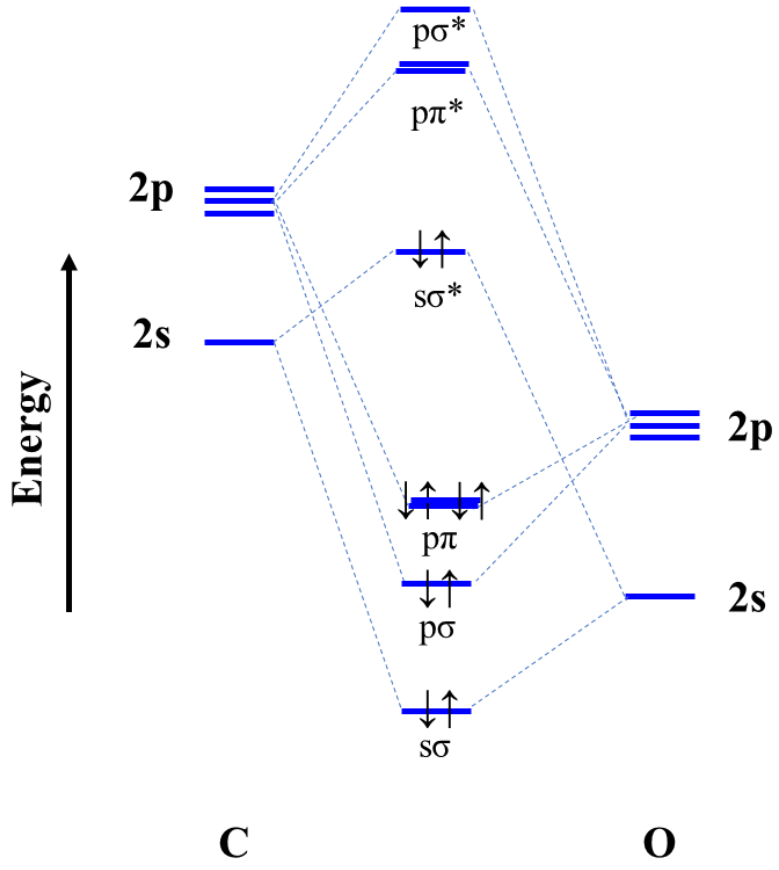

Figure 7. The molecular orbital diagram of CO.

As shown in Figure 8, donation of an electron pair from CO filled orbital (HOMO) to the empty d(σ) orbital of the metal center, results in the formation of a σ bond. A metal ion center with a low oxidation state such as Mn(I) can easily donate back its electron from its high energy d(π) orbital to the empty CO π* orbital to form a metal-CO π-backbonding interaction.[24]

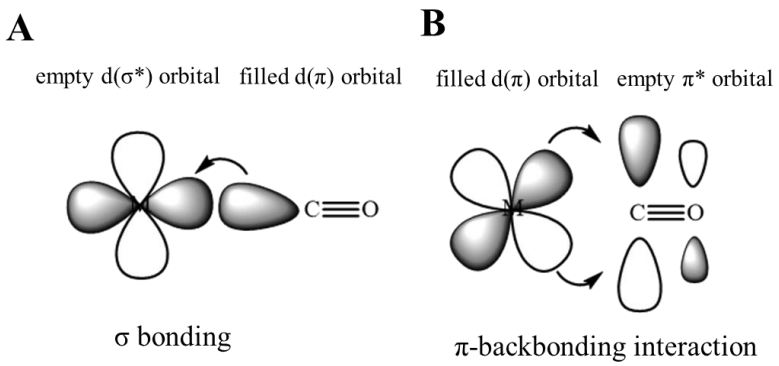

Figure 8. Interactions between an empty d(σ) orbital of the metal and filled σ molecular orbital of CO (σ bonding) (A) and interaction between a filled d(π) orbital of the metal and empty π* molecular orbital of CO (π-backbonding) (B).

Mechanisms of CO Dissociation

CO loss from many first-row transition metals photoCORMs is initiated by the population of the lowest energy metal-to-ligand charge-transfer (MLCT) excited state by absorption of a photon.[29] An MLCT transition results from the promotion of an electron from a primarily metal dπ-based orbital (the highest-occupied molecular orbital, or HOMO) to a primarily ligand-based π* orbital (the lowest unoccupied molecular orbital, or LUMO).[30] The MLCT transition in the calculated HOMO and LUMO for fac-[Mn(bpy)$(CO)_3$Br] (bpy: 2,2′-Bipyridine) with density functional theory (DFT) is shown in Figure 9. In this transition, while HOMO is mainly spread over (Mn–CO)dπ orbitals and p orbital of Br^-, the LUMO is located on π* orbital of bpy ligand. Population of the MLCT excited state reduces the electron density on the metal center, thus weakening the metal-CO π-backbonding interaction.[30]

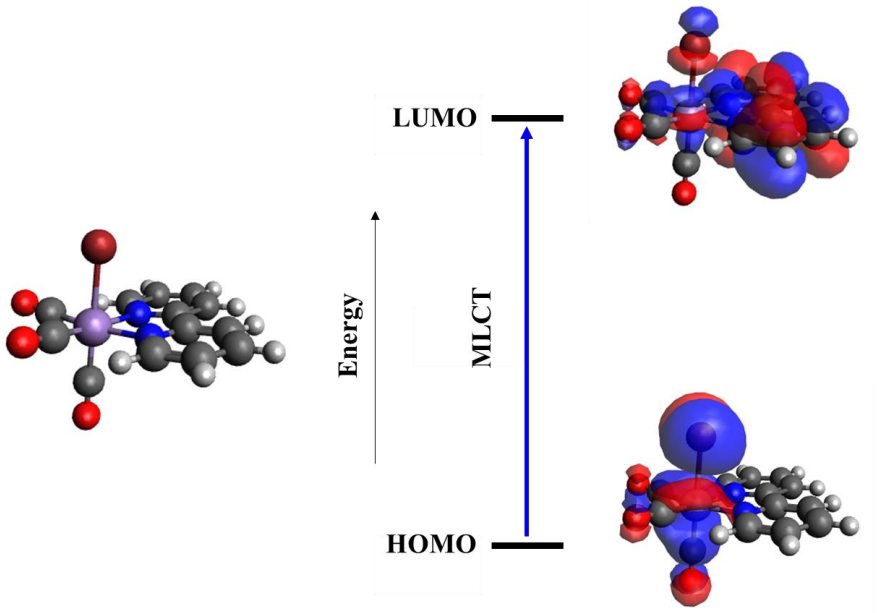

Figure 9. The MLCT transition from the HOMO which is mainly centered on the Mn center and the monodentate ligand to the LUMO which is mainly composed of the bidentate ligand.

Choice of Ancillary Ligands in photoCORMs

The MLCT absorption can be shifted into the visible region by tuning the HOMO and LUMO through the mono/bidentate ligand variations around the metal center. In a study performed by Mascharak and his group, they showed that the HOMO can be adjusted by the monodentate ligand, which is directly bound to the metal center.[31]

A π-donating monodentate ligand, such as Br^-, increases the energy level of HOMO by increasing the electron density on the metal. This will decrease the gap between the HOMO-LUMO, shifting the absorbance to the lower energy. In contrast, a π-accepting monodentate ligand, such as CH_3CN, decreases the energy level of HOMO by reducing the electron density on the metal.[31]

On the other hand, the LUMO becomes more stabilized by increasing the π-conjugation of the multidentate ligands, or by introducing an electron-withdrawing substituent on the NN bidentate ligand which increases the ligand's π-acidity.[31]

The quantum yield of CO dissociation (Φ_{CO}), which is defined as moles of CO lost over the moles of absorbed photons, is also affected by the ligand sets around the metal center. As the π-acidity of the NN ligand and the π-donating ability of the monodentate ligand increase, the quantum yield also increases.

For example, Mascharak and his group have reported a series of fac-[Mn(NN)(CO)$_3$Br] compounds, in which NN = 2-quinoline-N-(2′-methylthiophenyl)methyleneimine (qmtpm), (2-phenyliminomethyl)quinoline (pimq), and 2-pyridyl-N-(2′-methylthiophenyl)methyleneimine (pmtpm), which shows increasing Φ_{CO} with increasing NN conjugation or π-acidity (qmtpm > pmtpm > pimq).[32] The structure of the complexes is shown in Figure 10. In the case of the monodentate ligand effect, Φ_{CO} in fac-[Mn(qmtpm)(CO)$_3$L] photoCORMs decreases by exchange of π-donating Br^- with the π-accepting CH3CN ligand from 0.37 to 0.2.[32]

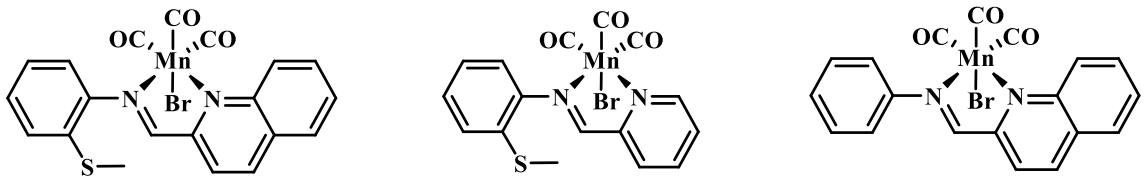

Figure 10. Structures of fac-Mn(NN)(CO)$_3$Br in order of increasing π-acidity of NN ligand.

1.4. Photodynamic Therapy (PDT)

Photodynamic Therapy (PDT) refers to a non-invasive therapeutic procedure for cancer treatment. The discovery of this phenomenon, previously known as "photodynamic action" is dated back to 1897-1898, when Oscar Raab, a student at the Munich Pharmacological Institute, realized that paramecium cells stained by fluorescing dyes are destroyed under sunlight irradiation.[33] The PDT approach utilizes a non-toxic photoactive compound known as photosensitizer (PS) to produce ROS in reaction with molecular oxygen under light irradiation. The generated ROS interfere with cancer cells' function by damaging DNA, lipids, or proteins.

When illuminated, the PS absorbs a photon and gets excited to the short-lived singlet excited state (S_x, x=1, 2, 3, …). If the PS has been excited to the higher excited state i.e. x= 2,3,…, it will relax back to the first excited state, or S1, through vibrational relaxation, as the fluorescence emission always occurs from S1 to S0.[34] From S1, the PS can either relax back to S0 by emitting photons (fluorescence) or undergo intersystem crossing (ISC) to populate the triplet excited state (T1).[34] From T1, the PS can return to the ground state (S0) by emitting light (phosphorescence), or alternatively, it can react with molecular oxygen to produce ROS. Triplet excited states are known to be chemically reactive, as they have a longer lifetime in comparison with singlet excited states.[35] T1 reacts with molecular oxygen in one of the two ways, known as Type I and Type II mechanisms. The Type II process is depicted in Figure 11.

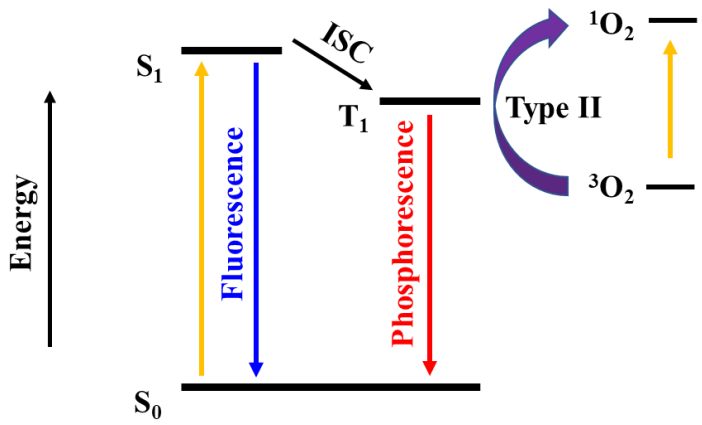

Figure 11. Simplified Jablonski diagram for Type II mechanism

In the Type II process, the T1 state transfers its energy to the molecular oxygen in its ground state ($^3O_2$), to form an excited state oxygen ($^1O_2$). The type I process is more complicated and involves the formation of PS radical anion by one-electron transfer to produce hydrogen peroxide (H_2O_2), superoxide anion ($O_2^{\bullet-}$), and hydroxyl radical (OH^-).[36] It is generally agreed that most PS in PDT follow a Type II mechanism and $^1O_2$ is the main destructive species in PDT. It is worth mentioning that energy transfer in the Type II process for $^1O_2$ production has a higher rate ($k \approx 1–3 \times 10^9\ M^{-1}\ s^{-1}$) compared with electron transfer in Type I ($\approx k \leq 1 \times 10^7\ M^{-1}\ s^{-1}$ for $O_2^{\bullet-}$).[37]

Singlet Oxygen ($^1O_2$)

While the molecular oxygen in its ground state is a spin triplet ($^3\sum_g^-$), it has two low-lying singlet excited states known as $^1\Delta_g$ and $^1\sum_g^+$. The first excited state with an electronic configuration of $^1\Delta_g$ is called singlet oxygen and is lying 94 kJ mol^{-1} above the ground state.[38] The $^1\Delta_g$ state has a relatively long lifetime, as the O_2 $^1\Delta_g \rightarrow {}^3\sum_g^-$ is

forbidden.[35] In contrast, due to the spin-allowed transition $^1\sum_g^+ \rightarrow {}^1\Delta_g$, the O_2 $^1\sum_g^+$ state has a short lifetime.[35] The electronic states of oxygen are depicted in Figure. 12.

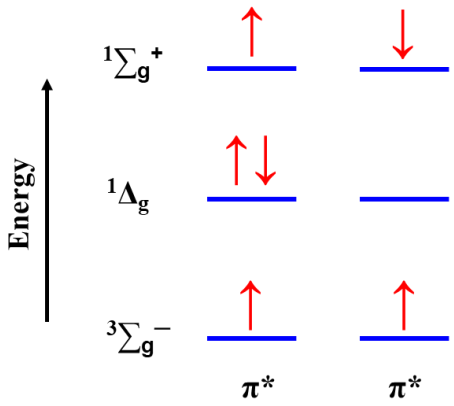

Figure 12. Schematic representation of molecular oxygen electronic states

Once $^1O_2$ is formed, it can undergo a non-radiative decay, oxidize other molecules, or undergo a radiative decay $^1\Delta_g \rightarrow {}^3\sum_g^-$ and emits at 1270 nm.[39] Proteins, nucleic acids, lipids, and vitamins are the major targets for singlet oxygen. Singlet oxygen damages the amino acids by an oxidative attack at electron-rich unsaturations and sulfur.[40] Singlet oxygen can also damage DNA by attacking guanosine residues to form 8-oxo-2'-deoxyguanosine.[40]

Singlet Oxygen Detection

The emission at 1270 nm would allow for direct detection of $^1O_2$ in the biological media. However, due to the low emission quantum yield and high reactivity of $^1O_2$ this method remains challenging.[39] Alternatively, $^1O_2$ can be detected by indirect methods such as quenchers, and fluorescence probes.[36] Fluorescence probes are emissive

molecules that are employed for studying $^1O_2$ through changes in fluorescence properties such as fluorescence quantum yield, intensity, and lifetime upon reaction with $^1O_2$.[41] 1,3,-diphenyllisobenzofuran (DPBF) and singlet oxygen sensor green (SOSG) are common examples of such probes. SOSG is only weakly emissive in the blue region. However, after reacting with $^1O_2$ it becomes emissive at 530 nm.[42]

Ideal Photosensitizer

PDT has been successfully used for various cancerous and non-cancerous conditions. Porfimer sodium, or Photofrin is one of the earliest clinical PDT photosensitizers that was approved in the 1990s for treating cancers. Photofrin is a hematoporphyrin derivative consisting of porphyrin units connected by ethers and esters. Photofrin with an excitation wavelength of 630 nm and a singlet oxygen quantum yield of 0.89 is still the most efficient photosensitizer.[43] Photofrin is widely used in the UK for obstructing esophageal and lung cancer treatment. However, despite the widespread use of Photofrin, it suffers from some limitations, including but not limited to poor tissue penetration (3-5 mm) due to low absorbance in the red region, and low impurity as it is composed of 60 molecules.[44]

These shortcomings have inspired the development of new and more efficient photosensitizers over the last few decades. An ideal photosensitizer should have a high extinction coefficient in the IR and NIR regions to reach deeper into the tissue. To efficiently populate the triplet excited state, an ideal photosensitizer should have a high quantum yield for ISC and singlet oxygen. It should show low dark toxicity and high

photostability. A photosensitizer should also be cost effective with high yielding and a suitable synthetic route.[45]

So far, the majority of photosensitizers for clinical usage have been based on cyclic tetrapyrroles. However, tuning their photophysical and photochemical properties has remained challenging, as such structures are hard to chemically modified.[46] Such limitations have led to the investigation of non-porphyrin photosensitizers.[46] Boron-dipyrromethenes (BODIPYs) are a new class of photosensitizers that have shown potential solutions to the previously mentioned limitations.

BODIPY

Boron-dipyrromethenes, 4,4- difluoro-4-borata-3a-azonia-4a-aza-s-indacene or BODIPY is an emissive organic dye characterized by a high extinction coefficient in the visible to IR/NIR region (up to 120 000 M^{-1} cm^{-1}), high photostability and fluorescent quantum yield, as well as easy tunable structure and synthetic versatility.[47]

The spectroscopic and chemical features of BODIPY dyes and their derivatives can be easily altered through functionalization at the meso and/or pyrrole C-ring positions, and the boron atom.[48] The structure of the BODIPY core is shown in Figure 13.

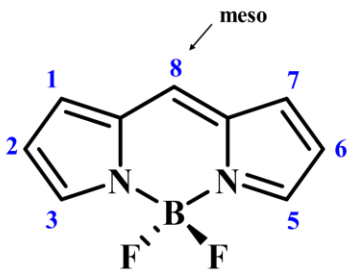

Figure 13. BODIPY core structure

While substitutions at the 3/5 and 2/6 positions result in a bathochromic shift of the absorbance and fluorescence wavelength, the meso position is being used to make the molecule water-soluble by introducing groups such as carboxyl anion or polymer chain.[49]

Despite the mentioned advantages, the high fluorescence quantum yields of BODIPY dyes have resulted in low ISC quantum efficiency and negligible population of triplet states in these dyes. It was not until 2005, that Nagano et al. showed that BODIPY could be used as an efficient photosensitizer to produce singlet oxygen by introducing heavy atoms at the 2/6 positions of the BODIPY core.[50]This effect is known as the heavy atom effect. Electrophilic substitution at the 2/6 positions with heavy atoms such as I or Br, efficiently increases the ISC rate through spin-orbit coupling, resulting in the population of triplet excited states.[50]

1.5. Multi-targeting Anticancer Drugs

For a long time, the strategy of "one molecule, one target" has been used in medicinal chemistry.[51] Despite the successful treatments of many diseases with this technique, there are still other diseases such as cancer in which a single therapy is not as effective.[51] Recent studies show that the drug efficacy can be improved by multi-targeted

therapeutics by either drug combinations (cocktail therapy) or "single molecule, multiple targets" strategy.[52,53] The latter offers several advantages over cocktail therapy. It reduces the risk of drug interactions and helps to overcome drug resistance.[54]

Cis-diammineplatinum(II) complex of curcumin is one example of a "single molecule, multiple targets" strategy. Curcumin is known for its anti-inflammatory properties and producing reactive singlet oxygen. This complex is able to release the cisplatin adduct and the curcumin upon exposure to the light.[55] Another compound, Dichlorido(toluene)[3-(1′-cyano-2′-(3″-hydroxy-4″-methoxyphenyl)(Z) ethenyl)pyridine]ruthenium(II) complex can bind to the DNA and interfere with mTOR signaling.[56]

As previously discussed, it has been shown that administration of CO along with a chemotherapy drug like doxorubicin increases the susceptibility of the cells to drug. Coupling the BODIPY ligand with the Mn(I) photoCORM not only generates singlet oxygen and releases CO under visible light but also might increase the susceptibility of the cancer cells toward singlet oxygen and reduces their resistance.

1.6. Project Description

The primary goal of this project is to investigate the electronic and steric effects of ligand set variation on the photophysical, photochemical, and redox properties, as well as the formation of photo intermediates in Mn(I) monometallic photoCORMs complexes. To gain a good understanding of these fundamental properties and the factors that dictate the photo intermediate formation, there is a need to study a simpler system first.

Accordingly, to study the electronic effect of ligands, a series of Mn(I) photoCORMs with the general structures of *fac*-$[Mn(NN)(CO)_3(L)]^{n+}$ compounds, in which NN = 4,4′-dimethylester-2,2′-bipyridine (dmebpy), 2,2′-bipyridine (bpy), or 4,4′-dimethyl-2,2′-bipyridine (Me_2bpy), and L = Br^- (n = 0) or pyridine (py; n = 1) were synthesized and their photophysical and photochemical properties were studied. The electronic effect of π-donor Br^- and π-acceptor py monodentate ligand (L), as well as the impact of varying the π-acidity of the NN bidentate ligand through the 4,4′-substitution on both the quantum yield for CO dissociation (Φ_{CO}) and the photo-generated intermediates investigated.

Moreover, in an effort to study the steric effect of NN ligand, two methyl substitutions were introduced on the 6,6′ positions of bpy ligand and their impacts on the photophysical and photochemical properties, as well as the photo intermediates were studied, and compared with the 4,4′-dimethyl-2,2′-bipyridine analogues.

Lastly, two Mn(I) photoCORMs sensitized with a fluorescent BODIPY, $Mn(CO)_3$(bpy-R-BODIPY)Br (R = H or I), were synthesized and their photophysical and photochemical properties, as well as $^1O_2$ production were investigated under low energy visible light irradiation.

Chapter 2: Impact of Mn(I) PhotoCORM Ligand Set on Photochemical Intermediate Formation during Visible Light-Activated CO Release

This chapter is adapted from a published article entitled "Impact of Mn(I) PhotoCORM Ligand Set on Photochemical Intermediate Formation during Visible Light-Activated CO Release" By Pordel S., and White J.K. *Inorganica Chimica Acta*, no. 500 (2020): 119206. [57]

2.1. Introduction

Carbon monoxide plays important roles in cell signaling pathways and has therapeutic potential as an anti-cancer agent.[6,58–61] CO is known to be anti-inflammatory and anti-apoptotic at low concentrations in healthy cells, yet pro-apoptotic and anti-proliferative at high concentrations in cancer cells.[6] Recently, CO was shown to sensitize various cancer cells to chemotherapy drugs such as cisplatin, doxorubicin, and camptothecin.[13,59] Clinical storage and delivery of gaseous CO presents health risks, as inhaled CO decreases the availability of O_2 to tissue and causes asphyxiation as it binds to hemoglobin with high affinity.[17] To overcome the safety issues concerning CO storage and delivery, a class of molecules called photoCORMs, or photoactivated CO releasing molecules, were developed to provide spatial and temporal control of CO delivery.[16,17,31] Transition metal-based photoCORMs provide a convenient method for storage and inactivation of CO in the form of chemical bonds until the M-CO bond is broken upon population of an excited state with UV or visible light.

PhotoCORMs have been reported featuring transition metals such as Fe, Ru, Cr, Mo, and W,[15,21,31,62–69] with much recent emphasis on Re and Mn.[11,13,16,18,26,31,32,70–89]

Mn(I)-tricarbonyl photoCORMs have been the focus of many researchers due to the ability to activate Mn-CO bond dissociation using visible light,[16,31,68] as a drawback of fac-[Re(NN)(CO)$_3$(phosphine)]n+ photoCORMs (NN = bidentate diimine ligand) is their requirement for triplet ligand field (3LF) state population with UV irradiation ($\lambda < 400$ nm) to initiate CO dissociation.[71,76,82,83] In contrast, analogous fac-[Mn(NN)(CO)$_3$Br] complexes effectively release CO as a result of populating a metal-to-ligand charge transfer (MLCT) excited state, typically achieved with visible light. [16,31,68] In this MLCT state, electron density is transferred from a molecular orbital (MO) with significant metal character to an MO with significant NN(π^*) character, thus weakening the π-backbonding from a filled Mn d-orbital to an empty CO(π^*) orbital and labilizing the coordinated CO.[90] Mascharak and co-workers have demonstrated that increased π-acidity of NN in fac-[Mn(NN)(CO)$_3$Br] photoCORMs increases the CO release quantum yield (ΦCO). For example, the series of fac-[Mn(NN)(CO)$_3$Br] compounds, in which NN = (2-phenyliminomethyl)quinoline (pimq), 2-quinoline-N-(2′-methylthiophenyl)methyleneimine (qmtpm), and 2-pyridyl-N-(2′-methylthiophenyl)methyleneimine (pmtpm), exhibits increasing Φ_{CO} with increasing NN conjugation (qmtpm > pmtpm > pimq).[32] Given that the low energy visible and NIR light in the 600-900 nm range (termed the "phototherapeutic window") is desirable for light-activated drugs,[91] the ability to enhance the ligand dissociation activity by lowering the activation energy is a great benefit of Mn(I) photoCORMs.

Recent reports have investigated the impact of the monodentate ancillary ligand, L, on CO release. Replacing a π-donating Br^- with a π-accepting PPh_3 decreases the rate

of CO release from the fac-[Mn(azpy)$(CO)_3$(L)]$^{n+}$ photoCORMs.[72,74] Similarly, the π-accepting CH_3CN ligand in fac-[Mn(qmtpm)$(CO)_3(CH_3CN)]^+$ and fac-[Mn(pmtpm)$(CO)_3(CH_3CN)]^+$ photoCORMs decreases the rate of CO release relative to the Br− analogues.[30] In both sets of compounds, the π-accepting ligand (PPh_3 or CH_3CN) blue shifts the MLCT band as it stabilizes the Mn(I)-based HOMO relative to L = Br^-. Mn(I) tricarbonyl compounds featuring imidazolyl ligands as the ancillary L have been reported for antibacterial and antiparasitic activity, but the photochemistry was not studied.[88] Imidazolyl- and piperazinyl-functionalized dansyl dyes were coupled to fac-[Mn(phen)$(CO)_3$(L)]$^+$ photoCORMs, where L = imidazoledansyl (Imdansyl) or 1-dansylpiperazine (Pipdansyl).[80,92] While the photochemistry of these compounds were not directly compared, they were reported to release CO with Φ_{CO} = 0.35 ± 0.03 and 0.39 ± 0.03 for L = Imdansyl[92] and Pipdansyl,[80] respectively, when irradiated with broad band visible light.

While this class of fac-[Mn(NN)$(CO)_3$(L)]$^{n+}$ photoCORMs has been primarily studied for the impact of ligand set on photophysical properties, CO dissociation efficiency and rate, and photocytotoxicity, fewer studies have focused on the photochemical intermediates formed during the ligand dissociation processes as a function of bidentate NN and monodentate L variation. Several fac-[Mn(NN)$(CO)_3$Br] photoCORMs report the formation of a dicarbonyl intermediate following exchange of one equatorial CO by a coordinating solvent molecule.[93] To the best of our knowledge, the only reports of structural information following the release of one CO from a Mn(I) photoCORM featuring a π-accepting monodentate L ligand is fac-[Mn(κ2-

tpy)$(CO)_3(CH_3CN)]$+ (and related compounds in the series with substituted tpy ligands), which forms cis-$[Mn(\kappa3\text{-tpy})(CO)_2(CH_3CN)]^+$ when irradiated in CH_3CN, as an equatorial CO is displaced by the uncoordinated py ring from the κ2-tpy which acts as a pre-organized chelating group.[77,78]Much information remains to be ascertained about the photochemical intermediate structures upon visible light-activated CO release from Mn(I) photoCORMs.

To probe the impact of the NN π-acidity as well as the influence of a π-donating or π-accepting monodentate ancillary ligand L on the efficiency and mechanism of photochemical CO dissociation in fac-$[Mn(NN)(CO)_3L]^{n+}$ photoCORMs, we have studied a series of fac-$[Mn(NN)(CO)_3Br]$ and fac-$[Mn(NN)(CO)_3(py)]$+ complexes (pictured in Figure 14A). In this series, NN = 4,4′-dimethyl-2,2′-bipyridine (Me_2bpy), 2,2′-bipyridine (bpy), or 4,4′-dimethylester-2,2′-bipyridine (dmebpy), and py = pyridine. These NN ligands are listed in order of increasing π-acidity as a result of their 4,4′-substituents. The impact of π-donating Br^- was investigated in comparison to π-accepting pyridine (py). While Br− is a commonly employed L in Mn(I) photoCORMs, py was chosen in this analysis because it has not been studied as an ancillary ligand in Mn(I) photoCORMs. Analytical techniques such as cyclic voltammetry, Fourier transform infrared (FTIR) spectroscopy, and electronic absorption spectroscopy indicate that the nature of L significantly impacts the electron density on the metal center, while varying the π-acidity of NN impacts the visible light absorption profile and only has a minor impact on the Mn(I) center's electron density. Irradiation of the compounds with visible light promotes the release of all three CO ligands, and the mechanism by which these

ligands are exchanged with solvent depends on the nature of L, as observed by ^{1}H NMR and FTIR spectroscopy. In particular, the nature of L dictates whether the first CO exchanges with a solvent molecule in the position trans to L or trans to NN (Figure 14B). Further irradiation of each complex eventually releases L and forms the same final dicarbonyl intermediate prior to decomposition and release of the remaining two CO ligands. In agreement with related compounds, the trend in the first CO release quantum yield as a function of NN π-acidity is observed, and in general, CO release is more efficient when L = Br^{-} compared to py.

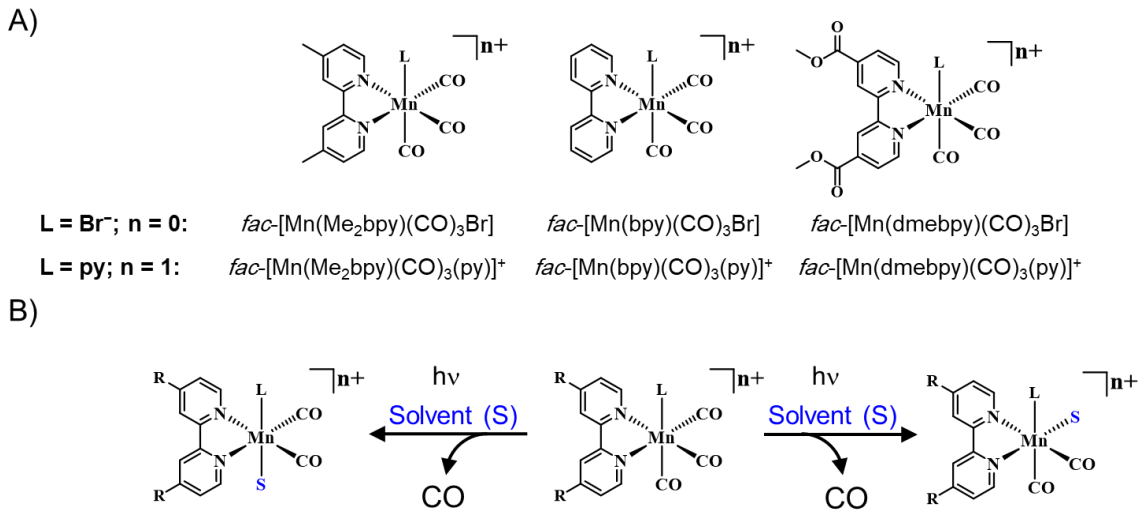

Figure 14. Structural representations of the *fac*-$[Mn(NN)(CO)_3(L)]^{n+}$ compounds, where NN = 4,4′-dimethyl-2,2′-bipyridine (Me_2bpy), 2,2′-bipyridine (bpy), and 4,4′-dimethylester-2,2′-bipyridine (dmebpy), and L = Br^{-} (n = 0) and py (n = 1) (A), and a scheme highlighting the two possible initial CO dissociation steps in *fac*-$[Mn(NN)(CO)_3(L)]^{n+}$ complexes (B).

2.2. Experimental Details

Materials and Reagents

All materials were used without further purification unless otherwise noted. Bromopentacarbonylmanganese(I) was purchased from Strem Chemicals. Silver trifluoromethanesulfonate (AgOTf) was purchased from Acros Organics. Trimethylamine N-oxide was purchased from TCI America. Pyridine, acetonitrile, diethyl ether, dichloromethane, chloroform, hexane, and methanol were purchased from Fisher Scientific. Tetrabutylammonium hexafluorophosphate (98 %; recrystallized from ethanol prior to electrochemical analyses) and potassium tris(oxalato)ferrate(III) were purchased from Alfa Aesar. Acetonitrile-d3 was purchased from Cambridge Isotope Laboratories. The previously reported compounds fac-[Mn(bpy)$(CO)_3$Br], fac-[Mn(Me_2bpy)$(CO)_3$Br], and fac-[Mn(dmebpy)$(CO)_3$Br] were prepared following published procedures.[88,94]

Methods and Instrumentation

All reactions and experiments were carried out in the absence of light to prevent photodecomposition of Mn(I) species.

Synthesis of fac-[Mn(bpy)$(CO)_3$(py)](OTf)

The compound was synthesized by a modification to a previously reported procedure.[95] The fac-[Mn(bpy)$(CO)_3$Br] (30 mg, 0.080 mmol) and AgOTf (30 mg, 0.11 mmol) were added to 20 mL of CH_2Cl_2 and stirred at room temperature for 16 h. To remove the precipitated AgBr, the mixture was filtered through Celite, and the solvent was removed under reduced pressure. The remaining solid was dissolved in 20 mL of methanol, and 1 mL of pyridine was added. The solution was heated at reflux under

argon for 16 h. After cooling to room temperature, the solvent was removed and the yellow residue was dissolved in 5 mL of CH_2Cl_2 and added dropwise to 150 mL of hexane to induce precipitation. The yellow solid was collected by vacuum filtration. Yield: 35 mg (0.066 mmol, 87 %). 1H NMR (500 MHz, CD_3CN): δ 9.34 (2H, d), 9.27 (2H, d), 8.19 (2H, m), 7.78 (2H, m), 7.75 (1H, m), 7.24 (2H, m). Elemental analysis calculated for C19H13O6N3MnF3S: 43.60% C, 2.50% H, 8.02% N, 6.12% S. Found: 43.36% C, 2.47% H, 7.97% N, 5.95% S. HR-ESI(+)-MS (CH_3CN): [M−OTf]+, m/z = 374.03293 (calcd m/z = 374.03319).

Synthesis of fac-[Mn(Me$_2$bpy)(CO)$_3$(py)](OTf)

This compound was repaired as described above using fac-[Mn(CO)$_3$(Me$_2$bpy)Br] (10 mg, 0.024 mmol) and AgOTf (10 mg, 0.039 mmol). Yield: 6.5 mg (0.0011 mmol, 67 %). 1H NMR (500 MHz, CD_3CN): δ 9.14 (2H, d), 8.16 (2H, d), 8.12 (2H, s), 7.77 (1H, m), 7.60 (2H, m), 7.24 (2H, m), 2.53 (6H, s). Elemental analysis calculated for C21H17O6N3MnF3S: 43.60% C, 2.50% H, 8.02% N, 6.12% S. Found: 43.36% C, 2.47% H, 7.97% N, 5.95% S. HR-ESI(+)-MS (CH_3CN): [M−OTf]+, m/z = 402.06558 (calcd m/z = 402.06449).

Synthesis of fac-[Mn(dmebpy)(CO)$_3$(py)](OTf)

This compound was repaired as described above using fac-[Mn(CO)$_3$(dmebpy)Br] (150 mg, 0.30 mmol) and AgOTf (150 mg, 0.58 mmol). Yield: 110 mg (0.17 mmol, 57 %). 1H NMR (500 MHz, CD_3CN): δ 9.52 (2H, d), 8.80 (2H, s), 8.22 (2H, dd), 8.13 (2H, m), 7.76 (1H, m), 7.23 (2H, m), 4.0 (6H, s). Elemental analysis calculated for C23H17O10N3MnF3S: 43.20% C, 2.68% H, 6.57% N, 5.01% S. Found: 42.93% C,

2.69% H, 6.30% N, 4.95% S. HR-ESI(+)-MS (CH_3CN): [M−OTf]+, m/z = 490.04585 (calcd m/z = 490.04415).

Synthesis of [Mn(dmebpy)$(CO)_2(CH_3CN)_2$](OTf)

This complex was synthesized according to previously published procedure.[93] A mixture of fac-[Mn(dmebpy)$(CO)_3$Br] (100 mg, 0.204 mmol) and AgOTf (120 mg, 0.467 mmol) in 25 mL of CH_3CN was stirred at rt overnight. To remove the AgBr, the solution was filtered through Celite, the solvent was removed under vacuum, and the remaining solid was washed with ether. The resulting solid and trimethylamine N-oxide (45 mg, 0.60 mmol) were then dissolved in 10 mL of anhydrous CH_3CN and stirred for 5 h at room temperature. The mixture was filtered through Celite and the solvent was removed under reduced pressure. The remaining solid was dissolved in 5 mL of CH_2Cl_2 and added dropwise to 150 mL of hexanes. The solid was collected by vacuum filtration. The 1H NMR spectrum showed a mixture of two isomers, cis,cis-[Mn(dmebpy)$(CO)_2(CH_3CN)_2]^+$ and cis,trans-[Mn(dmebpy)$(CO)_2(CH_3CN)_2]^+$. Yield: 20 mg, (0.032 mmol, 16 %). cis,cis-[Mn(dmebpy)$(CO)_2(CH_3CN)_2]^+$ 1H NMR (500 MHz, CD_3CN): δ 9.19 (1H, dd), 9.00 (1H, dd), 8.94 (1H, s), 8.75 (1H, dd), 8.20 (1H, dd), 7.75 (1H, dd), 4.05 (3H, s), 3.98 (3H, s). cis,trans-[Mn(dmebpy)$(CO)_2(CH_3CN)_2]^+$ 1H NMR (500 MHz, CD_3CN): δ 9.75 (2H, dd), 8.97 (2H, s), 8.16 (2H,dd), 4.04 (6H, s). HR-ESI(+)-MS (CH_3CN): [M−OTf]+, m/z = 465.059 (calcd m/z = 465.06).

^{1}H NMR

^{1}H NMR spectra were recorded on a Bruker Ascend 500 MHz spectrometer at 298 K. The spectra were calibrated to residual solvent peaks (acetonitrile at δ = 1.94 ppm).

High Resolution Electrospray Ionization Mass Spectrometry

HR-ESI(+)-MS spectra were obtained using a Thermo Fisher Scientific Q Exactive Plus hybrid quadrupole–Orbitrap mass spectrometer in the positive ion mode. 1 μM solution of each compound in CH_3CN was injected into the ESI source for ionization. The injection flow rate was 50 μL/min, the applied potential for ionization was 4.0 kV, and the scan range was m/z 100–1500.

Fourier Transform Infrared Spectroscopy (FTIR)

FTIR spectra were recorded with a Shimadzu IRAffinity-1S Fourier transform infrared spectrophotometer in a CaF¬2 liquid IR cell using CH_3CN solvent.

Cyclic Voltammetry

The electrochemical experiments were performed with a BASi Epsilon EClipse electrochemical analyzer (Bioanalytical Systems, Inc.; West Lafayette, Indiana, USA) with 1 mM complex in acetonitrile with 0.1 M n-Bu4NPF6 supporting electrolyte under N_2 at room temperature with a scan rate of 200 mV/s. The reference, working and auxiliary electrodes were Ag/AgCl (3 M NaCl(aq)), glassy carbon (3 mm diameter), and Pt wire, respectively. Ferrocene (Fc) was added to the solution following each measurement, and the potentials were referenced to the Fc+/Fc couple (E1/2 = +0.44 V

vs. Ag/AgCl, ΔE_p = 0.090 V in CH_3CN). This potential agrees with the reported value vs Ag/AgCl in CH_3CN.[96]

Electronic Absorption Spectroscopy

Electronic absorption spectra were obtained using an Agilent Cary 8454 diode array UV-visible spectrophotometer with 1 nm resolution and 0.5 s integration time in a 1 × 1 cm quartz cuvette at 25 °C. Extinction coefficient measurements in CH_3CN were carried out in triplicate.

Photolysis Experiments

All photolysis experiments were performed using either 405 or 470 nm LEDs (Luxeon Star LEDs, Quadica Developments, Inc., Lethbridge, Alberta, Canada). The sample was dissolved in CH_3CN in a CaF_2 cell (for FTIR analysis) or in a 1 × 1 cm quartz cuvette (for electronic absorption analysis) or CD3CN in an NMR tube (^{1}H NMR analysis), exposed to the appropriate LED for intervals of time, and analyzed by the appropriate spectroscopic method. Ferrioxalate chemical actinometry[97] was used to determine that the photon flux of the 405 and 470 nm LEDs were (5.7 ± 0.1) × 10−8 and (2.0 ± 0.1) × 10−8 mol photons/s, respectively. The quantum yield of CO dissociation was measured by monitoring the decreases in absorption at very early photolysis times (< 10 % change in absorbance) as a function of time in CH_3CN in a 1 × 1 cm quartz cuvette at room temperature. All the prepared samples had the same absorbance at the irradiation wavelength. The plot of the moles of reactant vs irradiation time resulted in a linear trend, and the slope represented the rate of moles of reactant lost. The value of Φ_{CO} was calculated by dividing the rate of moles of reactant lost by the photon flux for the LED.

The values were corrected for the fraction of light absorbed by the sample at the irradiation wavelength.

Computational Methods

Using the M06 level[98,99] of density functional theory (DFT) in the Gaussian 16 program,the geometries for each of the fac-[Mn(NN)$(CO)_3$Br], fac-[Mn(NN)$(CO)_3$(py)]$^+$, and proposed photochemical intermediates were fully optimized with the SMD continuum solvation model for CH_3CN solvent.[100] The 6-31G* basis set was used for H, C, N, and O,[101] and the SDD energy consistent pseudopotentials were used for Mn and Br.[102] Frequency analysis was performed after geometric optimization to confirm the presence of local minima on the potential energy surfaces. The calculated C-O stretching frequencies were obtained using the Avogradro program (Version 1.2.0)[103] and multiplied by a frequency scaling factor of 0.96.

2.3. Results and Discussion

Synthesis and Characterization

The *fac*-[Mn(NN)$(CO)_3$Br] complexes (NN = dmepby, bpy, and Me_2bpy) were synthesized according to previously reported procedures by heating at reflux a solution of the appropriate NN with $Mn(CO)_5Br$ in Et2O.[88,94] We adapted the previously reported procedure[95] for the preparation of fac-[Mn(bpy)$(CO)_3$(py)]$^+$ to synthesize the new complexes fac-[Mn(Me2bpy)$(CO)_3$(py)]$^+$ and fac-[Mn(dmebpy)$(CO)_3$(py)]$^+$. The appropriate fac-[Mn(NN)$(CO)_3$Br] was reacted with AgOTf in CH_2Cl_2 to replace Br^- with weakly coordinating OTf^-, followed by the reaction with an excess of py in MeOH to produce fac-[Mn(NN)$(CO)_3$(py)](OTf). We attempted to synthesize cis,cis-

$[Mn(dmebpy)(CO)_2(CH_3CN)_2]^+$, a proposed photochemical intermediate during photolysis in CH_3CN, following the procedure[93] reported for cis,cis-$[Mn(bpy)(CO)_2(CH_3CN)_2]^+$ by first reacting fac-$[Mn(dmebpy)(CO)_3Br]$ with AgOTf in CH_3CN, removing AgBr by vacuum filtration, then further reacting the product with trimethylamine-N-oxide. A mixture of cis,cis-$[Mn(dmebpy)(CO)_2(CH_3CN)_2]^+$ and cis,trans-$[Mn(dmebpy)(CO)_2(CH_3CN)_2]^+$ was isolated as identified by ^1H NMR. The identities and purities of the compounds were confirmed by ^1H NMR (Figures A1-A4), ESI-MS, and elemental analysis.

Vibrational Spectroscopy

The identity of NN and L directly impact the electron density on the Mn(I) center in the fac-$[Mn(NN)(CO)_3L]^{n+}$ compounds. The three CO ligands provide a convenient probe into this impact of NN and L variation, as the degree of π-backbonding from a filled Mn(dπ) orbital to an empty CO(π*) orbital is directly tuned by the electron density on the Mn(I) ion. The FTIR spectra of fac-$[Mn(NN)(CO)_3(L)]^{n+}$ complexes typically feature three C−O stretches as a result of their Cs point group. The impact of NN and L variation was assessed by comparing the CO stretching frequencies in the FTIR spectra. The C−O stretching region of the FTIR spectra are shown in Figure 15, and the experimental ν(CO) values and the theoretical ν(CO) values obtained by DFT calculations for all six compounds in CH_3CN are presented in Table 1. The ν(CO) values measured in our lab are in close agreement with the values reported for all three fac-$[Mn(NN)(CO)_3Br]$ compounds.[81,88,89] All theoretical values are within 2% error of the experimental values. Two different ligand effects on ν(CO) are analyzed across this

series of compounds: the electron-donating/withdrawing effect of the 4,4′-substituents on bpy, and the π-donating/accepting effect of the monodentate ligand L.

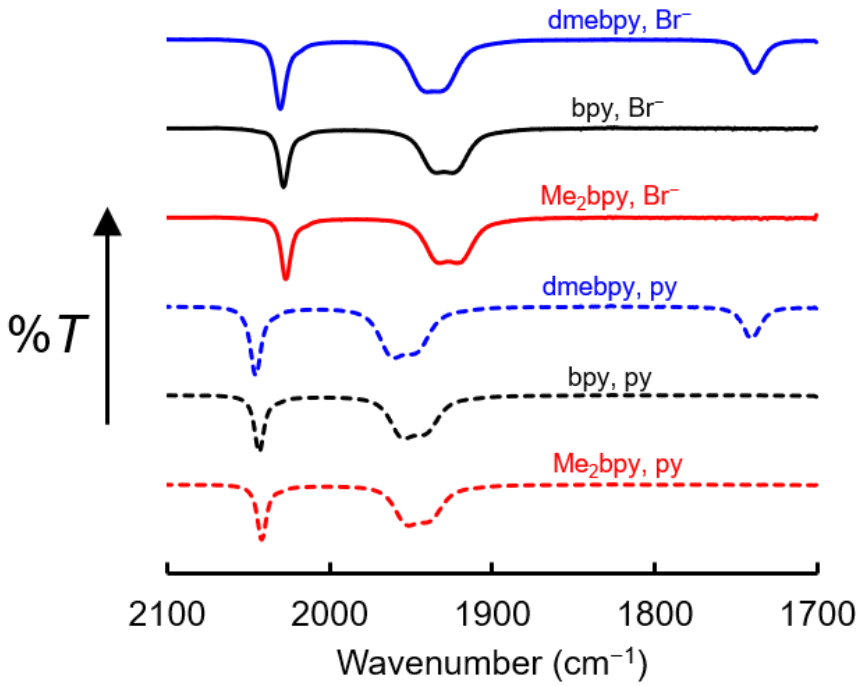

Figure 15. FTIR spectra in the C−O stretching region for fac-[Mn(dmebpy)$(CO)_3$Br] (blue solid), fac-[Mn(bpy)$(CO)_3$Br] (black solid), *fac*-[Mn(Me_2bpy)$(CO)_3$Br] (red solid), [Mn(dmebpy)$(CO)_3$(py)]$^+$ (blue dashed), *fac*-[Mn(bpy)$(CO)_3$(py)]$^+$ (black dashed), and *fac*-[Mn(Me_2bpy)$(CO)_3$(py)]$^+$ (red dashed), in room temperature CH_3CN.

Table 1. Experimental and theoretical C−O vibrational frequencies for *fac*-[Mn(NN)(CO)$_3$Br] and *fac*-[Mn(NN)(CO)$_3$(py)](OTf) in CH_3CN.

Compound	**Experimental ν(CO) (cm^{-1})** [a]	**Theoretical ν(CO) (cm^{-1})** [b]
***fac*-Mn(dmebpy)(CO)$_3$Br**	2030, 1940, 1931	2022, 1946, 1937
***fac*-Mn(bpy)(CO)$_3$Br**	2028, 1936, 1923	2020, 1940, 1932
***fac*-Mn(Me$_2$bpy)(CO)$_3$Br**	2026, 1933, 1919	2019, 1938, 1929
***fac*-[Mn(dmebpy)(CO)$_3$(py)](OTf)**	2046, 1961, 1947	2037, 1960, 1954
***fac*-[Mn(bpy)(CO)$_3$(py)](OTf)**	2043, 1955, 1941	2034, 1956, 1949
***fac*-[Mn(Me$_2$bpy)(CO)$_3$(py)](OTf)**	2042, 1954, 1939	2033, 1953, 1947

[a] Data collected in rt CH_3CN in a CaF_2 cell.
[b] Obtained from the energy optimized structures using the M06 level of DFT and the 6-31G* basis set for H, C, N, and O and the SDD basis set for Mn and Br.

Among each fac-[Mn(NN)(CO)$_3$Br] and fac-[Mn(NN)(CO)$_3$(py)]$^+$ pair, ν (CO) is greater for the py compounds than for the Br^- compounds. The neutral py ligand imparts an overall +1 charge on the compound, while its π-accepting nature decreases the electron density on the Mn(I) center. Conversely, the π-donating Br^- ligand imparts an overall neutral charge and increases the electron density on the metal center, thereby comparatively enhancing π-backbonding to the CO(π*) orbitals. For example, the ν(CO) for fac-[Mn(dmebpy)(CO)$_3$Br] at 2030, 1940, and 1931 cm^{-1} shift to 2046, 1961, and 1947 cm^{-1} when Br^- is replaced by py to form fac-[Mn(dmebpy)(CO)$_3$(py)]$^+$. The ν(CO) for the methyl ester substituents is not significantly impacted by monodentate ligand substitution (1739 and 1740 cm^{-1} for fac-[Mn(dmebpy)(CO)$_3$Br] and fac-[Mn(dmebpy)(CO)$_3$(py)]$^+$, respectively) due to the relatively large distance between the Br−/py ligand and the 4,4′-methyl ester substituents on the bpy ligand.

Variation of NN also impacts the ν(CO) frequencies, although not to the same degree as the L variation. As the π-acidity of NN decreases from dmebpy to bpy to Me_2bpy, the CO stretching frequencies decrease as a result of the increased Mn-CO π-backbonding. In the case of the fac-$[Mn(NN)(CO)_3(py)]^+$ compounds, the three ν(CO) values are 2043, 1955, and 1941 cm−1 when NN = bpy. The presence of electron donating methyl substituents (NN = Me_2bpy) slightly enhances the electron density on the Mn(I) center, shifting the ν (CO) values to 2042, 1954, and 1939 cm^{-1}. A larger effect is observed when electron-withdrawing methyl ester substituents (NN = dmebpy) decrease the electron density on Mn(I) relative to the NN = bpy compound, resulting in ν(CO) of 2046, 1961, and 1947 cm^{-1}. The impact of NN is more subtle than the impact of L, as the electron-withdrawing (methyl ester) or electron-donating (methyl) 4,4′-substitution on bpy serves to fine-tune the metal center's electron density.

Cyclic Voltammetry

The redox properties of the fac-$[Mn(NN)(CO)_3Br]$ and fac-$[Mn(NN)(CO)_3(py)]^+$ compounds were investigated using cyclic voltammetry in CH_3CN solution. Anodic scanning of tricarbonylmanganese(I) compounds typically reveals an irreversible MnI/II oxidation, and cathodic scanning is complicated by ligand dissociation and dimer formation. In the previously reported fac-$[Mn(NN)(CO)_3Br]$ complexes, the first reduction is assigned as $Mn^{I/0}$, an irreversible process that is followed by the rapid dissociation of Br− to form a five coordinate radical species.[94] Two of the one-electron reduced radical species dimerize to form a $[Mn(NN)(CO)_3]_2$ compound, which is then

reduced by one electron upon further cathodic scanning to generate two fac-$[Mn(NN)(CO)_3]^-$ species.

The cyclic voltammograms for the six compounds are presented in Figure 16, and the redox potentials are listed in Table 2. The nature of L exhibits a strong influence on the irreversible MnI/II potential, while the nature of NN has a minor influence on this potential. When L = py, the Epa values (1.48-1.56 V vs. Ag/AgCl) are approximately 0.38-0.40 V more positive than the L = Br^-, consistent with the π-donating nature of Br− and the π-accepting nature of py. This trend is consistent with that observed in the FTIR data in comparing L = Br^- vs py. As the NN ligand's π-acidity increases, the Mn(dπ) orbitals become slightly more stabilized, requiring a slightly greater potential to oxidize Mn(I) to Mn(II). This is reflected by the E_{pa} values of 1.48, 1.52, and 1.56 V vs Ag/AgCl for fac-$[Mn(Me_2bpy)(CO)_3(py)]^+$, fac-$[Mn(bpy)(CO)_3(py)]^+$, and fac-$[Mn(dmebpy)(CO)_3(py)]^+$, respectively. This trend resulting from NN ligand π-acidity is also observed in the series of fac-$[Mn(NN)(CO)_3Br]$ compounds. The Epc values for the first reduction are also influenced by the nature of L and NN. Replacing the π-donating Br^- with a π-accepting py shifts the E_{pc} to a less negative potential by 0.07-0.14 V, as observed in each pair of fac-$[Mn(NN)(CO)_3Br]$ and fac-$[Mn(NN)(CO)_3(py)]^+$ complexes. Among the L = py compounds, the first Epc value decreases from −0.83 to −1.09 to −1.19 V vs. Ag/AgCl for fac-$[Mn(dmebpy)(CO)_3(py)]^+$, fac-$[Mn(bpy)(CO)_3(py)]^+$, and fac-$[Mn(Me_2bpy)(CO)_3(py)]^+$, respectively, consistent with the decreasing π-acidity of the NN ligand.

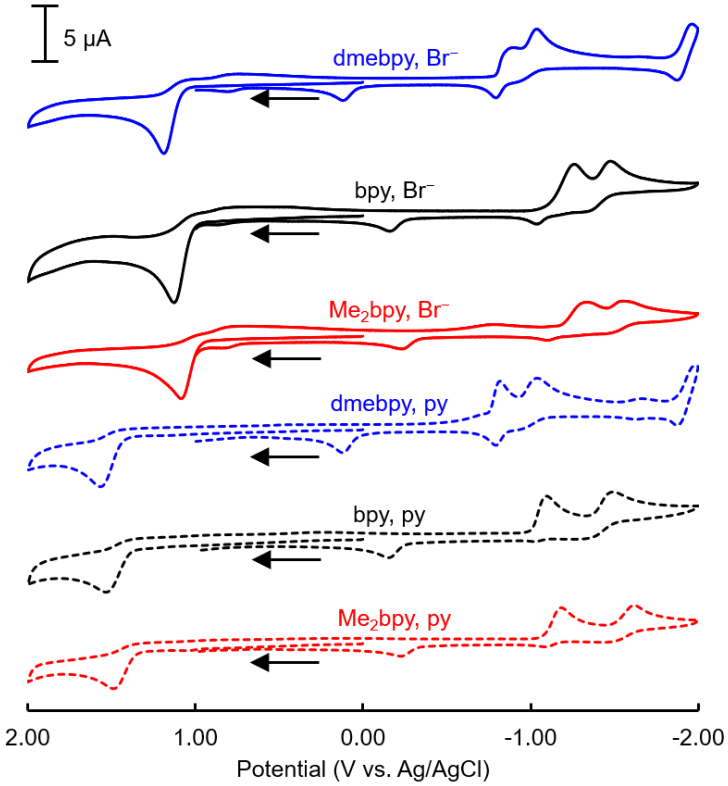

Figure 16. Cyclic voltammograms for 1 mM solutions of *fac*-[Mn(dmebpy)$(CO)_3$Br] (blue solid), *fac*-[Mn(bpy)$(CO)_3$Br] (black solid), *fac*-[Mn(Me_2bpy)$(CO)_3$Br] (red solid), [Mn(dmebpy)$(CO)_3$(py)]$^+$ (blue dashed), *fac*-[Mn(bpy)$(CO)_3$(py)]$^+$ (black dashed), and *fac*-[Mn(Me_2bpy)$(CO)_3$(py)]$^+$ (red dashed), in room temperature CH_3CN under a N_2 atmosphere with 0.1 M Bu_4NPF_6 as the supporting electrolyte, a glassy carbon working electrode, Pt wire auxiliary electrode, Ag/AgCl reference electrode, and a scan rate of 200 mV/s. Arrows indicate the scan direction.

Table 2. Cyclic voltammetry data for *fac*-[Mn(NN)(CO)$_3$Br] and fac-[Mn(NN)(CO)$_3$(py)](OTf) in CH_3CN.

	E_p^a (V) [a]	E_p^c (V) [a]	E_p^c (V) [a]
Mn(dmebpy)(CO)$_3$Br	1.18	−0.90	−1.04
Mn(bpy)(CO)$_3$Br	1.13	−1.27	−1.48
Mn(Me$_2$bpy)(CO)$_3$Br	1.08	−1.33	−1.55
[Mn(dmebpy)(CO)$_3$(py)](OTf)	1.56	−0.83	−1.05
[Mn(bpy)(CO)$_3$(py)](OTf)	1.52	−1.09	−1.49
[Mn(Me$_2$bpy)(CO)$_3$(py)](OTf)	1.48	−1.19	−1.63

[a] Room temperature CH_3CN under a N_2 atmosphere with 0.1 M Bu_4NPF_6 as the supporting electrolyte, a glassy carbon working electrode, Pt wire auxiliary electrode, Ag/AgCl reference electrode, and a scan rate of 200 mV/s. Potentials are reported vs. Ag/AgCl.

Electronic Absorption Spectroscopy

The electronic absorption spectra of the compounds in room temperature CH_3CN, as displayed in Figure 17 with absorption maxima (λ_{max}) and extinction coefficients (ε) given in Table 3, exhibit spectral features in both the UV and visible region ($\lambda < 600$ nm) that vary as a function of the ligand set. In all cases, the UV region is dominated by NN $\pi \rightarrow \pi^*$ transitions (λ_{max} = 285-314 nm, $\varepsilon = 1.7\text{-}1.9 \times 10^4$ $M^{-1}cm^{-1}$). The visible absorption band for *fac*-[Mn(NN)(CO)$_3$Br] is known to have contributions from both Mn(dπ)→NN(π^*) ^{1}MLCT (singlet metal-to-ligand charge transfer) and Br(p)→NN(π^*) ^{1}XLCT (singlet halide-to-ligand charge transfer).[31,74] The λ_{max} values are directly related to the electron-donating/withdrawing nature of the NN substituents (λ_{max} = 460, 416, and 411 nm for NN = dmebpy, bpy, and Me$_2$bpy, respectively), as a more electron-withdrawing substituent stabilizes the NN molecular orbital, thereby lowering the

^{1}MLCT/^{1}XLCT transition energy. These values for *fac*-[Mn(bpy)(CO)$_3$Br] and *fac*-[Mn(Me$_2$bpy)(CO)$_3$Br] are in agreement with the reported values.[59] Replacement of π-donating Br$^-$ with π-accepting py stabilizes the Mn(dπ) orbitals (as demonstrated with the CV data above), causing a blue-shift in the ^{1}MLCT band. The λ_{max} values for *fac*-[Mn(NN)(CO)$_3$(py)](OTf) are 420, 383, and 378 nm when NN = dmebpy, bpy, and Me$_2$bpy, respectively. These three compounds follow the same trend in NN electron-withdrawing/donating effect as described for the L = Br$^-$ analogues.

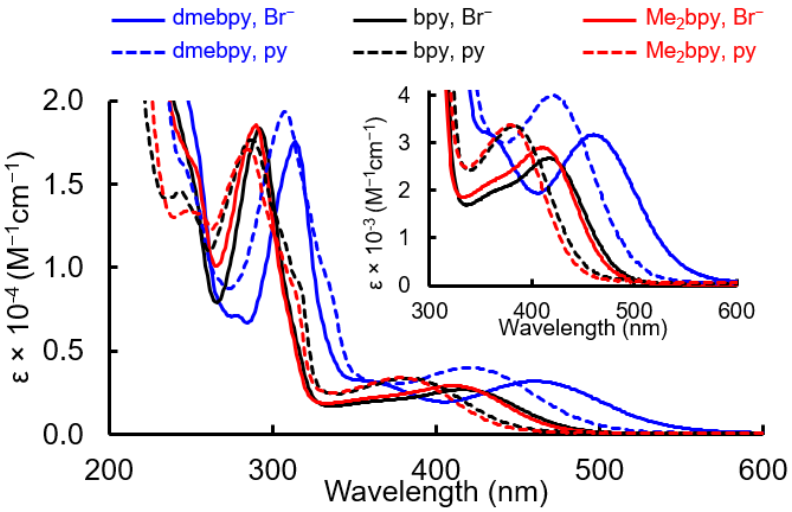

Figure 17. Overlaid electronic absorption spectra for fac-[Mn(dmebpy)(CO)$_3$Br] (blue solid), fac-[Mn(bpy)(CO)$_3$Br] (black solid), fac-[Mn(Me$_2$bpy)(CO)$_3$Br] (red solid), fac-[Mn(dmebpy)(CO)$_3$(py)](OTf) (blue dashed), fac-[Mn(bpy)(CO)$_3$(py)](OTf) (black dashed), and fac-[Mn(Me$_2$bpy)(CO)$_3$(py)](OTf) (red dashed), in room temperature CH$_3$CN.

Table 3. Electronic absorption spectroscopy data for *fac*-[Mn(NN)(CO)$_3$Br] and *fac*-[Mn(NN)(CO)$_3$(py)](OTf) in CH_3CN.[a]

Compound	λ (nm)	ε × 10^{-4} ($M^{-1}cm^{-1}$)	λ (nm)	ε × 10^{-4} ($M^{-1}cm^{-1}$)
***fac*-Mn(dmebpy)(CO)$_3$Br**	460	0.32	314	1.8
***fac*-Mn(bpy)(CO)$_3$Br**	416	0.29	292	1.8
***fac*-Mn(Me$_2$bpy)(CO)$_3$Br**	411	0.29	290	1.8
***fac*-[Mn(dmebpy)(CO)$_3$(py)](OTf)**	420	0.40	308	1.9
***fac*-[Mn(bpy)(CO)$_3$(py)](OTf)**	383	0.34	287	1.8
***fac*-[Mn(Me$_2$bpy)(CO)$_3$(py)](OTf)**	378	0.34	285	1.7

[a] Data collected in rt CH_3CN in a 1×1 cm quartz cuvette.

Photochemical CO Dissociation

As observed in related $Mn^I(NN)(CO)_3L$ photoCORMs, irradiation of each compound with visible light causes dissociation of the CO ligands. The photoinduced dissociation of CO from the *fac*-[Mn(NN)(CO)$_3$Br] and *fac*-[Mn(NN)(CO)$_3$(py)]$^+$ compounds in CH_3CN was monitored by FTIR, electronic absorption, and ^{1}H NMR spectroscopy. A combination of these techniques provides important information about the photochemical intermediate formation and efficiencies of CO dissociation upon photolysis with visible light. It is important to note that all six compounds are stable in CH_3CN solution when kept in the dark for at least one hour, as no FTIR spectral shifts are observed (Figure A5).

The photochemical ligand dissociation in CH_3CN was monitored by FTIR, as the C−O stretching frequencies are sensitive to the set of ligands coordinated to Mn(I). The FTIR spectral changes resulting from the irradiation of all six compounds with both 405 nm and 470 nm showed similar trends. The data for the 470 nm photolysis of *fac*-

[Mn(dmebpy)$(CO)_3$(py)]$^+$ and *fac*-[Mn(dmebpy)$(CO)_3$Br] are depicted in Figure 18, while the 470 nm data for the remaining four compounds and the 405 nm data for all six compounds are shown in Figures A6-A7. The FTIR spectra of the intermediate irradiation times provide important information about photochemical reaction intermediates. A comparison of each of the L = Br^- vs py analogues shows that one set of intermediate peaks is apparent for the *fac*-[Mn(NN)$(CO)_3$(py)]$^+$ complexes, while two sets of intermediate peaks are apparent for the *fac*-[Mn(NN)$(CO)_3$Br] complexes. In the case of *fac*-[Mn(dmebpy)$(CO)_3$(py)]$^+$, irradiation at early times shows a decrease in the original three ν(CO) bands at 2046, 1961, and 1947 cm^{-1} concomitant with the appearance of two new ν(CO) bands at 1877 and 1954 cm^{-1}. Further irradiation leads to the emergence of slightly higher energy shoulders on these bands at 1888 and 1966 cm^{-1}, and continued photolysis leads to eventual loss of all ν(CO) bands. In a similar first step, irradiation of *fac*-[Mn(dmebpy)$(CO)_3$Br] at early times shows a decrease in the intensity of the original three ν(CO) bands at 2030, 1940, and 1931 cm^{-1} concomitant with the appearance of two new ν(CO) bands at 1868 and 1941 cm^{-1}. Further irradiation decreases these first intermediate bands as a second set of intermediate bands form at 1891 and 1967 cm^{-1}. Further irradiation also leads to eventual loss of all ν(CO) bands. It should be noted that free CO is observed at 2143 cm^{-1} for all six compounds after the first irradiation interval, further supporting the loss of CO in the first photochemical step.

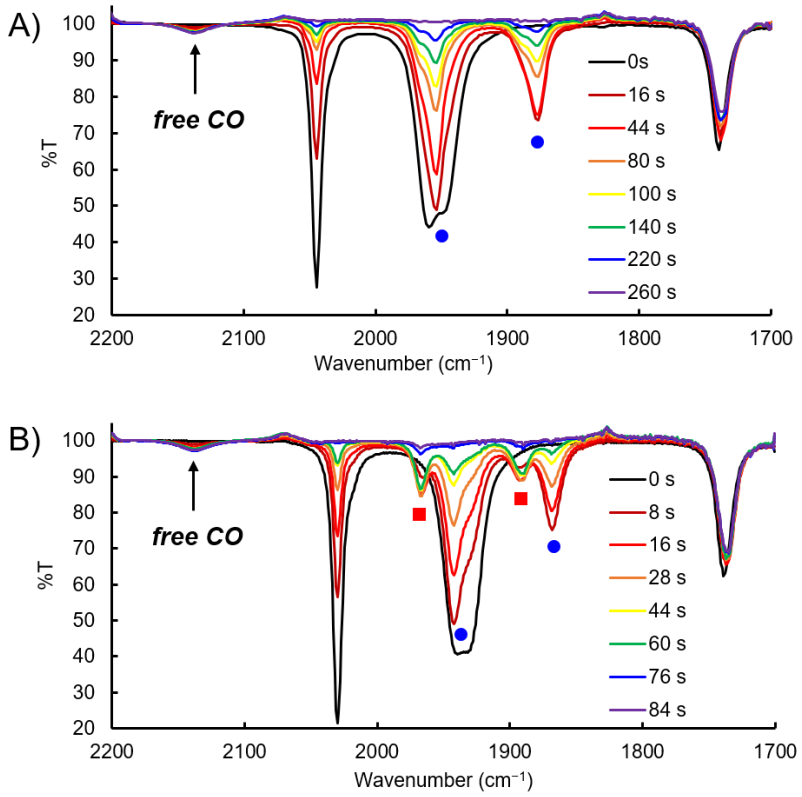

Figure 18. FTIR spectra for *fac*-[Mn(dmebpy)$(CO)_3$(py)]$^+$ (A) and *fac*-[Mn(dmebpy)$(CO)_3$Br] (B) in rt CH_3CN during photolysis with $\lambda_{irr} = 470$ nm. The observed intermediate bands are denoted by blue circles for *fac*-[Mn(dmebpy)$(CO)_3$(py)]$^+$ (A), and the first and second observed intermediate bands are denoted with blue circles and red squares, respectively, for *fac*-[Mn(dmebpy)$(CO)_3$Br] (B).

To aid in identification of the photochemical intermediates, the samples were irradiated in CD_3CN with 470 nm, and the ^{1}H NMR spectrum was monitored as a function of irradiation time for *fac*-[Mn(dmebpy)$(CO)_3$(py)]$^+$ and *fac*-[Mn(dmebpy)$(CO)_3$Br] (Figures 19 and 20, respectively). The ^{1}H NMR spectrum of *fac*-[Mn(dmebpy)$(CO)_3$Br] displays three aromatic signals prior to photolysis due to the molecule's symmetry (Figure 19). After 470 nm irradiation for 2 s, six new signals with equal integrations appear at 7.64, 8.12, 8.67, 8.89, 9.09, and 9.30 ppm, as the original

signals slightly decrease in intensity. Based on related analyses of photochemical CO dissociation,[77,78,86,89,93] and in agreement with the first photochemical intermediate observed in the FTIR spectrum which suggests a dicarbonyl species, we propose that the first photochemical step is exchange of an equatorial CO with CD_3CN to form *cis,cis*-[Mn(dmebpy)$(CO)_2(CD_3CN)$Br]. After 4 s of irradiation, a second set of six signals is observed at 7.75, 8.20, 8.75, 8.95, 9.00, and 9.19 ppm, suggesting the second intermediate has retained the same symmetry as the first intermediate. As the FTIR analysis indicates decreased π-backbonding to the bound CO ligands, this is consistent with the exchange of Br^- with CD_3CN to form *cis,cis*-[Mn(dmebpy)$(CO)_2(CD_3CN)_2]^+$ as the second intermediate. While only two intermediates are apparent by FTIR analysis, a third intermediate with three signals at 8.16, 8.97, and 9.75 ppm was observed. The reduction in aromatic signals suggests that each ring of the dmebpy ligand is equivalent, and we propose that this photochemical intermediate is *cis,trans*-[Mn(dmebpy)$(CO)_2(CD_3CN)_2]^+$. The stacked ^{1}H NMR spectra comparing the sample after 20 s of irradiation (containing both the second and third intermediate) and the synthesized mixture of *cis,cis*- and *cis,trans*-[Mn(dmebpy)$(CO)_2(CH_3CN)_2]^+$ are provided in Figure A8 to highlight the presence of these two intermediates. Photolysis for up to 90 s causes the disappearance of all peaks, as the Mn(I) center has presumably become photooxidized to form a paramagnetic species. While we have not identified the final photodecomposition products at this time, this has been the subject of much investigation, with the photoproducts often described as oxidized Mn species. Oxidized species such as MnO_2, $[Mn(NN)_2(solv)_2]^{2+}$, $[Mn(NN)_3]^{2+}$, $[Mn(solv)_4(OTf)]^+$, $[Mn(NN)_2(OTf)]^+$, and

$[Mn(NN)(solv)_3Br]^+$ are potential photoproducts based on reports of structurally related photoCORMs.[32,79,80,84]

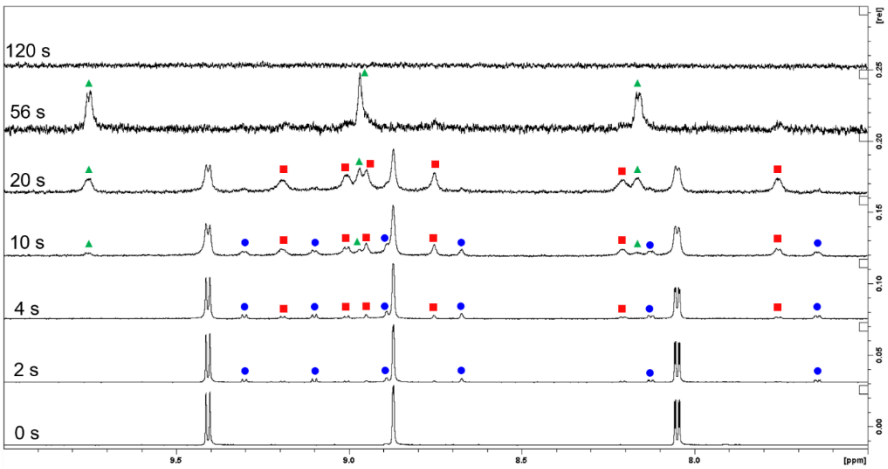

Figure 19. ^{1}H NMR spectra for *fac*-$[Mn(dmebpy)(CO)_3Br]$ in rt CD_3CN during photolysis with λ_{irr} = 470 nm for 0, 2, 4, 10, 20, 56, and 120 s. Spectra are normalized as a paramagnetic photoproduct form during the photolysis, lowering the overall signal intensity. The first, second, and third intermediate bands are denoted with blue circles, red squares, and green triangles, respectively.

The ^{1}H NMR spectrum of *fac*-$[Mn(dmebpy)(CO)_3(py)]^+$ displays six aromatic signals prior to photolysis: three dmebpy signals (all integrate to 2 H) and three py signals (two integrate to 2 H and one integrates to 1 H), as shown in Figure 20. After irradiation with 470 nm for 4 s, a new set of six signals with the same distribution of integrations arises at 6.95, 7.51, 8.01, 8.21, 8.89, and 9.93 ppm. This first step is quite different from that of the *fac*-$[Mn(dmebpy)(CO)_3Br]$ analogue. Because the symmetry of the first intermediate remains the same as the original species, and the first intermediate observed by FTIR indicates the formation of a dicarbonyl species, we propose that the first photochemical step when L = py is the exchange of the axial CO (*trans* to py) with

CD_3CN to form *cis,trans*-$[Mn(dmebpy)(CO)_2(CD_3CN)(py)]^+$. With further photolysis, a new set of three signals arises at 8.16, 8.97, 9.75 ppm, suggesting exchange of py with CD_3CN to form the symmetric *cis,trans*-$[Mn(dmebpy)(CO)_2(CD_3CN)_2]^{2+}$ species. The stacked ^1H NMR spectra comparing the sample after 20 s of irradiation (containing the second intermediate) and the synthesized mixture of *cis,cis*- and *cis,trans*-$[Mn(dmebpy)(CO)_2(CH_3CN)_2]^+$ are provided in Figure A8 to confirm the formation of the *cis,trans* isomer. The third intermediate spectrum in the photolysis of the *fac*-$[Mn(dmebpy)(CO)_3Br]$ analogue matches the spectrum for this second intermediate in the photolysis of the L = py analogue.

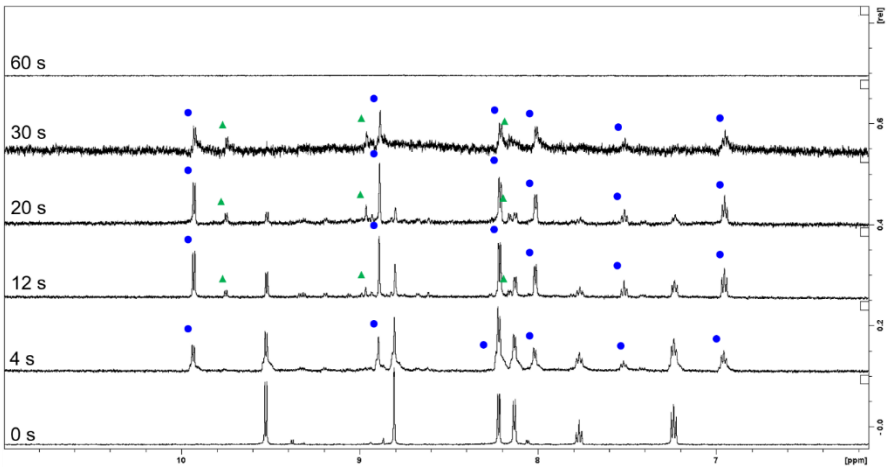

Figure 20. ^1H NMR spectra for *fac*-$[Mn(dmebpy)(CO)_3(py)]^+$ in rt CD_3CN during photolysis with λ_{irr} = 470 nm for 0, 4, 12, 20, 30, and 60 s. Spectra are normalized as a paramagnetic photoproduct forms during the photolysis, lowering the overall signal intensity. The first and second intermediate bands are denoted with blue circles and green triangles, respectively.

To further support the proposed photochemical intermediate identities, the theoretical ν(CO) frequencies for each of the proposed intermediates were calculated

using DFT. The experimental and theoretical vibrational frequencies for all proposed intermediates are provided in Table 4. The theoretical values are within 2% error of the experimental values, and the same trends are observed regardless of the nature of NN. The calculated frequencies for *cis,cis*-$[Mn(dmebpy)(CO)_2(CH_3CN)_2]^+$ and *cis,trans*-$[Mn(dmebpy)(CO)_2(CH_3CN)_2]^+$ (1974 and 1919 cm^{-1} vs 1975 and 1918 cm^{-1}, respectively) are nearly identical; this explains why the second and third intermediates during the photolysis of *fac*-$[Mn(dmebpy)(CO)_3Br]$ were not obvious in the FTIR spectra in Figure 17 as they appear as a single intermediate. Upon close inspection of the spectra following formation of the first intermediate during photolysis of *fac*-$[Mn(dmebpy)(CO)_3(py)]^+$, a higher energy shoulder is observed on each of the *cis,trans*-$[Mn(dmebpy)(CO)_2(CH_3CN)(py)]^+$ bands, consistent with substituting a π-accepting py ligand with a slightly stronger π-accepting CH_3CN.

Table 4. Experimental and theoretical C−O vibrational stretching frequencies for the photochemical intermediates during photolysis of *fac*-$[Mn(NN)(CO)_3Br]$ and *fac*-$[Mn(NN)(CO)_3(py)]^+$ in CH_3CN.

Photochemical intermediate	**Experimental ν(CO) (cm^{-1})** [a]	**Theoretical ν(CO) (cm^{-1})** [b]
***cis,cis*-[Mn(dmebpy)(CO)$_2$(CH$_3$CN)Br]**	1941, 1868	1950, 1892
***cis,trans*-[Mn(dmebpy)(CO)$_2$(CH$_3$CN)(py)]$^+$**	1954, 1877	1960, 1903
***cis,cis*-[Mn(dmebpy)(CO)$_2$(CH$_3$CN)$_2$]$^+$**	1967, 1891	1974, 1919
***cis,trans*-[Mn(dmebpy)(CO)$_2$(CH$_3$CN)$_2$]$^+$**	1966, 1888 [c]	1975, 1918
***cis,cis*-[Mn(bpy)(CO)$_2$(CH$_3$CN)Br]**	1939, 1855	1945, 1883
***cis,trans*-[Mn(bpy)(CO)$_2$(CH$_3$CN)(py)]$^+$**	1948, 1867	1958, 1897

***cis,cis*-[Mn(bpy)(CO)$_2$(CH$_3$CN)$_2$]$^+$**	1961, 1882	1969, 1911
***cis,trans*-[Mn(bpy)(CO)$_2$(CH$_3$CN)$_2$]$^+$**	1960, 1879 [c]	1972, 1911
***cis,cis*-[Mn(Me$_2$bpy)(CO)$_2$(CH$_3$CN)Br]**	1935, 1852	1943, 1880
***cis,trans*-[Mn(Me$_2$bpy)(CO)$_2$(CH$_3$CN)(py)]$^+$**	1948, 1867	1956, 1894
***cis,cis*-[Mn(Me$_2$bpy)(CO)$_2$(CH$_3$CN)$_2$]$^+$**	1960, 1878	1968, 1908
***cis,trans*-[Mn(Me$_2$bpy)(CO)$_2$(CH$_3$CN)$_2$]$^+$**	1962, 1879 [c]	1970, 1909

[a] Data collected in rt CH_3CN in a CaF_2 cell.
[b] Obtained from the energy optimized structures using the M06 level of DFT and the 6-31G* basis set for H, C, N, and O and the SDD basis set for Mn and Br.
[c] Approximate values obtained from the shoulders on the corresponding *cis,cis*-[Mn(NN)(CO)$_2$(CH$_3$CN)(py)]$^+$ intermediates bands.

Scheme 1 summarizes the proposed step-wise photochemical ligand dissociation processes as a function of ancillary ligand L π-donating/accepting nature based on the combination of FTIR and ^{1}H NMR spectroscopic analysis of intermediates. In the case of the *fac*-[Mn(NN)(CO)$_3$Br] compounds, absorption of a photon first exchanges an equatorial CO (*trans* to NN) with a CH_3CN solvent molecule to form the *cis,cis*-[Mn(NN)(CO)$_2$(CH$_3$CN)Br] intermediate. Next, the Br^- ligand exchanges with a second CH_3CN molecules to form the *cis,cis*-[Mn(NN)(CO)$_2$(CH$_3$CN)$_2$]$^+$ intermediate. While we observed this ligand exchange during constant irradiation, this step also proceeds in a dark thermal reaction. A sample of each *fac*-[Mn(NN)(CO)$_3$Br] was irradiated until the first set of intermediate bands formed, then the sample was protected from light for 15 minutes and the FTIR spectrum was collected (Figure A10). The thermal Br^- substitution is evident by the complete loss of the first intermediate bands along with the evolution of the second intermediate bands. This Br^- exchange from the intermediate was also

observed in the Ru(II),Mn(I) photoCORMs reported by us.[86] Finally, absorption of a photon drives an isomerization reaction to form the *cis,trans*-$[Mn(NN)(CO)_2(CH_3CN)_2]^+$ compound. Further irradiation then causes dissociation of the remaining two CO ligands as evidenced by FTIR analysis.

Scheme 1.Proposed step-wise photochemical ligand dissociation and intermediate formation for *fac*-$[Mn(NN)(CO)_3Br]$ and *fac*-$[Mn(NN)(CO)_3(py)]^+$.

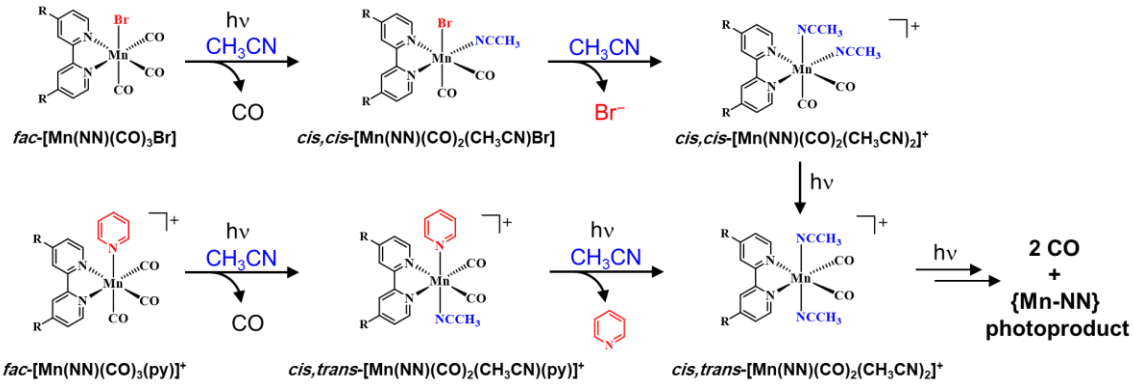

In the case of the *fac*-$[Mn(NN)(CO)_3(py)]^+$ analogues, the first photochemical step drives the exchange of the axial CO (*trans* to py) with a solvent CH_3CN molecule to provide the *cis,trans*-$[Mn(NN)(CO)_2(CH_3CN)(py)]^+$ intermediate. Absorption of a second photon exchanges py with a second CH_3CN, forming the *cis,trans*-$[Mn(NN)(CO)_2(CH_3CN)_2]^+$ compound. In contrast to the *cis,cis*-$[Mn(NN)(CO)_2(CH_3CN)Br]$ analogues, the py ligand does not dissociate by a dark thermal reaction (Figure A11), so a photon is required for this step. As observed for the L = Br^- intermediate, further photolysis dissociates the remaining two CO ligands. By

comparing these two photochemical mechanisms, we conclude that while the same final intermediate, *cis,trans*-$[Mn(NN)(CO)_2(CH_3CN)_2]^+$, is formed regardless of the nature of L, a π-donating L directs the dissociation of an equatorial CO (CO_{eq}) in the first step, while a π-accepting L directs the dissociation of the axial CO (CO_{ax}) in the first step. The accepted mechanism for CO dissociation from *fac*-$[Mn(NN)(CO)_3L]^{n+}$ photoCORMs involves population of the Mn(dπ)→NN(π*) MLCT state with a formally oxidized Mn(II) center and a formally reduced $NN^{\bullet-}$.[90] When L = Br^-, its π-donation provides a stronger bond Mn(II)−CO_{ax} due to π-backbonding relative to the Mn(II)−CO_{eq} bonds, causing CO_{eq} dissociation. However, when L = py, the Mn(II)−CO_{ax} bond is significantly weaker in the excited state than the Mn(II)−CO_{eq} bonds because the transferred electron density on NN is *trans* to the CO_{eq} ligands and not the CO_{ax} ligand; this causes CO_{ax} to dissociate more readily than CO_{eq}.

The ligand dissociation was also monitored by electronic absorption spectroscopy. Figure 21 shows the spectral changes for *fac*-$[Mn(dmebpy)(CO)_3(py)]^+$ and *fac*-$[Mn(dmebpy)(CO)_3Br]$ in rt CH_3CN upon irradiation with 470 nm light. The electronic absorption spectra for the 470 nm photolysis of the remaining four compounds and the 405 nm photolysis for all six compounds are provided in Figures A12-A13. The decreased absorbance of the lowest energy transition is observed in all cases, indicating consumption of the original species. Irradiation with 405 nm results in the formation of an intermediate species with a broad, low energy absorption band concomitant with the decrease in the lowest energy transition for all six compounds. This low energy absorption band is consistent with the formation of the dicarbonyl intermediates as

described in Scheme 1.[77] The intermediate bands cannot be resolved, as the FTIR data indicates a mixture of the dicarbonyl intermediates forms upon photolysis, especially at longer irradiation times. Interestingly, the low energy intermediate band upon 470 nm irradiation is only observable for *fac*-$[Mn(dmebpy)(CO)_3(py)]^+$ and not for *fac*-$[Mn(bpy)(CO)_3(py)]^+$ or *fac*-$[(Mn(Me_2bpy)(CO)_3(py)]^+$, which agrees with the FTIR spectral changes shown in Figures 18 and A6. We propose that the dicarbonyl intermediates for the NN = bpy and Me_2bpy compounds more efficiently absorb the incident 470 nm photons compared to the NN = dmebpy compound, so the intermediate is consumed at a rate in which not enough intermediate accumulates to be detected. In contrast, the 405 nm incident light is not absorbed by the dicarbonyl intermediates as efficiently as the original species, so a significant quantity of the intermediate accumulates before it undergoes further ligand photodissociation processes.

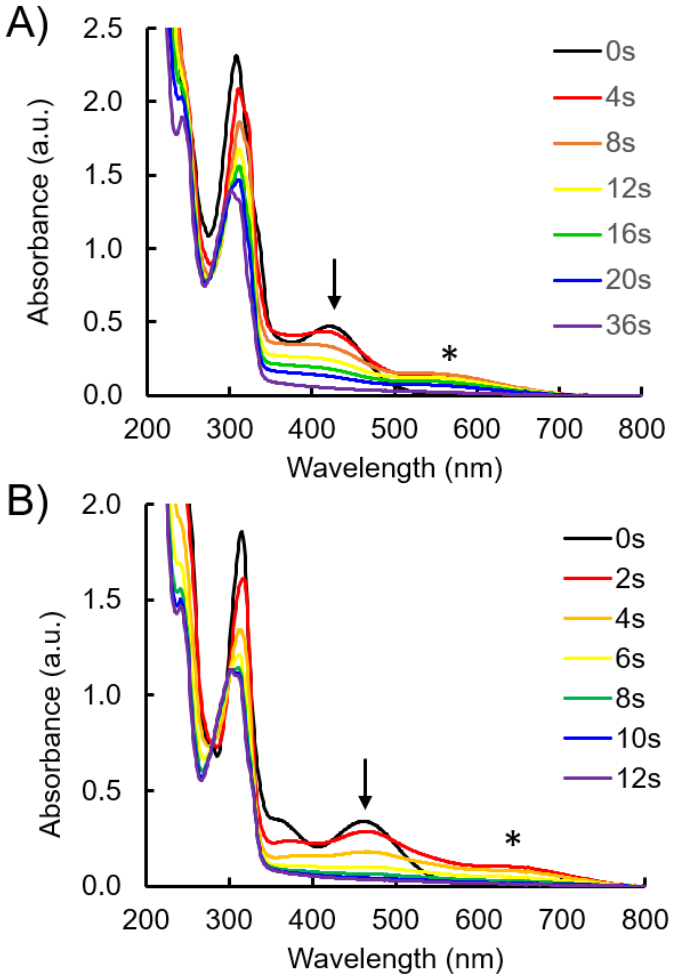

Figure 21. Electronic absorption spectra for the 470 nm photolysis of *fac*-[Mn(dmebpy)$(CO)_3$(py)]$^+$ (A) and *fac*-[Mn(dmebpy)$(CO)_3$Br] (B) in rt CH_3CN.

The efficiency of the first CO dissociation in CH_3CN solution to form the *cis,cis*-[Mn(NN)$(CO)_2(CH_3CN)$Br] or *cis,trans*-[Mn(NN)$(CO)_2(CH_3CN)$(py)]$^+$ photoproduct upon irradiation with 405 nm can be compared for each compound by measuring the quantum yield for CO release (Φ_{CO}). This value was determined by monitoring the loss of the original absorption spectrum at very early photolysis times (< 10 % change in

absorbance while isosbestic points are still present). Two clear trends exist between the six compounds involving the nature of NN and L. First, in both the series of L = Br^- and py compounds, the first CO dissociation event with λ_{irr} = 405 nm (flux = 5.7 ± 0.1 × 10^{-8} mol photons/s) is most efficient when NN = dmebpy and least efficient when NN = Me_2bpy. In the case of the *fac*-[Mn(NN)$(CO)_3$Br] series, Φ_{CO} = 0.32 ± 0.02, 0.22 ± 0.01, and 0.20 ± 0.01 when NN = dmebpy, bpy, and Me_2bpy, respectively (Table 5). Similarly in the case of the *fac*-[Mn(NN)$(CO)_3$(py)]$^+$ series, Φ_{CO} = 0.19 ± 0.01, 0.17 ± 0.01, and 0.15 ± 0.01 when NN = dmebpy, bpy, and Me_2bpy, respectively. This trend, in which CO release efficiency increases with increasing NN ligand π-acidity, is in agreement with related Mn(I) photoCORMs.[31,32,72,74] The second trend is that the first CO dissociation is more efficient when L = Br^- compared to when L = py. This trend agrees with that reported for *fac*-[Mn(azpy)$(CO)_3$Br] and *fac*-[Mn(azpy)$(CO)_3(PPh_3)]^+$ in which the π-donating Br^- ligand causes a greater rate of CO dissociation than the π-accepting PPh_3 ligand.[74] The authors used time dependent density functional theory (TD-DFT) to propose that this difference arises from a greater charge transfer from the PPh_3 ligand than the Mn-CO bonding MO to the azpy(π*) LUMO, while in the case of L = Br^-, the charge transfer to the LUMO exhibits a bigger contribution from the Mn-CO bonding MO than from Br^-. This explanation may explain the differences between L = Br^- vs py, as this series also compares the effects of a π-donor to a π-acceptor.

Table 5. Quantum yield of the first CO dissociation (Φ_{CO}) for *fac*-[Mn(NN)$(CO)_3$Br] and *fac*-[Mn(NN)$(CO)_3$(py)](OTf) in CH_3CN with λ_{irr} = 405 nm.

Compound	$\mathbf{\Phi_{CO}}$
***fac*-Mn(dmebpy)$(CO)_3$Br**	0.32 ± 0.02
***fac*-Mn(bpy)$(CO)_3$Br**	0.22 ± 0.01
***fac*-Mn(Me_2bpy)$(CO)_3$Br**	0.20 ± 0.01
***fac*-[Mn(dmebpy)$(CO)_3$(py)](OTf)**	0.19 ± 0.01
***fac*-[Mn(bpy)$(CO)_3$(py)](OTf)**	0.17 ± 0.01
***fac*-[Mn(Me_2bpy)$(CO)_3$(py)](OTf)**	0.15 ± 0.01

2.4. Conclusions

We have studied the redox and photophysical properties and the visible light-induced ligand dissociation reactions in a series of *fac*-[Mn(NN)$(CO)_3(L)]^{n+}$ complexes (NN = dmebpy, bpy, or Me_2bpy; L = Br^- or py; n = 0 or 1) to compare the effects of the bidentate and monodentate ancillary ligands on photochemical CO dissociation efficiency and mechanism. The relative energy of the Mn(I) center is strongly impacted by the nature of L, as observed in the FTIR and cyclic voltammetry data, and the Mn(I) HOMO is destabilized by L = Br^- relative to L = py. As a result, the absorption spectra for the *fac*-[Mn(NN)$(CO)_3$Br] compounds extend further into the visible region than the *fac*-[Mn(NN)$(CO)_3(py)]^+$ analogues, and these observations follow the expected trends based on previously report related systems. The first CO dissociation efficiency follows a clear trend, in which the stronger NN π-acidity enhances CO dissociation efficiency, and a π-donating Br^- causes more efficient CO dissociation in the first step. A combination of

FTIR and ^{1}H NMR analysis throughout the irradiation of the photoCORMs provided valuable information to identify the structures of the photochemical intermediates. The first photochemical ligand dissociation is quite different between the compounds with L = Br^- or py, as the π-donating Br^- directs the exchange of an equatorial CO (*cis* to L) while the π-accepting py directs the exchange of the axial CO (*trans* to L). The exchange of Br^- with CH_3CN solvent from the first dicarbonyl intermediate occurs by a thermal process, while the exchange of py with CH_3CN solvent from the first dicarbonyl intermediate requires absorption of a photon. Despite the differences in the ligand exchange mechanisms, the final dicarbonyl intermediate observed for each compound regardless of the nature of L is *cis,trans*-$[Mn(NN)(CO)_2(CH_3CN)_2]^+$. Work is underway to expand the series with varied L and further investigate the photochemical reaction mechanism of photoCORMs.

Chapter 3: Impact of steric bulk on photoinduced ligand exchange reactions in Mn(I) photoCORMs

This chapter is adapted from a published article entitled "Impact of steric bulk on photoinduced ligand exchange reactions in Mn(I) photoCORMs" By Pordel S., Schrage B.R., Ziegler C.J., and White J.K. *Inorganica Chimica Acta*, no. 511 (2020): 119845. [104]

3.1. Introduction

Carbon monoxide is a gaseous signaling molecule that participates in several cell signaling pathways. As a result, endogenously produced CO plays important physiological roles such as anti-inflammation, cytoprotection, vasodilation, and blood vessel formation.[6,14,15,58,60,105] Recent research has also indicated therapeutic potential for CO, such as anti-bacterial and anti-cancer activity.[6,11,13,58,59,106] At high concentrations, CO is anti-proliferative and pro-apoptotic in cancer cells, while it is anti-apoptotic and anti-inflammatory in healthy tissue.[6] Due to the toxicity and storage safety issues arising from inhalation of gaseous CO,[107] delivery of the small molecule with high spatiotemporal control is an important goal. The tendency of CO to act as a Lewis base, forming coordinate covalent (or dative) bonds with transition metal ions, has enabled the development of CO-releasing molecules (termed "CORMs"), in which the CO is deactivated through formation of metal-CO bond.[28,108,109] Upon bond cleavage, the CO is released and its pharmacological activity is restored.

CORMs that release CO through photochemical bond dissociation are known as "photoCORMs," or photo-activated CO-releasing molecules.[16–18,31,110–112] PhotoCORMs

allow for CO to remain coordinated to a metal complex pro-drug until irradiation with UV or visible light at a desired location, such as a tumor or infection, releases one or more equivalents of CO. The wavelength required for bond cleavage and the number of CO molecules released per metal complex depend on the molecular architecture. While many photoCORMs have been reported featuring Fe, Ru, Cr, W, Mo, and Re,[15,21,31,62,63,65–69] those featuring Mn(I) have been increasingly studied due to their ability to release multiple equivalents of CO with visible light,[11,13,57,61,70,72–75,77–81,84–89,92,93,95,113,114] a desirable feature to decrease photoinduced damage to healthy cells and tissue.[91]

A frequently studied architecture for Mn(I) photoCORMs is *fac*-$[Mn(NN)(CO)_3(L)]^{n+}$, in which NN is typically a diimine bidentate ligand and L is a monodentate ancillary ligand such as Br^-, CH_3CN, phosphines, or N-containing heterocycles. The identities of NN and L influence the photophysical properties and photochemical ligand dissociation. Excitation with visible light results in population of a lowest-lying metal-to-ligand charge transfer (MLCT) state, which may also have a significant amount of halide-to-ligand charge transfer (XLCT) character if L is a halide.[16,31] The reduced electron density on the metal weakens the π-backbonding between Mn and CO ligands, allowing ligand dissociation. It is generally reported that the quantum yield for CO release (Φ_{CO}) increases as π-acidity of the bidentate ligand increases.[31] For example, in the set of *fac*-$[Mn(NN)(CO)_3Br]$ compounds in which NN = (2-phenyliminomethyl)quinoline (pimq), 2-quinoline-N-(2′-methylthiophenyl)methyleneimine (qmtpm), and 2-pyridyl-N-(2′-

methylthiophenyl)methyleneimine (pmtpm), the value for Φ_{CO} with 509 nm irradiation increases from NN = pimq to pmtpm to qmtpm as conjugation on the NN ligand increases.[32]

The efficiency and rate of CO release are also influenced by the nature of the monodentate ancillary ligand L, as π-donor ligands tend to provide greater CO release efficiency compared to π-acceptor ligands. In the case of the *fac*-$[Mn(qmtpm)(CO)_3L]^{n+}$ and *fac*-$[Mn(pmtpm)(CO)_3L]^{n+}$ complexes, the CO release rate is greater when L = Br^- compared to L = CH_3CN.[32] The π-donor Br^- destabilizes the Mn(dπ) orbitals relative to the case when L is the π-acceptor CH_3CN, resulting in a lower energy MLCT state and enhanced absorptivity at longer wavelengths. Similarly, in photoCORMs with the *fac*-$[Mn(azpy)(CO)_3(L)]^{n+}$ (azpy = 2-phenylazopyridine) architecture, the rate of CO release from the compound when L = Br^- is greater than the rate when L = PPh_3.[72,74] Monodentate ligands that coordinate through imidazolyl groups also increase the quantum yield for CO dissociation compared to those with piperazinyl groups, as observed in the *fac*-$[Mn(phen)(CO)_3(L)]^+$ complexes, where phen = 1,10-phenanthroline and L = imidazoledanysl or 1-dansylpiperazine.[80,92]

Our previous work with *fac*-$[Mn(NN)(CO)_3Br]$ and *fac*-$[Mn(NN)(CO)_3(py)]^+$ photoCORMs, in which NN = 4,4′-dimethyl-2,2′-bipyridine (4,4′-Me_2bpy), 2,2′-bipyridine (bpy), and 4,4′-dimethylester-2,2′-bipyridine (4,4′-dmebpy), highlighted the strong influence of the monodentate L ligand in the photochemical ligand dissociation reactions.[57] We discovered that a π-donating Br^- directs photodissociation of an equatorial CO in the first step, while a π-accepting py directs photodissociation of the

axial CO in the first step. We observed this trend regardless of the electron-donating (methyl) or electron-withdrawing (methyl ester) substituents at the 4,4′ positions of 2,2′-bipyridine. Additionally, in agreement with reports of related Mn(I) photoCORMs, the Φ_{CO} increases with increasing NN π-acidity (4,4′-Me_2bpy < bpy < 4,4′-dmebpy) in each series, and all compounds with L = Br^- displayed larger Φ_{CO} values than their L = py analogues.

The purpose of this work is to broaden our investigation by probing the impact of a sterically bulky NN bidentate ligand on the photochemical ligand dissociation efficiency and mechanism in *fac*-$[Mn(NN)(CO)_3L]^{n+}$ photoCORMs. The impact of steric distortion on *fac*-$[Mn(NN)(CO)_3L]^{n+}$ photoCORMs has not been clearly investigated. In this study, we utilized 6,6′-dimethyl-2,2′-bipyridine (6,6′-Me_2bpy) to prepare two new photoCORMs, *fac*-[Mn(6,6′-Me_2bpy)$(CO)_3$Br] (6,6′-Me_2bpy-Br) and *fac*-[Mn(6,6′-Me_2bpy)$(CO)_3$(py)]$^+$ (6,6′-Me_2bpy-py) for direct comparison to our previously reported *fac*-[Mn(4,4′-Me_2bpy)$(CO)_3$Br] (4,4′-Me_2bpy-Br) and *fac*-[Mn(4,4′-Me_2bpy)$(CO)_3$(py)]$^+$ (4,4′-Me_2bpy-py) analogues.[57] The photoCORMs discussed in this work are shown in Figure 22. The methyl groups at the 4,4′- and 6,6′-positions are expected to impart similar electronic effects but significantly different steric effects as a result of the placement of the substituents relative to the Mn-CO bonds. Herein we present an investigation into the impact of steric bulk on the structure and photophysical and photochemical properties of *fac*-$[Mn(NN)(CO)_3L]^{n+}$ photoCORMs.

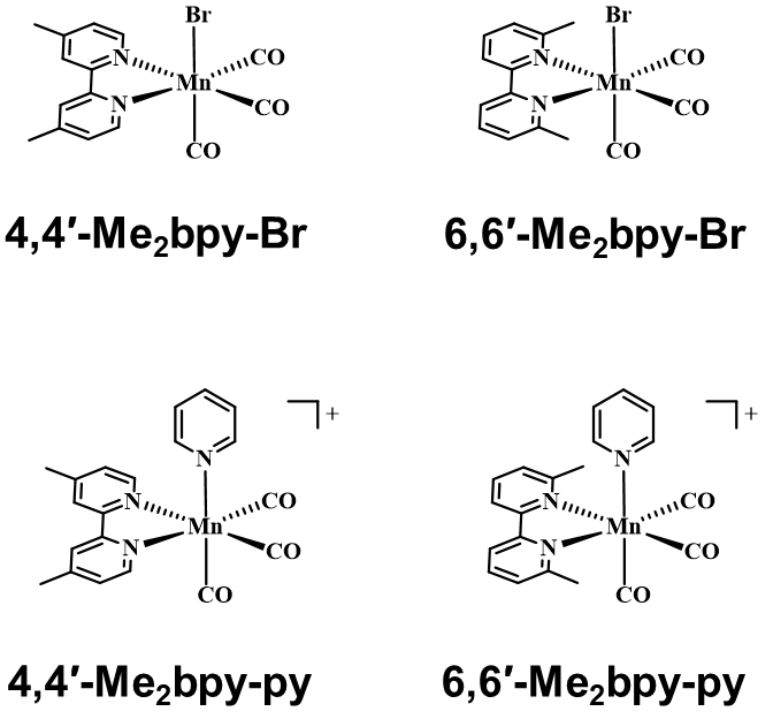

Figure 22. Structural representations and naming scheme for the Mn(I) photoCORMs.

3.2. Experimental Details

Materials

Bromopentacarbonylmanganese(I) was purchased from Strem Chemicals. Silver trifluoromethanesulfonate (AgOTf) was purchased from Acros Organics. Acetonitrile, pyridine, dichloromethane, diethyl ether, methanol, hexane, and chloroform were purchased from Fisher Scientific. Potassium tris(oxalato)ferrate(III) was purchased from Alfa Aesar. Acetonitrile-d_3 were purchased from Cambridge Isotope Laboratories. $[Mn(4,4'\text{-}Me_2bpy)_3]ClO_4$,[115] *fac*-$[Mn(4,4'\text{-}Me_2bpy)(CO)_3Br]$ (4,4′-Me_2bpy-Br),[94] and *fac*-

[Mn(4,4'-Me_2bpy)$(CO)_3$py]$^+$ (4,4′-Me_2bpy-py),[57] were synthesized according to reported procedures.

Methods

All reactions and experiments were performed in the dark (unless otherwise noted) to prevent unintentional photodecomposition.

Synthesis of fac-[Mn(6,6′-Me_2bpy)$(CO)_3$Br] (6,6′-Me_2bpy-Br)

The synthetic procedure was adapted from a previously reported procedure for related Mn(I) compounds.[94] $Mn(CO)_5Br$ (270 mg, 0.98 mmol) and 6,6′-dimethyl-2,2′-dipyridyl (200 mg, 1.0 mmol) were added to 30 mL of diethyl ether and heated at reflux for 4 h under Ar. After cooling to room temperature, the yellow precipitate was collected by vacuum filtration and washed with diethyl ether. Yield: 320 mg (0.79 mmol, 81%). 1H NMR (500 MHz, CD3CN): δ 8.01 (2H, d), 7.93 (2H, t), 7.48 (2H, m), 3.1 (6H, s). Elemental analysis calculated for C15H12O3N2MnBr: 44.69% C, 3.00% H, 6.94% N. Found: 44.6% C, 2.98% H, 7.00% N. HR-ESI(+)-MS (CH_3CN): [M−Br+CH_3CN]+, m/z = 364.048 (calcd m/z = 364.049).

Synthesis of fac-[Mn(6,6′-Me_2bpy)$(CO)_3$(py)](OTf) (6,6′-Me_2bpy-py)

The synthetic procedure was adapted from a previously reported procedure for related Mn(I) compounds.[57] A mixture of *fac*-[Mn(6,6′-Me_2bpy)$(CO)_3$Br] (100 mg, 0.24 mmol) and AgOTf (110 mg, 0.42 mmol) in 15 mL of CH_2Cl_2 was stirred at room temperature for 16 h. The precipitated AgBr was filtered through Celite, and the solvent was evaporated under reduced pressure. The obtained yellow solid was dissolved in 20 mL of methanol followed by addition of 1 mL of pyridine. The solution was heated at

reflux under argon for 5 h. After cooling to room temperature, the solvent was removed under reduced pressure. The yellow residue was dissolved in 5 mL of CH_2Cl_2 and added dropwise to 100 mL of hexane to induce precipitation. The yellow solid was collected by vacuum filtration and washed with diethyl ether. Yield: 90 mg (0.16 mmol, 67 %). ^{1}H NMR (500 MHz, CD_3CN): δ 7.97 (2H, t), 7.90 (2H, d), 7.76 (1H, m), 7.66 (2H, d), 7.62 (2H, d), 7.16 (2H, t), 3.15 (6H, s). Elemental analysis calculated for $C_{21}H_{17}O_6N_3MnF_3S•0.5H_2O$: 45.01% C, 3.24 % H, 7.50% N, 5.72% S. Found: 45.22% C, 3.00% H, 7.53% N, 5.76% S. HR-ESI(+)-MS (CH_3CN): $[M-OTf]^+$, *m/z* = 402.064 (calcd *m/z* = 402.065).

Elemental Analysis

Elemental analysis (C, H, N, S) was performed by Atlantic Microlabs, Inc. (Norcross, GA). Prior to combustion, samples were protected from light to prevent photodecomposition.

High Resolution Electrospray Ionization Mass Spectrometry

HR-ESI(+)-MS spectra were recorded using a Thermo Fisher Scientific Q Exactive Plus hybrid quadrupole–Orbitrap mass spectrometer with solvent flow rate of 20 μL/min in the positive mode. A potential of 4.0 kV was applied to ionize the 5 μM solution of each compound in CH_3CN.

Single Crystal X-ray Crystallography

Crystals suitable for X-ray diffraction were obtained by slow vapor diffusion of diethyl ether into a CH_2Cl_2 solution of each complex. X-ray intensity data were measured on a Bruker PHOTON II CPAD-based diffractometer with dual Cu/Mo ImuS microfocus

optics (Cu Kα radiation, λ = 1.54178 Å, Mo Kα radiation, λ =0.71073 Å). Crystals were mounted on a cryoloop using Paratone oil and placed under a steam of nitrogen at 100 K (Oxford Cryosystems). The detector was placed at a distance of 5.00 cm from the crystal. The data were corrected for absorption with the SADABS program. The structures were refined using the Bruker SHELXTL Software Package (Version 6.1) and were solved using direct methods until the final anisotropic full-matrix, least squares refinement of F^2 converged. Crystallographic data for 4,4′-Me_2bpy-Br, 6,6′-Me_2bpy-Br, 4,4′-Me_2bpy-py, and 6,6′-Me_2bpy-py are provided in Tables A1 and A2. CCDC numbers 1989788-1989791 contain the supplementary crystallographic data for this paper and can be obtained free of charge from The Cambridge Crystallographic Data Centre via www.ccdc.cam.ac.uk/structures.

Computational Methods

The geometries for 6,6′-Me_2bpy-Br, 6,6′-Me_2bpy-py, and proposed photochemical intermediates were fully optimized using the M06 level[98,99] of density functional theory (DFT) with the SMD continuum solvation model for CH_3CN solvent[100] in the Gaussian 16 program.[116] The 6-31G* basis set was utilized for C, H, N, and O,[101] while the SDD energy consistent pseudopotentials were utilized for Mn and Br.[117] To confirm the presence of local minima on the potential energy surfaces, frequency analysis was performed after geometric optimization. The Avogadro program (Version 1.2.0)[103] was used to obtain the calculate C−O stretching frequencies which were multiplied by an frequency scaling factor of 0.96 for comparison to experimental data.

^{1}H NMR

^{1}H NMR spectra were obtained on a Bruker Ascend 500 MHz spectrometer at 298 K. The chemical shifts were referenced to the CD_3CN solvent peak (δ = 1.94 ppm).

Fourier Transform Infrared (FTIR) Spectroscopy

FTIR spectra were collected using a Shimadzu IRAffinity-1S Fourier transform infrared spectrophotometer and a CaF¬2 liquid IR cell with CH_3CN solvent.

Electronic Absorption Spectroscopy

Electronic absorption spectra were recorded with an Agilent Cary 8454 diode array UV-visible spectrophotometer with 1 nm resolution and 0.5 s integration time in a 1 × 1 cm quartz cuvette at room temperature. Extinction coefficients in CH_3CN were measured in triplicate.

Photolysis Experiments

The photolysis studies were carried out with CH_3CN solutions of the compounds at room temperature and 405 nm LEDs (Luxeon Star LED, Quadica Developments, Inc., Lethbridge, Alberta, Canada). Each sample was irradiated for varied time intervals and analyzed by the appropriate spectroscopic method (FTIR, electronic absorption and ^{1}H NMR analysis). Analogous dark control experiments were performed in the absence of irradiation. Ferrioxalate chemical actinometry was performed to determine the photon flux of the 405 nm light source (2.7×10^{-8} mol photons/s).[97] The quantum yield of CO dissociation (Φ_{CO}) was measured using electronic absorption spectroscopy by monitoring the decrease in the MLCT absorbance band at very early times (<10% change in absorbance). All samples were absorbance matched at the irradiation wavelength (405 nm). The rate of moles of reactant lost was obtained from the slope of the moles of

reactant vs irradiation time plot. Values were corrected for the fraction of light absorbed by the sample at the 405 nm. The Φ_{CO} values were calculated by dividing the rate of moles of reactant lost (in moles reactant/s) by the photon flux (moles of photons/s). Representative data for 6,6′-Me_2bpy-Br and 6,6′-Me_2bpy-py are provided in Figure A14.

3.3. Results and Discussion

Synthesis and Characterization

The new compounds 6,6′-Me_2bpy-Br and 6,6′-Me_2bpy-py were prepared by adapting the previously reported methods for the 4,4′-Me_2bpy analogues.[57,94]. It is critical to keep all Mn(I)-containing solids and solutions in the dark, as rapid photodecomposition occurs under ambient light conditions. Elemental analysis (C, H, N, S) and ESI-MS were consistent with the proposed compositions, and the ^{1}H NMR spectra in CD_3CN (Figures A15 and A16) were consistent with the proposed structures.

Structural Analysis

A comparison of bond lengths and bond angles obtained by single crystal X-ray diffraction provides important information about the impact of steric bulk on the *fac*-$[Mn(NN)(CO)_3(L)]^{n+}$ complexes. The crystal structures for 4,4′-Me_2bpy-Br, 6,6′-Me_2bpy-Br, 4,4′-Me_2bpy-py and 6,6′-Me_2bpy-py are provided in Figure 23, and tabulated bond distances and angles are provided in Tables A3 and A4. For 6,6′-Me_2bpy-Br and 4,4′-Me_2bpy-py, there are three and two multiple equivalents in the asymmetric unit, respectively. In general, the bond lengths are not impacted significantly between the 4,4′-Me_2bpy complexes and their 6,6′-Me_2bpy analogues. The most notable exception is the Mn(1)−N(1) and Mn(1)-N(2) bonds (i.e. the bonds between Mn and the N atoms on

Me_2bpy), which increase from 2.023(3) and 2.040(3) Å to 2.079(2) and 2.080(2) Å for 4,4′-Me_2bpy-Br and 6,6′-Me_2bpy-Br, respectively, as a result of this interference between the methyl substituents and equatorial CO ligands. A comparison of bond angles suggests the structural impacts of steric bulk. In 4,4′-Me_2bpy-Br, the C(1)−Mn(1)−C(3) bond angle (between the two equatorial CO ligands) is 88.8(2)°, whereas this same bond angle in 6,6′-Me_2bpy-Br is contracted to 84.1(1)°, as a result of the interference between the 6,6′-methyl groups and the equatorial CO ligands (Figure 24). It should be noted that we cannot rule out contribution of crystal packing effects toward the differences in these bond angles, as a small yet significant difference in Mn-C bond lengths are observed as a function of methyl group placement (Table A3). Finally, the methyl substituents at the 6,6′-positions cause the bidentate ligand to tilt out of the "normal" plane as a result of interferences with the equatorial CO ligands (Figure 3). By defining the "normal" Me_2bpy ligand plane with Mn(1), N(1), and N(2), and the Me_2bpy plane with N(1), N(2), C(8), and C(11) (as shown in Figure A17), the 6,6′-Me_2bpy ligand is tilted toward L by ~21° and ~26° in the structure of 6,6′-Me_2bpy-Br and 6,6′-Me_2bpy-py, respectively, while the 4,4′-Me_2bpy ligand only tilts by ~9° and ~10° in 4,4′-Me_2bpy-Br and 4,4′-Me_2bpy-py, respectively. Tilting of the ligand is consistent with similar tilt angles reported in Ru(II) complexes with bulky bidentate ligands such as 6,6′-Me_2bpy, 2,2′-biquinoline, 2,9-dimethyl-1,10-phenathroline, and 3,6-dimethyldipyridylphenazine.[118–121]

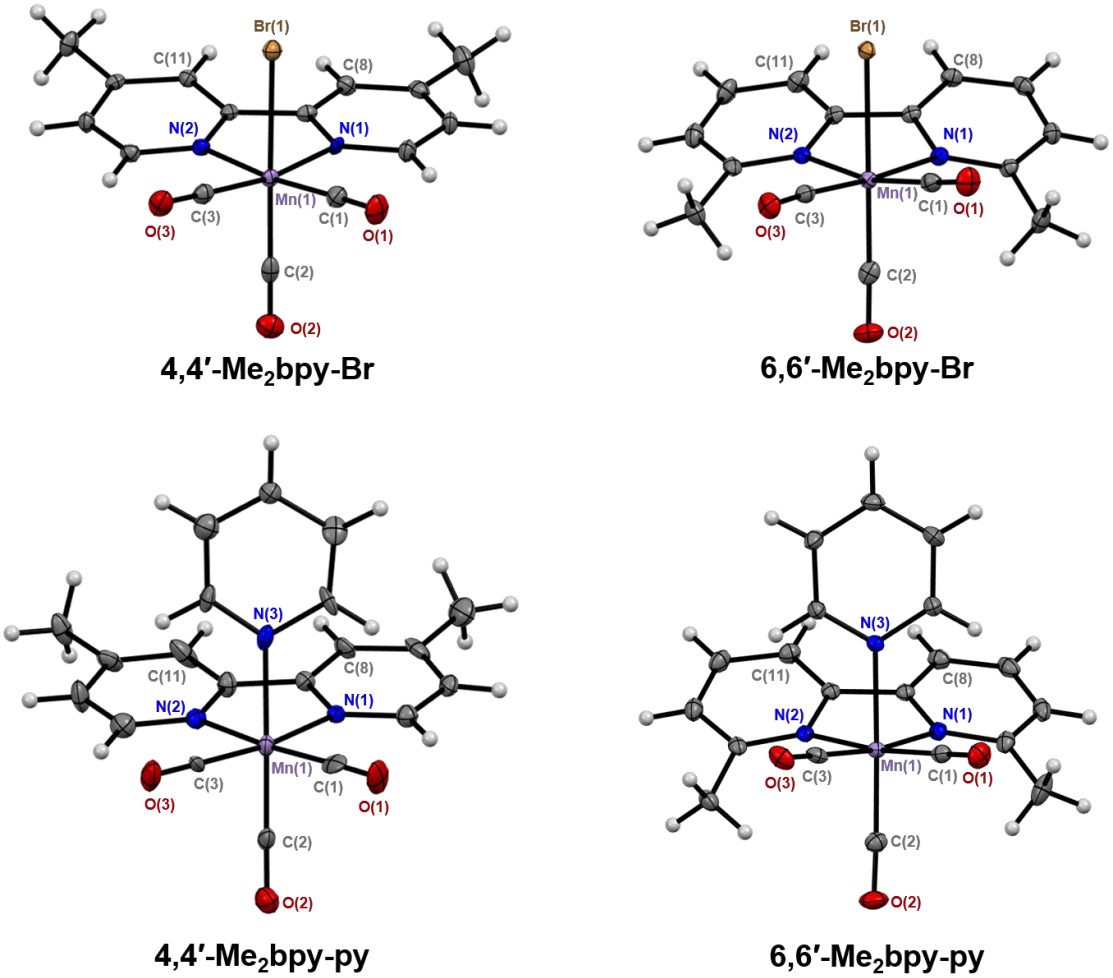

Figure 23. Crystal structures of 4,4′-Me_2bpy-Br, 6,6′-Me_2bpy-Br, 4,4′-Me_2bpy-py and 6,6′-Me_2bpy-py with thermal ellipsoids set at 50% probability level. Triflate counter ion for 4,4′-Me_2bpy-py and 6,6′-Me_2bpy-py is omitted for clarity.

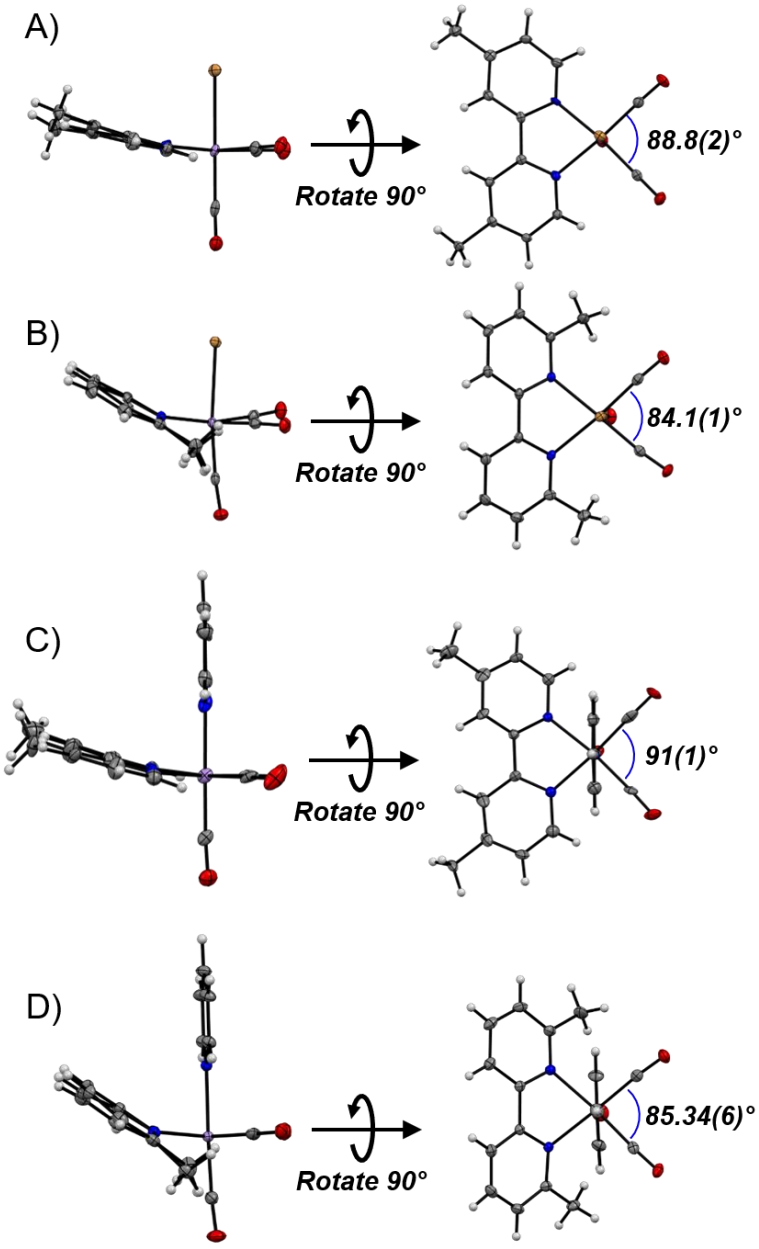

Figure 24. Crystal structures of 4,4′-Me_2bpy-Br (A), 6,6′-Me_2bpy-Br (B), 4,4′-Me_2bpy-py (C) and 6,6′-Me_2bpy-py (D) viewed from the side (left) and down the Br-Mn or py-Mn bond (right). Thermal ellipsoids set at 50% probability level.

Vibrational Spectroscopy

FTIR spectral analysis provides insight into the electron density on the Mn center by virtue of the C−O stretching frequencies. The FTIR spectra for all four compounds are shown in Figure 25, and the experimental vibrational frequencies compared to the calculated values predicted from DFT calculations are presented in Table 6. The FTIR spectra for all *fac*-[Mn(NN)$(CO)_3$Br] and *fac*-[Mn(NN)$(CO)_3$(py)]$^+$ compounds exhibit three vibrational bands in the C−O stretching region (1800-2200 cm^{-1}), in agreement with the compounds' C_s symmetry. The ν_{CO} values for the compounds are determined by the ligand set's impact on the Mn center's electron density, as decreasing the electron density on Mn causes weaker Mn-CO π-backbonding and higher C-O stretching frequency. Similar to our previously reported 4,4′-Me_2bpy compounds,[57] replacing the π-donor Br^- with π-accepting py in the 6,6′-Me_2bpy compounds shifts ν_{CO} from 2023, 1926, and 1919 cm^{-1} to 2042, 1954, and 1939 cm^{-1}, respectively. The placement of the methyl groups at either the 4,4′- or 6,6′-positions of bpy have very little impact on the vibrational frequencies, indicating that the electron donation is not significantly different at the *ortho* vs *para* positions of the pyridine rings.

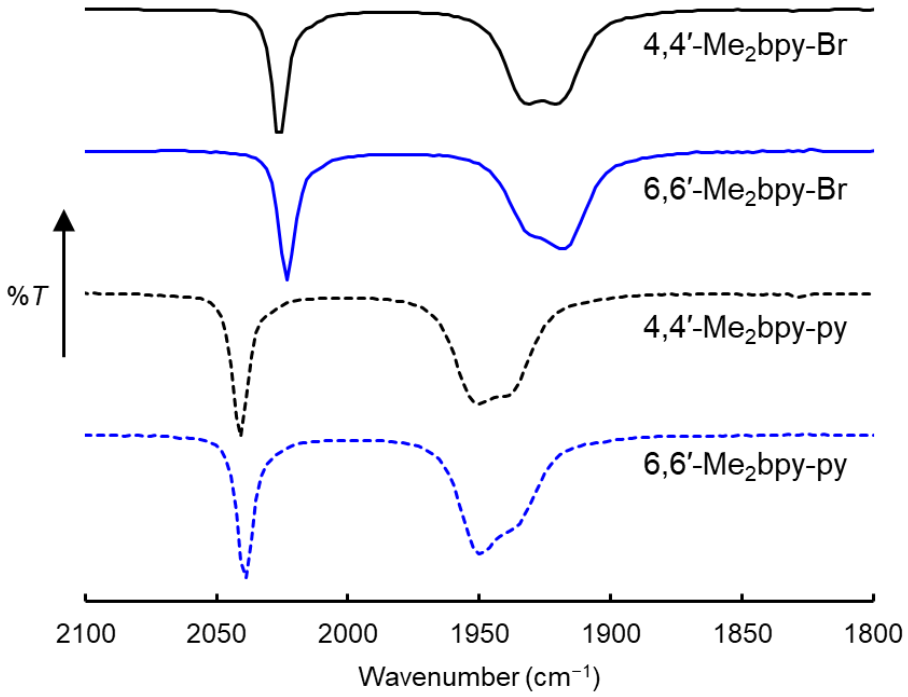

Figure 25. FTIR spectra for 4,4′-Me_2bpy-Br (black solid), 6,6′-Me_2bpy-Br (blue solid), 4,4′-Me_2bpy-py (black dashed) and 6,6′-Me_2bpy-py (blue dashed) in rt CH_3CN.

Table 6. Experimental and calculated C−O vibrational frequencies for *fac*-[Mn(NN)$(CO)_3$Br] and *fac*-[Mn(NN)$(CO)_3$(py)]$^+$ (NN = 4,4′-Me_2bpy and 6,6′-Me_2bpy) in rt CH_3CN.

Compound	**Experimental ν(CO) (cm^{-1})** [a]	**Calculated ν(CO) (cm^{-1})** [b]
4,4′-Me_2bpy-Br [c]	2026, 1933, 1919	2019, 1938, 1929
6,6′-Me_2bpy-Br	2023, 1926, 1919	2015, 1938, 1928
4,4′-Me_2bpy-py [c]	2042, 1954, 1939	2033, 1953, 1947
6,6′-Me_2bpy-py	2039, 1950, 1936	2031, 1951, 1946

[a] Data collected in rt CH_3CN in a CaF_2 cell.
[b] Obtained from the energy optimized structures using the M06 level of DFT and the 6-31G* basis set for H, C, N, and O and the SDD basis set for Mn and Br.
[c] From reference.[57]

Electronic Absorption Spectroscopy

The electronic absorption spectra of the four photoCORMs in CH_3CN are presented in Figure 26, and the absorption maxima and extinction coefficients are provided in Table 7. For *fac*-[Mn(NN)$(CO)_3$Br] compounds, the lowest energy absorbance band is known to have both Mn(dπ)→NN(π*) singlet metal-to-ligand charge transfer (^{1}MLCT) and Br(p)→NN(π*) singlet halide-to-ligand charge transfer (^{1}XLCT) character, while the *fac*-[Mn(NN)$(CO)_3$(py)]$^+$ analogues' lowest energy band is expected to have primarily ^{1}MLCT character. As expected based on the previously reported 4,4′-Me_2bpy-Br and 4,4′-Me_2bpy-py complexes,[57] a blue shift in the lowest energy band is observed by replacing the Br^- in 6,6′-Me_2bpy-Br (λ_{max} = 397 nm; ε = 2800 $M^{-1}cm^{-1}$) with py to afford 6,6′-Me_2bpy-py (λ_{max} = 374 nm; ε = 3300 $M^{-1}cm^{-1}$) due to the stabilization of the Mn(dπ) orbitals by the π-accepting py. In comparing the effects of the methyl substituent placement on Me_2bpy, a small blue shift in the MLCT band is observed for the 6,6′-Me_2bpy complexes compared to their 4,4′-Me_2bpy analogues. Moving the methyl substituents from the 4,4′ positions to the 6,6′ positions causes shifting from 411 to 397 nm (4,4′-Me_2bpy-Br and 6,6′-Me_2bpy-Br, respectively) and from 378 to 374 nm for 4,4′-Me_2bpy-py and 6,6′-Me_2bpy-py, respectively. While the cause of this small blue shift is not clear, and it may be a combination of both steric and electronic factors, a similar trend has been observed in related compounds featuring lowest energy ^{1}MLCT absorbance bands. For the analogous *fac*-[Re(Me_2bpy)$(CO)_3$(py)]$^+$ compounds in CH_3CN, the ^{1}MLCT band was found at 369 and 364 nm for 4,4′-Me_2bpy and 6,6′-Me_2bpy, respectively.[122] Similarly, moving the methyl substituents from 4,4′ to 6,6′ caused a shift

from 441 to 418 nm for the ^{1}MLCT band for [Mo(Me$_2$bpy)(CO)$_4$] in acetone.[123] This shift was also observed for [Ru(bpy)$_2$(Me$_2$bpy)]$^{2+}$, in which the lowest energy band, comprising both Ru(dπ)→bpy(π*) and Ru(dπ)→Me$_2$bpy(π*) MLCT transitions, has a maximum at 455 and 453 nm for 4,4′-Me$_2$bpy and 6,6′-Me$_2$bpy, respectively.[124]

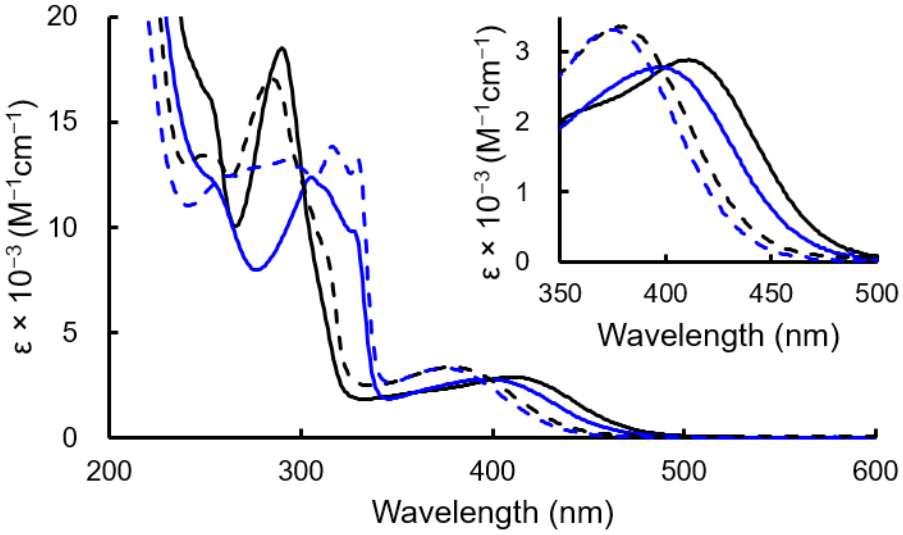

Figure 26. Electronic absorption spectra for 4,4′-Me$_2$bpy-Br (black solid), 6,6′-Me$_2$bpy-Br (blue solid), 4,4′-Me$_2$bpy-py (black dashed) and 6,6′-Me$_2$bpy-py (blue dashed) in rt CH$_3$CN. Inset: zoom-in region highlighting the lowest energy absorbance bands.

Table 7. Electronic absorption spectroscopy data for *fac*-[Mn(NN)(CO)$_3$Br] and *fac*-[Mn(NN)(CO)$_3$(py)]$^+$ (NN = 4,4′-Me$_2$bpy and 6,6′-Me$_2$bpy) in rt CH$_3$CN.

	MLCT	**π→π***
Compound	**λ, nm (ε × 10^{-4}, M^{-1}cm^{-1})**	**λ, nm (ε × 10^{-4}, M^{-1}cm^{-1})**
4,4′-Me$_2$bpy-Br [a]	411 (2.9)	290 (18)
6,6′-Me$_2$bpy-Br	397 (2.8)	328 (9.8)
4,4′-Me$_2$bpy-py [a]	378 (3.4)	287 (18)
6,6′-Me$_2$bpy-py	374 (3.3)	330 (13)

[a] From reference.[57]

Photochemical Ligand Dissociation

In our previous work using both FTIR and ^{1}H NMR to interrogate the photointermediates produced during irradiation with visible light,[57] we reported that irradiation of 4,4′-Me$_2$bpy-Br and 4,4′-Me$_2$bpy-py in CH_3CN results in formation of two dicarbonyl intermediates. In the first step, one CO is exchanged with a solvent molecule, and in the second step, the monodentate ligand L is replaced with a second solvent molecule. The carbonyl ligands provide a convenient probe into the ligand exchange processes that occur during photolysis of the *fac*-[Mn(NN)(CO)$_3$(L)]$^{n+}$ complexes with visible light, as the number of ν_{CO} signals and relative frequencies can be correlated to the molecule's point group and ligand set. Figure 6 highlights the comparison between the FTIR spectral changes during photolysis of the NN = 4,4′-Me$_2$bpy compounds (A and B) with the NN = 6,6′-Me$_2$bpy compounds (C and D). No spectral shifts are observed by FTIR, ^{1}H NMR, or electronic absorption spectroscopy when samples are stored in solution in the dark for at least 1 h (Figures A18-A21). ^{1}H NMR analysis (Figures A22-A23) complements the information obtained by FTIR because, although it gives no clear information about the number of CO ligands coordinated, it provides information about whether a mirror plane bisecting the NN ligand is present.

In the case of 4,4′-Me$_2$bpy-Br and 6,6′-Me$_2$bpy-Br, the most notable difference is that while two sets of intermediate ν_{CO} bands are observed for 4,4′-Me$_2$bpy-Br (Fig. 27A), only one set of intermediate bands is observed for 6,6′-Me$_2$bpy-Br (Fig. 27C). The loss of the original signals at 2023, 1926, 1919 cm^{-1} is accompanied by the appearance of new bands at 1960 and 1876 cm^{-1}. Considering the similar frequencies between this set

and the second intermediate bands for the 4,4′-Me_2bpy-Br analogue, this intermediate is likely a dicarbonyl intermediate in which one CO and Br^- are both replaced by CH_3CN solvent. The observed ν_{CO} bands are found at frequencies similar to those predicted by DFT calculations (Table A5) for either *cis,cis*-[Mn(6,6′-Me_2bpy)$(CO)_2(CH_3CN)_2]^+$ (1967 and 1908 cm^{-1}) or *cis,trans*-[Mn(6,6′-Me_2bpy)$(CO)_2(CH_3CN)_2]^+$ (1966 and 1908 cm^{-1}). As no evidence of a Br^--containing intermediate is observed on the time scale of this experiment, we propose that the Mn-Br bond is considerably more labile following the first CO dissociation with the addition of steric bulk at the 6,6′ positions than in the 4,4′-Me_2bpy analogue. ^{1}H NMR analysis for 4,4′-Me_2bpy-Br indicated that loss of Br^- from the *cis,cis*-[Mn(4,4′-Me_2bpy)$(CO)_2(CH_3CN)$Br] intermediate forms *cis,cis*-[Mn(4,4′-Me_2bpy)$(CO)_2(CH_3CN)_2]^+$ followed by conversion to the *cis,trans*-[Mn(4,4′-Me_2bpy)$(CO)_2(CH_3CN)_2]^+$ isomer (in which both CO ligands are in equatorial positions and both CH_3CN ligands are in axial positions). A similar analysis of 6,6′-Me_2bpy-Br by ^{1}H NMR (Figure A22) shows only the formation of a symmetric intermediate, *cis,trans*-[Mn(6,6′-Me_2bpy)$(CO)_2(CH_3CN)_2]^+$. DFT calculations predict that the ν_{CO} are very similar between the *cis,cis* and *cis,trans* isomer, so only ^{1}H NMR can differentiate between these two species. We propose that the structural distortion imparted by the 6,6′-Me_2bpy ligand increases the photolability, causing the formation and consumption of *cis,cis*-[Mn(6,6′-Me_2bpy)$(CO)_2(CH_3CN)$Br] and *cis,cis*-[Mn(6,6′-Me_2bpy)$(CO)_2(CH_3CN)_2]^+$ to occur on a timescale too fast to observe by FTIR and ^{1}H NMR spectroscopy (Scheme 2).

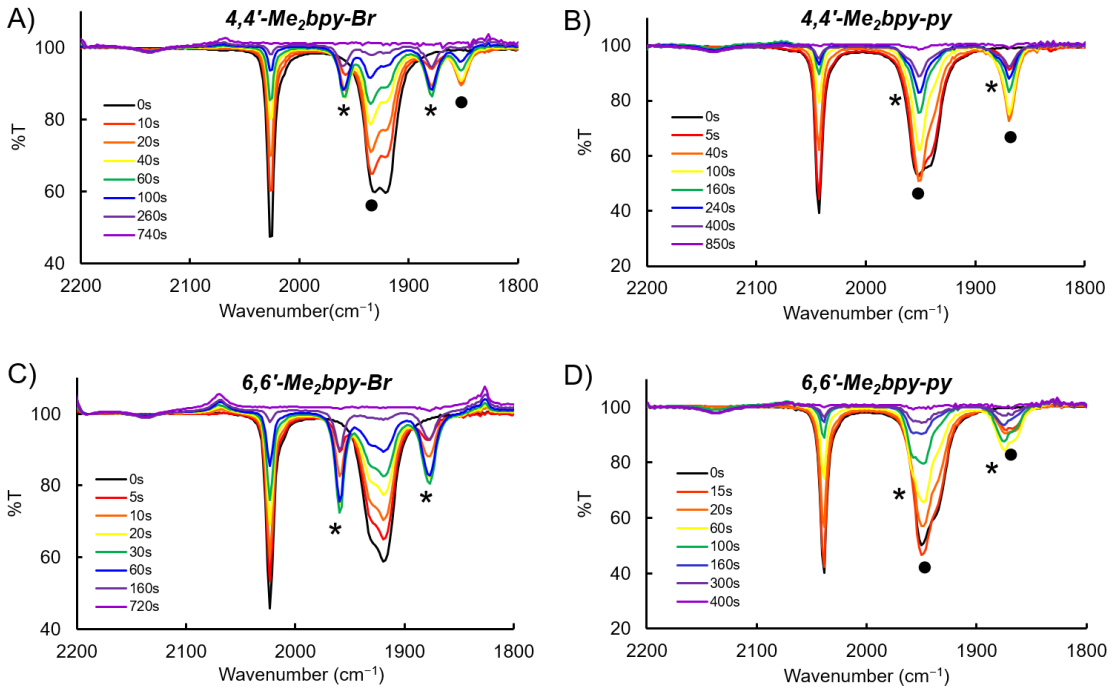

Figure 27. FTIR spectra for 4,4′-Me_2bpy-Br (A), 4,4′-Me_2bpy-py (B), 6,6′-Me_2bpy-Br (C), and 6,6′-Me_2bpy-py (D), in rt CH_3CN (1 mM) following irradiation with $\lambda = 405$ nm.

Scheme 2. Proposed photochemical ligand exchange mechanism for *fac*-[Mn(6,6′-Me_2bpy)$(CO)_3$Br] in CH_3CN.

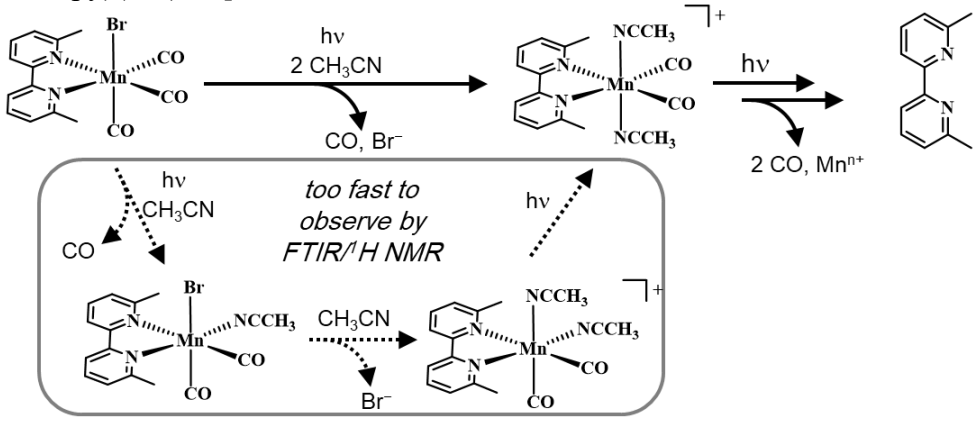

The FTIR spectra collected during photolysis of 4,4′-Me_2bpy-py (Figure 27B) and 6,6′-Me_2bpy-py (Figure 27D) show very similar changes. In our previous work with 4,4′-Me_2bpy-py,[57] we found that the first photochemical intermediate is *cis,trans*-[Mn(4,4′-Me_2bpy)$(CO)_2(CH_3CN)(py)]^+$ which forms through exchange of the axial CO with CH_3CN. Absorption of a photon is then required to exchange py with CH_3CN to form the second intermediate, *cis,trans*-[Mn(4,4′-Me_2bpy)$(CO)_2(CH_3CN)_2]^+$. Unlike the L = Br^- analogue, this process does not occur in the absence of light. In the FTIR spectrum (Figure 27B), the *cis,trans*-[Mn(4,4′-Me_2bpy)$(CO)_2(CH_3CN)(py)]^+$ bands at 1948 and 1867 cm^{-1} are followed by a slightly higher energy set (1962 and 1879 cm^{-1}) that appear as shoulders on the first intermediate bands, corresponding to *cis,trans*-[Mn(4,4′-Me_2bpy)$(CO)_2(CH_3CN)_2]^+$.[57] The same trend is observed for 6,6′-Me_2bpy-py, in which the original bands at 2039, 1950, and 1936 cm^{-1} decrease in intensity as the new bands at 1948 and 1863 cm^{-1} appear (Figure 6D). Further irradiation causes the decrease in the first intermediate bands concomitant with the appearance of the second intermediate bands at 1958 and 1875 cm^{-1}. These two intermediates are assigned as *cis,trans*-[Mn(6,6′-Me_2bpy)$(CO)_2(CH_3CN)(py)]^+$ and *cis,trans*-[Mn(6,6′-Me_2bpy)$(CO)_2(CH_3CN)_2]^+$, respectively, based on the 4,4′-Me_2bpy analogues and the ^1H NMR of the photointermediates (Figure A23). The theoretical ν_{CO} bands calculated by DFT for *cis,trans*-[Mn(6,6′-Me_2bpy)$(CO)_2(CH_3CN)(py)]^+$ (1893 and 1953 cm^{-1}) and *cis,trans*-[Mn(6,6′-Me_2bpy)$(CO)_2(CH_3CN)_2]^+$ (1908 and 1966 cm^{-1}), which highlight a small increase in stretching frequency upon replacement of py with CH_3CN, are in sound agreement with experimental results (Table A5).

The most notable difference arising from the placement of the methyl substituents is the lability of the py ligand from the *cis,trans*-[Mn(NN)$(CO)_2(CH_3CN)$(py)]$^+$ intermediate. A sample of 6,6′-Me_2bpy-py was irradiated in CH_3CN for 25 s (red line, Figure 28). At this time, both the first and second intermediates, *cis,trans*-[Mn(NN)$(CO)_2(CH_3CN)$(py)]$^+$ and *cis,trans*-[Mn(NN)$(CO)_2(CH_3CN)_2]^+$, respectively, were observed. The FTIR spectrum was then measured after the sample was stored in the dark for 5 min (gray line, Figure 28). At this point, the first intermediate completely converted into the second intermediate, indicating thermal dissociation of py from this dicarbonyl intermediate, as shown in Scheme 3. This is in stark contrast to the analogous experiment with 4,4′-Me_2bpy-py, in which this py exchange required irradiation.[57] The structural distortion imparted by the 6,6′-Me_2bpy apparently weakens the Mn-py bond in this intermediate, facilitating facile exchange with solvent. This thermal exchange of L with solvent in the dark was observed for 4,4′-Me_2bpy-Br,[57] and the Br^- ligand is even more labile in the 6,6′-Me_2bpy case, as no *cis,cis*-[Mn(6,6′-Me_2bpy)$(CO)_2(CH_3CN)$Br] intermediate can be observed on the timescales of these experiments. This steric bulk also leads to a shorter irradiation time required to fully dissociate all CO ligands from 1 mM CH_3CN solutions of 6,6′-Me_2bpy-py vs 4,4′-Me_2bpy-py, as shown in Figures 27B and 27D.

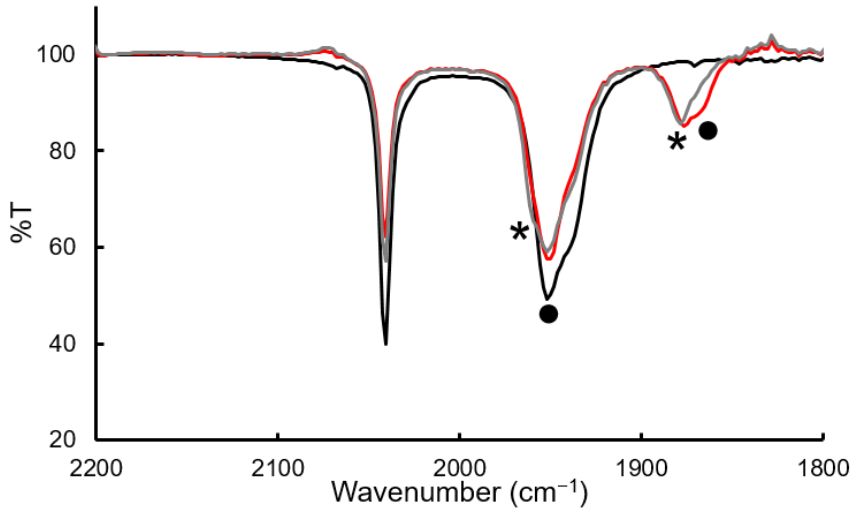

Figure 28. FTIR spectra for 6,6′-Me_2bpy-Br in CH_3CN after irradiation for 25 s with 405 nm light to form the first intermediate (red line), and after storing the sample (containing the original species and first intermediate) in the dark in solution for 5 minutes (gray line). The first and second intermediates are indicated with circles and asterisks, respectively.

Scheme 2. Proposed photochemical ligand exchange mechanism for *fac*-[Mn(6,6′-Me_2bpy)$(CO)_3$(py)]$^+$ in CH_3CN.

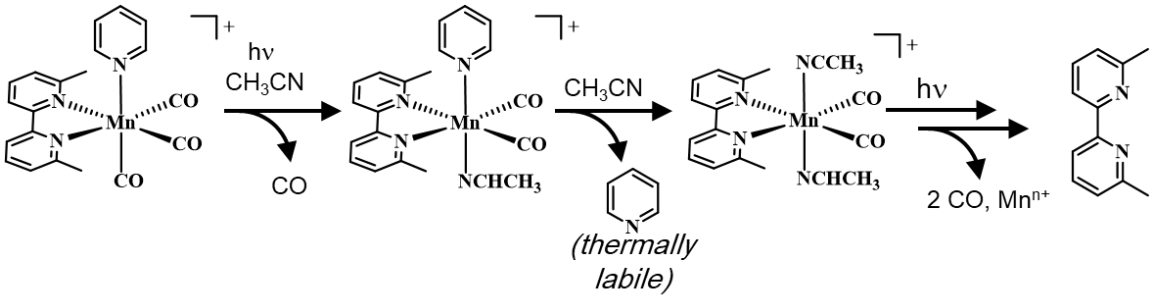

The quantum yield for exchange of the first CO ligand (Φ_{CO}) from Mn(I) photoCORMs has been reported to generally increase with increasing π-acidity of the NN ligand. We investigated the impact of steric distortion on Φ_{CO} by irradiating solutions of

6,6′-Me_2bpy-Br and 6,6′-Me_2bpy-py in CH_3CN with 405 nm light (flux = 2.7×10^{-8} mol photons/s). The electronic absorption spectra for the photolysis of 6,6′-Me_2bpy-Br in CH_3CN is presented in Figure A14. For 6,6′-Me_2bpy-Br and 6,6′-Me_2bpy-py, the values for Φ_{CO} were calculated to be 0.38 ± 0.01 and 0.27 ± 0.01, respectively. The greater Φ_{CO} for 6,6′-Me_2bpy-Br compared to 6,6′-Me_2bpy-py is consistent with the trend for 4,4′-Me_2bpy-Br and 4,4′-Me_2bpy-py (Φ_{CO} = 0.20 ± 0.01 and 0.15 ± 0.01, respectively).[57] The increased Φ_{CO} for each NN = 6,6′-Me_2bpy complex compared to its 4,4′-Me_2bpy analogue is presumably due to the steric distortion caused by the location of the methyl substituents and resulting bond angle distortions, as discussed above, which destabilize the metal-ligand bonds and makes them more susceptible to exchange with solvent. For 6,6′-Me_2bpy-Br and 6,6′-Me_2bpy-py, it should be noted that the measured Φ_{CO} is an "apparent" Φ_{CO}, as exchange of the first CO and Br^-/py occur on similar timescales. The inability to resolve these two processes from each other complicates the measurement of this value; however, the presence of an isosbestic point during early photolysis times (Figure A14) allows for determination of a quantum yield for the photochemical process.

As irradiation of 6,6′-Me_2bpy-Br and 6,6′-Me_2bpy-py with 405 nm leads to the eventual loss of all three coordinated CO ligands, as observed by FTIR analysis, the question remains about the fate of the rest of the metal complex. Analyses of related Mn(I) photoCORMs described the photoproducts containing oxidized Mn species, including $[Mn(NN)_3]^{2+}$, $[Mn(NN)_2(solvent)_2]^{2+}$, MnO_2, and solvated Mn^{2+} ion.[32,79,80,84] During irradiation of the *fac*-$[Mn(NN)(CO)_3L]^{n+}$ complexes, the ^1H NMR signals become significantly broadened, suggesting the formation of a paramagnetic species. An analysis

of the electronic absorption spectra of solutions following exhaustive photolysis (Figure A24), in comparison to the free 4,4′-Me_2bpy and 6,6′-Me_2bpy ligands, suggests that a significant amount of free 6,6′-Me_2bpy is present in solution following irradiation of both 6,6′-Me_2bpy-Br and 6,6′-Me_2bpy-py. In contrast, the electronic absorption spectra for the 4,4′-Me_2bpy-Br and 4,4′-Me_2bpy-py photoproduct solutions are much more similar to the spectrum of $[Mn(4,4'\text{-}Me_2bpy)_3]^{2+}$ (Figure A24). Additionally, free 6,6′-Me_2bpy is detected by ^{1}H NMR in solution after photolysis (Figure A25), while 4,4′-Me_2bpy is not. The 6,6′-position of the methyl groups is expected to inhibit the formation of $[Mn(6,6'\text{-}Me_2bpy)_3]^{2+}$, resulting in a greater amount of free ligand in solution.

3.4. Conclusions

Two new *fac*-$[Mn(NN)(CO)_3(L)]^{n+}$ photoCORMs, 6,6′-Me_2bpy-Br and 6,6′-Me_2bpy-py, featuring a sterically bulky bidentate ligand, were prepared, and their photophysical and photochemical properties were investigated compared to the previously reported 4,4′-Me_2bpy analogues. While the placement of the methyl substituents has little impact on the electronic properties of the complexes, the steric distortion is apparent in the crystal structures of the four compounds. Notably, the steric bulk of the 6,6′-Me_2bpy ligand causes a contraction of the angle between the two equatorial CO ligands and a significantly canted bidentate ligand relative to the 4,4′-Me_2bpy complexes. The steric bulk enhances the ligand exchange efficiencies and increases the labilities of both CO and ancillary Br^- or py ligands during irradiation with visible light while maintaining stability in solution in the dark. Work is underway to

further study the impact of ligand sets on photochemical ligand dissociation in photoCORMs.

Chapter 4: Release of CO and Production of $^1O_2$ from a Mn-BODIPY PhotoCORM with Visible Light

This chapter is adapted from a published article entitled "Release of CO and production of $^1O_2$ from a Mn-BODIPY photoCORM with visible light" By Pordel S., Pickens R.N., and White J.K. *Organometallics*, no. 40 (2021): 2983-2994. Copyright © 2021 American Chemical Society.[125]

4.1. Introduction

The main mechanism with which most chemotherapeutic and nonchemical therapies, such as radiation, effectively treat cancer is through production of highly reactive oxygen species (ROS).[126] ROS interfere with cellular functions by damaging DNA, lipids, and proteins.[127] However, the effectiveness of most chemotherapeutics is limited by drug resistance and lack of selectivity.[10] Drug resistance of some cancer cells is due to an elevated level of a tripeptide, γ-l-glutamyl-l-cysteinyl-glycine known as glutathione (GSH).[12] GSH is a cysteine-containing antioxidant that protects cells from the damaging effects of ROS, increasing the antioxidant capacity of cancer cells.[128] The elevated levels of GSH in cancer cells has been linked to the overexpression of cystathionine β-synthase (CBS).[12] CBS is an enzyme that catalyzes the first step of transsulfuration, forming cysteine, the limiting reagent in GSH production.[9,129]

A recent study by Mascharak, et. al. showed that released CO from a photoactivated CO releasing molecule (photoCORM) labeled as $[Mn(CO)_3(phen)(PTA)]^+$ (phen = 1,10-phenanthroline; PTA = 1,3,5-triaza-7-phosphaadamantane) increases the sensitivity of breast cancer cells lines to the generated ROS from doxorubicin by

inhibiting CBS activity and decreasing GSH level, diminishing the antioxidant capacity.[11] In addition to sensitizing cancer cells to ROS, CO has been shown to exhibit anticancer activity in various cancer cell lines.[75,80,130,131] In many studies the effect of exogenous CO has been investigated by photoCORMs. While stable in the dark, photoCORMs offer selectivity and controlled delivery of CO into a specific target upon exposure to light.[132] The majority of reported metal-based photoCORMs are based on Mn(I) complexes.

One of the main challenges in designing an efficient photoCORM is activation by light in the phototherapeutic window (600-950 nm). To date, various strategies, including ancillary ligand modifications,[133,134] multi-photon excitation,[135,136] mixing with a triplet-state photosensitizer,[137] quantum dots,[138] upconverting nanoparticles,[139] or as previously reported by our group, coupling with a visible light absorbing metal complex,[86] etc., have been employed to activate the photo-CO dissociation under visible and NIR irradiation. Alternatively, the use of dye photosensitizers as light harvesting components of the design allow for visible light-activated photoCORMs.[140]

In our system, we seek to take advantage of combining the CO release from the $Mn(CO)_3$ moiety and a dye photosensitizer capable of producing reactive singlet oxygen ($^1O_2$). This system would allow for visible light-activated production of $^1O_2$ and release of CO, allowing a single molecule to sensitize cells to ROS while simultaneously producing ROS ($^1O_2$).

The 4,4-difluoro-4-bora-3a,4a-diaza-s-indacene (BODIPY) dyes have attracted growing attention due to their high molar extinction coefficients and strong absorption in the visible region, easy structural modifications, and high photostability.[141] BODIPY

dyes are highly fluorescent molecules ($S_1 \rightarrow S_0$), limiting the ability to populate their triplet excited (T_1) states as the result of low intersystem crossing (ISC, $S_1 \rightarrow T_1$) efficiency.[142] Triplet excited state population is a requirement for singlet oxygen generation in photodynamic therapy (PDT) , where molecular oxygen in its triplet ground state reacts with a long-lived triplet excited state to produce $^1O_2$ by energy transfer.[142] BODIPY dyes can be easily modified in structure to increase the ISC and produce $^1O_2$. One strategy is to introduce a heavy atom on the 2,6 positions of the BODIPY core to facilitate the ISC and populate the triplet excited state.[143] So far, multiple studies have been done on various BODIPY-metal complexes including those of Ru(II),[144–146] Re(I),[147,148] Pt(II),[149–151] Ir(III),[152] and Co(II)[153,154] with different applications, mainly focused on PDT and photocatalysis. To the best of our knowledge, the Mn-BODIPY complex, with potential application in PDT, has yet to be reported. Herein, we report the synthesis, photophysical and photochemical properties, and formation of photo-intermediates from two Mn(I) complexes sensitized by emissive BODIPY (BDP) chromophores (4-BDP,4′-methyl-2,2′-bipyridine), in which two iodide (I^-) substituents have been incorporated on the 2,6 positions of one of the BDP ligands, labeled as Mn-bpy-I-BDP, and the other one with H atoms on the 2,6 positions labeled as Mn-bpy-H-BDP (Figure 29).

According to previous studies, the BDP units are anticipated to have perpendicular orientation with respect to the pyridine.[155] The iodide substituents facilitate the ISC in the bpy-I-BDP ligand, resulting in high $^1O_2$ quantum yield. Population of the triplet excited state in the bpy-I-BDP free ligand and Mn-bpy-I-BDP complex was

confirmed by a phosphorescence peak at 77 K. In comparison with Mn-bpy-H-BDP, introducing I^- substituents extends the Mn-bpy-I-BDP absorption further into the visible region, allowing the CO to photo-dissociate from the Mn(I) center with low energy light (590 nm) upon BDP excitation. The emission intensity of bpy-R-BDP (R = H or I) ligands quench by > 90%, upon complexation with $Mn(CO)_3$ moiety. Our mechanistic studies suggest that bpy-R-BDP (R = H or I) ligands photo-dissociate from Mn(I) center and restore their full emission intensity after releasing all CO. In addition to producing $^1O_2$, the I atoms significantly increase the dark stability of complex in the solution compared to non-iodinated Mn-bpy-H-BDP.

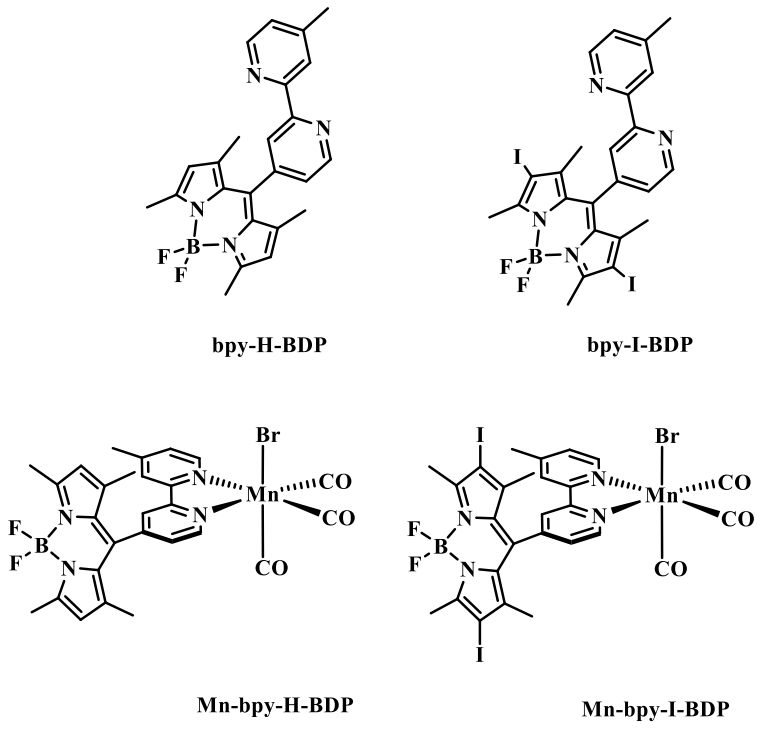

Figure 29. Schematic representation of BDP-based ligands and corresponding Mn(I) complexes

4.2. Results and Discussion

Synthesis

The 4-carbaldehyde-4′-methyl-2,2′-bipyridine and bpy-H-BDP ligands were prepared according to the previous reported methods.[156,157] The bpy-I-BDP was synthesized by a few modifications to a previously reported procedure.[158] The bpy-I-BDP was obtained by reacting the bpy-H-BDP with N-iodosuccinimide (NIS) in a mixture of CH_3Cl/AcOH at room temperature. The Mn-bpy-H-BDP and Mn-bpy-I-BDP complexes were prepared by reacting the $Mn(CO)_5Br$ with each of the bpy-H-BDP and bpy-I-BDP ligands, respectively, in Et_2O at reflux for 3 h (Scheme 3). The ^1H and ^{13}C NMR of the new compounds are shown in Appendix Figures A26, A27, S28, S29 and A30.

Scheme 3. Synthetic approach for BDP-based ligands and corresponding Mn(I) complexes.

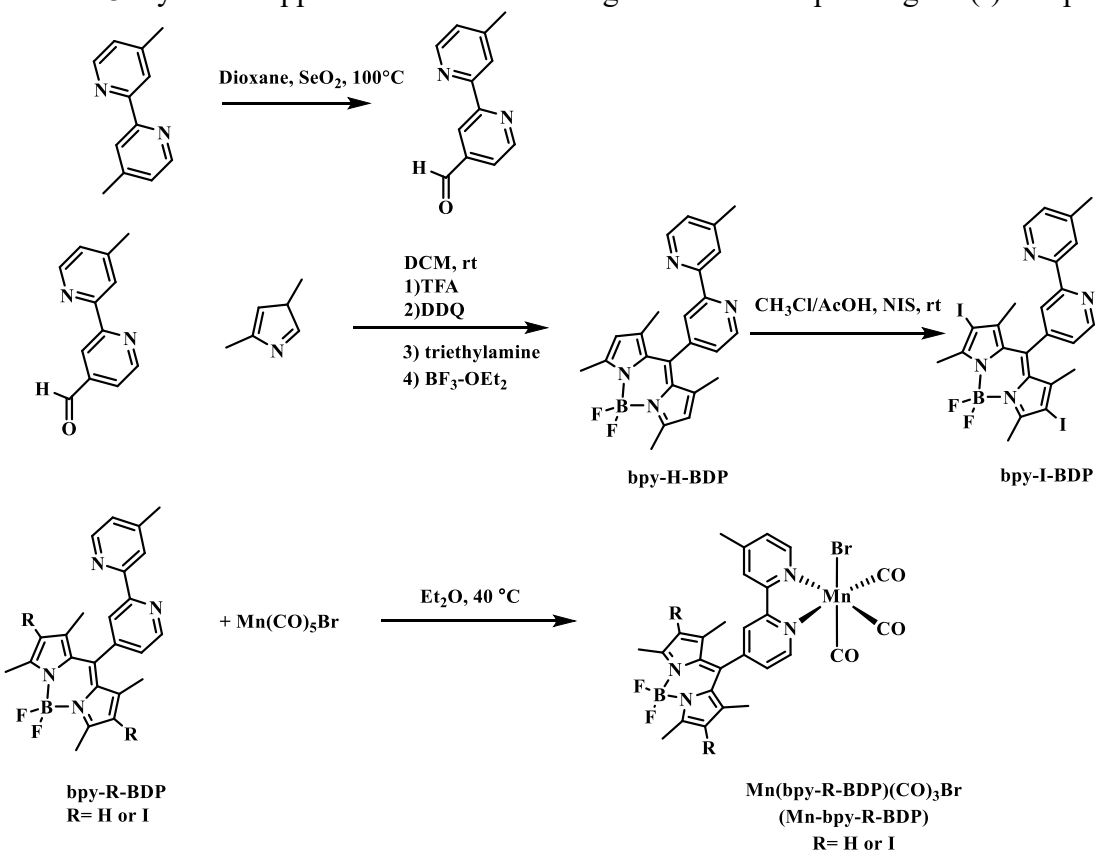

Photophysical and Electrochemical Properties

The spectroscopic properties for all compounds are collected in Table 8. As depicted in Figure 30 the absorption spectra of the bpy-R-BDP (R = H or I) ligands are dominated by the intense bands at 500 and 535 nm with high extinction coefficients of 64,400 and 68,000 $M^{-1}cm^{-1}$ and a higher energy shoulder at 485 and 505 nm for bpy-H-BDP and bpy-I-BDP, respectively. The main intense band is attributed to the 0-0 vibrational band of the $S_0 \rightarrow S_1$ transitions, (i.e. BDP-based spin allowed $\pi \rightarrow \pi^*$), while the high energy shoulder is assigned as the 0-1 vibrational band of the same

transition.[159,160] The 35 nm bathochromic shift of the absorption band in the bpy-I-BDP arises from the electron withdrawing ability of I atoms to conjugate with the BDP core.[161] The Mn complexes show similar absorption profiles to those of the free bpy-R-BDP (R = H or I) ligands. Upon complexation, the sharp BDP band undergoes a slight red shift of about 4 nm ($25 \times 10^5\ cm^{-1}$) in both Mn-bpy-H-BDP (504 nm) and Mn-bpy-I-BDP (539 nm). The reduced π conjugation between the BDP and pyridine portion of the bpy ligand due to the perpendicular orientation of BDP might account for the small red shift after coordination to the Mn.[162]

The photophysical and photochemical properties of these two new complexes have been compared to our previously reported model $Mn(Me_2bpy)(CO)_3Br$ complex where Me_2bpy is 4,4′-dimethyl-2,2′-bipyridine.[57,104] In Figure A31, the model complex $Mn(Me_2bpy)(CO)_3Br$ shows a $Mn(d\pi) \rightarrow bpy(\pi^*)$ MLCT band at 411 nm, suggesting that the peaks between 360 and 420 nm in both Mn-bpy-R-BDP (R = H or I) complexes are arising from $\pi \rightarrow \pi^*$ of BDP ligands with significant contribution from $Mn(d\pi) \rightarrow bpy(\pi^*)$ transition. This assignment is further supported by the higher intensity of this band in the both Mn-bpy-R-BDP (R = H or I) complexes compared to the free ligands seen in Figure 30.

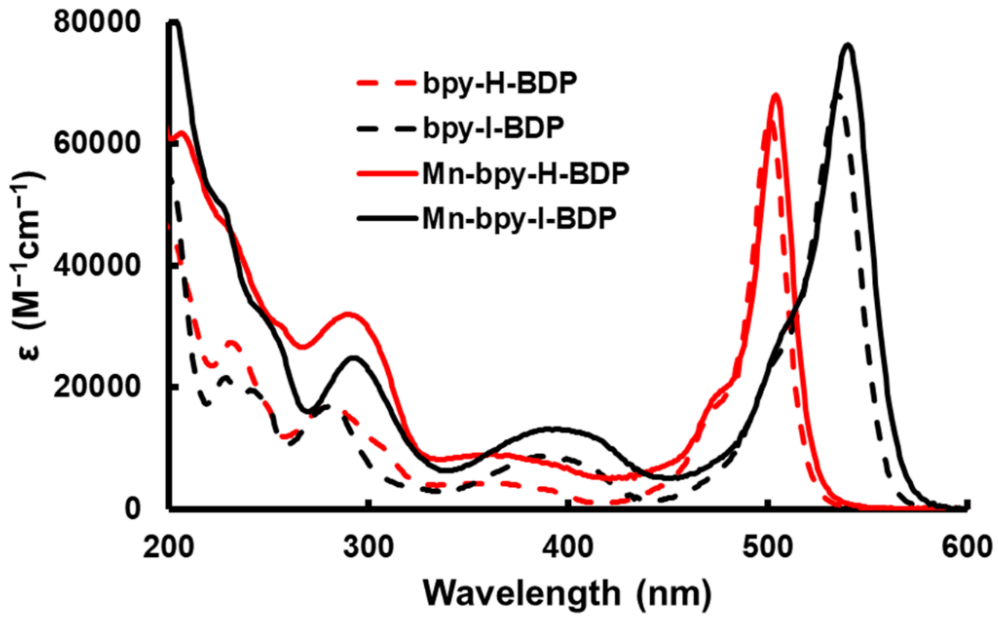

Figure 30. Overlaid electronic absorption spectra for bpy-H-BDP (red dashed), bpy-I-BDP (black dashed), Mn-bpy-H-BDP (red solid) and Mn-bpy-I-BDP (black solid) in room temperature CH_3CN.

As shown in Figure 31, 490 nm excitation of the bpy-R-BDP (R = H or I) ligands in CH_3CN resulted in a very strong emission band at 515 nm with $\Phi_{fl} = 0.32$ for bpy-H-BDP, and a relatively weak emission peak at 560 nm with $\Phi_{fl} = 0.014$ for bpy-I-BDP ligand (Rhodamine B as reference in EtOH, $\Phi_{fl} = 0.5$).[163] The lower Φ_{fl} of iodinated BDP ligand is attributed to the enhanced intersystem crossing (ISC) from $^1\pi\pi^*$ to $^3\pi\pi^*$ as the result of the heavy atom effect.[164–166] Upon complexation to the Mn center, the fluorescence quantum yields decrease from 0.32 to 0.012 for Mn-bpy-H-BDP, and from 0.014 to 0.0046 for Mn-bpy-I-BDP, suggesting the existence of a competitive non-emissive process.

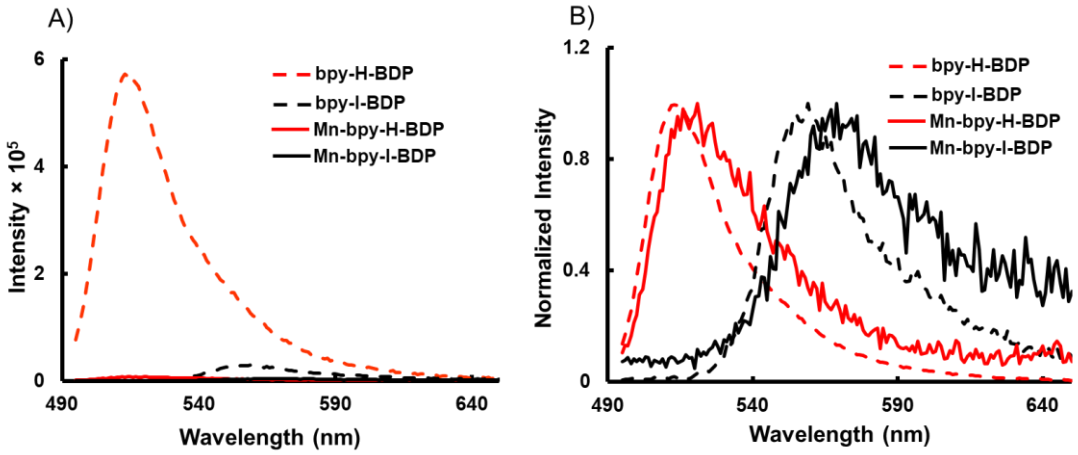

Figure 31. Overlaid emission spectra (relative intensities) (A) and normalized emission spectra (B) for bpy-H-BDP (red dashed), bpy-I-BDP (black dashed), Mn-bpy-H-BDP (red solid) and Mn-bpy-I-BDP (black solid) in room temperature CH_3CN, λ_{exc} = 490 nm, λ_{abs} at 490 nm: 0.1

Table 8. Photophysical properties of BDP-based ligands and corresponding Mn(I) complexes

Compound	λ_{abs} / nm[a]	$\varepsilon \times 10^{-3}$ / M^{-1} cm^{-1}[a]	λ_{em} / nm[a]	Φ_{fl}[b]
bpy-I-BDP	535	68	560	0.014
bpy-H-BDP	500	64	515	0.39
Mn-bpy-I-BDP	539	76	570	0.004
Mn-bpy-H-BDP	504	68	521	0.012
$Mn(Me_2bpy)(CO)_3Br$	411	-	-	-

[a] in CH_3CN, [b] fluorescence quantum yield was measured in EtOH using Rhodamine B (RhB) as reference (EtOH, Φ_{fl} = 0.5)

The excitation spectra in CH_3CN (Figure A32) overlay well with the corresponding absorption spectra throughout the scan range, alluding to no emissive impurities being present. The excitation peak for Mn-bpy-H-BDP, however, is blue

shifted by a few nanometers and matches with the free bpy-H-BDP ligand. We suggested that this is due to the partial bpy-H-BDP ligand dissociation from the Mn center during the excitation.

The electrochemical properties of all compounds were studied by cyclic voltammetry in room temperature DCM solution and the redox potentials are tabulated in Table 9. All potentials were referenced to the ferrocenium/ferrocene (Fc^+/Fc) couple ($E_{1/2}$ = 0.43 V vs Ag/AgCl in DCM). Both bpy-H-BDP and bpy-I-BDP ligands exhibited a quasi-reversible one-electron reduction peak at −1.65 and −1.38 V and a quasi-reversible one-electron oxidation peak at 0.85 and 0.99 V in DCM, respectively (Figure 32 and Figure A33). Each of the reduction and oxidation peaks are attributed to the formation of the π-radical anion and π-radical cation, respectively.[155,167] The higher chemical reversibility of bpy-I-BDP with respect to bpy-H-BDP ligand is attributed to the higher stability of the π-radical anion and cation as a result of the 2,6-substitution on BDP.[168]

Compared to bpy-H-BDP ligand, the introduction of two I atoms on the 2,6 positions shift both the oxidation and reduction potentials to more positive values. In line with UV-Vis data, the electron-withdrawing I substituents stabilize the π and π* orbitals of BDP by decreasing the electron density on the BDP core, leading to more positive oxidation and reduction BDP potentials.[169] This observation agrees with previously reported BDP data.[170] Complexation with Mn shifts the BDP redox potentials to more positive values with an additional irreversible manganese oxidation observed at 0.75 and 0.82 V for Mn-bpy-H-BDP and Mn-bpy-I-BDP, respectively. In the reduction region, in

addition to the peak observed for BDP ligand, formation of two new reduction peaks were observed at −1.58 and −1.87 V for Mn-bpy-H-BDP. Two additional reduction peaks were also observed for Mn-bpy-I-BDP, the first of which overlapped with the BDP peak at around −1.28 V, and the second new reduction peak appeared at −1.59 V in DCM.

After comparing the potentials with free ligands and the model complex $Mn(Me_2bpy)(CO)_3Br$ potentials,[57] we attributed the first irreversible oxidation peak in both complexes to the $Mn^{I/II}$ oxidation and second oxidation peak to the oxidation of BDP unit. The first reduction peak was attributed to $BDP^{0/-}$, and the next two reduction peaks assigned as $Mn^{I/0}$, followed by the rapid dissociation of Br^- to form a five coordinate radical species.[94] These assignments suggested that while the HOMO in both Mn-bpy-R-BDP (R = H or I) complexes is localized on the Mn orbitals, the LUMO is mainly centered on the BDP units.

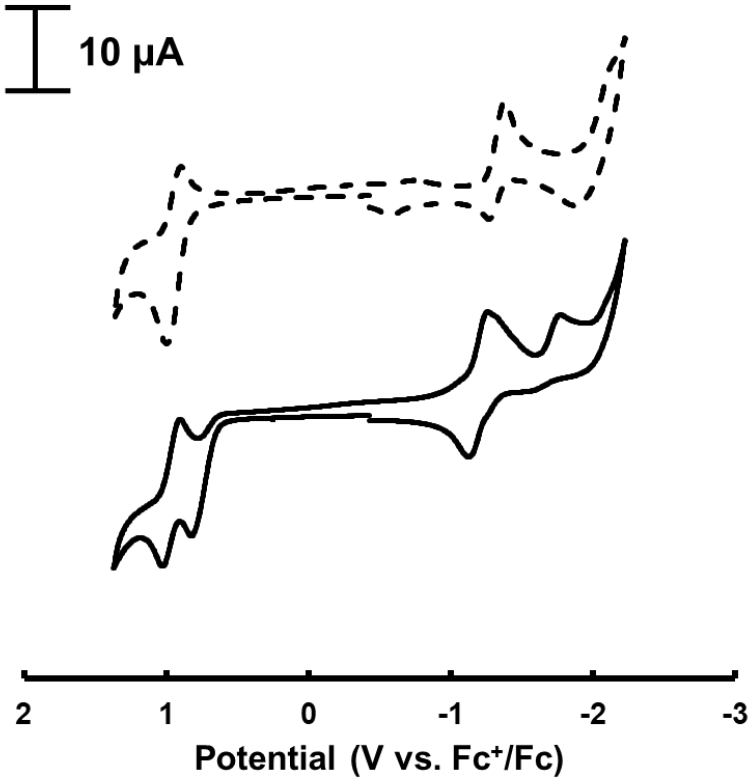

Figure 32. Cyclic voltammograms for 1 mM solutions of bpy-I-BDP (black dashed), Mn-bpy-I-BDP (black solid) in room temperature DCM under N_2 atmosphere with 0.1 M Bu_4NPF_6 as the supporting electrolyte, a Pt working electrode, Pt wire auxiliary electrode, Ag/AgCl reference electrode, and a scan rate of 200 mV/s. Potentials are referenced to the Fc^+/Fc couple (+0.43 V vs. Ag/AgCl).

Table 9. Cyclic voltammetry data for BDP-based ligands and corresponding Mn(I) complexes in DCM.

Compound	E_p^a (V) [a]	E_p^a (V) [a]	E_p^c (V) [a]	E_p^c (V) [a]	E_p^c (V) [a]
bpy-I-BDP	0.99	-	-1.38		-
bpy-H-BDP	0.85 [b]	-	-1.65 [b]	-	-
Mn-bpy-I-BDP	0.82	1.02	−1.26	-1.28	-1.59
Mn-bpy-H-BDP	0.75 [b]	0.96 [b]	−1.50 [b]	-1.58 [b]	-1.87 [b]
$Mn(Me_2bpy)(CO)_3Br$	0.69 [b]	-	-1.90 [b]	-2.11 [b]	

[a] Room temperature DCM under a N_2 atmosphere with 0.1 M Bu_4NPF_6 as the supporting electrolyte, a Pt working electrode, Pt wire auxiliary electrode, Ag/AgCl reference electrode, and a scan rate of 200 mV/s. Potentials are reported vs. Ag/AgCl.[b] Room temperature DCM under a N_2 atmosphere with 0.1 M Bu_4NPF_6 as the supporting electrolyte, a glassy carbon working electrode, Pt wire auxiliary electrode, Ag/AgCl reference electrode, and a scan rate of 200 mV/s. All potentials were referenced to the ferrocenium/ferrocene (Fc^+/Fc) couple ($E_{1/2}$ = 0.43 V vs Ag/AgCl in DCM).

The IR spectra of the two Mn-bpy-R-BDP (R = H or I) complexes in the carbonyl region (1800-2200 cm^{-1}) exhibited three CO stretches similar to previously reported *fac*-Mn(I) tricarbonyl complexes.[32,130] The FTIR spectra in CH_3CN are shown in Figure 33. The three CO stretches showed up at 2027, 1936 and 1923 cm^{-1} for Mn-bpy-H-BDP, and 2027, 1934 and 1924 cm^{-1} for Mn-bpy-I-BDP. These values are in good agreement with the previously reported values for the model complex $Mn(Me_2bpy)(CO)_3Br$.[57] The similar CO stretches in both Mn-bpy-R-BDP (R = H or I) complexes are consistent with the observed redox potentials discussed above. Since the Mn-based HOMOs are less affected by the complexation (shown by the similar oxidation potentials before and after complexation in Table 9), the CO stretches show up at similar frequencies for both Mn-bpy-R-BDP (R = H or I) complexes. The CO stretching frequencies calculated by DFT

were very similar for both Mn-bpy-R-BDP (R = H or I) complexes and in agreement with experimental values (Table 10).

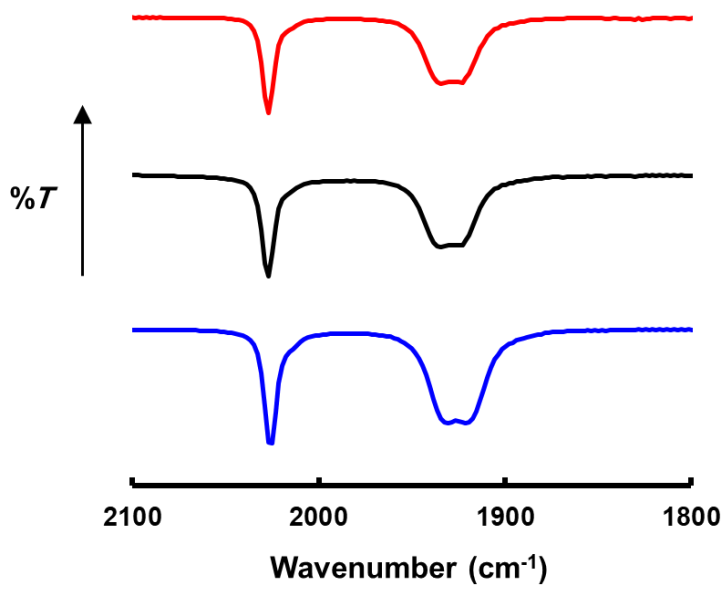

Figure 33. FTIR spectra in the C−O stretching region for Mn-bpy-H-BDP (red solid), Mn-bpy-I-BDP (black solid) and *fac*-[Mn(Me$_2$bpy)(CO)$_3$Br] (blue solid) in rt CH_3CN.

Table 10. Experimental and calculated C−O vibrational frequencies for Mn-bpy-R-BDP (R = H or I) in CH_3CN.

Compound	**Experimental ν(CO) (cm^{-1})** [a]	**Calculated ν(CO) (cm^{-1})** [b]
Mn-bpy-H-BDP	2027, 1936, 1923	2026, 1945, 1936
Mn-bpy-I-BDP	2027, 1934, 1924	2026, 1945, 1937
***fac*-Mn(Me$_2$bpy)(CO)$_3$Br**	2026, 1933, 1919	2019, 1938, 1929

[a] Data collected in rt CH_3CN in a CaF_2 cell.
[b] Obtained from the energy optimized structures using the B_3LYP level of DFT and the 6-31G* basis set for H, C, N, and O and the SDD basis set for Mn, Br and I.

Photochemical Ligand Dissociation

The photolysis studies were performed with CH_3CN solutions of the compounds with 535 and 590 nm LEDs for Mn-bpy-H-BDP and Mn-bpy-I-BDP, respectively. In dark control experiments (Figure A34) no spectral changes were observed through emission spectroscopy up to 90 min for both complexes. While the Mn-bpy-I-BDP was stable up to 24 h in the dark, a gradual bpy-H-BDP dissociation was observed for Mn-bpy-H-BDP after 90 min. The dark stability was further investigated by FTIR. No evidence of CO dissociation was observed for either complex in the solution up to 1 h in room temperature CH_3CN (Figure A35).

To study the photochemical behavior of Mn-bpy-R-BDP (R = H or I) complexes, a solution of each compound in CH_3CN was photolyzed with the appropriate LED, and the spectral changes were monitored at specified time intervals with emission, absorption, FTIR and ^1H NMR spectroscopies. Figure 34 exhibits the electronic absorption and emission spectral changes for Mn-bpy-I-BDP in CH_3CN during irradiation with 590 nm LED. The electronic absorption and fluorescence emission spectra for Mn-bpy-H-BDP (535 nm LED) are shown in Figure A36. During photolysis, the absorbance for Mn-bpy-I-BDP, blue shifted from 539 to 535 nm, accompanied by a decrease in intensity of the bands around 400 and 300 nm. Similarly, the emission spectral changes showed a gradual increase in the emission intensity as well as a blue shift in the emission maximum from 570 to 560 nm. Comparison of photoproducts with that of free ligands (Figure A37) revealed gradual release of bpy-I-BDP during photolysis. The Mn-bpy-H-BDP photolysis

also showed similar spectral changes. Such “turn on” fluorescence behavior has been previously reported by other groups.[70,92,171,172]

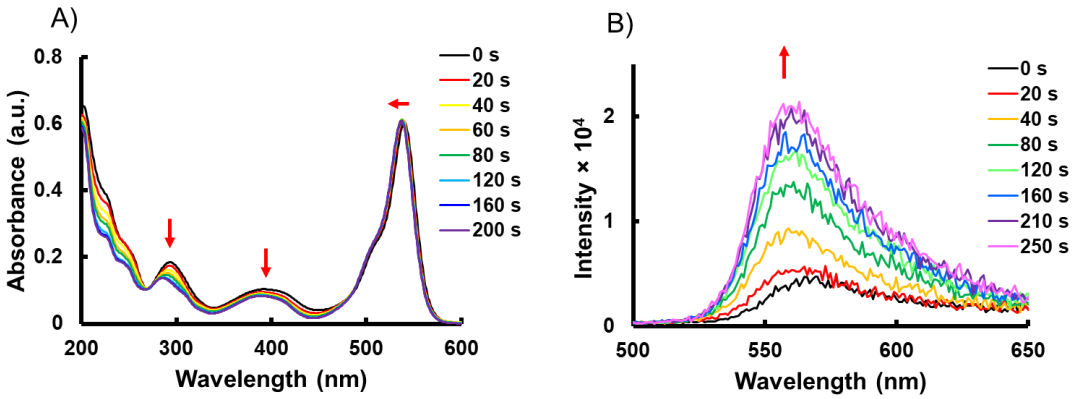

Figure 34. Absorption (A) and emission (B) spectra for the photolysis of Mn-bpy-I-BDP in rt CH_3CN with 590 nm LED.

To study the CO dissociation resulting from photolysis of Mn(I) photoCORMs and formation of corresponding photo-intermediates, the changes in the CO stretches were monitored by FTIR and ^1H NMR spectroscopies. Solutions of Mn-bpy-I-BDP and Mn-bpy-H-BDP in CH_3CN/CD_3CN were irradiated with the appropriate LED, and the FTIR and ^1H NMR spectra were collected at irradiation time intervals. For both complexes, photolysis resulted in very similar spectral observations. As illustrated in Figure 35A and Figure A38, FTIR irradiation at early time leads to emergence of two new stretches at 1936 and 1857 cm^{-1} along with a decrease in all three original bands, corresponding to the release of one CO and formation of the first dicarbonyl intermediate (shown by black circles). These values are comparable to our previously reported CO

stretches for the first intermediate during photolysis of $Mn(Me_2bpy)(CO)_3Br$ compound.[57,104]

In accordance with our previous studies of CO release, we assigned this intermediate as the exchange of one of the equatorial CO ligands with CH_3CN to form *cis,cis*-[Mn(bpy-R-BDP)$(CO)_2(CH_3CN)$Br] (R = H or I). Further irradiation results in appearance of the second dicarbonyl intermediate at 1963 and 1882 cm^{-1}. The frequencies of this intermediate are quite similar with the frequencies of the second intermediate detected in the model complex $Mn(Me_2bpy)(CO)_3Br$. We attributed this intermediate to the loss of Br^- and formation of the *cis,cis*-[Mn(bpy-R-BDP)$(CO)_2(CH_3CN)_2]^+$ (R = H or I) (shown by black asterisks). Further irradiation led to disappearance of all bands and loss of all remaining CO molecules.

During the ^1H NMR photolysis (Figure 35B and Figure A38), only one intermediate was detected for both complexes (shown by red squares) with similar chemical shifts. In this intermediate, the two proton signals on the 2 and 6 positions of the BODIPY pyrroles in Mn-bpy-H-BDP, appear as one signal (integrated as 2), consistent with those two protons experiencing the same chemical environment. We attributed this intermediate to the formation of *cis,trans*-[Mn(bpy-R-BDP)$(CO)_2(CH_3CN)_2]^+$ (R = H or I) in both complexes as the third photochemical intermediate, which cannot be distinguished from the *cis,cis* isomer through the use of FTIR.[57] Further irradiation leads to loss of all signals and very likely formation of an oxidized, paramagnetic Mn species.[79]

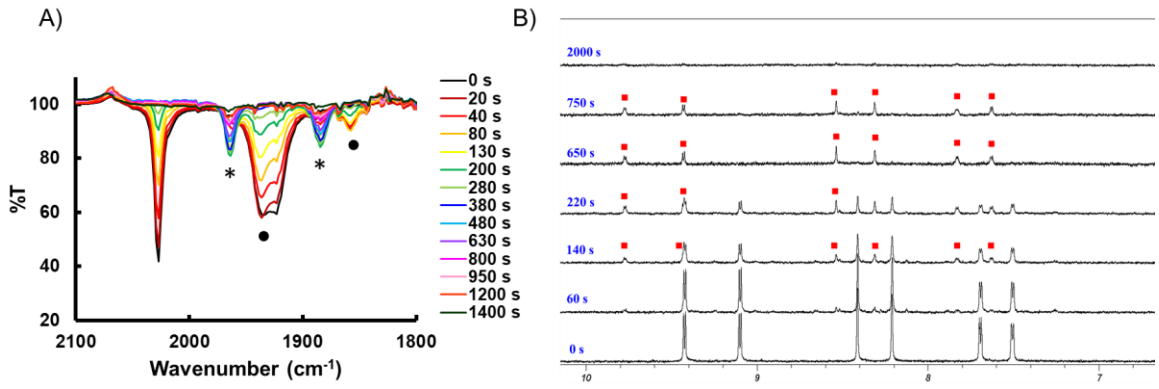

Figure 35. FTIR spectra (A) and ^{1}H NMR (B) photolysis of Mn-bpy-I-BDP in rt CH_3CN/CD_3CN. λ_{irr} = 590 nm

Table 11. Experimental and calculated C−O vibrational stretching frequencies for the photochemical intermediates during photolysis

Photochemical intermediate	**Experimental ν(CO) (cm^{-1})** [a]	**Calculated ν(CO) (cm^{-1})** [b]
***cis,cis*-[Mn(Me$_2$bpy)(CO)$_2$(CH$_3$CN)Br]**	1935, 1852	1943, 1880
***cis,cis*-[Mn(Me$_2$bpy)(CO)$_2$(CH$_3$CN)$_2$]$^+$**	1960, 1878	1968, 1908
***cis,trans*-[Mn(Me$_2$bpy)(CO)$_2$(CH$_3$CN)$_2$]$^+$**	1962, 1879	1970, 1909
***cis,cis*-[Mn(bpy-I-BDP)(CO)$_2$(CH$_3$CN)Br]**	1936, 1857	1956,1884
***cis,cis*-[Mn(bpy-I-BDP)(CO)$_2$(CH$_3$CN)$_2$]**	1963, 1882	1977,1910
***cis,cis*-[Mn(bpy-H-BDP)(CO)$_2$(CH$_3$CN)Br]**	1936, 1857	1955,1883
***cis,cis*-[Mn(bpy-H-BDP)(CO)$_2$(CH$_3$CN)$_2$]**	1963, 1884	1977,1909

[a] Data collected in rt CH_3CN in a CaF_2 cell.
[b] Obtained from the energy optimized structures using the B3LYP level of DFT and the 6-31G* basis set for H, C, N, and O and the SDD basis set for Mn, Br and I.

In probing the photo reactivity of these intermediates, their stability in the absence of light was studied with FTIR (Figure A39). A solution of each sample was prepared in CH_3CN, partially photolyzed with the appropriate LED, and kept in the dark for 30 min. After irradiation of both Mn complexes for a few seconds, the FTIR spectrum revealed three CO stretches of the parent complex as well as the first intermediate's bands shown by circles at 1936 and 1857 cm^{-1}. After 2 min in the dark, these intermediate bands disappeared and new bands (asterisks) at 1963 and 1882 cm^{-1} were observed, consistent with the first intermediate *cis,cis*-[Mn(bpy-R-BDP)$(CO)_2(CH_3CN)$Br] (R = H or I) converting to the second intermediate *cis,cis*-[Mn(bpy-R-BDP)$(CO)_2(CH_3CN)_2]^+$ (R = H or I) by a thermal exchange reaction in the dark. Keeping the samples in the dark up to 30 min did not show any further changes. From the emission, absorption, FTIR, and ^1H NMR photolysis discussed above and based on our previous CO release studies, we proposed that upon photolysis of the Mn-bpy-R-BDP (R = H or I) complexes in CH_3CN, one of the equatorial CO ligands exchanges with a CH_3CN solvent molecule to form *cis,cis*-[Mn(bpy-R-BDP)$(CO)_2(CH_3CN)$Br] (R = H or I). In the next step, the Br^- can be thermally replaced by another CH_3CN solvent molecule to generate *cis,cis*-[Mn(bpy-R-BDP)$(CO)_2(CH_3CN)_2]^+$ (R = H or I) . The last detectable intermediate is formed by photoisomerization of *cis,cis*-[Mn(bpy-R-BDP)$(CO)_2(CH_3CN)_2]^+$ to *cis,trans*-[Mn(bpy-R-BDP)$(CO)_2(CH_3CN)_2]^+$ (R = H or I). Further irradiation results in release of remaining CO ligands, and as shown by emission and absorption photolysis, release of the bpy-R-BDP (R = H or I) ligands. The proposed mechanism for the CO dissociation and formation of intermediates is depicted in Scheme 4.

Scheme 4. Proposed mechanism for intermediates formation for Mn-bpy-R-BDP complexes

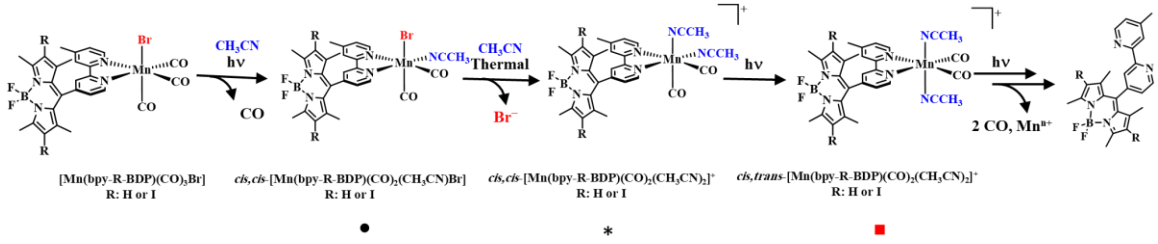

The I heavy atom is known to increase the spin-orbit coupling leading to a non-radiative transition from $^1\pi\pi^*$ to populate the $^3\pi\pi^*$ excited state.[173] In comparison with singlet excited states, triplet excited states have a longer lifetime which make them chemically reactive, allowing for reaction with molecular oxygen to produce singlet oxygen through energy transfer mechanism.[35,151]

To evaluate our compounds' singlet oxygen production, the decrease in the emission intensity of 1,3-diphenylisobenzofuran (DPBF), a well-known fluorescent $^1O_2$ scavenger, was monitored during irradiation with 513 nm light. The quantum yields of singlet oxygen (Φ_Δ) in Table 12 are reported with reference to Rose Bengal (QY of 0.53 in CH_3CN).[174] As expected, while the bpy-I-BDP generated a high amount of $^1O_2$ (Φ_Δ = 1.08) the value for bpy-H-BDP was not quantifiable. Interestingly, the Mn-bpy-I-BDP produced less singlet oxygen (Φ_Δ = 0.27) than that of free ligand. As previously discussed, this might further suggest the formation of a state upon coordination to the Mn that quenches the triplet excited state of bpy-I-BDP, and therefore singlet oxygen production, in the coordinated BDP. No changes were observed in the emission spectrum

of the complex after the experiment, indicating that the bpy-I-BDP ligand does not dissociate from Mn to a significant extent during the time frame of the experiment (Figure A40). However, partial ligand dissociation was observed from Mn-bpy-H-BDP complex during the experiment, making it impossible to collect a viable data for comparison. Another set of experiments was performed on the photoproducts of Mn-bpy-I-BDP complex. The measured Φ_{Δ} was comparable to the free bpy-I-BDP ligand, supporting the release of the ligand upon further irradiation.

To investigate the singlet oxygen generation in aqueous media, SOSG (singlet oxygen sensor green) was used as a probe in water with 5 % (v/v) methanol. The SOSG is highly selective for singlet oxygen and emits green fluorescence with a maximum at 525 nm upon reaction with singlet oxygen.[175,176] As shown in Figure A41, the increase in the emission intensity of SOSG at 525 nm in water:MeOH (95:5) was monitored during irradiation with 535 nm light to avoid SOSG photosensitization. The reported values are with reference to Rose Bengal (QY of 0.75 in H_2O).[35] It is worth mentioning that irradiation of SOSG alone with 535 nm light, did not produce a significant amount of singlet oxygen (Figure A41).

Table 12. Singlet oxygen quantum yields

Compound	Φ_{Δ}[a]	Φ_{Δ}[b]
bpy-I-BDP	1.08±0.01	0.90±0.004
bpy-H-BDP	-	-
Mn-I-BDP	0.27±0.02	0.17±0.02
Photoproduct of Mn-bpy-I-BDP	0.97±0.01	0.85±0.002
Mn-bpy-H-BDP	-	-
$Mn(Me_2bpy)(CO)_3Br$	-	-

[a] determined in CH_3CN with DPBF as $^1O_2$ scavenger and Rose Bengal (RB) as the reference ($QY_{\Delta} = 0.53$) with 513 nm light.
[b] determined in H_2O with SOSG as the $^1O_2$ probe and Rose Bengal (RB) as the reference ($QY_{\Delta} = 0.75$) with 535 nm light.

To provide more insights into the singlet oxygen production and quenching mechanism of the bpy-I-BDP ligand upon complexation, we measured the emission spectra of bpy-I-BDP and Mn-bpy-I-BDP at 77 K in an EtOH glass matrix (Figure 36). While the fluorescence intensity of coordinated bpy-I-BDP in Mn-bpy-I-BDP complex is quenched by about 90% at room temperature (Figure 31), at 77 K fluorescence intensity is restored to the same as that of free bpy-I-BDP, suggesting that electron transfer is the main mechanism of fluorescence quenching in the coordinated form.[162] The fluorescence maxima at 77 K showed small blue shifts compared to those recorded at room temperature, (i.e. from 560 to 551 nm in bpy-I-BDP, and from 570 to 556 nm in Mn-bpy-I-BDP). Interestingly, as shown in the insets of Figure 36, phosphorescence peaks with lower intensities at about 770 and 780 nm were detected for bpy-I-BDP and Mn-

bpy-I-BDP, respectively. This peak is assigned as the triplet excited state ($^3\pi\pi^*$) of the bpy-I-BDP ligand.[177,178] The energies of these triplet excited states were measured as 1.61 and 1.58 eV for bpy-I-BDP and Mn-bpy-I-BDP, respectively. The higher energy levels of these triplet excited states compared to the energy required for producing singlet oxygen (0.98 eV) are consistent with the production of singlet oxygen by energy transfer.[179,180]

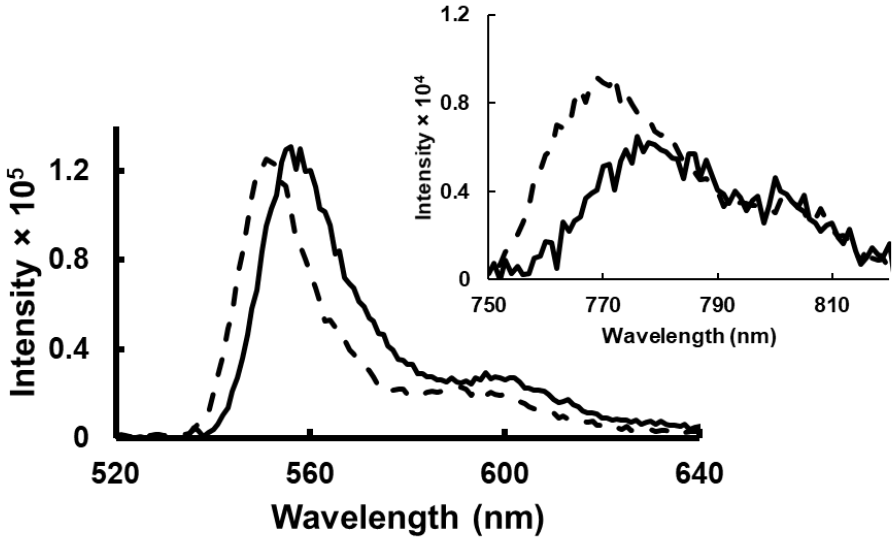

Figure 36. Fluorescence spectra of bpy-I- BDP (black dashed) and Mn-bpy-I-BDP (black solid), (inset: detected phosphorescence) in EtOH at 77 K, λ_{exc} 490 nm, λ_{abs} at 490 nm: 0.1

Computational Studies (TD-DFT)

We further studied the involved electronic transitions and absorption spectra of our compounds with the time-dependent DFT (TDDFT) at B3LYP level using SDD pseudopotentials for Mn, I, and Br, and 6-311G(d) basis set for other elements. Graphical representations of HOMOs and LUMOs and transitions for bpy-I-BDP and its Mn

complex are depicted in Figure 37. In the bpy-I-BDP ligand, the experimentally observed absorption maximum at 535 nm stem from the HOMO (π_{BDP})→LUMO(π^*_{BDP}) (84%, f: 0.43) transition corresponds to the first excited state (S_1) calculated at 452 nm (2.73 eV). The same transition was observed for bpy-H-BDP at 411 nm (95%, f: 0.47) (Figure A42). It should be noted that TDDFT calculations have been shown to overestimate the transition energies for BODIPY dyes.[181] In agreement with our experimental results, while the nature of the HOMO and LUMO are unaffected, introduction of electron-withdrawing I substituents on the BDP core stabilizes both the HOMO and LUMO in bpy-I-BDP compared to the bpy-H-BDP. In the case of Mn-bpy-I-BDP and Mn-bpy-H-BDP, in line with the cyclic voltammetry experiment, the HOMO and HOMO-1 are mainly located on the (Mn-CO)d_π orbitals and p orbital of Br^-, and the HOMO-2 is on the π orbital of the BDP ligand. The LUMO is on the π^* orbital of BODIPY and LUMO+1 is spread over the bpy(π^*) and Mn($d\sigma^*$). The TDDFT calculation predicts that the lowest absorption band observed at 539 nm in the absorption spectrum of Mn-bpy-I-BDP is mainly resulting from HOMO-2(π_{BDP})→LUMO(π^*_{BDP}) (80%, f: 0.36) calculated at 462 nm (2.67 eV) corresponds to the fifth singlet excited state ($S_0 \rightarrow S_5$). Additionally, the MLCT band in Mn-bpy-I-BDP was calculated at 405 nm (3.05 eV) from HOMO-4 (Mn(d_π)-π_{CO}^*)→LUMO+1((bpy(π^*)/Mn($d\sigma^*$)) (79%, f: 0.063). A similar transition was computed for Mn-bpy-H-BDP.

The impact of I on the singlet oxygen generation was studied by calculating the triplet excited states in bpy-I-BDP and its Mn complex. In line with the observed phosphorescence at 770 nm (1.61 eV) and 780 nm (1.58 eV) at 77 K for bpy-I-BDP and

Mn-bpy-I-BDP, respectively, the first triplet excited states (T_1) were calculated at 826 nm (1.49 eV) and 851 nm (1.45 eV) from the same orbital transition components as the first and fifth singlet excited states in bpy-I-BDP and Mn-bpy-I-BDP, respectively. This further illustrates the BDP-based $^3\pi\pi^*$ nature of observed phosphorescence at 77 K emission.

Table 13. Selected transitions and excitation energies of BDP-based ligands and corresponding Mn complexes

Compound	State	Oscillator strength (f)	Calculated energy (eV)	Observed energy (eV)	Transition	Character
bpy-I-BDP	S1	0.43	2.73	2.31	HOMO→LUMO	$\pi_{BDP}\rightarrow\pi^*_{BDP}$/ ILCT[a]
	T1	0	1.49	1.61	HOMO→LUMO	$^3\pi\pi^*$
bpy-H-BDP	S1	0.47	3.01	2.47	HOMO→LUMO	$\pi_{BDP}\rightarrow\pi^*_{BDP}$/ ILCT
Mn-bpy-I-BDP	S5	0.36	2.67	2.31	HOMO-2→LUMO	$\pi_{BDP}\rightarrow\pi^*_{BDP}$/ ILCT
	S14	0.06	3.05	-	OMO-4→LUMO+1	$Mn(d_\pi)$-$\pi_{CO}^*\rightarrow$ bpy(π^*)/Mn($d\sigma^*$)/MLCT[b]
	T1	0	1.45	1.58	HOMO-2→LUMO	$^3\pi\pi^*$
Mn-bpy-H-BDP	S7	0.42	3.00	2.46	HOMO-2→LUMO	$\pi_{BDP}\rightarrow\pi^*_{BDP}$/ILCT
	S11	0.07	3.38	-	OMO-4→LUMO+1	$Mn(d_\pi)$-$\pi_{CO}^*\rightarrow$ bpy(π^*)/Mn($d\sigma^*$)/MLCT

[a]Intra ligand charge transfer, [b]metal to ligand charge transfer

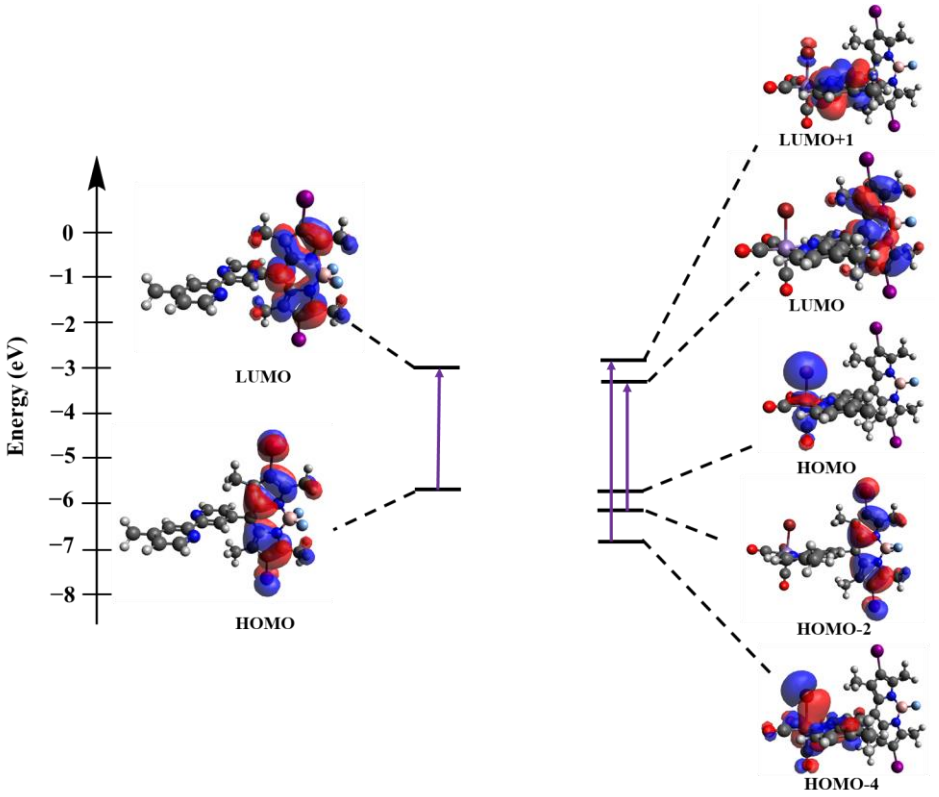

Figure 37. Frontier molecular orbitals, relative energies, and transitions of bpy-I-BDP (left) and Mn-bpy-I-BDP (right).

Based on absorption, emission, and CV experiments and TD-DFT calculations, we proposed the following excited states and transitions involved in the photolysis of Mn-bpy-I-BDP. Upon irradiation, the molecule is excited to its BDP-based singlet excited state ($^1\pi\pi^*$) HOMO-2 (π_{BDP})→LUMO(π^*_{BDP}). As evidenced by 77 K emission, the singlet excited state undergoes intersystem crossing to the BDP-based triplet excited state ($^3\pi\pi^*$). An electron from Mn(dπ) (HOMO) is likely transferred to the π orbital of BDP to create a charge separated (CS) state (Mn^+BDP^-). The lower energy of CS state compared to the $^3\pi\pi^*$ is the probable reason for lower Φ_Δ for Mn-bpy-I-BDP than the free

ligand. The reduced electron density on the Mn center as a result of electron transfer to the π of BDP weakens the π-backbonding between the Mn and CO, leading to CO photodissociation. After releasing all CO ligands, the formally oxidized Mn center dissociates from the bpy-I-BDP ligand.

4.3. Conclusions

In conclusion, we herein report the synthesis, characterization, and photo-reactivity of two emissive Mn-bpy-R-BDP (R = H or I) photoCORMs. Through the combination of emission, absorption, FTIR and ^{1}H NMR photolysis with DFT calculations, we demonstrated that in these complexes, the excitation of BDP core with low energy visible light resulted in CO photo dissociation through the formation of dicarbonyl species as intermediates followed by release of bpy-R-BDP (R = H or I) ligand from the Mn center. Introduction of two I substituents on the 2,6 positions of BDP core enhanced the ISC, leading to $^{1}O_2$ production. The presence of triplet excited in the bpy-I-BDP and its Mn complex were supported by a phosphorescence peak at 77 K emission. With respect to the non-iodinated analogue, the electron withdrawing I substituents extended the Mn-bpy-I-BDP absorption further into the visible region, leading to release of all CO by 590 nm light irradiation. Based on the obtained results from CV and TD-DFT calculations, we proposed that upon irradiation, the BDP excites to its singlet excited state ($^{1}\pi\pi^*$) and due to the I heavy atom effect, undergoes ISC to populate its $^{3}\pi\pi^*$. Upon excitation, an electron from the HOMO-based Mn fills the hole on the π orbital of BDP, reducing the electron density on the Mn center, weakening the

Mn-CO bond, allowing the CO to dissociate. A deeper investigation into the electron transfer is in progress to provide insight into the proposed mechanism of this system.

4.4. Experimental Section

Materials and Reagents

All materials were used without further purification. Selenium dioxide, 2,4dimethylpyrrole, 1,4-Benzoquinone, Boron trifluoride diethyl etherate and triethylamine were purchased from Acros Organics. 4,4'-Dimethyl-2,2'-bipyridine, N-Iodosuccinimide (NIS), 1,3-Diphenylisobenzofuran (DPBF) were purchased form TCI. Rose Bengal was purchased from Sigma Aldrich. $Mn(CO)_5Br$ was purchased from Strem Chemicals. SOSG, Dioxane, dichloromethane, acetonitrile, ethyl acetate, acetic acid and chloroform were purchased from Fischer Scientific. Acetonitrile-d3 and chloroform-d was purchased from Cambridge Isotope Laboratories. All reactions and experiments were performed in the dark to prevent photodecomposition.

^{1}H and ^{13}C NMR Spectroscopy

The spectra were collected on a Bruker Ascend 500 MHz spectrometer at 298 K. The spectra were calibrated to residual solvent peaks for acetonitrile at $\delta = 1.94$ and 118.26 and chloroform at $\delta = 7.26$ and 77.16 ppm.

Elemental Analysis

Elemental analysis (C, N, H) was carried out by Atlantic Microlabs, Inc. (Norcross, GA). samples were protected from light to prevent photodecomposition.

FTIR

FTIR spectra were obtained in CH_3CN solvent in a CaF_2 liquid IR cell or in the form of KBr pellet using a Shimadzu IRAffinity-1S Fourier transform infrared spectrophotometer.

High Resolution Electrospray Ionization Mass Spectrometry

HR-ESI(+)-MS spectra were collected using a Thermo Fisher Scientific Q Exactive Plus hybrid quadrupole–Orbitrap mass spectrometer in the positive mode. A potential of 4.0 kV was applied to ionize the 1 μM solution of each compound in CH_3CN with flow rate of 50 μL/min.

Electronic Absorption Spectroscopy

Electronic absorption spectra were obtained in a 1 × 1 cm quartz cuvette at room temperature using an Agilent Cary 8454 diode array UV–visible spectrophotometer. Extinction coefficient measurements were performed in triplicate in CH_3CN.

Cyclic Voltammetry

The electrochemical experiments were carried out with a BASi Epsilon EClipse electrochemical analyzer (Bioanalytical Systems, Inc.; West Lafayette, Indiana, USA) with 1 mM compound in DCM with 0.1 M n-Bu4NPF6 supporting electrolyte under N_2 with a scan rate of 200 mV/s at room temperature. The working, reference and auxiliary electrodes were glassy carbon or Pt (3 mm diameter), Ag/AgCl (3 M NaCl(aq)), and Pt wire, respectively. Ferrocene (Fc) was added to the solution following each measurement, and the potentials were referenced to the Fc^+/Fc couple ($E_{1/2}$ = +0.43 V vs. Ag/AgCl in DCM).

Emission and Excitation Spectroscopies

Steady-state emission and excitation spectra were recorded at room temperature and 77 K in CH_3CN or EtOH solvent using a Horiba Scientific Fluoromax-4C system equipped with a 150 W Xe arc lamp, Czerny-Turner excitation (1200 g/mm grating blazed at 330 nm) and emission (1200 g/mm grating blazed at 500 nm) monochromators, and a red-sensitive R928 PMT detector. Fluorescence quantum yields were measured by absorbance matching of each sample in EtOH at 470 nm to the reference compound, Rhodamine B ($\Phi_{fl} = 0.5$).[163] Singlet oxygen quantum yields with DPBF (1,3-diphenylisobenzofuran) as $^1O_2$ scavenger were performed with CH_3CN solutions containing 10 μM DPBF and the desired compound (A(513)=0.1). Each solution was photolyzed with 513 nm light (40 μW cm^{-2}) and excited at 405 nm. The decrease in the emission intensity of DPBF was monitored as a function of time at 479 nm for each compound. The slopes were calculated and compared to that of Rose Bengal as the reference ($\Phi_\Delta = 0.53$ in CH_3CN). When SOSG was used as the $^1O_2$ probe, a stock solution of 2.5 mM was prepared by adding 66 μL methanol into 100 μg of SOSG. 1.2 μL of SOSG stock solution was added to an emission cuvette containing 2.84 mL of water, followed by the addition of 0.15 mL of desired compound dissolved in methanol (A(535)=0.1). Each solution was photolyzed with 535 nm light (1 mW cm^{-2}) and excited at 505 nm. The increase in the emission intensity of SOSG was monitored as a function of time at 525 nm for each compound. The slopes were calculated and compared to that of Rose Bengal as the reference ($\Phi_\Delta = 0.75$ in H_2O).

Photolysis Experiment

All photolysis experiments were carried out using either 590 or 535 nm in-house built LEDs (35-50 mW cm^{-2}) (Luxeon Star LED, Quadica Developments, Inc., Lethbridge, Alberta, Canada). Each sample was dissolved in the appropriate solvent in a 1 × 1 cm quartz cuvette (for electronic absorption and emission analysis), CaF_2 cell (for FTIR analysis), and an NMR tube (^1H and ^{13}C NMR analysis), irradiated using the appropriate LED for different time intervals and analyzed by the appropriate instrument. All the experiments were performed in the dark to limit unwanted reactions initiated by room light.

Computational Methods

The ground state geometry optimization and frequency calculations were performed with DFT at B3LYP level using SDD pseudopotentials for Mn, I and Br and 6-311G(d) basis set for other elements with the Polarizable Continuum Model (PCM) solvation model for CH_3CN solvent in the Gaussian 16 program. The excited state calculations were performed with TD-DFT with the same functional and basis sets of ground state in the gas phase. To calculate CO stretching frequencies and visualize orbitals we used Avogadro program (Version 1.2.0). All stretching frequencies are multiplied by a frequency scaling factor of 0.97.

Synthesis of 4-carbaldehyde-4′-methyl-2,2′-bipyridine

The compound was prepared according to the previously reported procedure.[157] 4,4'-dimethyl-2,2'-bipyridine (1.5 g, 8.1 mmol) and SeO_2 (1.8 g, 16 mmol) were added to 60 ml of dioxane and heated at reflux for 3 days under Ar. After stopping the reaction,

the hot mixture was filtered through Celite to remove Se. The solvent was removed under reduced pressure and the remaining solid suspended in 500 ml of ethyl acetate. The solution was washed with 0.1 $Na_2CO_{3(aq)}$ and extracted with 0.2 $NaHSO_{4(aq)}$. After adjusting the pH to 9, the product was extracted from bisulfite layer with DCM. Yield: 280 mg (1.4 mmol, 17%). ^{1}H NMR (500 MHz, $CDCl_3$): δ 10.18 (s, 1H), 8.89 (d, 1H), 8.83 (s, 1H), 8.57 (d, 1H), 8.28 (s, 1H), 7.72 (d, 1H), 7.19 (d, 1H), 2.46 (s, 3H). Elemental analysis calculated for $C_{12}H_{10}N_2O$*0.15H_2O: 71.73%C, 5.17%H, 13.94%N. Found: 71.79%C, 4.96%H, 13.85%N. HR-ESI(+)-MS (CH_3CN): calcd for $C_{12}H_{10}N_2O$ $[M+H]^+$, m/z = 199.085; found, m/z = 199.087.

Synthesis of 4-BDP(H),4′-methyl-2,2′-bipyridine (bpy-H-BDP)

The synthetic procedure was adapted from a previously reported procedure.[156] 2,4-dimethylpyrrole (0.14 ml, 1.3 mmol), followed by a few drops of trifluoroacetic acid was added to a degassed solution of 4-carbaldehyde-4'-methyl-2,2'-bipyridine (130 mg, 0.65 mmol) in 30 ml DCM. After stirring at rt for 45 min, 2,3-dichloro-5,6-dicyano-p-benzoquinone (170 mg, 69 mmol) was added to the solution and stirred for 45 min. Subsequently, 1.5 ml of triethylamine was added and stirred for 30 min. Then 1.5 ml BF_3-OEt_2 was added to the solution and stirred for 4 h at rt. The solvent was removed under reduced pressure and the remaining solid was purified by column chromatography (DCM:ethyl acetate (90:10)). The product was obtained as orange solid. Yield: 80 mg (0.19 mmol, 29%). %). ^{1}H NMR (500 MHz, $CDCl_3$): δ 8.82 (dd, 1H), 8.52 (d, 1H), 8.48 (s, 1H), 8.31 (s, 1H), 7.31 (dd, 1H), 7.17 (d, 1H), 5.99 (s, 2H), 2.56 (s, 6H), 2.47 (s, 3H),

1.46 (s, 6H). Elemental analysis calculated for $C_{24}H_{23}BF_2N_4$*0.5 H_2O: 67.78%C, 5.69%H, 13.17% N. Found: 67.83%C, 5.6%H, 12.99%N. HR-ESI(+)-MS (CH_3CN): calcd for $C_{24}H_{23}BF_2N_4$ $[M+H]^+$, m/z = 417.206; found, m/z = 417.204.

Synthesis of 4-BDP(I),4′-methyl-2,2′-bipyridine (bpy-I-BDP)

The compound was synthesized by a few modifications to a previously reported procedure.[158] bpy-BDP (100 mg, 0.23 mmol) and N-Iodosuccinimide (NIS) (1.4 mg, 0.62 mmol) were added to 25 ml of chloroform: acetic acid (3:1) and stirred under Ar at rt for 6 h. The solution was then washed with water and the solvent was removed under reduced pressure. The remaining residue was purified by column chromatography (DCM:ethyl acetate (90:10)). The product was obtained as red solid. Yield: 100 mg (0.15 mmol, 62^{1}H NMR (500 MHz, $CDCl_3$): δ 8.85 (dd, 1H), 8.51 (d, 1H), 8.47 (s, 1H), 8.33 (s, 1H), 7.28 (dd, 1H), 7.18 (d, 1H), 2.65 (s, 6H), 2.47 (s, 3H), 1.49 (s, 6H). ^{13}C NMR (500 MHz, $CDCl_3$):1.13, 14.24, 16.28, 17.75, 21.48, 15,31.80, 86.62, 120.94, 122.27, 122.96, 125.74, 130.42, 145.09, 150.34, 157.86. Elemental analysis calculated for $C_{24}H_{21}BF_2I_2N_4$: 43.15%C, 3.17H, 8.39N. Found: 43.14%C, 3.16%H, 8.24%N. HR-ESI(+)-MS (CH_3CN): calcd for $C_{24}H_{21}BF_2I_2N_4$ $[M+H]^+$, m/z = 668.999; found, m/z = 669.013.

Synthesis of Mn(bpy-H-BDP)$(CO)_3$Br (Mn-bpy-H-BDP)

The compound was synthesized by our previously reported procedure.[57] $Mn(CO)_5Br$ (10 mg, 0.037 mmol) and bpy-H-BDP (18 mg, 0.043 mmol) were added to 15 ml diethyl ether and heated to reflux for 3 h under Ar. After cooling to room

temperature, the orange precipitate was collected by vacuum filtration and washed with diethyl ether. Yield: 10 mg (0.015 mmol, 43%). ^{1}H NMR (500 MHz, CD_3CN): δ 9.39 (d, 1H), 9.09 (d, 1H), 8.43 (s, 1H), 8.24 (s, 1H), 7.69 (d, 1H), 7.49 (d, 1H), 6.20 (s, 1H), 6.17 (s, 1H), 2.54 (s, 6H), 2.53 (s, 3H), 1.59 (s, 3H), 1.44 (s, 3H). The ^{13}C NMR (number of scans: 1500) could not collect due to the stability issue of the complex**.** FTIR (KBr pellet, cm^{-1}): 2962 (C-H stretching aromatic), 2868 (C-H stretching aliphatic), 2024, 1918 and 1937 (C≡O stretching), 1400-1600 (C=C and C=N stretching) and 530-650 (Mn-CO bending). Elemental analysis calculated for $C_{27}H_{23}BBrF_2MnN_4O_3$: 51.06%C, 3.65%H, 8.82%N. Found: 51.35%C, 3.85%H, 8.60%N. HR-ESI(+)-MS (CH_3CN): calcd for $C_{27}H_{23}BBrF_2MnN_4O_3$ $[M-Br-CO+2CH_3CN]^+$, *m*/*z* = 609.179; found, *m*/*z* = 609.172.

Synthesis of Mn(bpy-I-BDP)(CO)$_3$Br (Mn-bpy-I-BDP).

This compound was prepared as described above using $Mn(CO)_5Br$ (10 mg, 0.037 mmol) and bpy-I-BDP (25 mg, 0.037 mmol). Yield: 10 mg (0.011 mmol ,31%). ^{1}H NMR (500 MHz, CD_3CN): δ 9.42(d, 1H), 9.09 (d, 1H), 8.40 (s, 1H), 8.20 (s, 1H), 7.69 (d, 1H), 7.50 (d, 1H), 2.65 (s, 3H), 2.64 (s, 3H), 2.53 (s, 3H), 1.61 (s, 3H), 1,45 (s, 3H). ^{13}C NMR (500 MHz, CD_3CN): δ 158.94, 158.25, 155.78, 155.59, 153.87, 152.53, 146.14, 146.20, 137.25, 131.01, 128.80, 126.61, 125.71, 123.44, 66.23, 21.26, 18.29, 16.54, 15.57. FTIR (KBr pellet, cm^{-1}): 2932 (C-H stretching aromatic), 2848 (C-H stretching aliphatic), 2024, 1916 and 1940 (C≡O stretching), 1400-1600 (C=C and C=N stretching) and 530-650 (Mn-CO bending). Elemental analysis calculated for $C_{27}H_{21}BBrF_2I_2MnN_4O_3.0.50.5$: 37.70%C, 2.84%H, 6.06%N. Found: 37.73%C, 2.65%H,

6.01%N. HR-ESI(+)-MS (CH_3CN): calcd for $C_{27}H_{21}BBrF_2I_2MnN_4O_3$ $[M-Br-CO+2CH_3CN]^+$, m/z = 860.972; found, m/z = 860.963.

Chapter 5: Design, Synthesis and Recognition Properties of Water-Soluble Lanthanide Cages

5.1. Introduction

In contrast to the molecular chemistry that deals with the covalent bond, supramolecular chemistry can be described as the "chemistry beyond the molecule".[182] Supramolecular chemistry is generally defined as the spontaneous self-assembly of molecular structures of higher complexity from smaller components.[183] The self-assembly process is central to life and demonstrated by nature, from protein folding and cytoplasmic membrane to the viral coats of all viruses.[184]

These structures are being held together through weak intermolecular forces, including van der Waals forces, ionic forces, hydrophilic and hydrophobic interactions, hydrogen bonding, and electrostatic interactions.[183] Supramolecular structures have wide applications in drug delivery, metal extraction, sensing, and as nanoreactors in catalytic reactions.

5.2. Supramolecular Coordination Chemistry

Over the last few decades, two interesting new branches of supramolecular coordination chemistry, including Metal Organic Frameworks (MOFs) and Supramolecular Coordination Complexes (SCCs) have emerged (Figure 38). While MOFs are defined as infinite coordination polymers or networks, consisting of metal centers bridged by organic linkers, SCCs are described as finite 2D or 3D structures, in which the metal centers undergo self-assembly with multidentate ligands.[185]

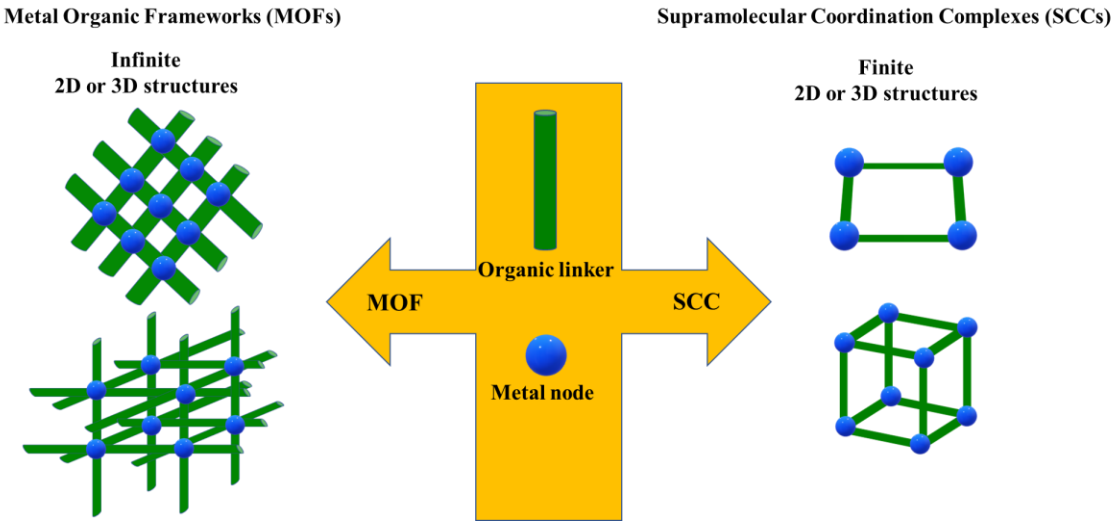

Figure 38. Metal-based supramolecular assemblies

5.3. Supramolecular Coordination Cages

Among the SCCs family, the coordination-driven self-assembly 3D cage-like structures, also known as metallacages, with the general formula of M_XL_Y (M=metal, L= ligand), are of much interest due to their fascinating structures and remarkable applications.[186] Such assemblies are usually obtained by mixing the metal cation precursor with the organic linkers to form the thermodynamically most stable structure through the spontaneous metal-ligand bond formation.[185] The SCCs have been classified based on their shapes, including octahedral, tetrahedral, lantern, cubic, spherical, etc.[187]

One of the main goals of supramolecular chemistry is the construction of water-soluble coordination cages with wide applications in industrial, environmental, and medical processes.[188] Water-soluble coordination cages can be prepared by introducing an overall positive or negative charge on the cage, as well as incorporation of polar groups on the ligand framework.[188] However, the construction of a stable water-soluble

cage can be challenging as the water may prevent the formation of the cage by competing with the ligand to bind with metal ions. Furthermore, the hydrophobic effect of water may result in aromatic ligand stacking, preventing cage construction.[188]

Host-Guest Complexation in Water

The hydrophobic effect is the primary driving force for the formation of host-guest complexes in water, but other factors such as electrostatic interactions, hydrogen bonding, dispersion interactions, and the shape and size of the host and guest cannot be overlooked.

Entropically, the dissolution of a non-polar guest in water is an unfavorable process. One possible (and to some extent accepted) explanation for the hydrophobic effect is when a non-polar molecule (gray objects in Figure 39) is dissolved in water (blue circles), the hydrogen bonds between the water molecules break to accommodate the molecule. Water molecules then surround the dissolved molecule, forming a so-called ice cage and reaching a highly ordered state. Once the guest is removed from water, the ice-like cage around the molecule breaks and releases the water molecules into the bulk solution, leading to a positive entropy (Figure 39).[189,190] This process is crucial in entropy-driven guest binding.

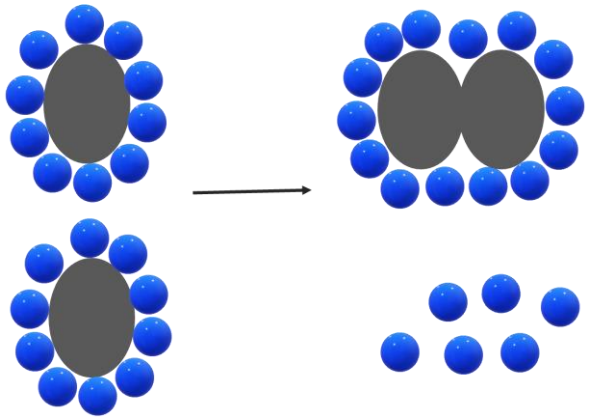

Figure 39. Hydrophobic effect

Interestingly, in 2005, the formation of a "molecular ice" with ten water molecules inside the cavity of a Pd_6L_4 cage was confirmed by X-ray structural analysis.[191] The analysis revealed that the molecular ice is encapsulated within the cavity through the $H_2O{:}\cdots\pi$ interaction. Fujita and co-workers suggested that melting the molecular ice and release of water molecules upon guest binding is the main driving force for the guest binding.

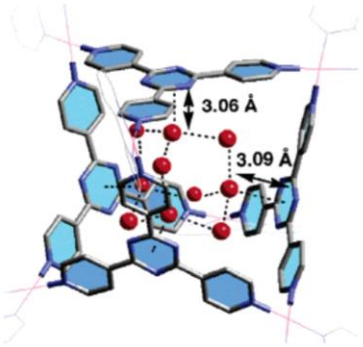

Figure 40. Crystal structure of Pd_6L_4 with ten water molecules encapsulated inside the cavity. (Adapted with permission from ref. 191. Copyright 2005 American Chemical Society.)

As mentioned previously, for a host-guest complex to form, different intermolecular interactions should work synergistically. As a result, in addition to the hydrophobic effect, there are other interactions that may also be involved. Some of these forces are as follows[192]: the CH–π and the π–π stacking interactions, ionic interactions between two oppositely charged species, and aromatic interactions including cation−π and anion-π interactions. While the cation−π interactions increase the free energy of binding, the anion-π interactions are repulsive in nature, as the interaction between the π-electrons of the aromatic rings and the negatively charged species is unfavorable. It is worth mentioning that enhancing the nonpolar contacts between the guest and the internal cavity of the host would increase the binding affinity values.[192]

Examples of "host-guest" complexes in the following section provide more details on different interactions between various guests and supramolecular coordination cages in aqueous media.

Water Soluble Coordination Cages

The first Pd_6L_4 cage-like structure with octahedral geometry shown in Figure 41 was synthesized by Fujita and co-workers in 1995 using palladium (II) and tridentate ligand 2,4,6-tris (4-pyridyl)-1,3,5-triazine (TPT) as the building components. This water-soluble assembly was reported to encapsulate both anionic and neutral guests.[193] The cation−anion interactions were suggested as the main driving force for the anionic guests encapsulation. Neutral guests, on the other hand, were shown to be strongly size dependent, as 1:4, 1:2, and 1:1 host−guest complexations were reported for spherical, twisted medium sized, and larger guests, respectively.

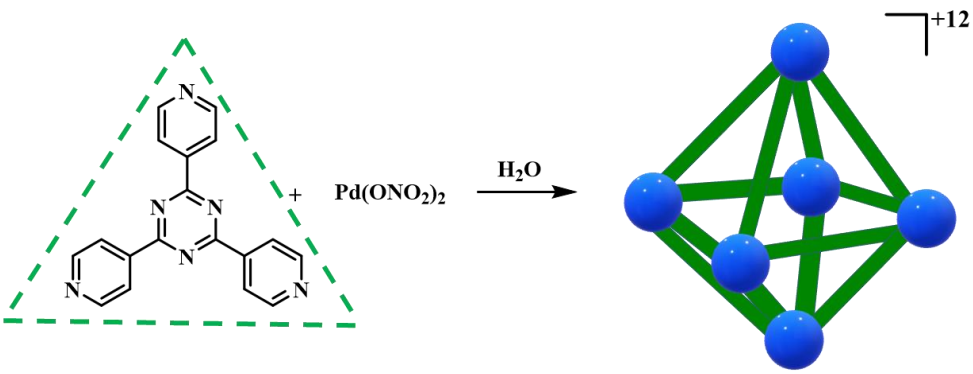

Figure 41. M_6L_4 octahedral self-assembly

Using the above-mentioned Pd cage, Fujita, Takezawa, and a co-worker reported the non-covalent inclusion of twisted conformers of secondary aromatic amides in the cavity of the Pd_6L_4 cage with T_d-symmetry in 2020.[194] Distortion of the amide groups increases their reactivity towards nucleophiles. Crystal structures revealed that upon inclusion of the secondary aryl amides, the cis-twisted conformation is favored over the trans-planar conformation. Inclusion of five secondary electron-rich amides including N-(2,4-dimethoxyphenyl)-4-methoxybenzamide (A1), N-(2,4-dimethoxyphenyl)thiophene-2-carboxamide (A2), N-(2,4-dimethoxyphenyl)furan-2-carboxamide (A3), N-(2,4-dimethoxyphenyl)-2-methoxybenzamide (A4), and -Methoxy-1-(4′-methoxybenzoyl)indole (A5) were confirmed by ^{1}H NMR in D_2O. In contrast, the non-electron-rich amides (shown in Figure 42 B) did not show any binding, suggesting the necessity of interactions between the electron-deficient cage and the electron-rich amides. Under basic conditions, the confined cis-twisted amides displayed increased reactivity for hydrolysis.

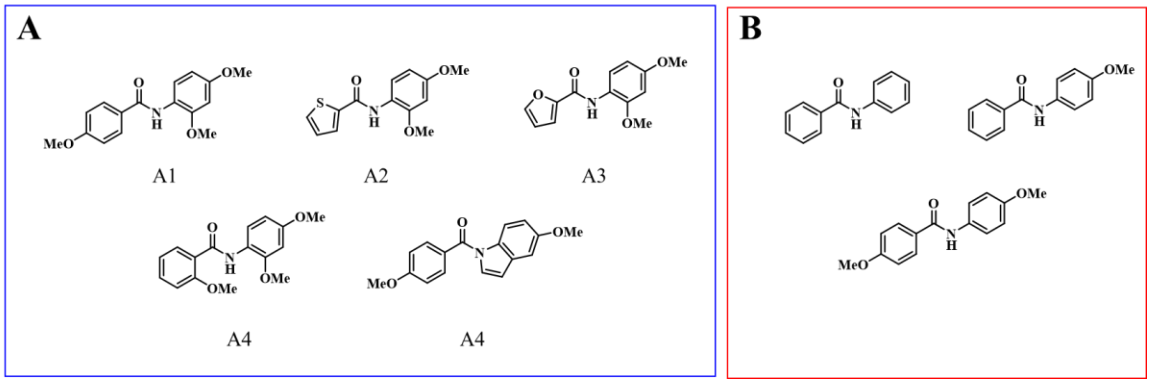

Figure 42. Secondary electron-rich amides (A), secondary electron-deficient amides (B)

As a near relative of the above-mentioned Pd_6L_4 cage, Sun and co-workers introduced a new redox-active water-soluble Pd_4L_2 cage in 2018.[195]Compared to the previous cage, two cis-blocked palladium were replaced by p-xylene bridges to expand the internal cavity. The presence of pyridinium moieties in this structure, not only provided redox and photochromic activities but also increased the electron deficiency of the cage framework.

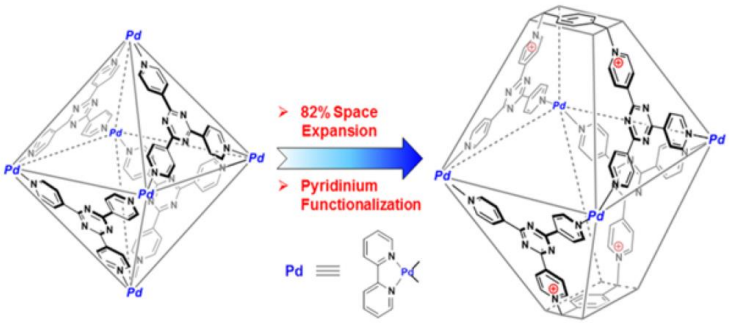

Figure 43. Pd_4L_2 cage with expanded cavity. (Adapted with permission from ref. 195. Copyright 2018 American Chemical Society.)

The guest binding properties of this cage were studied by a series of aromatic guests, including thiolesters (dibenzothiophene (DBT), thioanisole (MBT), diphenyl sulfide (DPS)), and polycyclic aromatic hydrocarbons (PAHs, pyrene, and naphthalene). In all cases, the formation of host-guest complexes was confirmed by ^{1}H NMR spectroscopy. In the cases of naphthalene, DPS, and DBT guests, the inclusion of more than one guest was evidenced by NMR titration and the host-to-guest integral ratio. The crystal structure of the DBT⊂cage showed the inclusion of three DBT guests inside the cavity, stabilized by π–π stacking interactions between the TPT panel of the framework and DBT molecules. In addition to organic guest binding, three POMs anions, including $Mo_6O_{19}^{2-}$, $Mo_8O_{26}^{4-}$, and $PMo_{12}O_{40}^{3-}$ (in the order of increasing size), were also investigated. The formation of $Mo_6O_{19}^{2-}$⊂cage and $Mo_8O_{26}^{4-}$⊂cage with the inclusion of two $Mo_6O_{19}^{2-}$ and one $Mo_8O_{26}^{4-}$ inside the cavity was confirmed by NMR experiments. Anion-π and electrostatic interactions between the $Mo_6O_{19}^{2-}$ and the pyridinium panels were suggested as the main driving forces for guest inclusion. Due to the larger size of $PMo_{12}O_{40}^{3-}$, no encapsulation was observed.

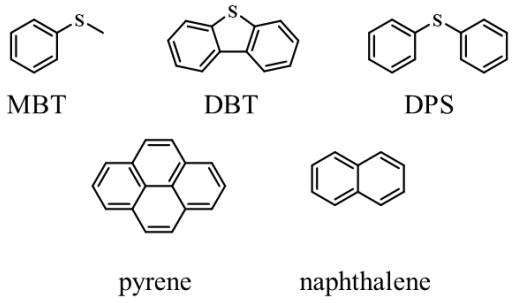

Figure 44. Prospective guests for binding studies

In another study, Raymond and co-workers introduced an M_4L_6 tetrahedron cage-like structure, using Ga(III) and Fe(III) and 1,5-Bis(2,3-dihydroxybenzamido)naphthalene as the bridging ligand.[196] This water-soluble cage was used for encapsulation of Et_4N^+. The structure is shown in Figure 45.

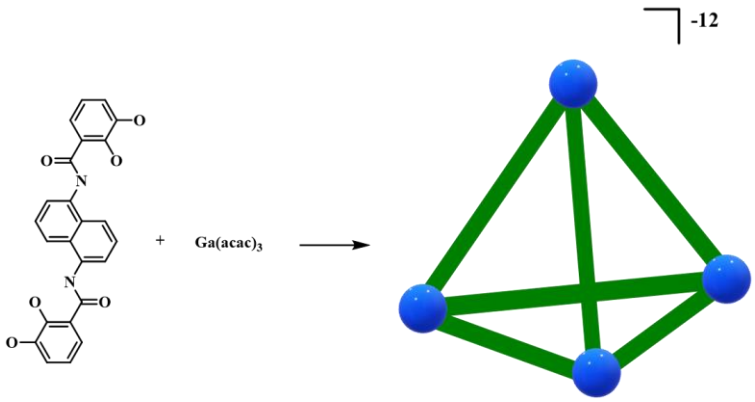

Figure 45. M_4L_6 tetrahedral self-assembly

In 2013, Ward, Hunter, and co-workers studied the impact of solvent (water versus acetonitrile) on the binding of a series of organic guests (Figure 46). In this study, they prepared a water-soluble cubic cage, $[Co_8(L^w)_{12}](BF_4)_{16}$, and compared it with an organic-soluble cubic cage $[Co_8(L)_{12}](BF_4)_{16}$.[197] Guest encapsulation is usually a combination of three factors; 1) non-polar interactions such as van der Waals and aromatic interactions, 2) hydrogen-bonding interactions, and 3) solvophobic interactions. The authors quantified the solvophobic contribution by comparing the obtained ΔG values for the guest binding in acetonitrile and water. This study was performed with guests that only differed in the presence or absence of a fused aromatic ring. While using

the organic-soluble cage allows identification of aromatic and s bonding contributions, the water-soluble cage allows for quantification of hydrophobic contributions. The ΔG values showed that while the bicyclic guest encapsulation in acetonitrile is associated with the aromatic interactions, its binding in water is mainly governed by the hydrophobic effect, with an insignificant contribution from H-bonding.

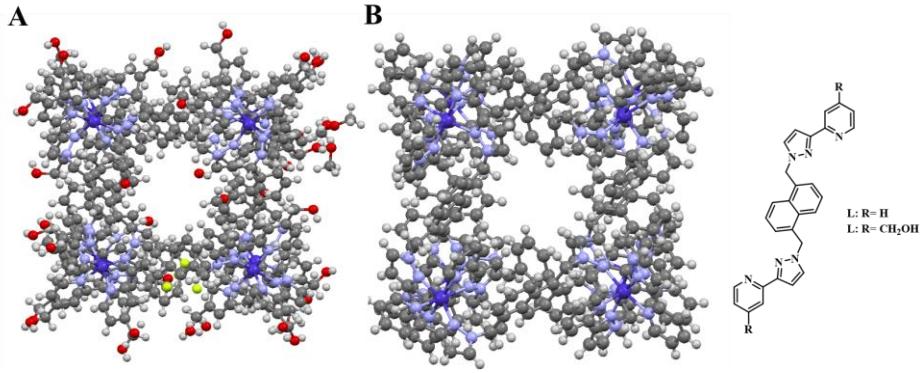

Figure 46. Water-soluble cubic coordination cage $[Co_8(L^w)_{12}](BF_4)_{16}$ (A), and organic soluble cubic cage $[Co_8(L)_{12}](BF_4)_{16}$ (B)ss

In another study, Ward and co-workers showed that the previously mentioned $[Co_8(L^w)_{12}](BF_4)_{16}$ cage catalyzes the aldol condensation of indane-1,3-dione to bindone in water.[198] A general scheme of the aldol condensation reaction is shown in Figure 47. The presence of two stacked indane-1,3-dione molecules inside the cage cavity and another molecule bound to the exterior of the cage through hydrogen binding were confirmed by the crystal structure. The authors suggested that the outside bounded guests are either neutral indane-1,3-dione or the enolate anions that are stabilized by the positive charge of the cage. They proposed that the cage facilitates the reaction by attracting the neutral indane-1,3-dione to its hydrophobic cavity, and stabilizing the enolate anion

through the 16+ surface of the cage. The binding constant of indane-1,3-dione was determined as 2.4 (±1.2) × 10^3 M^{-1}.

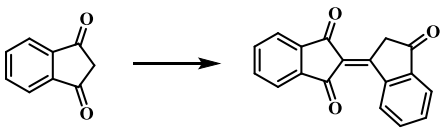

Figure 47. Aldol condensation reaction.

In another study led by Nitschke and co-workers, they reported the formation of a water-soluble enantiopure cage, ΔΔΔΔ-Fe_4L_6, and its enantiomer, ΛΛΛΛ-Fe_4L_6.[199] This cage was shown to encapsulate organic guests of different sizes and differentiate between the enantiomers of organic guests. The selected guests of various sizes, depicted in Figure 48 B (i-iii), showed binding to the ΔΔΔΔ-Fe_4L_6 cage. However, guests shown in Figure B (iv) were either too hydrophilic or too large to bind. Due to the large hydrophobic cavity of ΔΔΔΔ-Fe_4L_6, while the ^{1}H NMR titration with larger guests resulted in slow exchange, titration with smaller guests led to fast exchange. The authors proposed that the flexible glyceryl groups allow the ΔΔΔΔ-Fe_4L_6 cage to adjust the volume of its cavity to the size of the guest, allowing guests of various sizes to encapsulate.

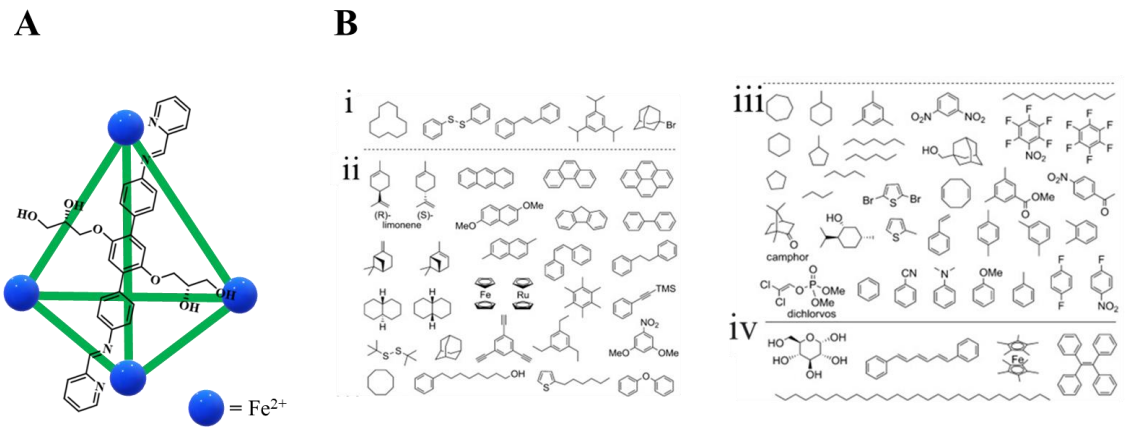

Figure 48. ΔΔΔΔ-Fe_4L_6 cage (A), larger guests (B-i), medium guests (B- ii), smaller guests (B- iii), *and* guests that did not show binding (B-iv). (Adapted with permission from ref. 199. Copyright 2013 John Wiley and Sons.)

In 2017, Nitschke and co-workers reported an anion exchange protocol for making a water-soluble cage by exchanging the trifluoromethanesulfonate counterions for the hydrophilic sulfate.[200] In this process, they initially prepared a cubic $Fe^{II}_8L_6$ built on zinc porphyrin faces with trifluoromethanesulfonate counterions ($Fe^{II}_8L_6$.OTf). This cage was reported to be insoluble in water. The water-soluble cage was then prepared by adding the $Fe^{II}_8L_6$.OTf into a solution of tetrabutylammonium or potassium sulfate to obtain $Fe^{II}_8L_6.SO_4$ (Figure 49A). It is worth mentioning that direct synthesis of $Fe^{II}_8L_6.SO_4$ is not possible. The preliminary host–guest studies were performed with $Fe^{II}_8L_6$.OTf and $Fe^{II}_8L_6.SO_4$ in acetonitrile and water, respectively. ^{1}H NMR titration of $Fe^{II}_8L_6.SO_4$ with the selected guests exhibited in Figure 49 B (left) showed fast exchange binding in water. Surprisingly, none of the shown guests showed binding to $Fe^{II}_8L_6$.OTf in acetonitrile. These findings suggest that the hydrophobic effect is the main driving

force for the guests' binding. The selected guests in Figure 49 (right), however, did not show any binding, suggesting the necessity of conformational flexibility for the guest encapsulation.

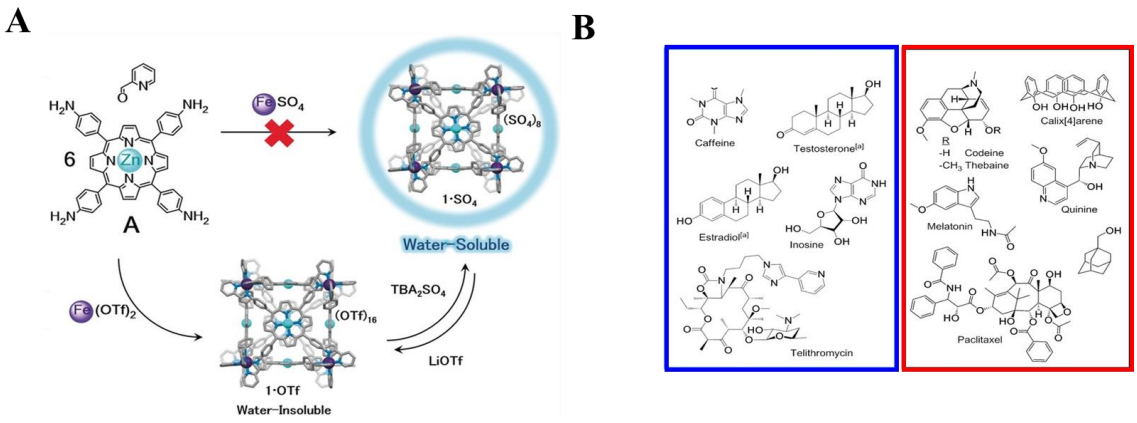

Figure 49. Reversible counterions exchange (A) selected guests for binding studies, guests that showed binding to $Fe^{II}_8L_6.SO_4$ in water (B) left, guests that did not show binding (B) right. (Adapted with permission from ref. 200. Copyright 2017 John Wiley and Sons)

Similarly, a research from Ward and Weinstein's groups corroborates the use of counterion exchange from perchlorate to chloride to prepare a water-soluble luminescent octanuclear cubic cage $[Os_4Zn_4(L)_{12}]Cl_{16}$ where L is a bis-bidentate bridging ligand containing two pyrazolyl−pyridine chelating units separated by a 1,5-naphthalenediyl group.[201] Encapsulation of electron-deficient 1,4-naphthoquinone (NQ), 1,2,4,5-tetracyanobenzene (TCNB), and 1-nitronaphthalene (NN) guests with binding constants of $10^3 - 10^4$ M^{-1} (shown in Figure 50B) resulted in quenching of the cage luminescence. Ultrafast transient absorption revealed that the formation of a charge-separated

Os(III)/guest$^{\bullet-}$ state is responsible for the observed quenching upon binding of the electron-accepting guests. The addition of the cycloundecanone with a large binding constant as the competing guest to a solution of electron-deficient guest⊂cage, resulted in the disappearance of the charge-separated state.

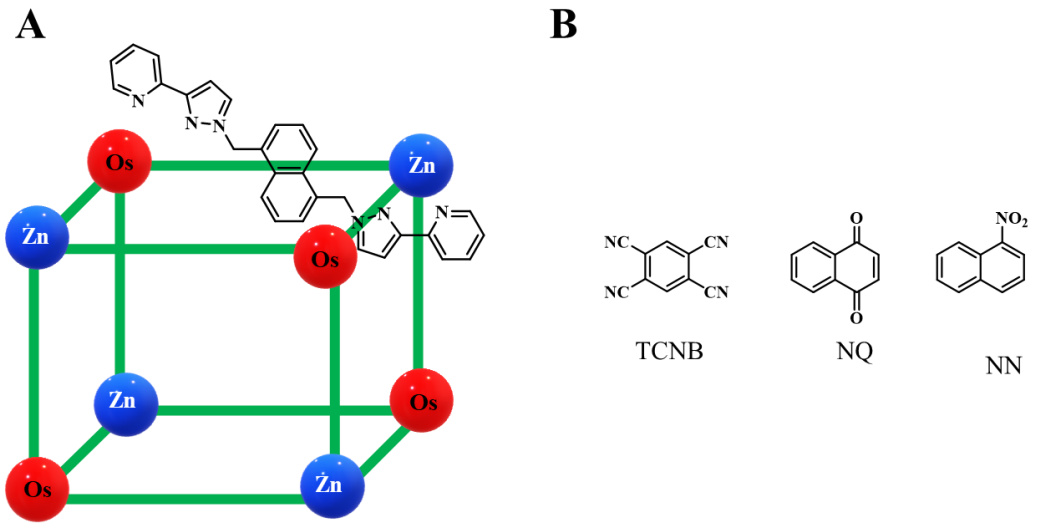

Figure 50. Cubic $[Os_4Zn_4(L)_{12}]Cl_{16}$ cage (A), electron-deficient guests (B)

In 2012, Mukherjee and co-workers introduced a cationic highly water-soluble $Pd^{II}_6L_4$ semi-cylindrical open cage, where L= 1,3,5-tris(1-imidazolyl)benzene.[202] The imidazole moieties can easily rotate around the single bonds (attached to the benzene ring), resulting in a flexible framework. This cage was studied for the encapsulation of hydrophobic and hydrophilic guests. The obtained crystal structures showed that while the hydrophobic 1-pyrenecarboxaldehyde guest can encapsulate inside the cavity and form a 2:1 (guest:cage) complex in water, the hydrophilic 2,3-dichloro-5,6-dicyano-1,4-

benzoquinone (DDQ) would form weak interactions with the outside walls of the cages and stack between them. This further suggested that while the Pd_6L_4 cage possesses a hydrophobic cavity, the outer sphere is hydrophilic. The authors also showed that this cage can be used in the catalysis of a series of aromatic mono-aldehydes in the Knoevenagel condensation reactions with 1,3-dimethylbarbituric acid and Meldrum′s acid in water under ambient conditions. They further utilized the hydrophobic confined cavity for the catalytic Diels–Alder reactions of 9-hydroxymethylanthracene with N-cyclohexylmaleimide or N-phenylmaleimide.

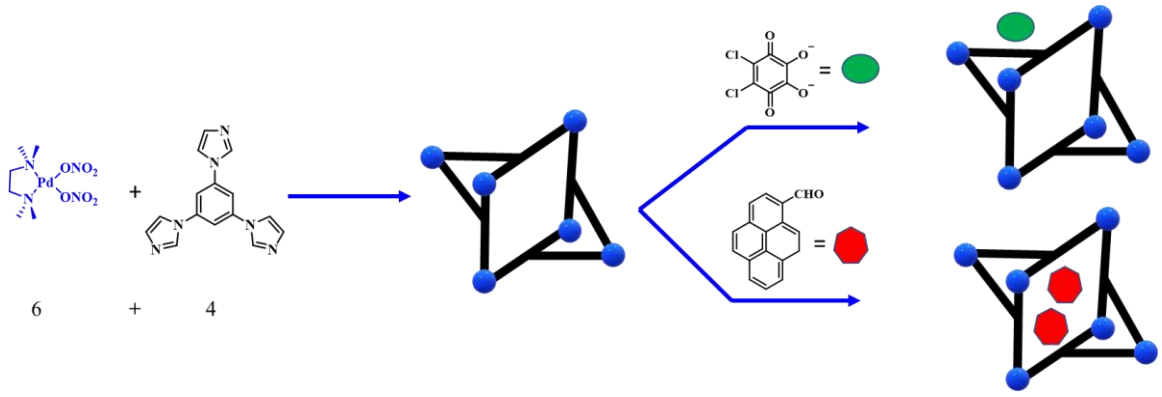

Figure 51. Interaction of two hydrophobic (red) and hydrophilic (green) guests with $Pd^{II}_6L_4$ semi-cylindrical cage

In 2022, Klajn, Bialek, and co-workers reported the encapsulation of resorufin and resazurin dyes within the above-mentioned $Pd^{II}_6L_4$ cage.[203]The inclusion of the guests notably reduced the resazurin to resorufin conversion and subsequent reduction of resorufin to dihydroresorufin. Furthermore, encapsulation within the $Pd^{II}_6L_4$ cage resulted

in modulating the photophysical properties of the mentioned dyes by shifting their absorbances and quenching the emission of resorufin. The authors suggested that the driving force for the guest encapsulation is a combination of the hydrophobic effect, van der Waals, and π–π stacking interactions, with a significant contribution from the Coulombic interactions resulting from the negative charge of the guests, and the positive charge (+12) on the cage. In both the resorufin and resazurin cases, the crystal structures revealed the inclusion of two guests inside the cage cavity with cumulative binding constants of $Ka_1Ka_2 = 1.1 \times 10^{12}$ M^{-2} for (resorufin)$_2$⊂cage and 1.2×10^{12} M^{-2} for (resazurin)$_2$ ⊂cage. They further showed that at lower concentrations, the cage disassembles to yield $Pd^{II}_2L_2$ species. However, interestingly, adding strongly binding resorufin/resazurin guests can reverse this process to the assembled cage.

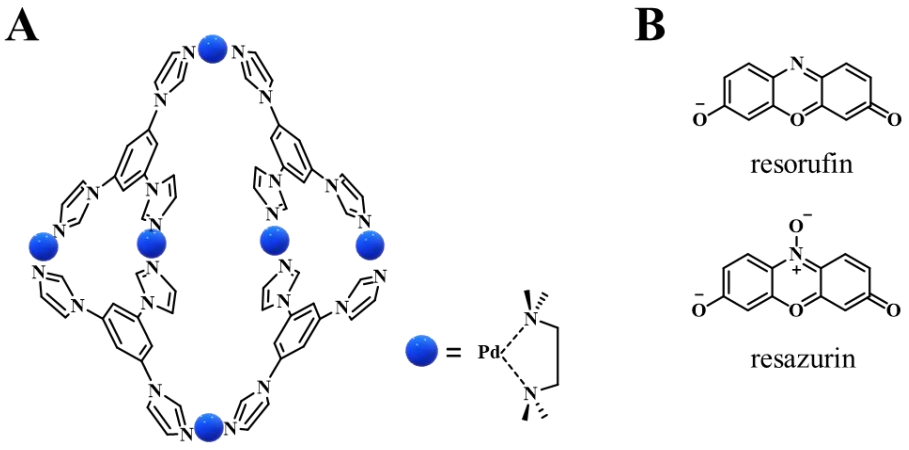

Figure 52. $Pd^{II}_6L_4$ cage (A), prospective dyes for binding study (B)

In another study, Su, Pan, and co-workers presented a nanosized Pd−Ru ($Pd_6(RuL_3)_8$) heteronuclear cage with a rhombododecahedral shape and 12 open windows.[204] The large incorporated hydrophobic cavity with a volume of 5350 $Å^3$ prompted the authors to study the host-guest chemistry of the Pd−Ru cage with water-immiscible and neutral nonpolar guests, including phenanthrene, pyrene, anthracene, and perylene (in order of increasing size). The DOSY/^{1}H NMR titration suggested that the Pd−Ru cage can encapsulate ∼18 ±2 phenanthrene guest molecules in DMSO/D_2O (1:2) mixture. Similarly, a Pd−Ru cage can encapsulate 12 larger pyrene or longer anthracene. However, no evidence of inclusion was observed for the bulky perylene. The cage was also investigated for the encapsulation of photosensitive polar guests that are also soluble in the DMSO/D_2O mixture. All three 2,2-dimethoxy-2-phenylacetophenone (DMPA), 2-hydroxy-2-methylpropiophenone (HMPP),1-hydroxycyclohexyl phenyl ketone (HCPK) guests were encapsulated inside the cavity with a fast exchange mechanism as the result of solubility in the solvent mixture. More interestingly, the Pd−Ru cage protected these photosensitive encapsulated guests from UV irradiation. The cage was shown to protect the trapped guests from 365 nm light irradiation for up to 120 h.

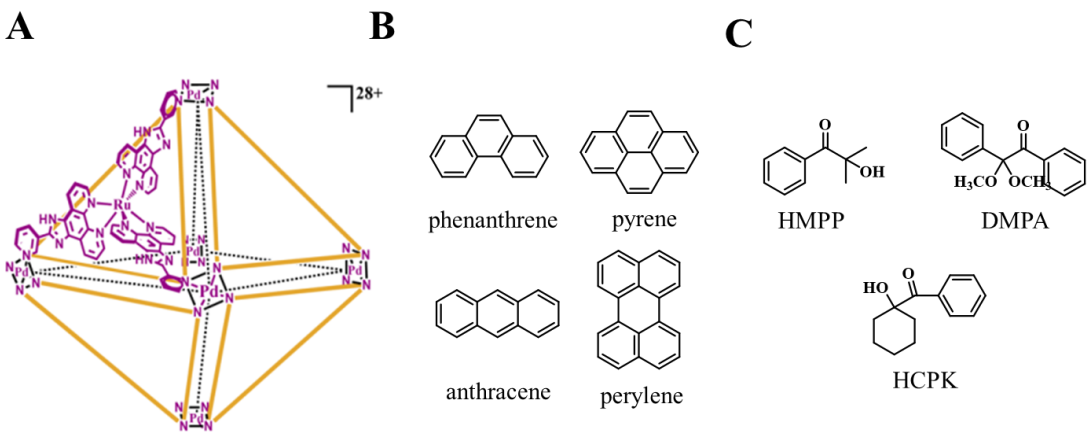

Figure 53. The nanosized $Pd_6(RuL_3)_8$ cage (A), nonpolar guests (B), and photosensitive polar guests (C). (Adapted with permission from ref. 204. Copyright 2014 American Chemical Society.)

In 2018, Mukherjee and co-workers introduced a new Pd_8L_4 barrel shape cage, where L= [benzene-1,4-di(4-terpyridine)].[205] As shown in Figure 54, treatment of L with cis-(tmeda)Pd- $(NO_3)_2$ (M) in a 1:2 ratio in DMSO yielded two isometric Pd(II) barrels (B1 and B3). However, interestingly, the pure B1 form was obtained by heating the B1 and B3 mixture in water.

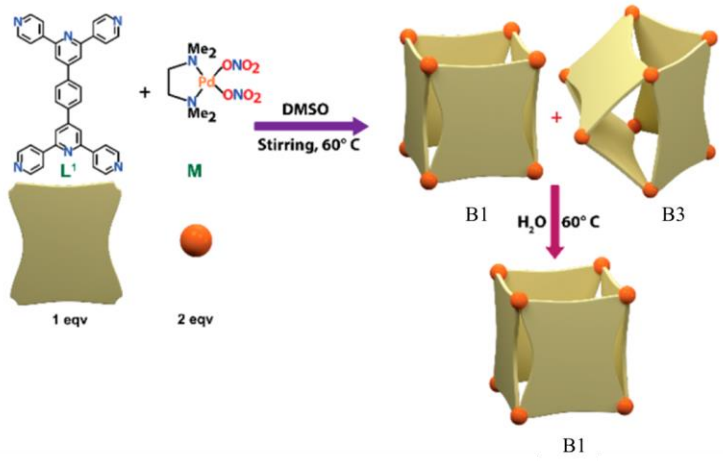

Figure 54. Isomeric Pd_8L_4 barrels. (Adapted with permission from ref. 205. Copyright 2018 American Chemical Society.)

While existing in a closed spiro form under visible light, the spiropyran compounds convert to a transient open merocyanine form upon heating or under UV light irradiation. This process can be reversed under visible light irradiation (Figure 55). The inclusion of a merocyanine molecule inside the B1 cavity was shown to protect this unstable molecule from converting to the closed spiro form under visible/UV light or heating.

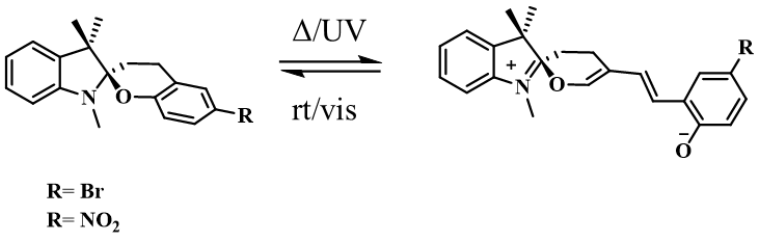

Figure 55. Reversible conversion of closed spiropyran compounds to the open merocyanine form

Recently, Ballester, Escobar, and co-workers have reported the self-assembly of a water soluble $(Pt\text{-}L)^{6+}$ cage (L: tetra-cationic super aryl-extended calix[4]pyrrole tetra-pyridyl) by the inclusion of polar mono- and ditopic pyridyl N-oxide and aliphatic formamide guests.[206]Despite the positive charges on both the free ligand L^{4+} and the $(Pt\text{-}L)^{6+}$ cage, they experienced aggregation in water. The authors showed that the 1:1 inclusion of polar guests shown in Figure 56 with $(Pt\text{-}L)^{6+}$ reduces the aggregation tendency of guest⊂$(Pt\text{-}L)^{6+}$. They reported that while the ditopic guests completely fill the cage's cavity and complement the two endohedral polar binding sites, the monotopic guests only partially fill the cavity and are bound to the C[4]P unit of the cage.

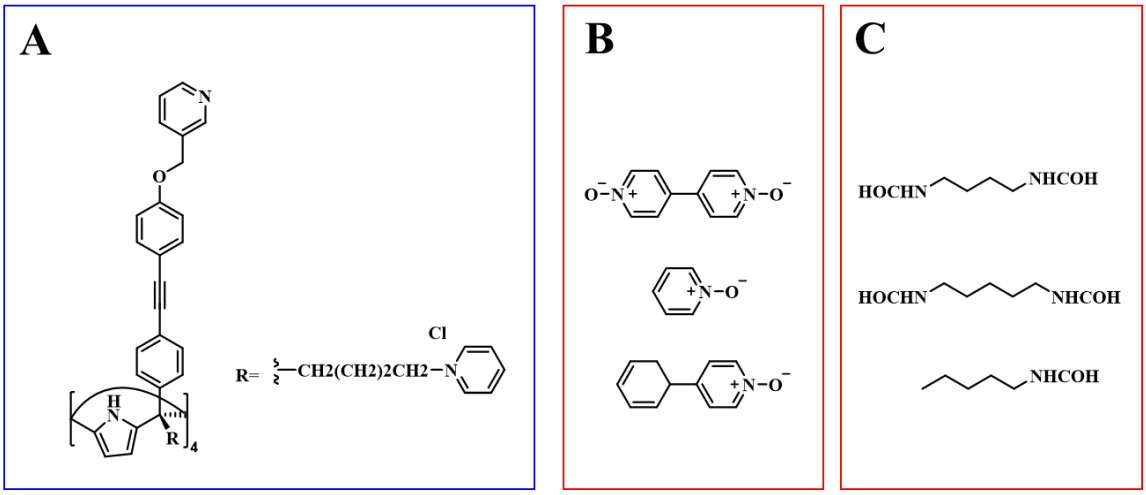

Figure 56. Tetra-cationic super aryl-extended calix[4]pyrrole tetra-pyridyl ligand (A), mono- and ditopic pyridyl N-oxide (B), and mono- and ditopic and aliphatic formamide guests

So far, due to the high thermodynamic stability and predictable stereochemical outcomes, the majority of reported metallacages have been based on transition metals and

main group ions.[207] However, due to the increasing demands for more efficient luminescent and magnetic materials for lighting devices, LEDs, lasers, sensors, and biological imaging, lanthanide ions (Ln(III)) are attracting growing attention.

Lanthanide Based Supramolecular Cages

In 2009, He and co-workers reported two new tetrahedral ($Ce_4L_6^1$) and ($Ce_4L_6^2$) cages and studied their host−guest interactions for sensing natural saccharides.[208] From crystal structures, the inner volumes of ($Ce_4L_6^1$) and ($Ce_4L_6^2$) were calculated as 300 and 550 $Å^3$, respectively. As evidenced by the luminescence titration (in DMF: acetone) and ESI-MS (in DMF: methanol), the ($Ce_4L_6^2$) cage showed size-selective (1:1) inclusion toward disaccharides (maltose, sucrose, and trehalose,). In the case of ($Ce_4L_6^1$), only mannose and glucose monosaccharides showed binding. No inclusion was observed for the larger disaccharides or smaller pentoses.

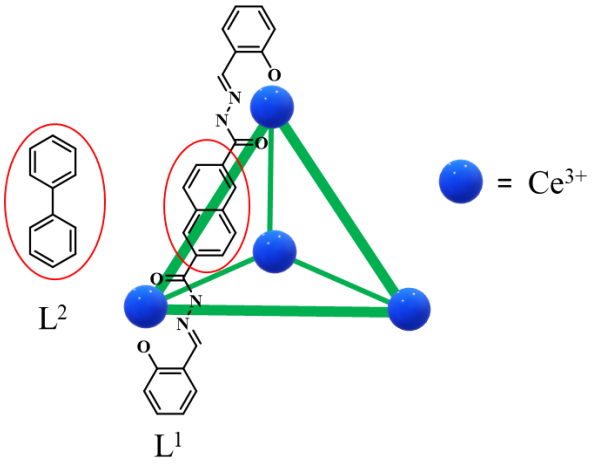

Figure 57. Two tetrahedral ($Ce_4L_6^1$) and ($Ce_4L_6^2$) cages

In 2017, Sun and co-workers reported a concentration- and/or solvent-triggered helicate to tetrahedron transformation.[209] When $Eu(OTf)_3$ was treated with L1 ligand in low concentration in CH_3CN, the ^1H NMR and ESI-MS suggested the formation of a dinuclear Eu_2L_3 with a helicate structure (Figure 58A). Interestingly, at a higher concentration of L, another set of signals corresponding to Eu_4L_6 with a tetrahedron structure showed up in the ^1H NMR. The crystal structure of pure Eu_4L_6 was obtained when a less polar solvent (ethyl acetate) was diffused into the reaction mixture (acetonitrile). The Eu_4L_6 was used as a safe container for the encapsulation of explosive nitroaromatic compounds. Emission quenching titration experiments were carried out using Eu_4L_6 in acetonitrile with electron-deficient 1-(4-nitrophenyl) ethanone, 1-methyl-4-nitrobenzene, 1,3-dinitrobenzene, and 1-methyl-2,4-dinitrobenzene nitroaromatic compounds (Figure 58B). In all these cases, significant fluorescence quenching was observed. However, this effect was more than 3 times higher when picric acid was used as the guest, suggesting that Eu_4L_6 is highly efficient in sensing picric acid at ppb levels. The formation of ground state charge transfer between the electron-deficient nitroaromatic guests and the electron-rich cage framework was proposed to be responsible for the Eu_4L_6 emission quenching.

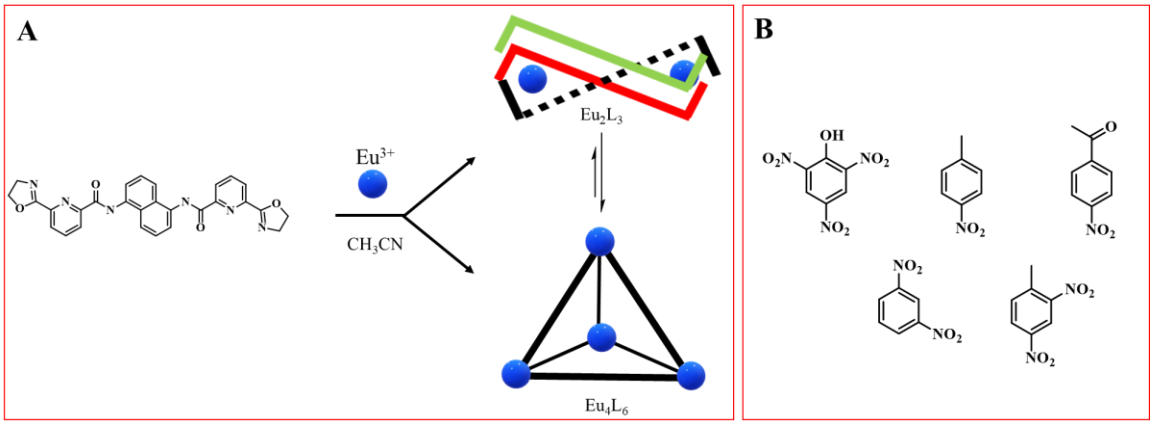

Figure 58. Helicate to tetrahedron transformation (A), electron deficient nitroaromatic guests (B)

In another study by Sun and co-workers, they reported the synthesis of a group of Ln_2Pd_6 heterometallic cages, where Ln= Nd^{III}, Eu^{III}, and Yb^{III}.[210] The crystal structure of Eu_2Pd_6 showed a cage with a triple-stranded helicate structure, with an overall M helicity (Figure 59A). This cage was studied for the sensing of antibiotics. To this end, luminescence titration was performed with five classes of common antibiotics in methanol. The results indicated that the Eu_2Pd_6 cage was sensitive to β-lactams at ppb levels (Figure 59B).

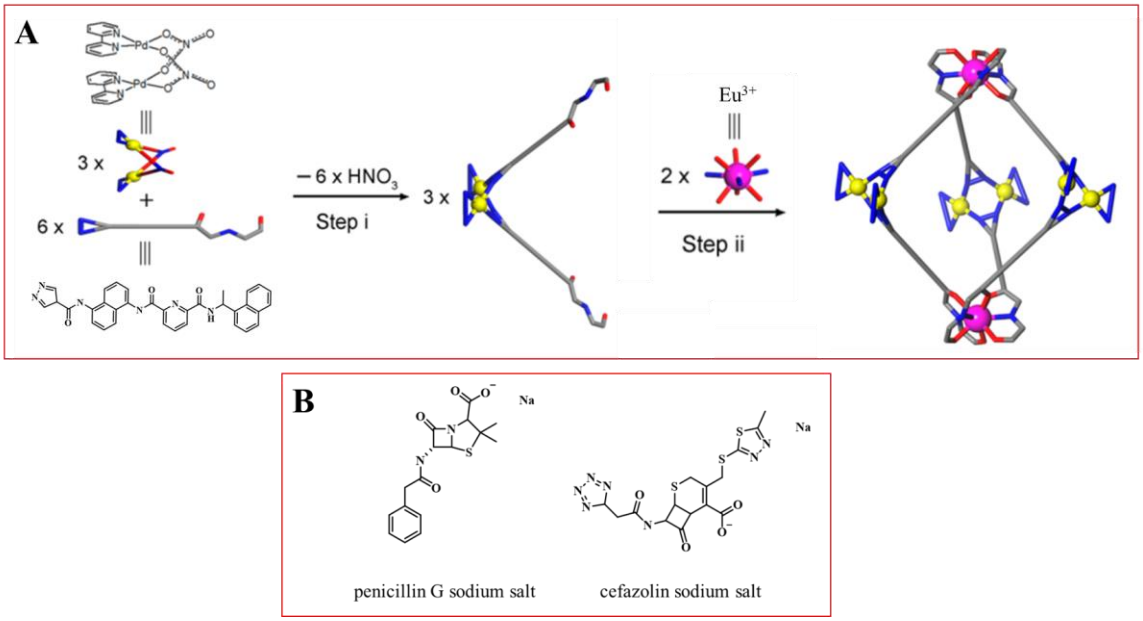

Figure 59. Formation of Eu^{III} based triple-stranded helicate structure (A), selected β-lactams antibiotics (B) (Adapted with permission from ref. 210. Copyright 2018 American Chemical Society.)

Recently, Yan and co-workers have reported a Eu_4L_4 (where L is 4,4′,4″-Tri(4,4,4-trifluoro-1,3-dioxobutyl)triphenylamine) tetrahedral cage as a fluorescence sensor for volatile compounds (Figure 60).[211] The designed cage showed a turn-on fluorescence response toward NH_3.

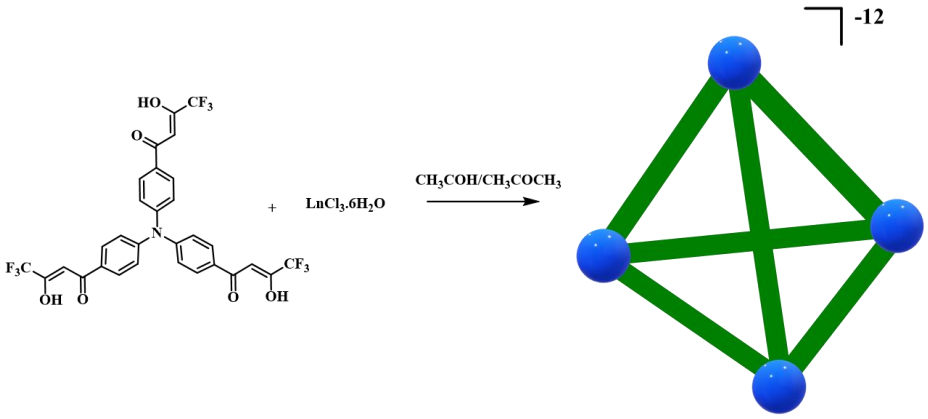

Figure 60. Eu_4L_4 tetrahedral self-assembly

In another study, Liu and co-workers introduced three lanthanide-based defective coordination cages, using bulky bis-tridentate ligands with pyridine-2,6-dicarboxamides (pcam) L1–L3.[212] Treating the lanthanides with L1, L2, and L3 resulted in the formation of defective $Ln_8(L_1)_{10}$ hexahedral with two missing edges, $Ln_4(L_2)_5$ tetrahedron with one missing edge, and twisted $Ln_6(L3)_9$ triangular prism without any missing edges, where Ln= Eu, Sm, Gd and La (Figure 61). Using a DOSY experiment, the hydrodynamic radii for $Ln_8(L1)_{10}$, $Ln_4(L2)_5$, and $Ln_6(L3)_9$ were measured as 19.6, 14.7, and 18.4 Å, respectively. In each of these cages, different guests were bound in CH_3CN solution. Encapsulation of fullerene, leucocrystal violet, mes-BODIPY, anthracene, and perylene guests within the $Eu_8(L_1)_{10}$, $Eu_4(L_2)_5$, and $Eu_6(L_3)_9$ cages were monitored via UV-Vis titration in CH_3CN. Interestingly, while the non-defective $Eu_6(L_3)_9$ cage did not bind to any of the above guests, the $Eu_8(L_1)_{10}$ with two missing edges formed host-guest complexes with all the guests. The binding constants increased from 6.8×10^3 to 1.4×10^4 M^{-1} as a function of increase in the π-conjugation of the guests. These findings suggest

that the missing edges provide more conformation flexibility to adjust the internal cavity for the accommodation of larger guests.

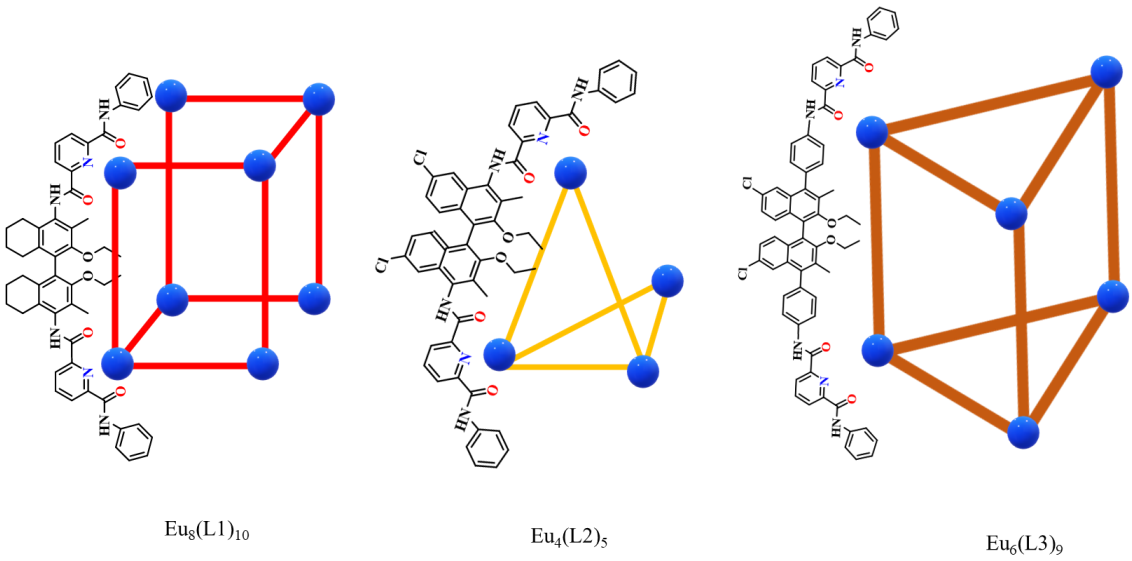

Figure 61. Lanthanide-based defective coordination cages

Despite the growing interest and advancement of Ln(III) supramolecular cages, the host-guest chemistry of Ln(III) based cages are far less well studied due to the liability of Ln(III) coordination bonds.[213] Due to the same reason, the majority of reported lanthanide cages and their host-guest chemistry are reported in organic solvents such as acetonitrile, since water can compete with the ligand to bind with metal ions, preventing cage formation. More studies are needed to unravel the factors that govern the Ln(III) cage formation and guest binding in aqueous media.

5.3. Lanthanide Ions

Lanthanide ions, also known as rare earth elements, consist of 15 elements, from Lanthanum to Lutetium. The lanthanide ions' electronic configurations are [Xe]4fn (n=0-14) with the most stable oxidation number of +3 and a high coordination number of 9. All lanthanide ions are paramagnetic and have unpaired electrons in their f orbitals, except for La^{3+} and Lu^{3+}.

In the lanthanides series, the formation of covalent bonds with ligands is almost impossible as the 4f orbitals are shielded by 5s and 5p orbitals.[214] Consequently, the interaction between the lanthanide ions and the ligand is only weakly covalent and largely electrostatic, and the complex stereochemistry is mainly governed by the steric properties of the ligand, rather than electronic properties. The resulting magnetic and photophysical properties of lanthanide ions are less impacted by the environment surrounding them.[215]

Due to the poor shielding of electrons in f orbitals on the 5s and 5p orbitals, the lanthanide ionic radii decrease across the series, known as "lanthanide contraction".[216] This is because the nuclei shielding effect is caused by the electron-electron repulsion in the orbital, and since f orbitals are larger compared to s and p orbitals, the electron repulsion is less noticeable, leading to a poor shielding effect.

The high charge density of lanthanide ions causes them to behave as a hard "Lewis acid" and tend to interact with hard "Lewis base" ligands such as carboxylates.[216] Generally, lanthanide ions have a large hydration enthalpy in aquas media, and this value increases across the series. This means that the ligand of choice has to overcome the

unfavorable endothermic desolvation enthalpy to form a stable complex with the lanthanide ions.[215] Thermodynamically, the positive enthalpy in the complexation process can be compensated by increasing the entropy to the variation in Gibbs free energy using multidentate ligands, known as the "chelating effect".[217] The trend in lanthanide ionic radii and hydration enthalpy are shown in Figure 62.[218]

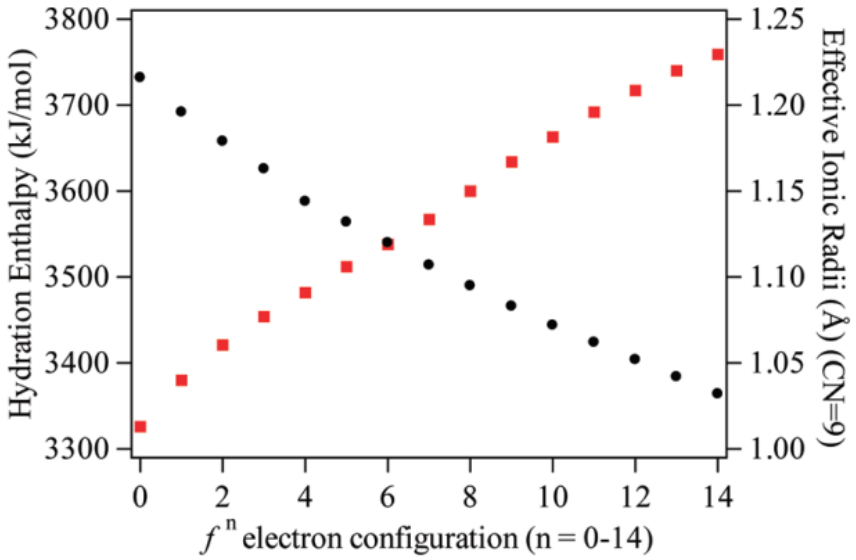

Figure 62. Ionic radii (black circles) and hydration enthalpy (red squares) of Ln(III) ions. (Adapted with permission from ref. 218. Copyright 2009 American Chemical Society.)

Luminescence Properties of Lanthanide Ions

The lanthanide ions are either fluorescent or phosphorescent with long lifetimes ranging from seconds (s) to microseconds (μs). While the strong shielding effect of 5s and 5p on the 4f orbital, results in the line-like shape of the lanthanide emission band, their long life arises from the forbidden transition in the 4f orbital.[219]

As mentioned above, the lanthanide ions' electronic transitions and photophysical properties involve 4f orbital.[219] For an emission to happen, the lanthanide ions are required to get excited to their excited state, and relax back to the ground state by emitting a photon. However, the direct excitation of lanthanide ions is not very efficient and is close to impossible as the f-f transition is Laporte forbidden and shows a very low extinction coefficient in the range of 5-10 $M^{-1}cm^{-1}$.

Using light absorbing chromophores or ligands, also known as antennas, to efficiently populate the 4f excited state of a lanthanide ion is one strategy to remove this limitation. In this strategy, the antenna absorbs the irradiated light and gets excited to its singlet excited state, followed by an inter system crossing to populate its triplet excited state (Figure 42). The excited antenna, in its triplet state, can now excite the lanthanide ion by passing its energy to the lanthanide ion through intramolecular energy transfer (ET). The excited lanthanide ion then relaxes back to its ground state by emitting photons, leading to the lanthanide emission spectra (Figure 63).[220] In most cases, the ISC in the antenna can be facilitated by the heavy atom effect of the lanthanide ions.

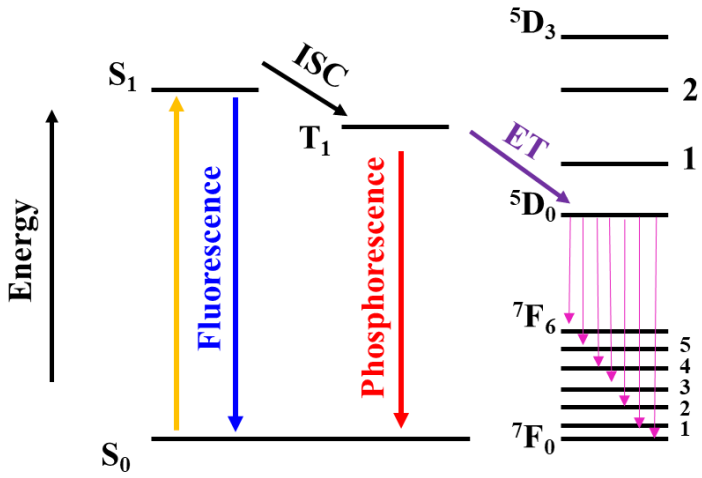

Figure 63. Jablonski diagram for Eu^{3+} luminescence.

5.4. Host-Guest Interaction

The internal cavity incorporated in these structures allows them to encapsulate the guest molecules. Consequently, such 3D structures can be used as nanoreactors for catalytic reactions, drug delivery, in host-guest chemistry for encapsulation, stabilizing unstable intermediates, and molecular recognition.[221] The incorporated cavity has a different microenvironment from the bulk solution. This may change the physical and chemical properties of the guest.[187] The guest encapsulation within the cage cavity is dictated by several factors, including solvation, size, charge, and the shape of both guest and host.[187] Due to the release of trapped solvent molecules into the bulk solution, the guest encapsulation is entropically driven.[222]

Interaction between the host and guest is mainly through weak supramolecular interactions, including van der Waals, hydrogen bonding, Coulombic, steric interactions, and ion association forces.[222] Without strong bonds such as covalent bonds to glue the

guest molecules to the internal cavity of the supramolecular hosts, the guests can freely exchange from the interior to the exterior of the cavity.[223] This process is known as "guest exchange".

Guest Exchange Mechanism

The guest exchange usually follows either a dissociative or non-dissociative pathway. The former refers to a mechanism in which partial dissociation of the host structure is necessary to temporarily open a gate for guest ingress.[224] The temporary partial dissociation of the ligand from the metal center happens in a way that preserves the entire host assembly structure during the guest exchange. This process resembles a door on a hinge.[224] On the other hand, the non-dissociative mechanism requires the host assembly to undergo deformation without rupture, to make enough space for the guest exchange.[224] The mechanisms are shown in Figure 64. The exchange pathway is usually determined by the existing interactions among the components of the host as well as the orientation of the host and guest, and the cavity accessibility.[224]

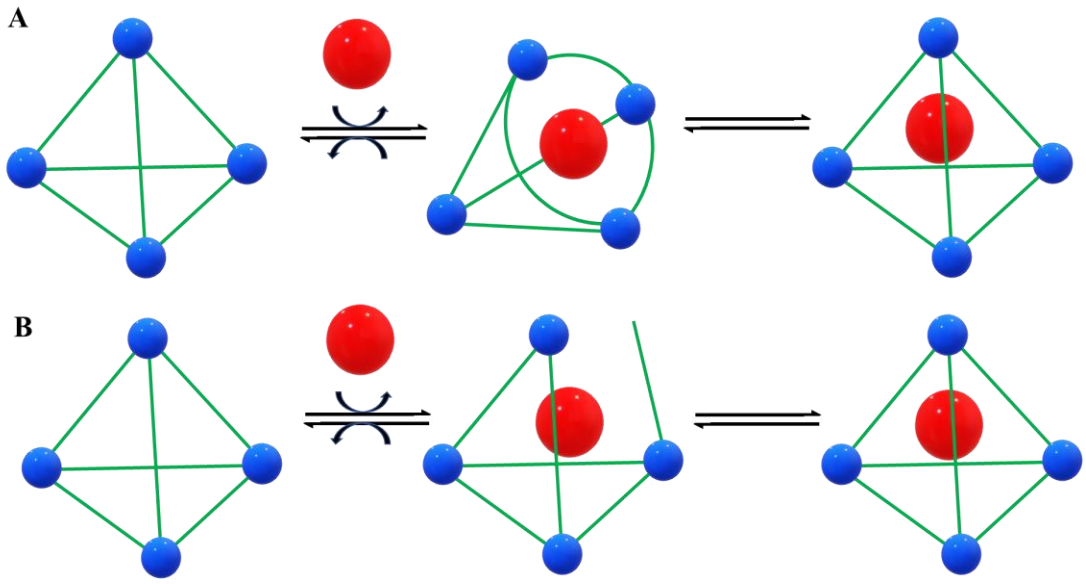

Figure 64. Associative mechanism (A), Dissociative mechanism (B)

Binding Constant

In host-guest chemistry, the binding constant is a quantitative measurement of the interaction between the host and guest. The binding constant, which is the inverse of the dissociation constant with the simple 1:1 equilibrium, is shown in equation 1.

$$Host + Guest \leftrightarrow Host.Guest \qquad K = \frac{[Host.Guest]}{[Host][Guest]} \qquad \text{equation 1}$$

The [Host] and [Guest] are the free species in the solution, and [Host.Guest] is the encapsulated guest inside the host. The binding constant of the [Host.Guest] complex can be measured by host-guest titration. In this method, the guest is gradually added to the host solution and the changes in the physical property of the system are monitored via different techniques, including NMR, isothermal titration calorimetry (ITC), and UV-vis. The obtained information is then used to derive information such as enthalpy (ΔH),

entropy (ΔS), Gibbs free energy (ΔG), binding constant, and stoichiometry from the fitted binding models.[225] Binding constant is related to ΔH, ΔS, and ΔG by equations 2 and 3.

$$\Delta G = -RTlnK \qquad \text{equation 2}$$

$$\Delta G = \Delta H - T\Delta S \qquad \text{equation 3}$$

T represents the temperature and R is the ideal gas constant.

5.5. Project Description

The primary focus of this project is on designing and synthesizing a bridging ligand with limited rotational freedom and functionalized with pyridine 2,6-dicarboxylate groups. An aqueous solution of $EuCl_3(H_2O)_6$ is then titrated into a solution of the ligand in D_2O, and SCC formation with the general formula Eu_2L_3 is monitored by nuclear magnetic resonance spectroscopy (NMR).

Accordingly, to study the recognition properties of the as-prepared cage-like structure, a series of mono- and di-cationic guests were synthesized and their encapsulation was monitored by NMR spectroscopy and Isothermal Titration Calorimetry (ITC) in aqueous media.

5.6. Experimental Details

General Synthetic Scheme

The synthetic scheme for the preparation of the bridging ligand (L) precursor to the Eu_2L_3 cage is shown in Scheme 5. The bridging ligand (L) functionalized with two pyridine 2,6-dicarboxylate groups was prepared in seven steps. The scheme starts with the commercially available 3-bromo-2,6-dimethyl-pyridine, which is converted to 3-bromo-pyridine-2,6-dicarboxylic acid (1) by an oxidation reaction in the presence of

$KMnO_4$.[226] Through an esterification reaction, (1) converts to 3-bromo-pyridine-2,6-dimethyl ester (2) in high yield.[226] The 3-[2-(trimethylsilyl)ethynyl]-pyridine-2,6-dimethyl ester (3) obtained from (2) through the Sonogashira cross-coupling reaction, followed by a deprotection reaction in the presence of KF to afford the 3-ethynyl-pyridine-2,6-dimethyl ester (4).[226,227] We adapted a one-pot copper-catalyzed azide–alkyne cycloaddition (CuAAC) method from a previously reported procedure to prepare compound (5).[228] The final bridging ligand (L) was obtained from (5) through a saponification reaction in the presence of LiOH. The Eu_2L_3 was prepared by mixing an appropriate ratio of L and $EuCl_3.6H_2O$ precursor in D_2O. ^1H NMR was used to monitor the formation of Eu_2L_3 upon mixing. The ^1H NMR spectra of the bridging ligands (5 and L) and Eu_2L_3 assemblies are shown in Appendix Figures A43, A44, and A45.

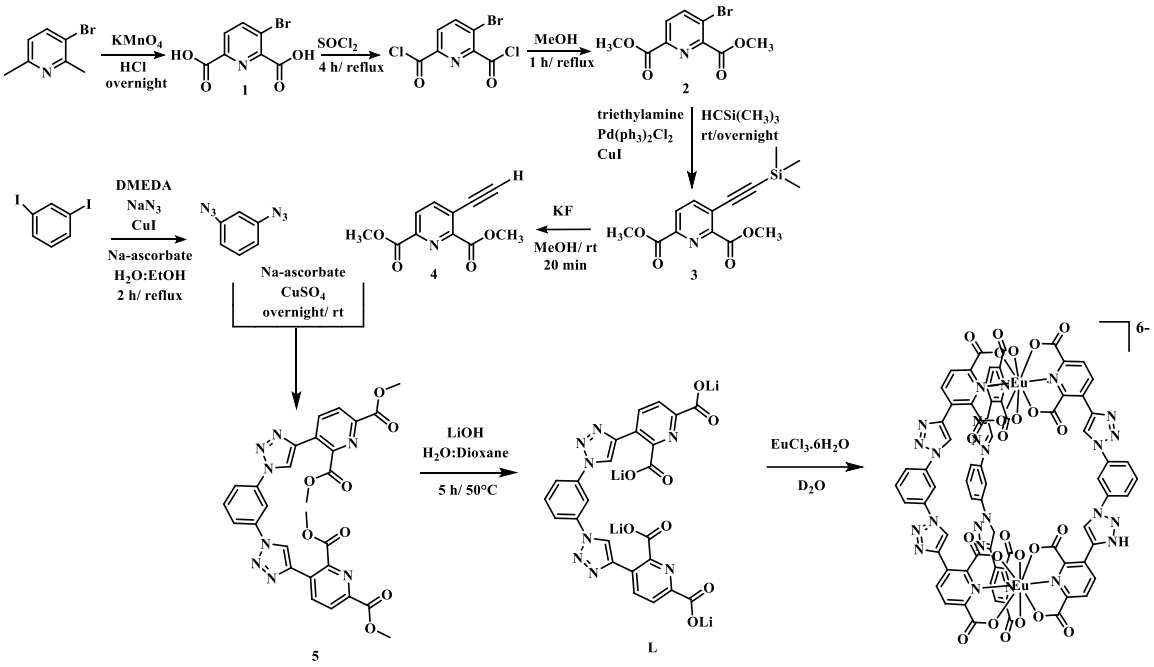

Scheme 5. Synthetic approach for L and corresponding Eu_2L_3 assembly

Synthesis of 3-Bromo-pyridine-2,6-dicarboxylic acid (1)

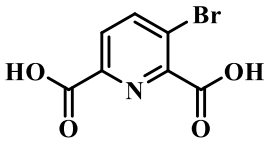

The compound was synthesized by a modification to a previously reported procedure.[226] To a solution of 3-bromo-2,6-dimethyl-pyridine (4.0 g, 21 mmol) in water (0.10 L), $KMnO_4$ (13 g, 85 mmol) was added over the course of 5 h at 90°C. The solution was heated at 90°C overnight. The mixture was filtered hot and washed with hot water. HCl (7.0 mL) was added to the concentrated filtrate to induce precipitation. The filtrate was stored in the fridge overnight. The resulting white precipitation was filtered off, washed with cold water (0.060 L) and dried under vacuum to give 5-bromo-pyridine-2,6-

dicarboxylic acid. Yield: 2.6 g (0.010 mol, 50%); (^{1}H-NMR (500 MHz, d_6-DMSO) δ 8.38 (1 H, s), 8.01 (1H, s).

Synthesis of 3-Bromo-pyridine-2,6-dimethyl ester (2)

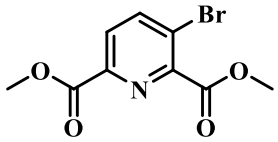

The compound was synthesized according to a previously reported procedure.[226] The 3-bromo-pyridine-2,6-dicarboxylic acid (1) (2.0 g, 8.1 mmol) was dissolved in $SOCl_2$ (6.0 mL) and heated at reflux for 4 h. The solvent was removed and methanol (15 mL) was added. The solution was heated at reflux for 1 h. After cooling down, the solvent was removed under reduced pressure to give 3-bromo-pyridine-2,6-dimethyl ester (2). Yield: 1.7 g (6.1 mmol g, 75%); ^{1}H-NMR (500 MHz, d_6-DMSO) δ 8.46 (1H, d), 8.09 (1H, d), 3.93 (3H, s), 3.89 (3H, s).

Synthesis of 3-[2-(trimethylsilyl)ethynyl]-pyridine-2,6-dimethyl ester (3)

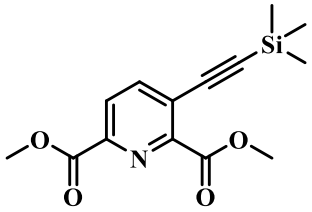

The compound was prepared according to a previously reported procedure.[229] To a degassed Et_3N solvent (3.0 mL) were added (2) (150 mg, 0.54 mmol), trimethylsilyl acetylene (0.090 mL, 0.65 mmol), $(Ph_3P)_2PdCl_2$ (8.0 mg, 0.012 mmol), and CuI (2.2 mg, 0.012 mmol). The mixture was stirred at room temperature overnight. After stopping the reaction, dichloromethane (0.020 L) was added to the mixture and filtered through a

silica plug (3x). The solvent was removed under reduced pressure and the remaining solid was purified by column chromatography (hexanes/ethyl acetate (50:50)). The product was obtained as orange oil. Yield: 0.10 g (0.34 mmol, 62%). ^{1}H-NMR (500 MHz, d_6-DMSO) δ 8.22 (1H, d), 8.16 (1H, d), 3.31 (6H, s), 0.25 (9H, s).

Synthesis of 3-ethynyl-pyridine-2,6-dimethyl ester (4)

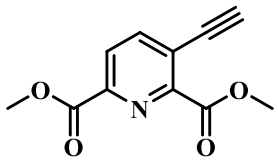

The compound was prepared according to a modified previously reported procedure.[227] 3-[2-(trimethylsilyl)ethynyl]-pyridine-2,6-dimethyl ester (3) (0.090 g, 0.30 mmol) and KF (0.040 g, 0.75 mmol) were added to methanol (8.0 mL) and stirred for 25 min at room temperature. The mixture was poured into ethyl acetate (0.030 L), washed with brine, and dried over $MgSO_4$. The product was obtained as a brown solid. Yield: 52 mg (23 mmol, 77%). ^{1}H-NMR (500 MHz, d_1-$CDCl_3$) δ 8.22 (1H, d), 8.09 (1H, d), 4.02 (6H, s), 3.67 (1H, s).

Synthesis of (5)

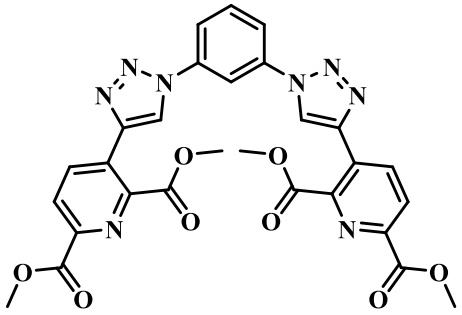

The compound was synthesized according to a modified previously reported procedure.[228] N,N'-dimethylethylenediamine (18 μL, 0.70 mmol), NaN_3 (85 mg, 1.3 mmol), sodium ascorbate (64 mg, 0.32 mmol), and CuI (25 mg, 0.13 mmol) were added to a degassed solution of 1,3-diiodobenzene (220 mg, 0.66 mmol) in H_2O/ethanol (0.010 L) and heated to reflux under Ar. After 2 h, the mixture was cooled to room temperature and 3-ethynyl-pyridine-2,6-dimethyl ester (4) (0.30 g, 1.4 mmol), sodium ascorbate (64 mg, 0.32 mmol), and $CuSO_4$ (42 mg, 0.17 mmol) were added to the mixture and stirred overnight at room temperature under Ar. The reaction mixture was then poured into NH_4OH/EDTA (0.020 L). The resulting brown precipitation was filtered, washed with water, and dried under the vacuum. The crude was purified by column chromatography (ethyl acetate/methanol (97:3). The product was obtained as an orange solid. Yield: 66 mg (0.11 mmol, 17%). ^{1}H-NMR (500 MHz, d_6-DMSO) δ 9.62 (2H, s), 8.65 (1H, s), 8.53 (2H, d), 8.36 (2H, d), 8.16 (2H, d), 7.95 (1H, dd), 3.94 (6H, s), 3.90 (6H, s).

Synthesis of L

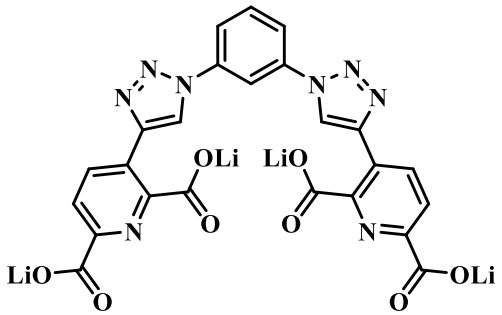

Compound 5 (45 mg, 0.075 mmol) and LiOH (7.6 mg, 0.30 mmol) were added to a 6.0 mL of H_2O/dioxane (1:1) and heated at 50°C for 5 h. The solvent was removed

under reduced pressure and the desired product was obtained as an orange solid. Yield: 0.030 g (0.052 mmol, 71%). ^{1}H-NMR (500 MHz, d_2-D_2O) δ 8.78 (2H, s), 8.46 (1H, s), 8.41 (2H, d), 8.05 (2H, d), 8.04 (2H, d), 7.88 (1H, dd).

Preparation of Eu_2L_3

Generally, 0.50 mL of L solution in D_2O (3.0- 0.50 mM) was placed into an NMR tube. Aliquots of $EuCl_3.6H_2O$ in D_2O (10- 30 mM) were added to the NMR tube. The Formation of Eu_2L_3 (2:3 ratio) was monitored by ^{1}H-NMR upon mixing. The desired ratio (Eu_2L_3) resulted in two sets of signals in ^{1}H-NMR spectrum. ^{1}H-NMR (500 MHz, d_2-D_2O) δ 9.98 (2H, s), 9.09 (1H, s), 7.98 (2H, d), 7.67 (1H, dd), 6.10 (2H, d), 4.58 (2H, d). ^{1}H-NMR (500 MHz, d_2-D_2O) δ 9.96 (2H, s), 8.89 (1H, s), 8.00 (2H, d), 7.73 (1H, dd), 6.03 (2H, d), 4.63 (2H, d).

^{1}H NMR

The spectra were collected on a Bruker Ascend 500 MHz spectrometer at 298 K. The spectra were calibrated to residual solvent peaks for D_2O at δ = 4.79 ppm.

ITC

ITC experiments were carried out using an iTC200 calorimeter (Microcal Inc., GE Healthcare, Piscataway, NJ).

Host-Guest NMR Titration Experiments

Aliquots of each guest solution (20-40 mM) in D_2O were added to a solution of cage Eu_2L_3 (0.5 mM) in D_2O into the NMR tube, and the changes in the cage and guest signals were recorded after each addition upon mixing.

5.7. Results and Discussion

Self-assembly of Eu_2L_3

Upon the addition of $EuCl_3.6H_2O$ into the solution of free ligand in D_2O, two new sets of signals shown by black circles and squares started to show up. This was concomitant with the decrease in the free ligand's signals. When 0.64 equivalent of $EuCl_3.6H_2O$ was added, all signals corresponding to the free ligand vanished. The titration is shown in Figure 65. The two new sets of signals (circles and squares) were assigned to the formation of two new assemblies with a 2:3 (Eu:L) ratio with different chirality.

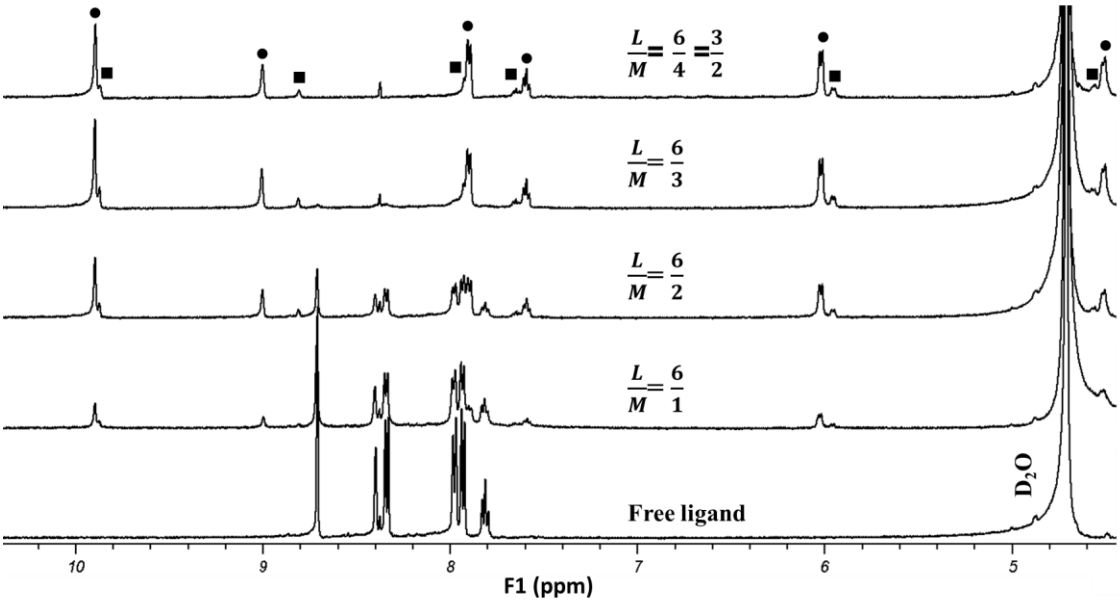

Figure 65. ^1H NMR titration of L (3 mM in 500µL D_2O) with $EuCl_3.6H_2O$ (30 mM)

To further assign all the signals in the Eu_2L_3 assemblies, we performed two-dimensional nuclear Overhauser effect spectroscopy (NOESY) and Correlation spectroscopy (COSY) experiments (Figures 66 and 67). The assignments are shown in Figure 68.

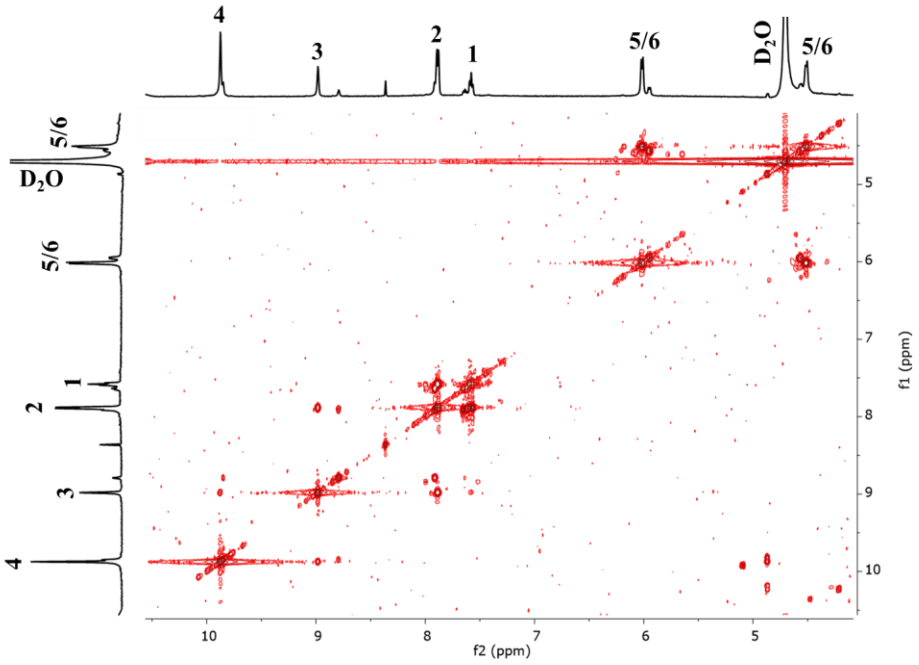

Figure 66. COSY spectrum of Eu_2L_3 assemblies in D_2O

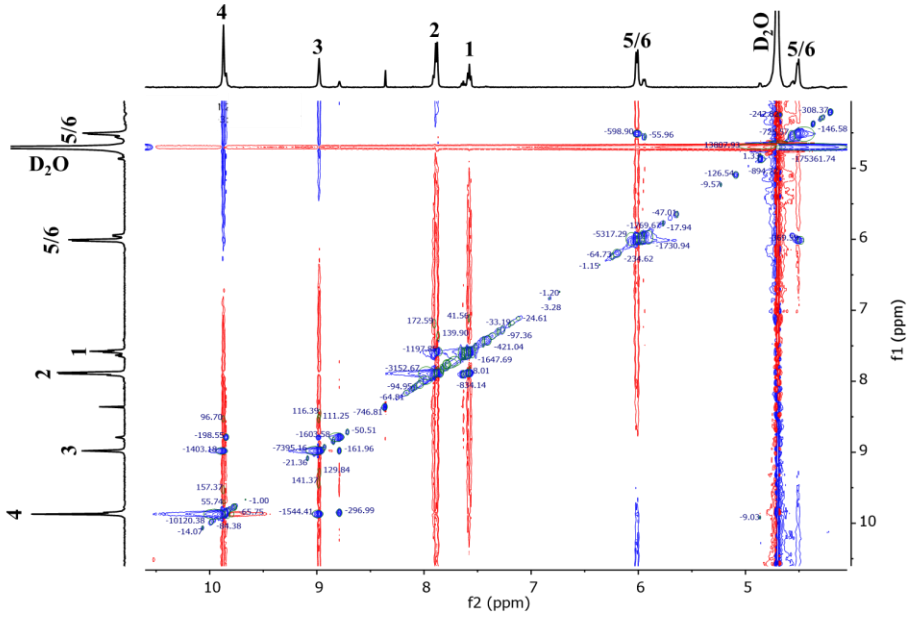

Figure 67. NOESY spectrum of Eu_2L_3 assemblies in D_2O

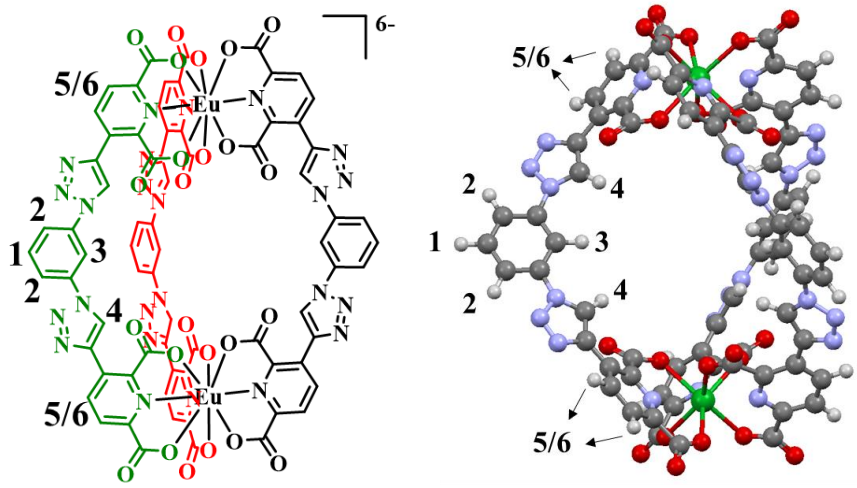

Figure 68. Assignment of the protons

Diffusion-ordered NMR spectroscopy (DOSY) confirmed the formation of two assemblies with very similar diffusion coefficients (Figure 69). This further suggested

that both assemblies have the same chemical structures but different conformations. Each set of proton signals of both assemblies showed a diffusion coefficient of D=1.80×10^{-10} m^2 · s^{-1}. The Stoke-Einstein equation (equation 4) was used to calculate the Stokes radius (r_s) of Eu_2L_3 assemblies.[230]

$$D = \frac{k_B T}{6\pi\eta r_s} \qquad \text{equation 4}$$

Where k_B is the Boltzmann constant, T is the absolute temperature, η is the viscosity of the solvent, and r_s is the radius. Using the above equation, the hydrodynamic radius of both assemblies was calculated as 12 Å.

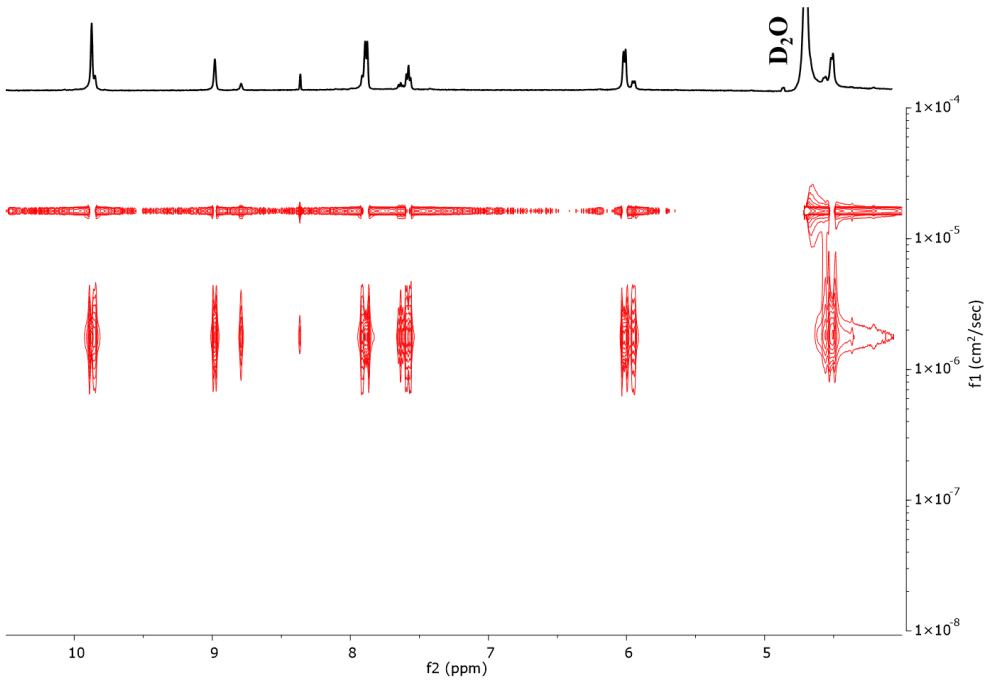

Figure 69. DOSY spectrum of Eu_2L_3 assemblies in D_2O

To predict the conformations of the two assemblies observed in the NMR spectrum, we optimized the Eu_2L_3 assemblies using the GFN2 XTB method. To avoid problems during optimization, we have used Lu instead of Eu.

Computational calculations suggest that the two assemblies are a mixture of two structures with M, M and M, P chiralities. Figure 70A shows a structure with an M, M helical chirality, meaning that all 6 pyridyl groups are left-handed around the lanthanide. On the other hand, Figure 70B exhibits a structure with an M, P chirality, i.e., one lanthanide has left-handed pyridyl blades and the other one right-handed pyridyl.

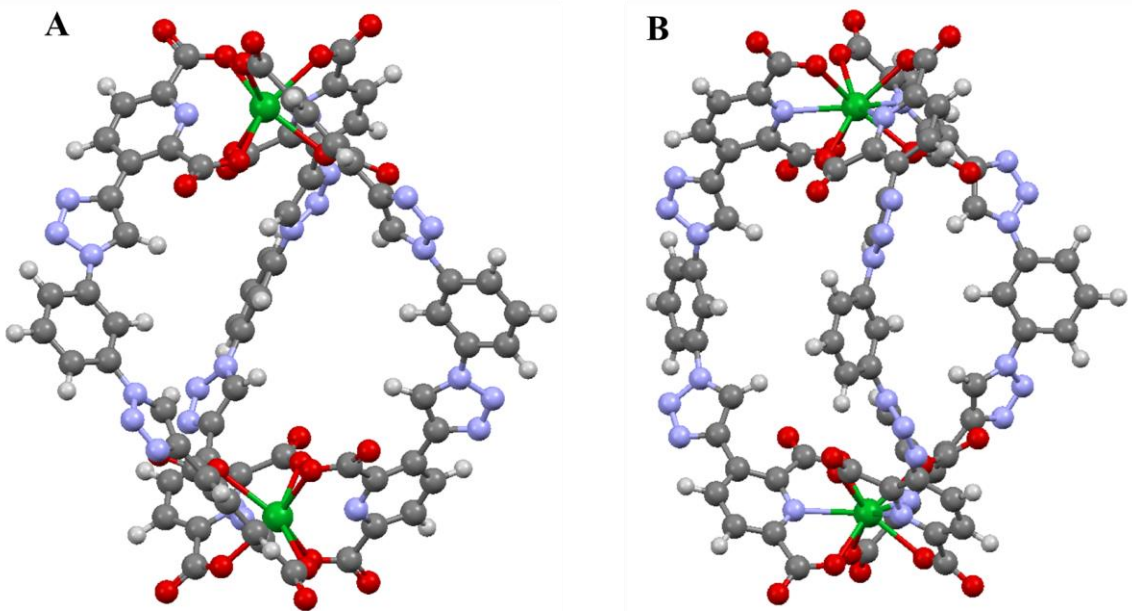

Figure 70. Optimized structures of Lu_2L_3 with (A) M,M chirality (B) M,P chirality

Encapsulation of Cationic Guests

The incorporated cavity inside the Eu_2L_3 structure prompts us to study the cationic guests' encapsulation inside the internal cavity. As shown in Figure 71, as the result of the overall negative charge on the Eu_2L_3 cage, a series of water-soluble mono- and di-cationic guests were synthesized, and their encapsulation was studied through ^{1}H NMR titration in D_2O. In this series, while the smaller mono-cationic guest did not show any binding, the 2,2':6',2''-terpyridinium,1-methyl iodide with a bigger size was encapsulated inside the cavity of Eu_2L_3. On the other hand, most of the di-cationic guests bound within the Eu_2L_3.

During the titration, we monitored the changes in the signals of protons 3 and 4 on the host (see Figure 67 for the assignment), as those are the protons that point toward the inside of the cavity and are involve directly with the guest's binding. Any guest encapsulation should lead to bigger shifts in those protons. Similarly, compared with the free guest, the guest encapsulation should result in bigger chemical shifts in the bound guest signals. The chemical shift of the bound guest results from changing its electronic environment due to encapsulation, as the host's cavity has a different microenvironment from the bulk solution.[187]

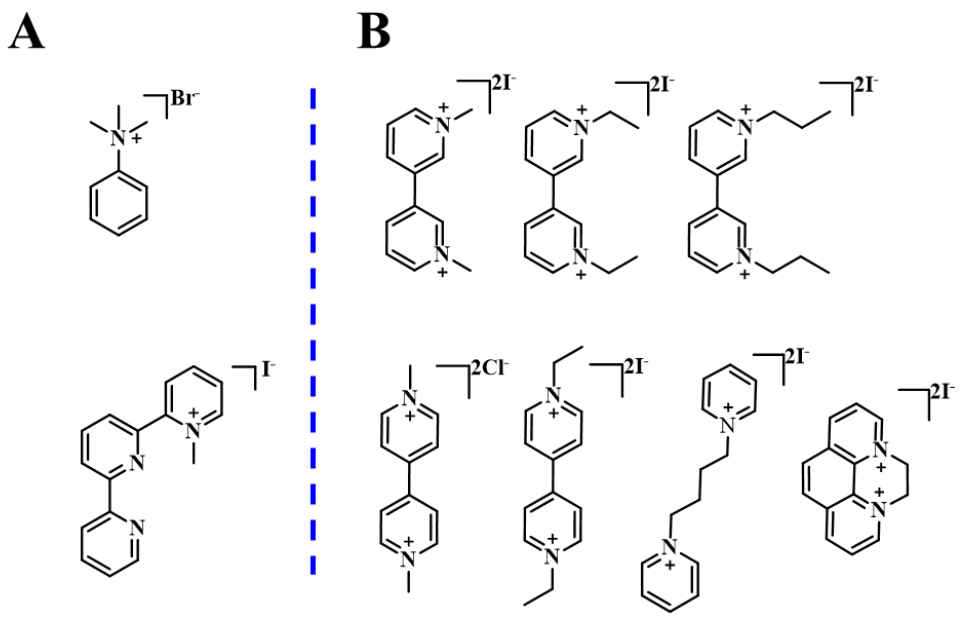

Figure 71. A series of mono- (A) and di-cationic (B) guests.

^{1}H NMR Mono-Cationic Guests Titration

The mono-cationic guest binding was studied by adding aliquots of guest solution (20 mM) into a solution of Eu_2L_3 (0.5 mM) in D_2O in the NMR tube, and the changes in the host and guest signals were monitored after each addition upon mixing. As shown in Figure 72, no shift was observed after adding 1 eq of the trimethylphenylammonium bromide guest, indicating that no binding is happening.

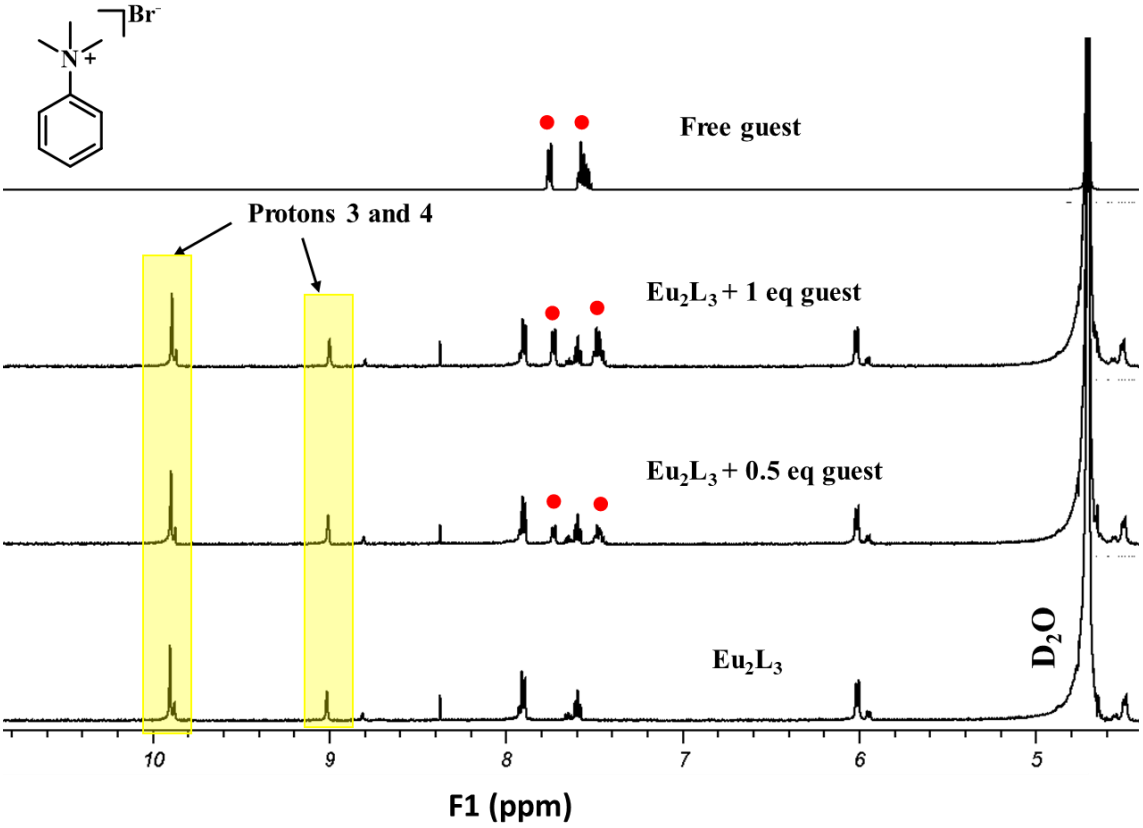

Figure 72. ^{1}H NMR titration of Eu_2L_3 with trimethylphenylammonium bromide in D_2O

Interestingly, as exhibited in Figure 73 titration of the Eu_2L_3 cage with mono-cationic 2,2':6',2"-terpyridinium,1-methyl guest resulted in an upfield shift of protons 3 and 4's signals on the host. The guest's signals also showed up at different chemical shifts as compared to the free guest. The observed encapsulation can be attributed to the larger size of the guest, which provides a better fit for the cage's cavity, resulting in a stronger dispersion interaction.

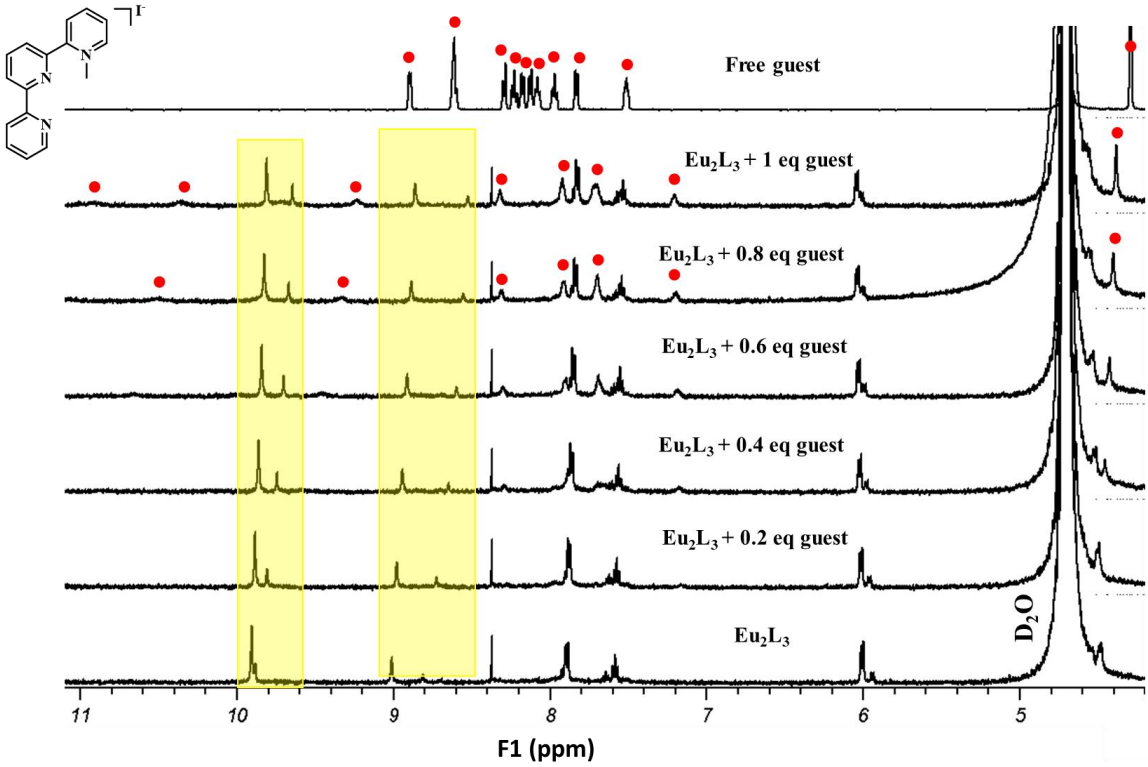

Figure 73. ^{1}H NMR titration of Eu_2L_3 with 2,2':6',2''-terpyridinium,1-methyl iodide in D_2O

^{1}H NMR Di-Cationic Guests Titration

Similar to mono-cationic guest titration, we monitored the changes in the chemical shift of protons 3 and 4 on the host, as well as the guest's signals. Starting with 1,1′-dimethyl-4,4′-bipyridinium dichloride (methyl viologen) guest titration, gradual addition of methyl viologen into the host solution resulted in a progressive upfield shift of protons 3 and 4's signals on the host (Figure 74). The bound guest's signals also appeared as broad signals at more downfield chemical shifts as compared to the free guest.

The addition of more guests resulted in an upfield shift of the bound guest toward the free guest's signals. The steady change in the chemical shifts is an indication of a fast guest exchange.[190]

Similar results were observed for 1,1′-dimethyl-4,4′-bipyridinium diiodide, 1,1′-dimethyl-3,3′-bipyridinium diiodide, 1,1′-diethyl-3,3′-bipyridinium diiodide, 1,1′-dipropyl-3,3′-bipyridinium diiodide, and 1,1'-propylenedipyridinium diiodide. The ^{1}H NMR titrations are shown in Figures 75-80.

Binding of di-cationic guests might be arising from the fact that higher charged guest molecules are surrounded by more water molecules, resulting in a more significant entropic driving force for binding.[231] Additionally, di-cationic guests provide stronger electrostatic interactions with the overall negative charge on the Eu_2L_3 assembly.

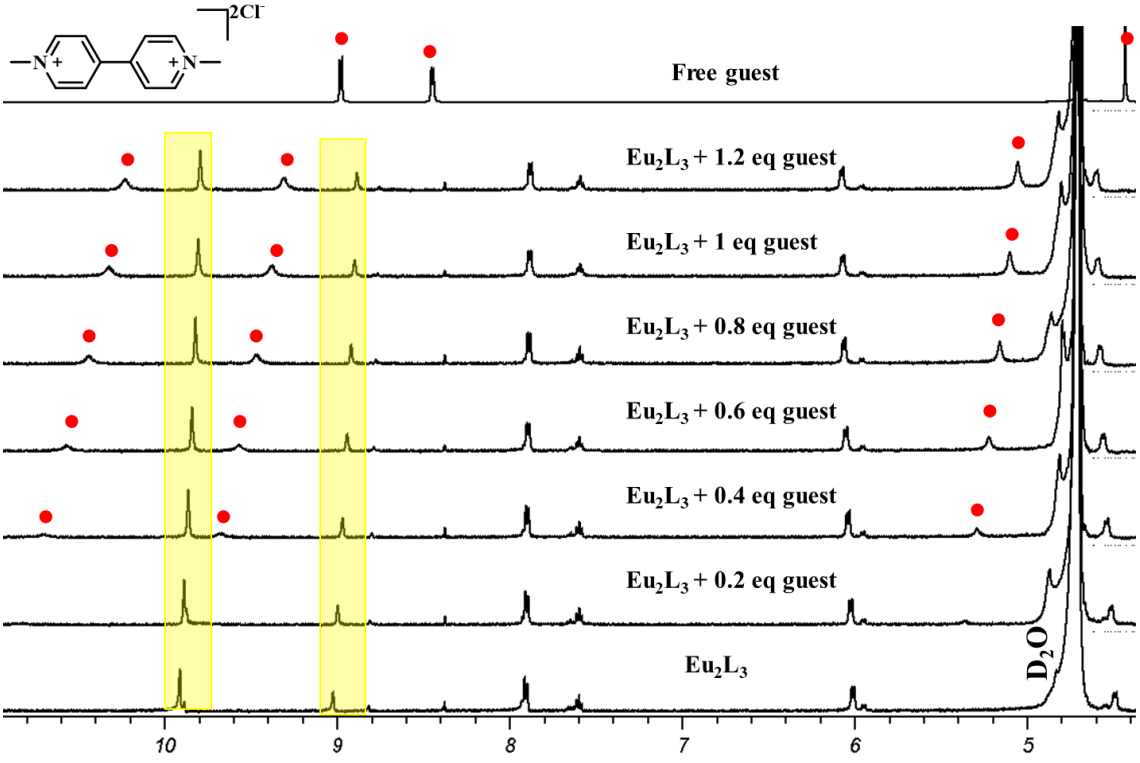

Figure 74. ^{1}H NMR titration of Eu_2L_3 with 1,1′-dimethyl-4,4′-bipyridinium dichloride in D_2O

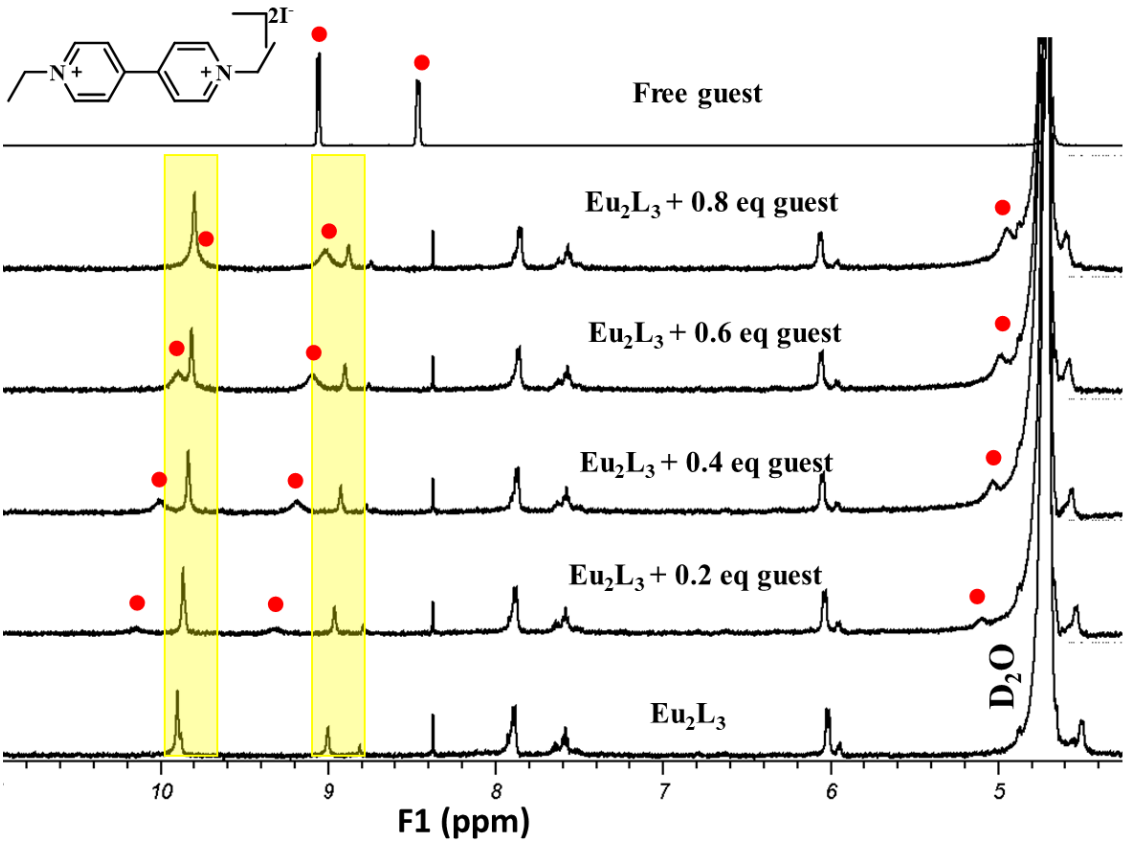

Figure 75. ^{1}H NMR titration of Eu_2L_3 with 1,1′-diethyl-4,4′-bipyridinium dichloride in D_2O

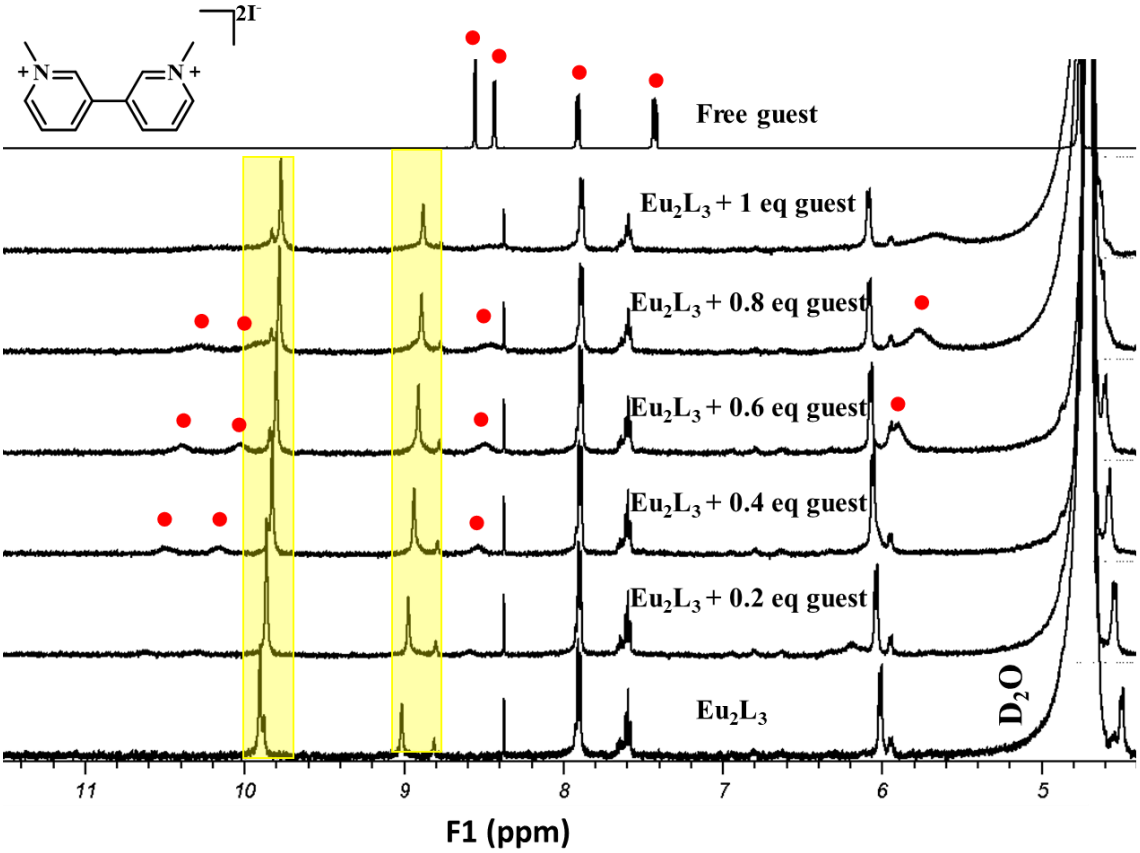

Figure 76. ^{1}H NMR titration of Eu_2L_3 with 1,1′-dimethyl-3,3′-bipyridinium diiodide in D_2O

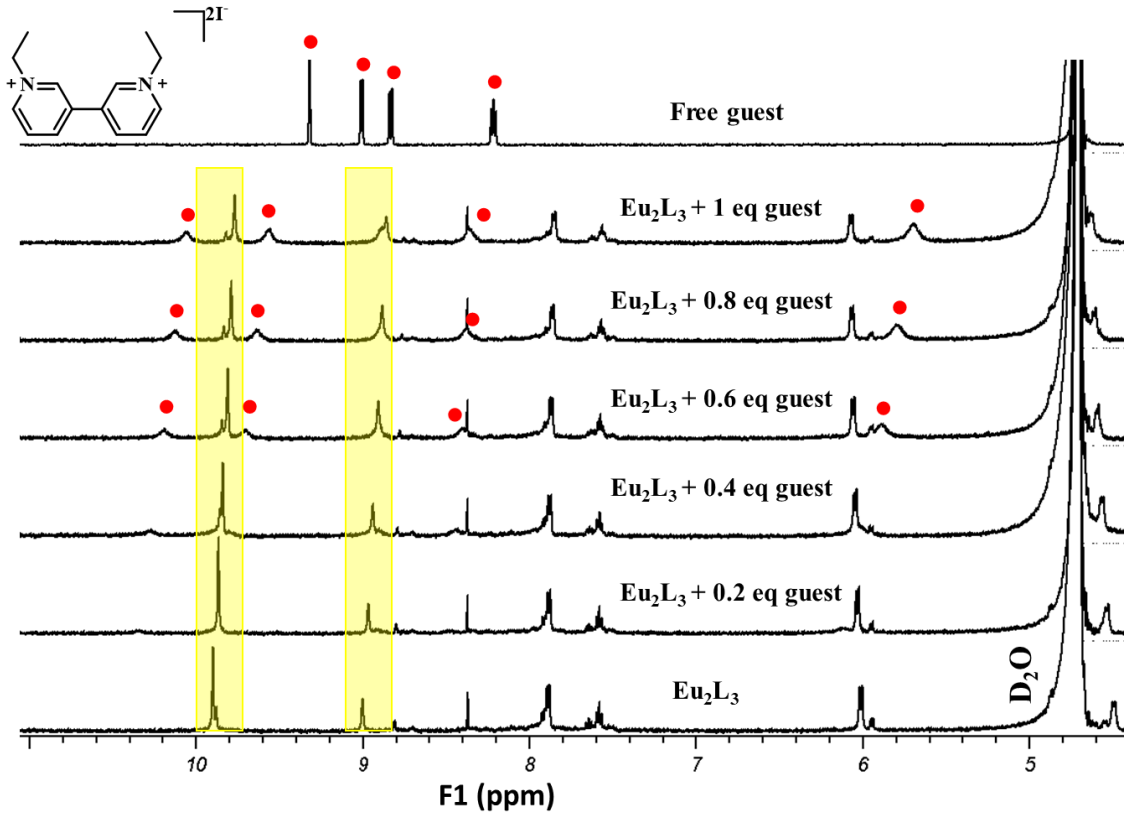

Figure 77. ^{1}H NMR titration of Eu_2L_3 with 1,1′-diethyl-3,3′-bipyridinium diiodide in D_2O

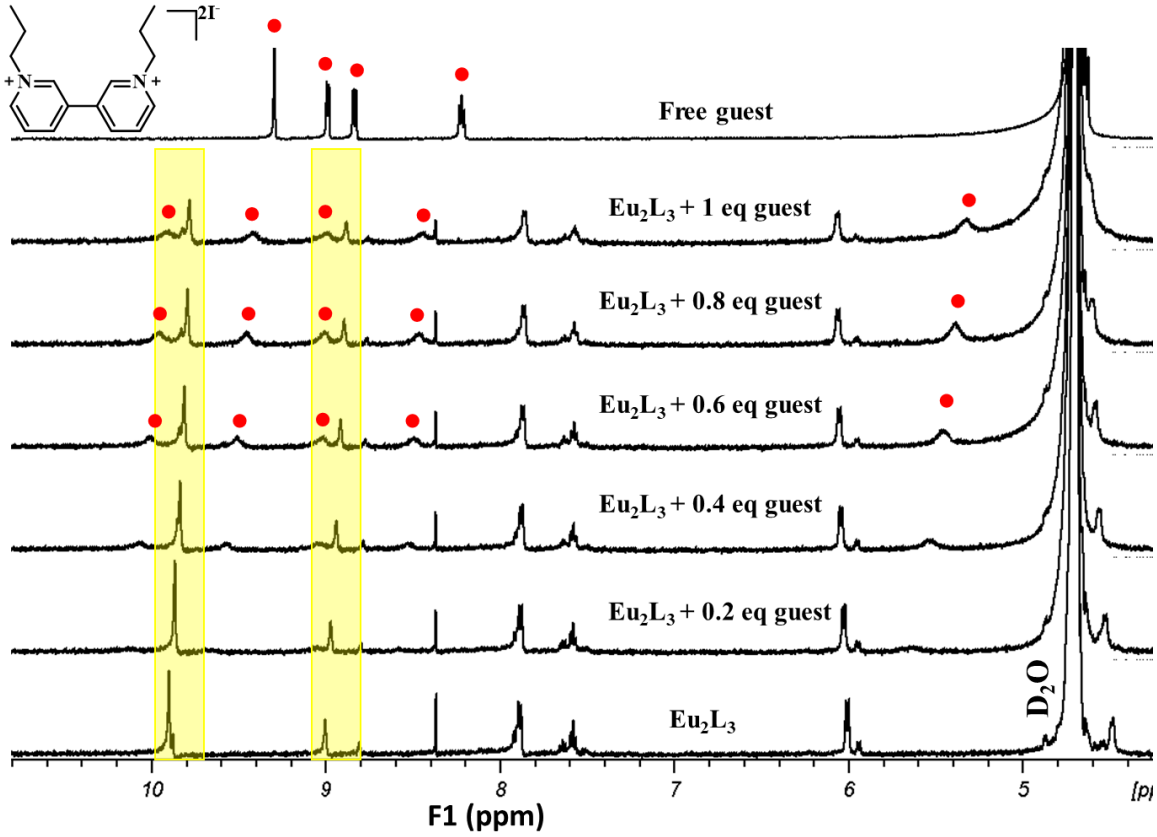

Figure 78. ^{1}H NMR titration of Eu_2L_3 with 1,1′-propyl-3,3′-bipyridinium diiodide in D_2O

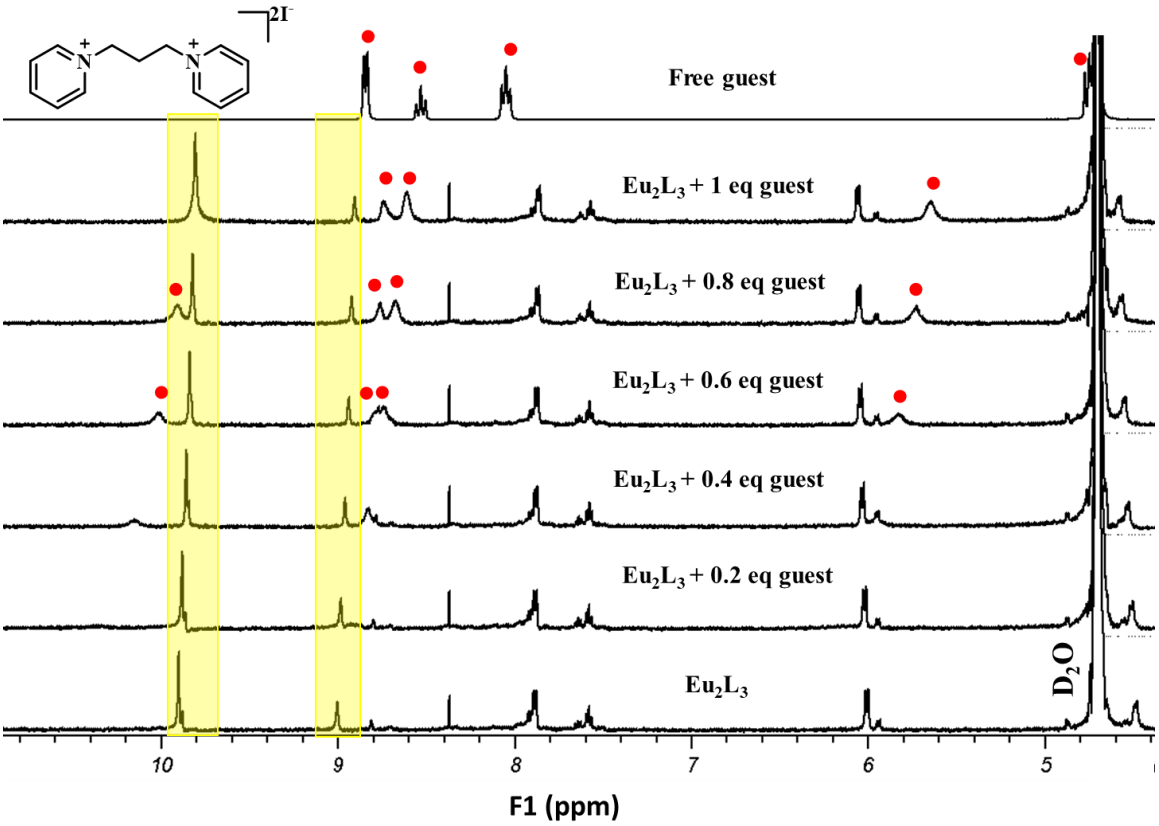

Figure 79. ^{1}H NMR titration of Eu_2L_3 with 1,1'-propylenedipyridinium diiodide in D_2O

In case of titration with 5,6-dihydropyrazino[1,2,3,4-lmn]-1,10-phenanthrolinium diiodide, addition of guest to the host solution resulted in an immediate precipitation. This might be arising from cage aggregation due to outside binding of the guest.[232]

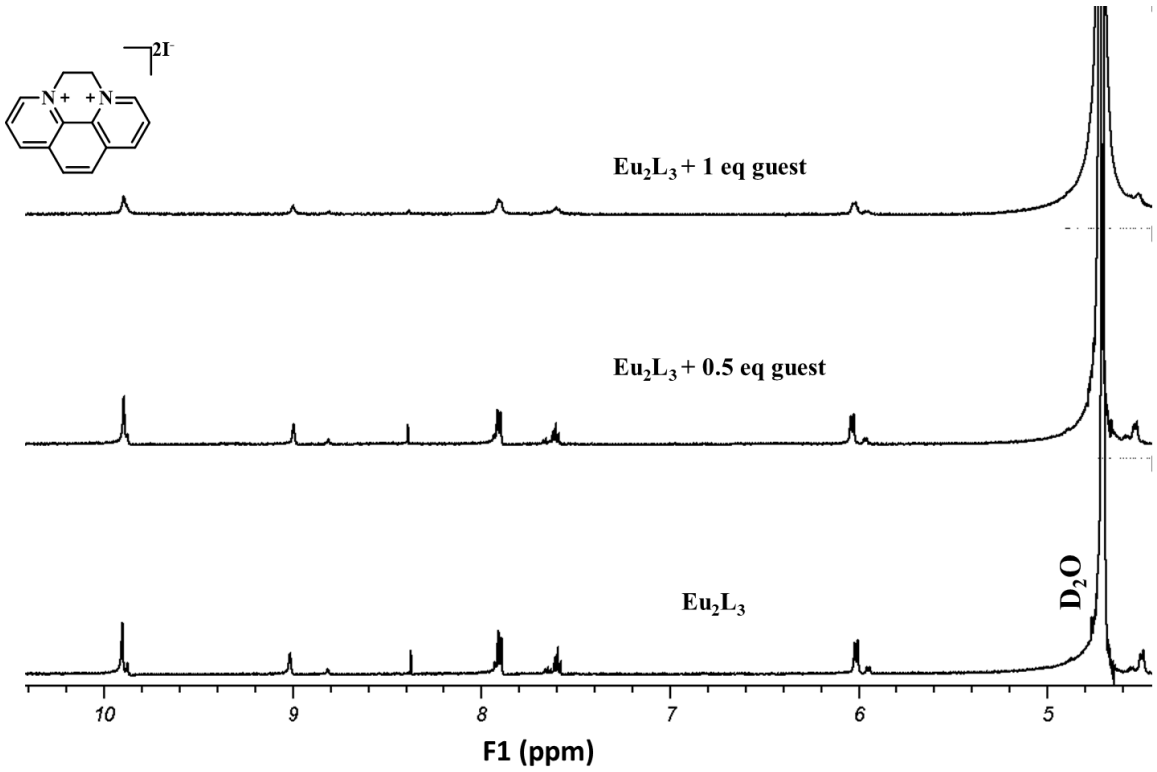

Figure 80. ^{1}H NMR titration of Eu_2L_3 with 5,6-dihydropyrazino[1,2,3,4-lmn]-1,10-phenanthrolinium diiodide in D_2O

ITC Guests Titration

To determine the binding constant (K_A) and the binding stoichiometry of each host: guest complex, a 100 µL, 5 mM of the guest, and a 300 µL, 0.5 mM of the host (Eu_2L_3) solution were prepared in water. The guest solution (60 µL) was loaded into the syringe, and 300 µL of the host was loaded into the cell. ITC experiments were performed by adding 2 µL aliquots of the guest solution into the host solution in the cell up to 1.6 eq. After the first injection, the microcalorimeter records the heat released until the binding reaches to an equilibrium. The data collected results in a plot of heat released after each injection in the solution over time. The area under each peak is calculated and

plotted over the molar ratio of ligand to host. The binding constant is then obtained by fitting the resulting isotherm to a binding model.

In agreement with ^{1}H NMR titration with trimethylphenylammonium bromide, no binding was observed during ITC titration with the same guest. Titration of di-cationic guests i.e., 1,1′-dimethyl-4,4′-bipyridinium dichloride and 3,3′-dimethyl-4,4′-bipyridinium diiodide, however, resulted in a weak binding between the guest and the host. This is also in good agreement with the fast exchange mechanism observed during ^{1}H NMR titrations. The binding affinities for 1,1′-dimethyl-4,4′-bipyridinium dichloride and 3,3′-dimethyl-4,4′-bipyridinium diiodide were calculated as 1.1 (± 0.03) × 10^{3} M^{-1} and 2.0 (±0.08) × 10^{3} M^{-1}, respectively. The enthalpograms are shown in Figures 81 and 82. Unfortunately, due to the solubility issues and precipitation at the higher guest's equivalent, we were unable to obtain good results for the other di-cationic guests.

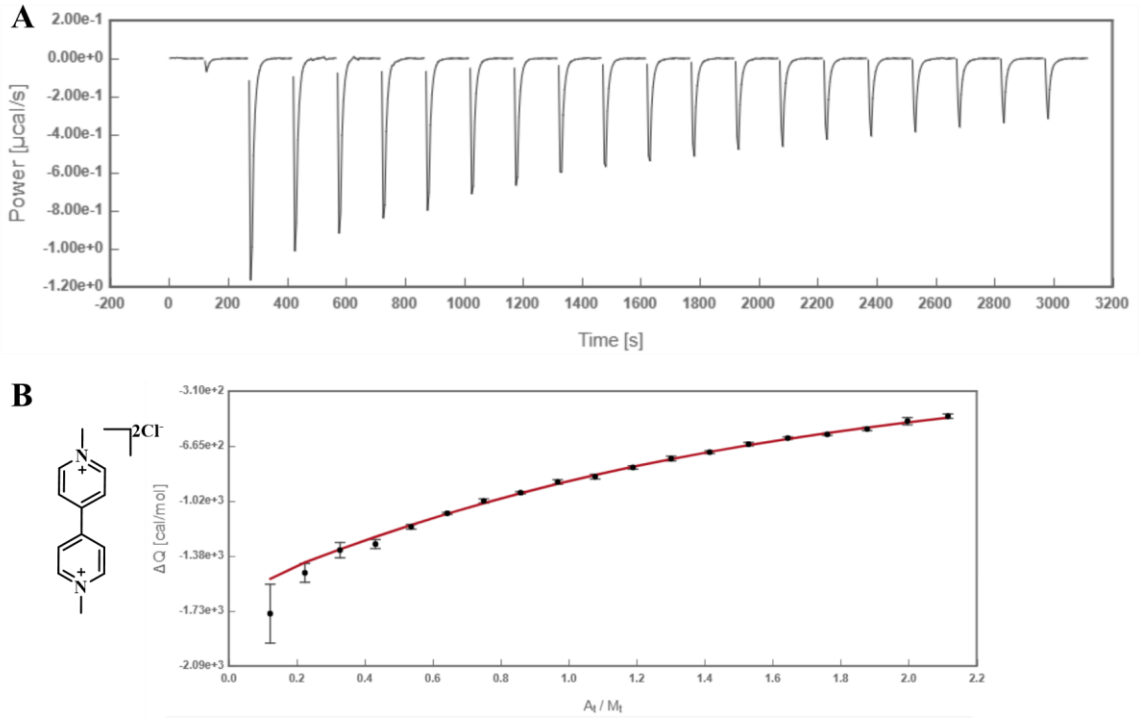

Figure 81. ITC titration with 1,1′-dimethyl-4,4′-bipyridinium dichloride (A) enthalpogram isotherm (B)

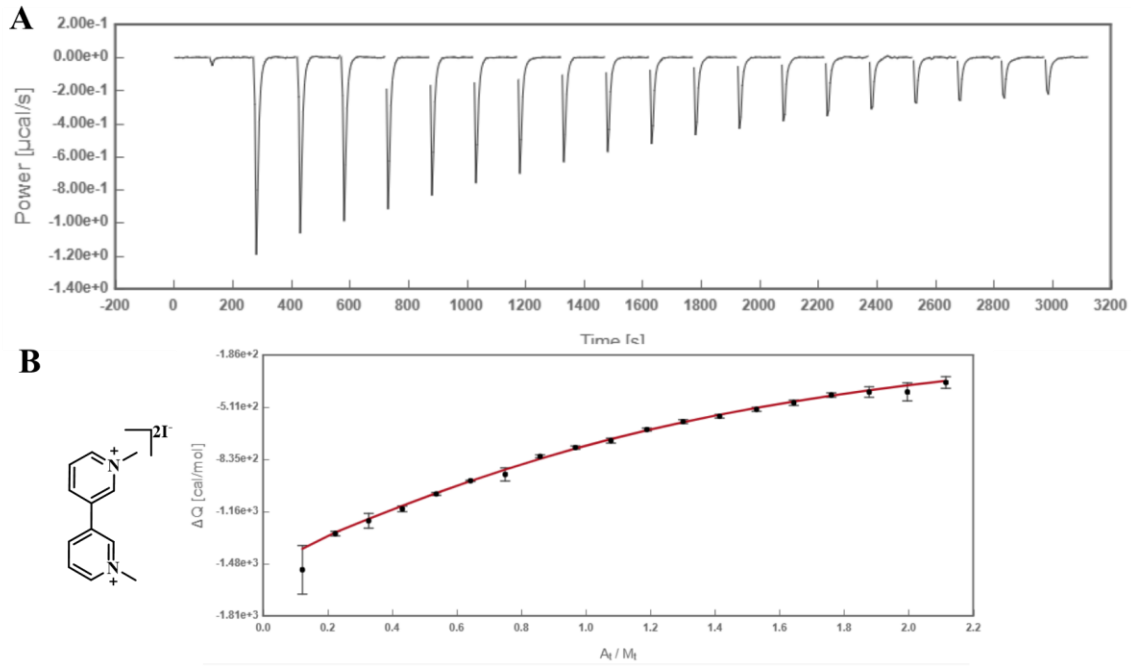

Figure 82. ITC titration with 3,3′-dimethyl-4,4′-bipyridinium diiodide (A) enthalpogram isotherm (B)

5.8. Conclusions

In this study, a bridging ligand with limited rotational freedom and functionalized with pyridine 2,6-dicarboxylate groups was designed and synthesized. An aqueous solution of $EuCl_3(H_2O)_6$ was then titrated into a solution of the ligand in D_2O, and SCC formation was monitored by NMR spectroscopy. At a 3:2 ligand-to-metal ratio, 2 sets of signals corresponding to two conformations of the SCC were observed. Optimized structures obtained by semi-empirical methods suggest the formation of a pair of chiral and achiral M_2L_3 cages. Each proton was further assigned by 2D NOESY and COSY NMR techniques. We assigned protons 3 and 4, as the three protons that face toward the inside of the cavity and used them as a probe to monitor the guest encapsulation during

the NMR titration. Using a 2D DOSY experiment, we measured the diffusion coefficient of both assemblies as 1.80×10^{-10} $m^2 \cdot s$, and the hydrodynamic radius of the incorporated cavity was calculated as 12 Å using the Stoke-Einstein equation.

A series of mono- and di-cationic guests were synthesized, and their encapsulation was monitored by the NMR spectroscopy and ITC. At this point, we cannot draw any precise conclusions as this study is still in its infancy. Further studies with a series of more guests are needed to confirm the impact of the charge and size of the guests on their encapsulation.

Chapter 6: Future Work

6.1. Extending the Absorbance of Mn(I) Based BODIPY photoCORM into the NIR Region

The presented studies in Chapters 2,3, and 4 were focused on designing a series of Mn(I) photoCORMs and studying the electronic and steric impacts of ligand variations around the Mn(I) metal centers on the photophysical, photochemical properties, and formation of photo intermediates. In order to enhance the efficacy of Mn(I) photoCORM, we combined the $Mn(CO)_3$ moiety with the BODIPY ligand to concurrently produce $^1O_2$ while releasing CO under visible light irradiation. Coordination of BODIPY to the Mn(I) center, extended the Mn(I) photoCORM absorption more into the visible region, such that the CO release was activated under low energy 590 nm light irradiation. Despite the improvement in the extending the absorption of Mn(I) photoCORM into the visible region, it is not still within the phototherapeutic window (600-950 nm).

This goal can be achieved by introducing electron withdrawing groups at positions 3 and 5 on the BODIPY core. Previous studies have shown that this is a straightforward strategy to push the BODIPY absorption toward the IR/NIR region.[48,233] Therefore, designing a Mn(I) based BODIPY photoCORM, with suitable substituents at 3 and 5 position, not only would allow to produce $^1O_2$ at longer wavelength but also activate the CO release with IR/NIR light.

6.2. Studying the Interaction of Mn(I) Based BODIPY photoCORM with DNA

The next goal will be studying the DNA photocleavage in the presence of Mn(I) based BODIPY photoCORM under NIR light irradiation. It's been previously shown that

DNA is one of the main targets of singlet oxygen. A convenient way to investigate the impact of produced singlet oxygen from Mn(I) based BODIPY photoCORM on the DNA is using the gel electrophoresis. In this experiment, as the result of photocleavage, the supercoiled DNA (SC) converts to the nicked-circular (NC) form. This conversion will be evident by the slower migration of NC DNA in the gel following photolysis as compared to the SC DNA.

6.3. Studying the Effect of Charge and Size on the Guest Binding

The presented work in Chapter 5 was focused on designing and synthesizing a 3D cage-like structure composed of lanthanide ions (Eu(III)) as the metal nodes and bridging ligands as the organic linkers with general formula of M_2L_3. The internal cavity incorporated in the as-prepared assembly encouraged us to study its host-guest chemistry with smaller organic molecules. To this end, we synthesized a series of mono- and di-cationic guests and monitored their encapsulation within the cavity by ^{1}H NMR.

However, to fully understand the impact of the charge and size on guest binding we need to expand our guest library and conduct a more systematic study of guests of different sizes and charges, including various mono-, di-, and tri-cationic guests. To achieve this goal, the proposed structures in Figure 83 can be used to study the systematic effect of size and charge on guest binding.

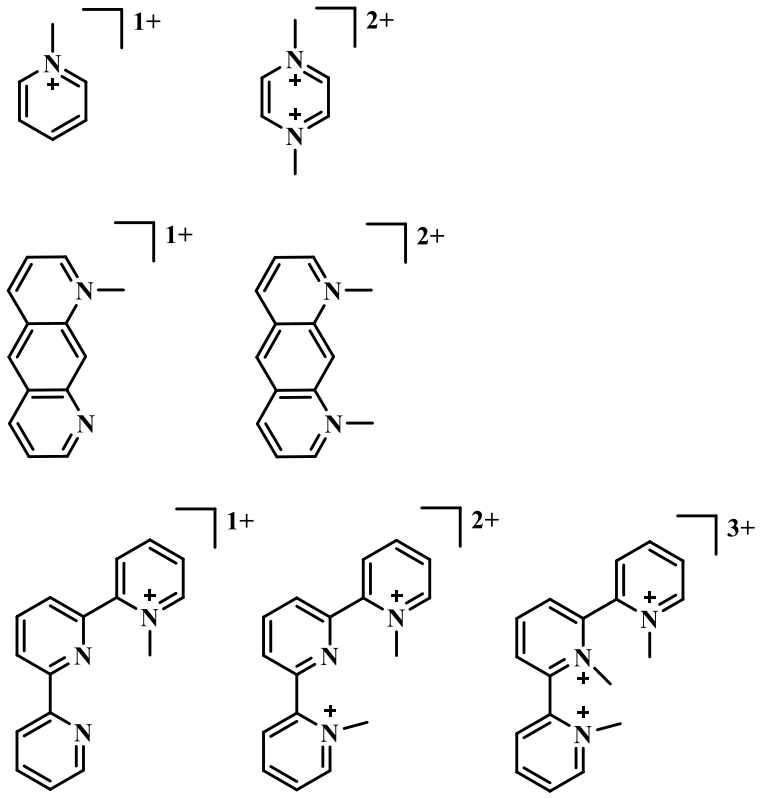

Figure 83. Proposed structures for studying the impact of size and charge on the guest binding

6.4. Measuring the Binding Constants

The second goal will be the quantitative measurement of the binding constants with UV-Vis spectroscopy. Similar to the NMR titration, in the UV-Vis titration, aliquots of each guest solution in H_2O are added to an aqueous solution of the host in the cuvette, and the change in the absorbance is recorded after each addition upon mixing. The binding constants for 1:1 host-guest assemblies are calculated by a nonlinear least-squares fit of the absorbance (A) against the concentration of guest added (C_G) using below equation (5)[234]:

$$A = A_0 + \frac{A_{lim} - A_0}{2[C_0]}\{[C_0] + [C_G] + \frac{1}{K_A} - [([C_0] + [C_G] + \frac{1}{K_A})^2 - 4[C_0][C_G]]^{\frac{1}{2}}\}$$

Where, A is the absorbance of the host at the given wavelength in the presence of the guest, and A_0 is the absorbance of the host in the absence of the guest, A_{lim} is the limiting value of absorbance in the presence of excess guest, C_0 is the concentration of the host, C_G is the concentration of the guest, and K_A is the binding constant.

References

(1) Ryter, S. W.; Ma, K. C.; Choi, A. M. K. Carbon Monoxide in Lung Cell Physiology and Disease. *American Journal of Physiology-Cell Physiology* **2018**, *314* (2), C211–C227. https://doi.org/10.1152/ajpcell.00022.2017

(2) Braubach, M.; Algoet, A.; Beaton, M.; Lauriou, S.; Héroux, M.-E.; Krzyzanowski, M. Mortality Associated with Exposure to Carbon Monoxide in WHO European Member States. *Indoor Air* **2013**, *23* (2), 115–125. https://doi.org/10.1111/ina.12007

(3) Kim, H.-H.; Choi, S. Therapeutic Aspects of Carbon Monoxide in Cardiovascular Disease. *IJMS* **2018**, *19* (8), 2381. https://doi.org/10.3390/ijms19082381

(4) Varon, J.; Marik, P. E.; Fromm Jr, R. E.; Gueler, A. Carbon Monoxide Poisoning: A Review for Clinicians. *The Journal of Emergency Medicine* **1999**, *17* (1), 87–93. https://doi.org/10.1016/S0736-4679(98)00128-0

(5) Tien Vo, T. T.; Vo, Q. C.; Tuan, V. P.; Wee, Y.; Cheng, H.-C.; Lee, I.-T. The Potentials of Carbon Monoxide-Releasing Molecules in Cancer Treatment: An Outlook from ROS Biology and Medicine. *Redox Biology* **2021**, *46*, 102124. https://doi.org/10.1016/j.redox.2021.102124

(6) Motterlini, R.; Otterbein, L. E. The Therapeutic Potential of Carbon Monoxide. *Nat Rev Drug Discov* **2010**, *9* (9), 728–743. https://doi.org/10.1038/nrd3228

(7) Giustarini, D.; Tsikas, D.; Colombo, G.; Milzani, A.; Dalle-Donne, I.; Fanti, P.; Rossi, R. Pitfalls in the Analysis of the Physiological Antioxidant Glutathione (GSH) and Its Disulfide (GSSG) in Biological Samples: An Elephant in the Room. *Journal of Chromatography B* **2016**, *1019*, 21–28. https://doi.org/10.1016/j.jchromb.2016.02.015

(8) Backos, D. S.; Franklin, C. C.; Reigan, P. The Role of Glutathione in Brain Tumor Drug Resistance. *Biochemical Pharmacology* **2012**, *83* (8), 1005–1012. https://doi.org/10.1016/j.bcp.2011.11.016

(9) Zhu, H.; Blake, S.; Chan, K. T.; Pearson, R. B.; Kang, J. Cystathionine β -Synthase in Physiology and Cancer. *BioMed Research International* **2018**, *2018*, 1–11. https://doi.org/10.1155/2018/3205125

(10) Conklin, K. A. Chemotherapy-Associated Oxidative Stress: Impact on Chemotherapeutic Effectiveness. *Integr Cancer Ther* **2004**, *3* (4), 294–300. https://doi.org/10.1177/1534735404270335

(11) Kawahara, B.; Moller, T.; Hu-Moore, K.; Carrington, S.; Faull, K. F.; Sen, S.; Mascharak, P. K. Attenuation of Antioxidant Capacity in Human Breast Cancer Cells by Carbon Monoxide through Inhibition of Cystathionine β-Synthase Activity: Implications in Chemotherapeutic Drug Sensitivity. *J. Med. Chem.* **2017**, *60* (19), 8000–8010. https://doi.org/10.1021/acs.jmedchem.7b00476

(12) Kawahara, B.; Sen, S.; Mascharak, P. K. Reaction of Carbon Monoxide with Cystathionine β-Synthase: Implications on Drug Efficacies in Cancer Chemotherapy. *Future Medicinal Chemistry* **2020**, *12* (4), 325–337. https://doi.org/10.4155/fmc-2019-0266

(13) Kawahara, B.; Ramadoss, S.; Chaudhuri, G.; Janzen, C.; Sen, S.; Mascharak, P. K. Carbon Monoxide Sensitizes Cisplatin-Resistant Ovarian Cancer Cell Lines toward Cisplatin via Attenuation of Levels of Glutathione and Nuclear Metallothionein. *Journal of Inorganic Biochemistry* **2019**, *191*, 29–39. https://doi.org/10.1016/j.jinorgbio.2018.11.003
(14) Heinemann, S. H.; Hoshi, T.; Westerhausen, M.; Schiller, A. Carbon Monoxide – Physiology, Detection and Controlled Release. *Chem. Commun.* **2014**, *50* (28). 3644–3660. https://doi.org/10.1039/C3CC49196J
(15) Motterlini, R.; Clark, J. E.; Foresti, R.; Sarathchandra, P.; Mann, B. E.; Green, C. J. Carbon Monoxide-Releasing Molecules: Characterization of Biochemical and Vascular Activities. *Circulation Research* **2002**, *90* (2). https://doi.org/10.1161/hh0202.104530
(16) Rimmer, R. D.; Pierri, A. E.; Ford, P. C. Photochemically Activated Carbon Monoxide Release for Biological Targets. Toward Developing Air-Stable PhotoCORMs Labilized by Visible Light. *Coordination Chemistry Reviews* **2012**, *256* (15–16), 1509–1519. https://doi.org/10.1016/j.ccr.2011.12.009
(17) Schatzschneider, U. PhotoCORMs: Light-Triggered Release of Carbon Monoxide from the Coordination Sphere of Transition Metal Complexes for Biological Applications. *Inorganica Chimica Acta* **2011**, *374* (1), 19–23. https://doi.org/10.1016/j.ica.2011.02.068
(18) Wright, M. A.; Wright, J. A. PhotoCORMs: CO Release Moves into the Visible. *Dalton Trans.* **2016**, *45* (16), 6801–6811. https://doi.org/10.1039/C5DT04849D
(19) Gasser, G.; Metzler-Nolte, N. The Potential of Organometallic Complexes in Medicinal Chemistry. *Current Opinion in Chemical Biology* **2012**, *16* (1–2), 84–91. https://doi.org/10.1016/j.cbpa.2012.01.013
(20) Rimmer, R. D.; Richter, H.; Ford, P. C. A Photochemical Precursor for Carbon Monoxide Release in Aerated Aqueous Media. *Inorg. Chem.* **2010**, *49* (3), 1180–1185. https://doi.org/10.1021/ic902147n
(21) Kretschmer, R.; Gessner, G.; Görls, H.; Heinemann, S. H.; Westerhausen, M. Dicarbonyl-Bis(Cysteamine)Iron(II): A Light Induced Carbon Monoxide Releasing Molecule Based on Iron (CORM-S1). *Journal of Inorganic Biochemistry* **2011**, *105* (1), 6–9. https://doi.org/10.1016/j.jinorgbio.2010.10.006
(22) Thompson, K. H.; Orvig, C. Metal Complexes in Medicinal Chemistry: New Vistas and Challenges in Drug Design. *Dalton Trans.* **2006**, No. 6, 761–764. https://doi.org/10.1039/B513476E
(23) Thompson, K. H.; Orvig, C. Boon and Bane of Metal Ions in Medicine. *Science* **2003**, *300* (5621), 936–939. https://doi.org/10.1126/science.1083004
(24) Romão, C. C.; Blättler, W. A.; Seixas, J. D.; Bernardes, G. J. L. Developing Drug Molecules for Therapy with Carbon Monoxide. *Chem. Soc. Rev.* **2012**, *41* (9), 3571. https://doi.org/10.1039/c2cs15317c
(25) Wright, M. A. Delivery of CO by Bio-Inspired Metallocentres. 173.

(26) Gonzales, M. A.; Mascharak, P. K. Photoactive Metal Carbonyl Complexes as Potential Agents for Targeted CO Delivery. *Journal of Inorganic Biochemistry* **2014**, *133*, 127–135. https://doi.org/10.1016/j.jinorgbio.2013.10.015
(27) Niesel, J.; Pinto, A.; Peindy N'Dongo, H. W.; Merz, K.; Ott, I.; Gust, R.; Schatzschneider, U. Photoinduced CO Release, Cellular Uptake and Cytotoxicity of a Tris(Pyrazolyl)Methane (Tpm) Manganese Tricarbonyl Complex. *Chem. Commun.* **2008**, No. 15, 1798. https://doi.org/10.1039/b719075a
(28) Schatzschneider, U. Novel Lead Structures and Activation Mechanisms for CO-Releasing Molecules (CORMs): CO-Releasing Molecules (CORMs). *Br J Pharmacol* **2015**, *172* (6), 1638–1650. https://doi.org/10.1111/bph.12688
(29) Guillaumont, D.; Vlček, A.; Daniel, C. Photoreactivity of $Cr(CO)_4$(2,2'-Bipyridine): Quantum Chemistry and Photodissociation Dynamics. *J. Phys. Chem. A* **2001**, *105* (7), 1107–1114. https://doi.org/10.1021/jp994435o
(30) VlcekJr., A. Mechanistic Roles of Metal-to-Ligand Charge-Transfer Excited States in Organometallic Photochemistry. *Coordination Chemistry Reviews* **1998**, *177* (1), 219–256. https://doi.org/10.1016/S0010-8545(98)00187-8
(31) Chakraborty, I.; Carrington, S. J.; Mascharak, P. K. Design Strategies To Improve the Sensitivity of Photoactive Metal Carbonyl Complexes (PhotoCORMs) to Visible Light and Their Potential as CO-Donors to Biological Targets. *Acc. Chem. Res.* **2014**, *47* (8), 2603–2611. https://doi.org/10.1021/ar500172f
(32) Gonzalez, M. A.; Carrington, S. J.; Fry, N. L.; Martinez, J. L.; Mascharak, P. K. Syntheses, Structures, and Properties of New Manganese Carbonyls as Photoactive CO-Releasing Molecules: Design Strategies That Lead to CO Photolability in the Visible Region. *Inorg. Chem.* **2012**, *51* (21), 11930–11940. https://doi.org/10.1021/ic3018216
(33) Krasnovsky, A. A. Singlet oxygen and primary mechanisms of photodynamic therapy and photodynamic diseases. *Photodynamic therapy at the cellular level* 2007, 17-62.
(34) Plaetzer, K.; Krammer, B.; Berlanda, J.; Berr, F.; Kiesslich, T. Photophysics and Photochemistry of Photodynamic Therapy: Fundamental Aspects. *Lasers Med Sci* **2009**, *24* (2), 259–268. https://doi.org/10.1007/s10103-008-0539-1
(35) DeRosa, M. Photosensitized Singlet Oxygen and Its Applications. *Coordination Chemistry Reviews* **2002**, *233–234*, 351–371. https://doi.org/10.1016/S0010-8545(02)00034-6
(36) Garcia-Diaz, M.; Huang, Y.-Y.; Hamblin, M. R. Use of Fluorescent Probes for ROS to Tease Apart Type I and Type II Photochemical Pathways in Photodynamic Therapy. *Methods* **2016**, *109*, 158–166. https://doi.org/10.1016/j.ymeth.2016.06.025
(37) Benov, L. Photodynamic Therapy: Current Status and Future Directions. *Med Princ Pract* **2015**, *24* (s1), 14–28. https://doi.org/10.1159/000362416
(38) Ogilby, P. R. Singlet Oxygen: There Is Indeed Something New under the Sun. *Chem. Soc. Rev.* **2010**, *39* (8), 3181. https://doi.org/10.1039/b926014p

(39) Li, B.; Lin, H.; Chen, D.; Wilson, B. C.; Gu, Y. SINGLET OXYGEN DETECTION DURING PHOTOSENSITIZATION. *J. Innov. Opt. Health Sci.* **2013**, *06* (01), 1330002. https://doi.org/10.1142/S1793545813300024
(40) Pibiri, I.; Buscemi, S.; Palumbo Piccionello, A.; Pace, A. Photochemically Produced Singlet Oxygen: Applications and Perspectives. *ChemPhotoChem* **2018**, *2* (7), 535–547. https://doi.org/10.1002/cptc.201800076
(41) Wu, H.; Song, Q.; Ran, G.; Lu, X.; Xu, B. Recent Developments in the Detection of Singlet Oxygen with Molecular Spectroscopic Methods. *TrAC Trends in Analytical Chemistry* **2011**, *30* (1), 133–141. https://doi.org/10.1016/j.trac.2010.08.009
(42) Liu, H.; Carter, P. J. H.; Laan, A. C.; Eelkema, R.; Denkova, A. G. Singlet Oxygen Sensor Green Is Not a Suitable Probe for $^1O_2$ in the Presence of Ionizing Radiation. *Sci Rep* **2019**, *9* (1), 8393. https://doi.org/10.1038/s41598-019-44880-2
(43) Ormond, A.; Freeman, H. Dye Sensitizers for Photodynamic Therapy. *Materials* **2013**, *6* (3), 817–840. https://doi.org/10.3390/ma6030817.
(44) Kwiatkowski, S.; Knap, B.; Przystupski, D.; Saczko, J.; Kędzierska, E.; Knap-Czop, K.; Kotlińska, J.; Michel, O.; Kotowski, K.; Kulbacka, J. Photodynamic Therapy – Mechanisms, Photosensitizers and Combinations. *Biomedicine and Pharmacotherapy* **2018**, *106*, 1098–1107. https://doi.org/10.1016/j.biopha.2018.07.049
(45) Garland, M. J.; Cassidy, C. M.; Woolfson, D.; Donnelly, R. F. Designing Photosensitizers for Photodynamic Therapy: Strategies, Challenges and Promising Developments. *Future Medicinal Chemistry* **2009**, *1* (4), 667–691. https://doi.org/10.4155/fmc.09.55
(46) Kamkaew, A.; Lim, S. H.; Lee, H. B.; Kiew, L. V.; Chung, L. Y.; Burgess, K. BODIPY Dyes in Photodynamic Therapy. *Chem. Soc. Rev.* **2013**, *42* (1), 77–88. https://doi.org/10.1039/C2CS35216H
(47) Bassan, E.; Gualandi, A.; Cozzi, P. G.; Ceroni, P. Design of BODIPY Dyes as Triplet Photosensitizers: Electronic Properties Tailored for Solar Energy Conversion, Photoredox Catalysis and Photodynamic Therapy. *Chem. Sci.* **2021**, *12* (19), 6607–6628. https://doi.org/10.1039/D1SC00732G
(48) Boens, N.; Verbelen, B.; Dehaen, W. Postfunctionalization of the BODIPY Core: Synthesis and Spectroscopy: Postfunctionalization of the BODIPY Core. *Eur. J. Org. Chem.* **2015**, *2015* (30), 6577–6595. https://doi.org/10.1002/ejoc.201500682
(49) Liu, M.; Ma, S.; She, M.; Chen, J.; Wang, Z.; Liu, P.; Zhang, S.; Li, J. Structural Modification of BODIPY: Improve Its Applicability. *Chinese Chemical Letters* **2019**, *30* (10), 1815–1824. https://doi.org/10.1016/j.cclet.2019.08.028
(50) Awuah, S. G.; You, Y. Boron Dipyrromethene (BODIPY)-Based Photosensitizers for Photodynamic Therapy. *RSC Adv.* **2012**, *2* (30), 11169. https://doi.org/10.1039/c2ra21404k
(51) Fu, R.; Sun, Y.; Sheng, W.; Liao, D. Designing Multi-Targeted Agents: An Emerging Anticancer Drug Discovery Paradigm. *European Journal of Medicinal Chemistry* **2017**, *136*, 195–211. https://doi.org/10.1016/j.ejmech.2017.05.016

(52) Zheng, W.; Zhao, Y.; Luo, Q.; Zhang, Y.; Wu, K.; Wang, F. Rational Design of Multi-Targeting Ruthenium- and Platinum-Based Anticancer Complexes. *Sci. China Chem.* **2016**, *59* (10), 1240–1249. https://doi.org/10.1007/s11426-016-0178-7

(53) Mokhtari, R. B.; Homayouni, T. S.; Baluch, N.; Morgatskaya, E.; Kumar, S.; Das, B.; Yeger, H. Combination Therapy in Combating Cancer. *Oncotarget* **2017**, *8* (23), 38022–38043. https://doi.org/10.18632/oncotarget.16723

(54) Wang, J.; Zigler, D. F.; Hurst, N.; Othee, H.; Winkel, B. S. J.; Brewer, K. J. A New, Bioactive Structural Motif: Visible Light Induced DNA Photobinding and Oxygen Independent Photocleavage by RuII, RhIII Bimetallics. *Journal of Inorganic Biochemistry* **2012**, *116*, 135–139. https://doi.org/10.1016/j.jinorgbio.2012.06.015

(55) Kenny, R. G.; Marmion, C. J. Toward Multi-Targeted Platinum and Ruthenium Drugs—A New Paradigm in Cancer Drug Treatment Regimens? *Chem. Rev.* **2019**, *119* (2), 1058–1137. https://doi.org/10.1021/acs.chemrev.8b00271

(56) Biersack, B.; Zoldakova, M.; Effenberger, K.; Schobert, R. (Arene)Ru(II) Complexes of Epidermal Growth Factor Receptor Inhibiting Tyrphostins with Enhanced Selectivity and Cytotoxicity in Cancer Cells. *European Journal of Medicinal Chemistry* **2010**, *45* (5), 1972–1975. https://doi.org/10.1016/j.ejmech.2010.01.040

(57) Pordel, S.; White, J. K. Impact of Mn(I) PhotoCORM Ligand Set on Photochemical Intermediate Formation during Visible Light-Activated CO Release. *Inorganica Chimica Acta* **2020**, *500*, 119206. https://doi.org/10.1016/j.ica.2019.119206

(58) Wegiel, B.; Hanto, D. W.; Otterbein, L. E. The Social Network of Carbon Monoxide in Medicine. *Trends in Molecular Medicine* **2013**, *19* (1), 3–11. https://doi.org/10.1016/j.molmed.2012.10.001

(59) Wegiel, B.; Gallo, D.; Csizmadia, E.; Harris, C.; Belcher, J.; Vercellotti, G. M.; Penacho, N.; Seth, P.; Sukhatme, V.; Ahmed, A.; Pandolfi, P. P.; Helczynski, L.; Bjartell, A.; Persson, J. L.; Otterbein, L. E. Carbon Monoxide Expedites Metabolic Exhaustion to Inhibit Tumor Growth. *Cancer Research* **2013**, *73* (23), 7009–7021. https://doi.org/10.1158/0008-5472.CAN-13-1075

(60) Ryter, S. W., Alam, J., Choi, A. M Heme Oxygenase-1/Carbon Monoxide: From Basic Science to Therapeutic Applications | *Physiological Reviews* **2006**. *86*(2), 583-650. https://journals.physiology.org/doi/full/10.1152/physrev.00011.2005

(61) Christin Kautz, A.; C. Kunz, P.; Janiak, C. CO-Releasing Molecule (CORM) Conjugate Systems. *Dalton Transactions* **2016**, *45* (45), 18045–18063. https://doi.org/10.1039/C6DT03515A

(62) Jackson, C. S.; Schmitt, S.; Dou, Q. P.; Kodanko, J. J. Synthesis, Characterization, and Reactivity of the Stable Iron Carbonyl Complex $[Fe(CO)(N_4Py)](ClO_4)_2$: Photoactivated Carbon Monoxide Release, Growth Inhibitory Activity, and Peptide Ligation. *Inorg. Chem.* **2011**, *50* (12), 5336–5338. https://doi.org/10.1021/ic200676s

(63) Schwenzer, G.; Darensbourg, M. Y.; Darensbourg, D. J. Photochemical substitution reactions of substituted Group VI metal carbonyls. *Inorganic Chemistry* **1972**, 11(8), 1967-1970. https://pubs.acs.org/doi/pdf/10.1021/ic50114a055
(64) Vlček, A. Highlights of the Spectroscopy, Photochemistry and Electrochemistry of [$M(CO)_4$(α-Diimine)] Complexes, M=Cr, Mo, W. *Coordination Chemistry Reviews* **2002**, *230* (1), 225–242. https://doi.org/10.1016/S0010-8545(02)00047-4
(65) Wieland, S.; Reddy, K. B.; Eldik, R. V. Ligand-field and charge-transfer photochemistry of M(CO)4(1,10-phenanthroline) (M = chromium, molybdenum, tungsten). Mechanistic information from high-pressure effects. *Organometallics* **1990**, 9(6), 1802-1806. https://pubs.acs.org/doi/pdf/10.1021/om00156a019
(66) Balk, R. W.; Snoeck, T.; Stufkens, D. J.; Oskam, A. (Diimine)carbonyl complexes of chromium, molybdenum, and tungsten: relationship between resonance Raman spectra and photosubstitution quantum yields upon excitation within the lowest metal to diimine charge-transfer band. *Inorganic Chemistry* **1980**, 19(10), 3015-3021. https://pubs.acs.org/doi/pdf/10.1021/ic50212a035
(67) Wrighton, M. S.; Morse, D. L. The Nature of the Lowest Excited State and Photosubstitution Reactivity of Tetracarbonyl-1,10-Phenanthrolinetungsten(0) and Related Complexes. *Journal of Organometallic Chemistry* **1975**, *97* (3), 405–419. https://doi.org/10.1016/S0022-328X(00)89307-9
(68) Gonzalez, M. A.; Carrington, S. J.; Chakraborty, I.; Olmstead, M. M.; Mascharak, P. K. Photoactivity of Mono- and Dicarbonyl Complexes of Ruthenium(II) Bearing an N,N,S-Donor Ligand: Role of Ancillary Ligands on the Capacity of CO Photorelease. *Inorg. Chem.* **2013**, *52* (19), 11320–11331. https://doi.org/10.1021/ic4016004
(69) Carrington, S. J.; Chakraborty, I.; Alvarado, J. R.; Mascharak, P. K. Differences in the CO Photolability of Cis- and Trans-[$RuCl_2$(Azpy)$(CO)_2$] Complexes: Effect of Metal-to-Ligand Back-Bonding. *Inorganica Chimica Acta* **2013**, *407*, 121–125. https://doi.org/10.1016/j.ica.2013.07.047
(70) Carrington, S. J.; Chakraborty, I.; Bernard, J. M. L.; Mascharak, P. K. Synthesis and Characterization of a "Turn-On" PhotoCORM for Trackable CO Delivery to Biological Targets. *ACS Med. Chem. Lett.* **2014**, *5* (12), 1324–1328. https://doi.org/10.1021/ml500399r
(71) Carrington, S. J.; Chakraborty, I.; Bernard, J. M. L.; Mascharak, P. K. A Theranostic Two-Tone Luminescent PhotoCORM Derived from Re(I) and (2-Pyridyl)-Benzothiazole: Trackable CO Delivery to Malignant Cells. *Inorg. Chem.* **2016**, *55* (16), 7852–7858. https://doi.org/10.1021/acs.inorgchem.6b00511
(72) Carrington, S. J.; Chakraborty, I.; Mascharak, P. K. Rapid CO Release from a Mn(I) Carbonyl Complex Derived from Azopyridine upon Exposure to Visible Light and Its Phototoxicity toward Malignant Cells. *Chem. Commun.* **2013**, *49* (96), 11254–11256. https://doi.org/10.1039/C3CC46558F
(73) Carrington, S. J.; Chakraborty, I.; Mascharak, P. K. Exceptionally Rapid CO Release from a Manganese(I) Tricarbonyl Complex Derived from Bis(4-Chloro-

Phenylimino)Acenaphthene upon Exposure to Visible Light. *Dalton Trans.* **2015**, *44* (31), 13828–13834. https://doi.org/10.1039/C5DT01007A
(74) Chakraborty, I.; Carrington, S. J.; Mascharak, P. K. Photodelivery of CO by Designed PhotoCORMs: Correlation between Absorption in the Visible Region and Metal–CO Bond Labilization in Carbonyl Complexes. *ChemMedChem* **2014**, *9* (6), 1266–1274. https://doi.org/10.1002/cmdc.201402007
(75) Chakraborty, I.; Carrington, S. J.; Roseman, G.; Mascharak, P. K. Synthesis, Structures, and CO Release Capacity of a Family of Water-Soluble PhotoCORMs: Assessment of the Biocompatibility and Their Phototoxicity toward Human Breast Cancer Cells. *Inorg. Chem.* **2017**, *56* (3), 1534–1545. https://doi.org/10.1021/acs.inorgchem.6b02623
(76) Chakraborty, I.; Jimenez, J.; Sameera, W. M. C.; Kato, M.; Mascharak, P. K. Luminescent Re(I) Carbonyl Complexes as Trackable PhotoCORMs for CO Delivery to Cellular Targets. *Inorg. Chem.* **2017**, *56* (5), 2863–2873. https://doi.org/10.1021/acs.inorgchem.6b02999
(77) Compain, J.-D.; Bourrez, M.; Haukka, M.; Deronzier, A.; Chardon-Noblat, S. Manganese Carbonyl Terpyridyl Complexes: Their Synthesis, Characterization and Potential Application as CO-Release Molecules. *Chem. Commun.* **2014**, *50* (19), 2539–2542. https://doi.org/10.1039/C4CC00197D
(78) Compain, J.-D.; Stanbury, M.; Trejo, M.; Chardon-Noblat, S. Carbonyl-Terpyridyl-Manganese Complexes: Syntheses, Crystal Structures, and Photo-Activated Carbon Monoxide Release Properties. *European Journal of Inorganic Chemistry* **2015**, *2015* (35), 5757–5766. https://doi.org/10.1002/ejic.201500973
(79) Jimenez, J.; Chakraborty, I.; Mascharak, P. K. Synthesis and Assessment of CO-Release Capacity of Manganese Carbonyl Complexes Derived from Rigid α-Diimine -Ligands of Varied Complexity. *European Journal of Inorganic Chemistry* **2015**, *2015* (30), 5021–5026. https://doi.org/10.1002/ejic.201500816
(80) Jimenez, J.; Pinto, M. N.; Martinez-Gonzalez, J.; Mascharak, P. K. Photo-Induced Eradication of Human Colorectal Adenocarcinoma HT-29 Cells by Carbon Monoxide (CO) Delivery from a Mn-Based Green Luminescent PhotoCORM. *Inorganica Chimica Acta* **2019**, *485*, 112–117. https://doi.org/10.1016/j.ica.2018.09.088
(81) Kleverlaan, C. J.; Hartl, F.; Stufkens, D. J. Mechanistic Aspects of the Thermal Mer-to-Fac Isomerization of Mer-[Mn(X)(CO)$_3$(α-Diimine)] (X=Cl, Br, I). *Journal of Organometallic Chemistry* **1998**, *561* (1), 57–65. https://doi.org/10.1016/S0022-328X(98)00489-6
(82) Koike, K.; Okoshi, N.; Hori, H.; Takeuchi, K.; Ishitani, O.; Tsubaki, H.; Clark, I. P.; George, M. W.; Johnson, F. P. A.; Turner, J. J. Mechanism of the Photochemical Ligand Substitution Reactions of Fac-[Re(Bpy)(CO)3(PR3)]+ Complexes and the Properties of Their Triplet Ligand-Field Excited States. *J. Am. Chem. Soc.* **2002**, *124* (38), 11448–11455. https://doi.org/10.1021/ja017032m
(83) Marker, S. C.; MacMillan, S. N.; Zipfel, W. R.; Li, Z.; Ford, P. C.; Wilson, J. J. Photoactivated in Vitro Anticancer Activity of Rhenium(I) Tricarbonyl Complexes

Bearing Water-Soluble Phosphines. *Inorg. Chem.* **2018**, *57* (3), 1311–1331. https://doi.org/10.1021/acs.inorgchem.7b02747

(84) Mede, R.; Hoffmann, P.; Neumann, C.; Görls, H.; Schmitt, M.; Popp, J.; Neugebauer, U.; Westerhausen, M. Acetoxymethyl Concept for Intracellular Administration of Carbon Monoxide with $Mn(CO)_3$-Based PhotoCORMs. *Chemistry – A European Journal* **2018**, *24* (13), 3321–3329. https://doi.org/10.1002/chem.201705686

(85) Nagel, C.; McLean, S.; Poole, R. K.; Braunschweig, H.; Kramer, T.; Schatzschneider, U. Introducing $[Mn(CO)_3(Tpa\text{-}K_3N)]^+$ as a Novel Photoactivatable CO-Releasing Molecule with Well-Defined ICORM Intermediates – Synthesis, Spectroscopy, and Antibacterial Activity. *Dalton Trans.* **2014**, *43* (26), 9986–9997. https://doi.org/10.1039/C3DT51848E

(86) Pickens, R. N.; Neyhouse, B. J.; Reed, D. T.; Ashton, S. T.; White, J. K. Visible Light-Activated CO Release and 1O2 Photosensitizer Formation with Ru(II),Mn(I) Complexes. *Inorg. Chem.* **2018**, *57* (18), 11616–11625. https://doi.org/10.1021/acs.inorgchem.8b01759

(87) Sachs, U.; Schaper, G.; Winkler, D.; Kratzert, D.; Kurz, P. Light- or Oxidation-Triggered CO Release from $[Mn(I)(CO)_3(\kappa_3\text{-}L)]$ Complexes: Reaction Intermediates and a New Synthetic Route to [Mn III/IV2 (μ-O) 2 (L) 2] Compounds. *Dalton Transactions* **2016**, *45* (43), 17464–17473. https://doi.org/10.1039/C6DT02020H

(88) Simpson, P. V.; Nagel, C.; Bruhn, H.; Schatzschneider, U. Antibacterial and Antiparasitic Activity of Manganese(I) Tricarbonyl Complexes with Ketoconazole, Miconazole, and Clotrimazole Ligands. *Organometallics* **2015**, *34* (15), 3809–3815. https://doi.org/10.1021/acs.organomet.5b00458

(89) Üstün, E.; Çol Ayvaz, M.; Sönmez Çelebi, M.; Aşcı, G.; Demir, S.; Özdemir, İ. Structure, CO-Releasing Property, Electrochemistry, DFT Calculation, and Antioxidant Activity of Benzimidazole Derivative Substituted $[Mn(CO)_3(Bpy)L]PF_6$ Type Novel Manganese Complexes. *Inorganica Chimica Acta* **2016**, *450*, 182–189. https://doi.org/10.1016/j.ica.2016.05.027

(90) Baerends, E. Metal–CO Photodissociation in Transition Metal Complexes: The Role of Ligand-Field and Charge-Transfer Excited States in the Photochemical Dissociation of Metal–Ligand Bonds. *Coordination Chemistry Reviews* **1998**, *177* (1), 97–125. https://doi.org/10.1016/S0010-8545(98)00128-3

(91) Higgins, S. L. H.; Brewer, K. J. Designing Red-Light-Activated Multifunctional Agents for the Photodynamic Therapy. *Angewandte Chemie International Edition* **2012**, *51* (46), 11420–11422. https://doi.org/10.1002/anie.201204933

(92) Jimenez, J.; Chakraborty, I.; Dominguez, A.; Martinez-Gonzalez, J.; Sameera, W. M. C.; Mascharak, P. K. A Luminescent Manganese PhotoCORM for CO Delivery to Cellular Targets under the Control of Visible Light. *Inorg. Chem.* **2018**, *57* (4), 1766–1773. https://doi.org/10.1021/acs.inorgchem.7b02480

(93) Yempally, V.; Moncho, S.; Hasanayn, F.; Fan, W. Y.; Brothers, E. N.; Bengali, A. A. Ancillary Ligand Effects upon the Photochemistry of $Mn(bpy)(CO)_3X$

Complexes (X = Br–, PhCC–). *Inorg. Chem.* **2017**, *56* (18), 11244–11253. https://doi.org/10.1021/acs.inorgchem.7b01543
(94) Bourrez, M.; Molton, F.; Chardon-Noblat, S.; Deronzier, A. [Mn(bipyridyl)$(CO)_3$Br]: An Abundant Metal Carbonyl Complex as Efficient Electrocatalyst for CO2 Reduction. *Angewandte Chemie International Edition* **2011**, *50* (42), 9903–9906. https://doi.org/10.1002/anie.201103616
(95) Twala, T. N.; Schutte-Smith, M.; Roodt, A.; Visser, H. G. Activation of the Manganese(I) Tricarbonyl Core by Selective Variation of Bidentate Ligands (L,L′-Bid = N,N′ and N,O Donor Atom Sets) in Fac-[Mn$(CO)_3$(L,L′-Bid)(CH_3OH)]n Complexes. *Dalton Trans.* **2015**, *44* (7), 3278–3288. https://doi.org/10.1039/C4DT03524K
(96) Connelly, N. G.; Geiger, W. E. Chemical Redox Agents for Organometallic Chemistry. *Chem. Rev.* **1996**, *96* (2), 877–910. https://doi.org/10.1021/cr940053x
(97) Montalti, M.; Credi, A.; Prodi, L.; Gandolfi, M. T. *Handbook of Photochemistry*, 3rd ed.; CRC Press: Boca Raton, 2006. https://doi.org/10.1201/9781420015195
(98) Zhao, Y.; Truhlar, D. G. The M06 Suite of Density Functionals for Main Group Thermochemistry, Thermochemical Kinetics, Noncovalent Interactions, Excited States, and Transition Elements: Two New Functionals and Systematic Testing of Four M06-Class Functionals and 12 Other Functionals. *Theor Chem Account* **2008**, *120* (1), 215–241. https://doi.org/10.1007/s00214-007-0310-x
(99) Zhao, Y.; Truhlar, D. G. Density Functionals with Broad Applicability in Chemistry. *Acc. Chem. Res.* **2008**, *41* (2), 157–167. https://doi.org/10.1021/ar700111a
(100) Marenich, A. V.; Cramer, C. J.; Truhlar, D. G. Universal Solvation Model Based on Solute Electron Density and on a Continuum Model of the Solvent Defined by the Bulk Dielectric Constant and Atomic Surface Tensions. *J. Phys. Chem. B* **2009**, *113* (18), 6378–6396. https://doi.org/10.1021/jp810292n
(101) Wiberg, K. B. Ab Initio Molecular Orbital Theory by W. J. Hehre, L. Radom, P. v. R. Schleyer, and J. A. Pople, John Wiley, New York, 548pp. Price: $79.95 (1986). *Journal of Computational Chemistry* **1986**, *7* (3), 379–379. https://doi.org/10.1002/jcc.540070314
(102) Hoover, W. G. Theoretical Chemistry: Statistical Mechanics. Bruce J. Berne, Ed. In Two Parts. Part A, Equilibrium Techniques. Xvi, 242 Pp., Illus. $39.50. Part B, Time-Dependent Processes. Xvi, 262 Pp., Illus. $39.50. Plenum, New York, 1977. Modern Theoretical Chemistry, Vols. 5 and 6. *Science* **1978**. https://doi.org/10.1126/science.199.4336.1430
(103) Hanwell, M. D.; Curtis, D. E.; Lonie, D. C.; Vandermeersch, T.; Zurek, E.; Hutchison, G. R. Avogadro: An Advanced Semantic Chemical Editor, Visualization, and Analysis Platform. *Journal of Cheminformatics* **2012**, *4* (1), 17. https://doi.org/10.1186/1758-2946-4-17
(104) Pordel, S.; Schrage, B. R.; Ziegler, C. J.; White, J. K. Impact of Steric Bulk on Photoinduced Ligand Exchange Reactions in Mn(I) PhotoCORMs. *Inorganica Chimica Acta* **2020**, *511*, 119845. https://doi.org/10.1016/j.ica.2020.119845

(105) Boczkowski, J.; Poderoso, J. J.; Motterlini, R. CO–Metal Interaction: Vital Signaling from a Lethal Gas. *Trends in Biochemical Sciences* **2006**, *31* (11), 614–621. https://doi.org/10.1016/j.tibs.2006.09.001
(106) Song, R.; Zhou, Z.; Kim, P. K. M.; Shapiro, R. A.; Liu, F.; Ferran, C.; Choi, A. M. K.; Otterbein, L. E. Carbon Monoxide Promotes Fas/CD95-Induced Apoptosis in Jurkat Cells *. *Journal of Biological Chemistry* **2004**, *279* (43), 44327–44334. https://doi.org/10.1074/jbc.M406105200
(107) Prockop, L. D.; Chichkova, R. I. Carbon Monoxide Intoxication: An Updated Review. *Journal of the Neurological Sciences* **2007**, *262* (1), 122–130. https://doi.org/10.1016/j.jns.2007.06.037
(108) Motterlini, R.; Mann, B. E.; Foresti, R. Therapeutic Applications of Carbon Monoxide-Releasing Molecules. *Expert Opinion on Investigational Drugs* **2005**, *14* (11), 1305–1318. https://doi.org/10.1517/13543784.14.11.1305
(109) García-Gallego, S.; Bernardes, G. J. L. Carbon-Monoxide-Releasing Molecules for the Delivery of Therapeutic CO In Vivo. *Angewandte Chemie International Edition* **2014**, *53* (37), 9712–9721. https://doi.org/10.1002/anie.201311225
(110) Ford, P. C. Metal Complex Strategies for Photo-Uncaging the Small Molecule Bioregulators Nitric Oxide and Carbon Monoxide. *Coordination Chemistry Reviews* **2018**, *376*, 548–564. https://doi.org/10.1016/j.ccr.2018.07.018
(111) Pierri, A. E.; Muizzi, D. A.; Ostrowski, A. D.; Ford, P. C. Photo-Controlled Release of NO and CO with Inorganic and Organometallic Complexes. In *Luminescent and Photoactive Transition Metal Complexes as Biomolecular Probes and Cellular Reagents*; Lo, K. K.-W., Ed.; Structure and Bonding; Springer: Berlin, Heidelberg, 2015; pp 1–45. https://doi.org/10.1007/430_2014_164
(112) Pinto, M. N.; Mascharak, P. K. Light-Assisted and Remote Delivery of Carbon Monoxide to Malignant Cells and Tissues: Photochemotherapy in the Spotlight. *Journal of Photochemistry and Photobiology C: Photochemistry Reviews* **2020**, *42*, 100341. https://doi.org/10.1016/j.jphotochemrev.2020.100341
(113) Carlos, R. M.; Carlos, I. Ap.; Neto, B. S. L.; Neumann, M. G. Spectroscopic and Electrochemical Properties of [Mn(Phen)$(CO)_3$(Imidazole)](SO_3CF_3) Complexes. *Inorganica Chimica Acta* **2000**, *299* (2), 231–237. https://doi.org/10.1016/S0020-1693(99)00505-8
(114) Hartl, F.; Mahabiersing, T.; Le Floch, P.; Mathey, F.; Ricard, L.; Rosa, P.; Záliš, S. Electronic Properties of 4,4‘,5,5‘-Tetramethyl-2,2‘-Biphosphinine (Tmbp) in the Redox Series Fac-[Mn(Br)$(CO)_3$(Tmbp)], [Mn$(CO)_3$(Tmbp)]$_2$, and [Mn$(CO)_3$(Tmbp)]-: Crystallographic, Spectroelectrochemical, and DFT Computational Study. *Inorg. Chem.* **2003**, *42* (14), 4442–4455. https://doi.org/10.1021/ic0206894
(115) Rao, J. M.; Hughes, M. C.; Macero, D. J. Further Studies on the Stabilization of High and Low Oxidation States in Aromatic Imine Ligand Complexes of First Row Transition Metals. I. Substituted Bipyridine Complexes of Cobalt and Iron. *Inorganica Chimica Acta* **1979**, *35*, L369–L373. https://doi.org/10.1016/S0020-1693(00)93402-9

(116) M. Frisch, G. Trucks, H. Schlegel, G. Scuseria, M. Robb, J. Cheeseman, G. Scalmani, V. Barone, G. Petersson, H. Nakatsuji Gaussian, 16 (2016)
(117) T.H. Dunning, P.J. Hay Methods of Electronic Structure Theory Modern Theoretical Chemistry, Plenum Press, New York (1977
(118) Knoll, J. D.; Albani, B. A.; Durr, C. B.; Turro, C. Unusually Efficient Pyridine Photodissociation from Ru(II) Complexes with Sterically Bulky Bidentate Ancillary Ligands. *J. Phys. Chem. A* **2014**, *118* (45), 10603–10610. https://doi.org/10.1021/jp5057732
(119) Bonnet, S.; Collin, J.-P.; Sauvage, J.-P.; Schofield, E. Photochemical Expulsion of the Neutral Monodentate Ligand L in Ru(Terpy*)(Diimine)(L)$^{2+}$: A Dramatic Effect of the Steric Properties of the Spectator Diimine Ligand. *Inorg. Chem.* **2004**, *43* (26), 8346–8354. https://doi.org/10.1021/ic0491736
(120) Wachter, E.; Heidary, D. K.; Howerton, B. S.; Parkin, S.; Glazer, E. C. Light-Activated Ruthenium Complexes Photobind DNA and Are Cytotoxic in the Photodynamic Therapy Window. *Chem. Commun.* **2012**, *48* (77), 9649–9651. https://doi.org/10.1039/C2CC33359G
(121) Wachter, E.; Howerton, B. S.; Hall, E. C.; Parkin, S.; Glazer, E. C. A New Type of DNA "Light-Switch": A Dual Photochemical Sensor and Metalating Agent for Duplex and G-Quadruplex DNA. *Chem. Commun.* **2013**, *50* (3), 311–313. https://doi.org/10.1039/C3CC47269H
(122) Thorp-Greenwood, F. L.; Platts, J. A.; Coogan, M. P. Experimental and Theoretical Characterisation of Phosphorescence from Rhenium Polypyridyl Tricarbonyl Complexes. *Polyhedron* **2014**, *67*, 505–512. https://doi.org/10.1016/j.poly.2013.09.033
(123) Baxter, P. N. W.; Connor, J. A. Solvatochromism in Substituted 2,2′-Bipyridinetetracarbonyl-Metal Complexes of Chromium, Molybdenum and Tungsten. *Journal of Organometallic Chemistry* **1995**, *486* (1), 115–121. https://doi.org/10.1016/0022-328X(94)05058-J
(124) Yoshikawa, N.; Kimura, H.; Yamabe, S.; Kanehisa, N.; Inoue, T.; Takashima, H. Emission Property and DFT Calculation for the ^{3}MLCT Luminescence of Ru(Bpy)$_2$(L)$^{2+}$ Complex. *Journal of Molecular Structure* **2016**, *1117*, 49–56. https://doi.org/10.1016/j.molstruc.2016.03.069
(125) Pordel, S.; Pickens, R. N.; White, J. K. Release of CO and Production of $^1O_2$ from a Mn-BODIPY Photoactivated CO Releasing Molecule with Visible Light. *Organometallics* **2021**, *40* (17), 2983–2994. https://doi.org/10.1021/acs.organomet.1c00331
(126) Cui, Q.; Wang, J.-Q.; Assaraf, Y. G.; Ren, L.; Gupta, P.; Wei, L.; Ashby, C. R.; Yang, D.-H.; Chen, Z.-S. Modulating ROS to Overcome Multidrug Resistance in Cancer. *Drug Resistance Updates* **2018**, *41*, 1–25. https://doi.org/10.1016/j.drup.2018.11.001
(127) Adeel, M.; Duzagac, F.; Canzonieri, V.; Rizzolio, F. Self-Therapeutic Nanomaterials for Cancer Therapy: A Review. *ACS Appl. Nano Mater.* **2020**, *3* (6), 4962–4971. https://doi.org/10.1021/acsanm.0c00762

(128) Dharmaraja, A. T. Role of Reactive Oxygen Species (ROS) in Therapeutics and Drug Resistance in Cancer and Bacteria. *J. Med. Chem.* **2017**, *60* (8), 3221–3240. https://doi.org/10.1021/acs.jmedchem.6b01243
(129) Banerjee, R.; Zou, C. Redox Regulation and Reaction Mechanism of Human Cystathionine-β-Synthase: A PLP-Dependent Hemesensor Protein. *Archives of Biochemistry and Biophysics* **2005**, *433* (1), 144–156. https://doi.org/10.1016/j.abb.2004.08.037
(130) Rossier, J.; Delasoie, J.; Haeni, L.; Hauser, D.; Rothen-Rutishauser, B.; Zobi, F. Cytotoxicity of Mn-Based PhotoCORMs of Ethynyl-α-Diimine Ligands against Different Cancer Cell Lines: The Key Role of CO-Depleted Metal Fragments. *Journal of Inorganic Biochemistry* **2020**, *209*, 111122. https://doi.org/10.1016/j.jinorgbio.2020.111122
(131) Khaled, R. M.; Friedrich, A.; Ragheb, M. A.; Abdel-Ghani, N. T.; Mansour, A. M. Cytotoxicity of Photoactivatable Bromo Tricarbonyl Manganese(I) Compounds against Human Liver Carcinoma Cells. *Dalton Trans.* **2020**, *49* (27), 9294–9305. https://doi.org/10.1039/D0DT01539C
(132) Li, Z.; Pierri, A. E.; Huang, P.-J.; Wu, G.; Iretskii, A. V.; Ford, P. C. Dinuclear PhotoCORMs: Dioxygen-Assisted Carbon Monoxide Uncaging from Long-Wavelength-Absorbing Metal–Metal-Bonded Carbonyl Complexes. *Inorg. Chem.* **2017**, *56* (11), 6094–6104. https://doi.org/10.1021/acs.inorgchem.6b03138
(133) Stenger-Smith, J.; Chakraborty, I.; Ouattara, R.; Sameera, W. M. C.; Rue, K.; Mascharak, P. CO Release from Mn(I)-Based PhotoCORMs with Single Photons in the Phototherapeutic Region. *Chem. Commun.* **2021**, *57* (9), 1101–1104. https://doi.org/10.1039/D0CC07405E
(134) Kottelat, E.; Ruggi, A.; Zobi, F. Red-Light Activated PhotoCORMs of Mn(I) Species Bearing Electron Deficient 2,2′-Azopyridines. *Dalton Trans.* **2016**, *45* (16), 6920–6927. https://doi.org/10.1039/C6DT00858E
(135) Jiang, Q.; Xia, Y.; Barrett, J.; Mikhailovsky, A.; Wu, G.; Wang, D.; Shi, P.; Ford, P. C. Near-Infrared and Visible Photoactivation to Uncage Carbon Monoxide from an Aqueous-Soluble PhotoCORM. *Inorg. Chem.* **2019**, *58* (16), 11066–11075. https://doi.org/10.1021/acs.inorgchem.9b01581
(136) Ramu, V.; Upendar Reddy, G.; Liu, J.; Hoffmann, P.; Sollapur, R.; Wyrwa, R.; Kupfer, S.; Spielmann, C.; Bonnet, S.; Neugebauer, U.; Schiller, A. Two-Photon-Induced CO-Releasing Molecules as Molecular Logic Systems in Solution, Polymers, and Cells. *Chemistry – A European Journal* **2019**, *25* (36), 8453–8458. https://doi.org/10.1002/chem.201901396
(137) Askes, S. H. C.; Reddy, G. U.; Wyrwa, R.; Bonnet, S.; Schiller, A. Red Light-Triggered CO Release from $Mn_2(CO)_{10}$ Using Triplet Sensitization in Polymer Nonwoven Fabrics. *J. Am. Chem. Soc.* **2017**, *139* (43), 15292–15295. https://doi.org/10.1021/jacs.7b07427
(138) Ruggi, A.; Zobi, F. Quantum-CORMs: Quantum Dot Sensitized CO Releasing Molecules. *Dalton Transactions* **2015**, *44* (24), 10928–10931. https://doi.org/10.1039/C5DT01681A

(139) Pierri, A. E.; Huang, P.-J.; Garcia, J. V.; Stanfill, J. G.; Chui, M.; Wu, G.; Zheng, N.; Ford, P. C. A PhotoCORM Nanocarrier for CO Release Using NIR Light. *Chem. Commun.* **2015**, *51* (11), 2072–2075. https://doi.org/10.1039/C4CC06766E
(140) Potocny, A. M.; Teesdale, J. J.; Marangoz, A.; Yap, G. P. A.; Rosenthal, J. Spectroscopic and $^1O_2$ Sensitization Characteristics of a Series of Isomeric $Re(Bpy)(CO)_3Cl$ Complexes Bearing Pendant BODIPY Chromophores. *Inorg. Chem.* **2019**, *58* (8), 5042–5050. https://doi.org/10.1021/acs.inorgchem.9b00102
(141) Weinstain, R., Slanina, T., Kand, D., and Klan, P. Visible-to-NIR-Light Activated Release: From Small Molecules to Nanomaterials. *Chemical Reviews* **2020.** *120*(24), 13135-13272 https://pubs.acs.org/doi/full/10.1021/acs.chemrev.0c00663
(142) Zhang, X.-F. BODIPY Photosensitizers Based on PET and Heavy Atom Effect: A Comparative Study on the Efficient Formation of Excited Triplet State and Singlet Oxygen in BODIPY Dimers and Monomers. *Journal of Photochemistry and Photobiology A: Chemistry* **2018**, *355*, 431–443. https://doi.org/10.1016/j.jphotochem.2017.07.019
(143) Lee, Y.; Malamakal, R. M.; Chenoweth, D. M.; Anna, J. M. Halogen Bonding Facilitates Intersystem Crossing in Iodo-BODIPY Chromophores. *J. Phys. Chem. Lett.* **2020**, *11* (3), 877–884. https://doi.org/10.1021/acs.jpclett.9b03753
(144) Paul, S.; Kundu, P.; Bhattacharyya, U.; Garai, A.; Maji, R. C.; Kondaiah, P.; Chakravarty, A. R. Ruthenium(II) Conjugates of Boron-Dipyrromethene and Biotin for Targeted Photodynamic Therapy in Red Light. *Inorg. Chem.* **2020**, *59* (1), 913–924. https://doi.org/10.1021/acs.inorgchem.9b03178
(145) Wu, W.; Sun, J.; Cui, X.; Zhao, J. Observation of the Room Temperature Phosphorescence of Bodipy in Visible Light-Harvesting Ru(II) Polyimine Complexes and Application as Triplet Photosensitizers for Triplet–Triplet-Annihilation Upconversion and Photocatalytic Oxidation. *J. Mater. Chem. C* **2013**, *1* (30), 4577–4589. https://doi.org/10.1039/C3TC30592A
(146) Qiao, L.; Liu, J.; Han, Y.; Wei, F.; Liao, X.; Zhang, C.; Xie, L.; Ji, L.; Chao, H. Rational Design of a Lysosome-Targeting and near-Infrared Absorbing Ru(II)–BODIPY Conjugate for Photodynamic Therapy. *Chem. Commun.* **2021**, *57* (14), 1790–1793. https://doi.org/10.1039/D0CC06926D
(147) Andrade, G. A.; Pistner, A. J.; Yap, G. P. A.; Lutterman, D. A.; Rosenthal, J. Photocatalytic Conversion of CO_2 to CO Using Rhenium Bipyridine Platforms Containing Ancillary Phenyl or BODIPY Moieties. *ACS Catal.* **2013**, *3* (8), 1685–1692. https://doi.org/10.1021/cs400332y
(148) Teesdale, J. J.; Pistner, A. J.; Yap, G. P. A.; Ma, Y.-Z.; Lutterman, D. A.; Rosenthal, J. Reduction of CO2 Using a Rhenium Bipyridine Complex Containing Ancillary BODIPY Moieties. *Catalysis Today* **2014**, *225*, 149–157. https://doi.org/10.1016/j.cattod.2013.10.091
(149) Lazarides, T.; McCormick, T. M.; Wilson, K. C.; Lee, S.; McCamant, D. W.; Eisenberg, R. Sensitizing the Sensitizer: The Synthesis and Photophysical Study of Bodipy−Pt(II)(Diimine)(Dithiolate) Conjugates. *J. Am. Chem. Soc.* **2011**, *133* (2), 350–364. https://doi.org/10.1021/ja1070366

(150) Irmler, P.; Winter, R. F. σ-Pt-BODIPY Complexes with Platinum Attachment to Carbon Atoms C_2 or C_3: Spectroscopic, Structural, and (Spectro)Electrochemical Studies and Photocatalysis. *Organometallics* **2018**, *37* (2), 235–253. https://doi.org/10.1021/acs.organomet.7b00806
(151) Raza, M. K.; Gautam, S.; Howlader, P.; Bhattacharyya, A.; Kondaiah, P.; Chakravarty, A. R. Pyriplatin-Boron-Dipyrromethene Conjugates for Imaging and Mitochondria-Targeted Photodynamic Therapy. *Inorg. Chem.* **2018**, *57* (22), 14374–14385. https://doi.org/10.1021/acs.inorgchem.8b02546
(152) Aksakal, N. E.; Eçik, E. T.; Kazan, H. H.; Çiftçi, G. Y.; Yuksel, F. Novel Ruthenium(II) and Iridium(III) BODIPY Dyes: Insights into Their Application in Photodynamic Therapy in Vitro. *Photochem Photobiol Sci* **2019**, *18* (8), 2012–2022. https://doi.org/10.1039/c9pp00201d
(153) Bartelmess, J.; Francis, A. J.; El Roz, K. A.; Castellano, F. N.; Weare, W. W.; Sommer, R. D. Light-Driven Hydrogen Evolution by BODIPY-Sensitized Cobaloxime Catalysts. *Inorg. Chem.* **2014**, *53* (9), 4527–4534. https://doi.org/10.1021/ic500218q
(154) Bartelmess, J.; Weare, W. W.; Sommer, R. D. Synthesis, Characterization and Structural Investigation of Novel Meso-Pyridyl BODIPY–Cobaloxime Complexes. *Dalton Trans.* **2013**, *42* (41), 14883–14891. https://doi.org/10.1039/C3DT51849C
(155) Chen, Y.; Wan, L.; Zhang, D.; Bian, Y.; Jiang, J. Modulation of the Spectroscopic Property of Bodipy Derivates through Tuning the Molecular Configuration. *Photochem Photobiol Sci* **2011**, *10* (6), 1030–1038. https://doi.org/10.1039/c1pp00001b
(156) Juárez, L. A.; Barba-Bon, A.; Costero, A. M.; Martínez-Máñez, R.; Sancenón, F.; Parra, M.; Gaviña, P.; Terencio, M. C.; Alcaraz, M. J. A Boron Dipyrromethene (BODIPY)-Based Cu(II)–Bipyridine Complex for Highly Selective NO Detection. *Chemistry – A European Journal* **2015**, *21* (44), 15486–15490. https://doi.org/10.1002/chem.201502191
(157) Eckermann, A. L.; Barker, K. D.; Hartings, M. R.; Ratner, M. A.; Meade, T. J. Synthesis and Electrochemical Characterization of a Transition-Metal-Modified Ligand−Receptor Pair. *J. Am. Chem. Soc.* **2005**, *127* (34), 11880–11881. https://doi.org/10.1021/ja042922y
(158) Guo, S.; Ma, L.; Zhao, J.; Küçüköz, B.; Karatay, A.; Hayvali, M.; Gul Yaglioglu, H.; Elmali, A. BODIPY Triads Triplet Photosensitizers Enhanced with Intramolecular Resonance Energy Transfer (RET): Broadband Visible Light Absorption and Application in Photooxidation. *Chemical Science* **2014**, *5* (2), 489–500. https://doi.org/10.1039/C3SC52323C
(159) Baruah, M.; Qin, W.; Flors, C.; Hofkens, J.; Vallée, R. A. L.; Beljonne, D.; Van der Auweraer, M.; De Borggraeve, W. M.; Boens, N. Solvent and PH Dependent Fluorescent Properties of a Dimethylaminostyryl Borondipyrromethene Dye in Solution. *J. Phys. Chem. A* **2006**, *110* (18), 5998–6009. https://doi.org/10.1021/jp054878u

(160) Agazzi, M. L.; Ballatore, M. B.; Reynoso, E.; Quiroga, E. D.; Durantini, E. N. Synthesis, Spectroscopic Properties and Photodynamic Activity of Two Cationic BODIPY Derivatives with Application in the Photoinactivation of Microorganisms. *European Journal of Medicinal Chemistry* **2017**, *126*, 110–121. https://doi.org/10.1016/j.ejmech.2016.10.001
(161) Zou, J.; Yin, Z.; Ding, K.; Tang, Q.; Li, J.; Si, W.; Shao, J.; Zhang, Q.; Huang, W.; Dong, X. BODIPY Derivatives for Photodynamic Therapy: Influence of Configuration versus Heavy Atom Effect. *ACS Appl. Mater. Interfaces* **2017**, *9* (38), 32475–32481. https://doi.org/10.1021/acsami.7b07569
(162) Zhou, Q.-X.; Lei, W.-H.; Hou, Y.-J.; Chen, Y.-J.; Li, C.; Zhang, B.-W.; Wang, X.-S. BODIPY-Modified Ru(II) Arene Complex—a New Ligand Dissociation Mechanism and a Novel Strategy to Red Shift the Photoactivation Wavelength of Anticancer Metallodrugs. *Dalton Trans.* **2013**, *42* (8), 2786–2791. https://doi.org/10.1039/C2DT32527F
(163) Brouwer, A. M. Standards for photoluminescence quantum yield measurements in solution (IUPAC Technical Report). *Pure and Applied Chemistry* **2011**, *83* (12), 2213–2228. https://doi.org/10.1351/PAC-REP-10-09-31
(164) Gorbe, M.; Costero, A. M.; Sancenón, F.; Martínez-Máñez, R.; Ballesteros-Cillero, R.; Ochando, L. E.; Chulvi, K.; Gotor, R.; Gil, S. Halogen-Containing BODIPY Derivatives for Photodynamic Therapy. *Dyes and Pigments* **2019**, *160*, 198–207. https://doi.org/10.1016/j.dyepig.2018.08.007
(165) Yogo, T.; Urano, Y.; Ishitsuka, Y.; Maniwa, F.; Nagano, T. Highly Efficient and Photostable Photosensitizer Based on BODIPY Chromophore. *J. Am. Chem. Soc.* **2005**, *127* (35), 12162–12163. https://doi.org/10.1021/ja0528533
(166) Sabatini, R. P.; McCormick, T. M.; Lazarides, T.; Wilson, K. C.; Eisenberg, R.; McCamant, D. W. Intersystem Crossing in Halogenated Bodipy Chromophores Used for Solar Hydrogen Production. *J. Phys. Chem. Lett.* **2011**, *2* (3), 223–227. https://doi.org/10.1021/jz101697y
(167) Harriman, A.; Mallon, L. J.; Ulrich, G.; Ziessel, R. Rapid Intersystem Crossing in Closely-Spaced but Orthogonal Molecular Dyads. *ChemPhysChem* **2007**, *8* (8), 1207–1214. https://doi.org/10.1002/cphc.200700060
(168) Rosenthal, J.; Nepomnyashchii, A. B.; Kozhukh, J.; Bard, A. J.; Lippard, S. J. Synthesis, Photophysics, Electrochemistry, and Electrogenerated Chemiluminescence of a Homologous Set of BODIPY-Appended Bipyridine Derivatives. *J. Phys. Chem. C* **2011**, *115* (36), 17993–18001. https://doi.org/10.1021/jp204487r
(169) Sabatini, R. P.; Lindley, B.; McCormick, T. M.; Lazarides, T.; Brennessel, W. W.; McCamant, D. W.; Eisenberg, R. Efficient Bimolecular Mechanism of Photochemical Hydrogen Production Using Halogenated Boron-Dipyrromethene (Bodipy) Dyes and a Bis(Dimethylglyoxime) Cobalt(III) Complex. *J. Phys. Chem. B* **2016**, *120* (3), 527–534. https://doi.org/10.1021/acs.jpcb.5b11035
(170) Luo, G.-G.; Fang, K.; Wu, J.-H.; Dai, J.-C.; Zhao, Q.-H. Noble-Metal-Free BODIPY–Cobaloxime Photocatalysts for Visible-Light-Driven Hydrogen

Production. *Phys. Chem. Chem. Phys.* **2014**, *16* (43), 23884–23894. https://doi.org/10.1039/C4CP03343D
(171) Liu, J.; Hoffmann, P.; Steinmetzer, J.; Askes, S. H. C.; Kupfer, S.; Görls, H.; Gräfe, S.; Neugebauer, U.; Gandra, U. R.; Schiller, A. Visible Light-Activated Biocompatible Photo-CORM for CO-Release with Colorimetric and Fluorometric Dual Turn-on Response. *Polyhedron* **2019**, *172*, 175–181. https://doi.org/10.1016/j.poly.2019.04.031
(172) Weiss, V. C.; Farias, G.; Amorim, A. L.; Xavier, F. R.; Camargo, T. P.; Bregalda, M. B.; Haukka, M.; Nordlander, E.; de Souza, B.; Peralta, R. A. Luminescent PhotoCORMs: Enabling/Disabling CO Delivery upon Blue Light Irradiation. *Inorg. Chem.* **2020**, *59* (18), 13078–13090. https://doi.org/10.1021/acs.inorgchem.0c00638
(173) Miao, X.; Hu, W.; He, T.; Tao, H.; Wang, Q.; Chen, R.; Jin, L.; Zhao, H.; Lu, X.; Fan, Q.; Huang, W. Deciphering the Intersystem Crossing in Near-Infrared BODIPY Photosensitizers for Highly Efficient Photodynamic Therapy. *Chemical Science* **2019**, *10* (10), 3096–3102. https://doi.org/10.1039/C8SC04840A
(174) Epelde-Elezcano, N.; Martínez-Martínez, V.; Peña-Cabrera, E.; A. Gómez-Durán, C. F.; López Arbeloa, I.; Lacombe, S. Modulation of Singlet Oxygen Generation in Halogenated BODIPY Dyes by Substitution at Their Meso Position: Towards a Solvent-Independent Standard in the Vis Region. *RSC Advances* **2016**, *6* (48), 41991–41998. https://doi.org/10.1039/C6RA05820E
(175) Entradas, T.; Waldron, S.; Volk, M. The Detection Sensitivity of Commonly Used Singlet Oxygen Probes in Aqueous Environments. *Journal of Photochemistry and Photobiology B: Biology* **2020**, *204*, 111787. https://doi.org/10.1016/j.jphotobiol.2020.111787
(176) Prasad, A.; Sedlářová, M.; Pospíšil, P. Singlet Oxygen Imaging Using Fluorescent Probe Singlet Oxygen Sensor Green in Photosynthetic Organisms. *Sci Rep* **2018**, *8* (1), 13685. https://doi.org/10.1038/s41598-018-31638-5
(177) Rachford, A. A.; Ziessel, R.; Bura, T.; Retailleau, P.; Castellano, F. N. Boron Dipyrromethene (Bodipy) Phosphorescence Revealed in $[Ir(Ppy)_2(Bpy\text{-}C{\equiv}C\text{-}Bodipy)]^+$. *Inorg. Chem.* **2010**, *49* (8), 3730–3736. https://doi.org/10.1021/ic901996u
(178) Zhang, X.-F.; Yang, X.; Niu, K.; Geng, H. Phosphorescence of BODIPY Dyes. *Journal of Photochemistry and Photobiology A: Chemistry* **2014**, *285*, 16–20. https://doi.org/10.1016/j.jphotochem.2014.04.009
(179) Prieto-Montero, R.; Sola-Llano, R.; Montero, R.; Longarte, A.; Arbeloa, T.; López-Arbeloa, I.; Martínez-Martínez, V.; Lacombe, S. Methylthio BODIPY as a Standard Triplet Photosensitizer for Singlet Oxygen Production: A Photophysical Study. *Phys. Chem. Chem. Phys.* **2019**, *21* (36), 20403–20414. https://doi.org/10.1039/C9CP03454D
(180) Hu, W.; Liu, M.; Zhang, X.-F.; Shi, M.; Jia, M.; Hu, X.; Liu, L.; Wang, T. Minimizing the Electron Donor Size of Donor–Acceptor-Type Photosensitizer: Twisted Intramolecular Charge-Transfer-Induced Triplet State and Singlet Oxygen

Formation. *J. Phys. Chem. C* **2020**, *124* (43), 23558–23566. https://doi.org/10.1021/acs.jpcc.0c07679
(181) Momeni, M. R.; Brown, A. Why Do TD-DFT Excitation Energies of BODIPY/Aza-BODIPY Families Largely Deviate from Experiment? Answers from Electron Correlated and Multireference Methods. *J. Chem. Theory Comput.* **2015**, *11* (6), 2619–2632. https://doi.org/10.1021/ct500775r
(182) Lehn, J.-M. Perspectives in Supramolecular Chemistry—From Molecular Recognition towards Molecular Information Processing and Self-Organization. *Angewandte Chemie International Edition in English* **1990**, *29* (11), 1304–1319. https://doi.org/10.1002/anie.199013041
(183) Lessmann, J. J.; Horrocks, W. DeW. Supramolecular Coordination Chemistry in Aqueous Solution: Lanthanide Ion-Induced Triple Helix Formation. *Inorg. Chem.* **2000**, *39* (15), 3114–3124. https://doi.org/10.1021/ic9906981
(184) Mendes, A. C.; Baran, E. T.; Reis, R. L.; Azevedo, H. S. Self-Assembly in Nature: Using the Principles of Nature to Create Complex Nanobiomaterials. *WIREs Nanomedicine and Nanobiotechnology* **2013**, *5* (6), 582–612. https://doi.org/10.1002/wnan.1238
(185) Cook, T. R.; Zheng, Y.-R.; Stang, P. J. Metal–Organic Frameworks and Self-Assembled Supramolecular Coordination Complexes: Comparing and Contrasting the Design, Synthesis, and Functionality of Metal–Organic Materials. *Chem. Rev.* **2013**, *113* (1), 734–777. https://doi.org/10.1021/cr3002824
(186) Casini, A.; Woods, B.; Wenzel, M. The Promise of Self-Assembled 3D Supramolecular Coordination Complexes for Biomedical Applications. *Inorg. Chem.* **2017**, *56* (24), 14715–14729. https://doi.org/10.1021/acs.inorgchem.7b02599
(187) Yadav, S.; Kannan, P.; Qiu, G. Cavity-Based Applications of Metallo-Supramolecular Coordination Cages (MSCCs). *Organic Chemistry Frontiers* **2020**, *7* (18), 2842–2872. https://doi.org/10.1039/D0QO00681E
(188) Percástegui, E. G.; Ronson, T. K.; Nitschke, J. R. Design and Applications of Water-Soluble Coordination Cages. *Chem. Rev.* **2020**, *120* (24), 13480–13544. https://doi.org/10.1021/acs.chemrev.0c00672
(189) Frank, H. S.; Evans, M. W. Free Volume and Entropy in Condensed Systems III. Entropy in Binary Liquid Mixtures; Partial Molal Entropy in Dilute Solutions; Structure and Thermodynamics in Aqueous Electrolytes. *J. Chem. Phys.* **1945**, *13* (11), 507–532. https://doi.org/10.1063/1.1723985
(190) Cullen, W. M. Host-Guest Chemistry of Polyhedral Coordination Cages. phd, University of Sheffield, **2015.**
(191) Yoshizawa, M.; Kusukawa, T.; Kawano, M.; Ohhara, T.; Tanaka, I.; Kurihara, K.; Niimura, N.; Fujita, M. Endohedral Clusterization of Ten Water Molecules into a "Molecular Ice" within the Hydrophobic Pocket of a Self-Assembled Cage. *J. Am. Chem. Soc.* **2005**, *127* (9), 2798–2799. https://doi.org/10.1021/ja043953w

(192) Escobar, L.; Ballester, P. Molecular Recognition in Water Using Macrocyclic Synthetic Receptors. *Chem. Rev.* **2021**, *121* (4), 2445–2514. https://doi.org/10.1021/acs.chemrev.0c00522
(193) Kusukawa, T.; Fujita, M. Self-Assembled M_6L_4 -Type Coordination Nanocage with 2,2‘-Bipyridine Ancillary Ligands. Facile Crystallization and X-Ray Analysis of Shape-Selective Enclathration of Neutral Guests in the Cage. *J. Am. Chem. Soc.* **2002**, *124* (45), 13576–13582. https://doi.org/10.1021/ja020712k
(194) Takezawa, H.; Shitozawa, K.; Fujita, M. Enhanced Reactivity of Twisted Amides inside a Molecular Cage. *Nat. Chem.* **2020**, *12* (6), 574–578. https://doi.org/10.1038/s41557-020-0455-y
(195) Cai, L.-X.; Li, S.-C.; Yan, D.-N.; Zhou, L.-P.; Guo, F.; Sun, Q.-F. Water-Soluble Redox-Active Cage Hosting Polyoxometalates for Selective Desulfurization Catalysis. *J. Am. Chem. Soc.* **2018**, *140* (14), 4869–4876. https://doi.org/10.1021/jacs.8b00394
(196) Caulder, D. L.; Brückner, C.; Powers, R. E.; König, S.; Parac, T. N.; Leary, J. A.; Raymond, K. N. Design, Formation and Properties of Tetrahedral M_4L_4 and M_4L_6 Supramolecular Clusters [1]. *J. Am. Chem. Soc.* **2001**, *123* (37), 8923–8938. https://doi.org/10.1021/ja0104507
(197) Tidmarsh, I. S.; Faust, T. B.; Adams, H.; Harding, L. P.; Russo, L.; Clegg, W.; Ward, M. D. Octanuclear Cubic Coordination Cages. *J. Am. Chem. Soc.* **2008**, *130* (45), 15167–15175. https://doi.org/10.1021/ja805605y
(198) Mozaceanu, C.; Taylor, C. G. P.; Piper, J. R.; Argent, S. P.; Ward, M. D. Catalysis of an Aldol Condensation Using a Coordination Cage. *Chemistry* **2020**, *2* (1), 22–32. https://doi.org/10.3390/chemistry2010004
(199) Bolliger, J. L.; Belenguer, A. M.; Nitschke, J. R. Enantiopure Water-Soluble [Fe4L6] Cages: Host–Guest Chemistry and Catalytic Activity. *Angewandte Chemie International Edition* **2013**, *52* (31), 7958–7962. https://doi.org/10.1002/anie.201302136
(200) Percástegui, E. G.; Mosquera, J.; Nitschke, J. R. Anion Exchange Renders Hydrophobic Capsules and Cargoes Water-Soluble. *Angewandte Chemie* **2017**, *129* (31), 9264–9268. https://doi.org/10.1002/ange.201705093
(201) Train, Jennifer S., Ashley B. Wragg, Alexander J. Auty, Alexander J. Metherell, Dimitri Chekulaev, Christopher GP Taylor, Stephen P. Argent, Julia A. Weinstein, and Michael D. Ward. Photophysics of Cage/Guest Assemblies: Photoinduced Electron Transfer between a Coordination Cage Containing Osmium(II) Luminophores, and Electron-Deficient Bound Guests in the Central Cavity. *Inorganic Chemistry* **2019**, *58*(4), 2386-2396 https://pubs.acs.org/doi/full/10.1021/acs
(202) Samanta, D.; Mukherjee, S.; Patil, Y. P.; Mukherjee, P. S. Self-Assembled Pd6 Open Cage with Triimidazole Walls and the Use of Its Confined Nanospace for Catalytic Knoevenagel- and Diels–Alder Reactions in Aqueous Medium. *Chemistry – A European Journal* **2012**, *18* (39), 12322–12329. https://doi.org/10.1002/chem.201201679

(203) Yanshyna, O.; Białek, M. J.; Chashchikhin, O. V.; Klajn, R. Encapsulation within a Coordination Cage Modulates the Reactivity of Redox-Active Dyes. *Commun Chem* **2022**, *5* (1), 1–12. https://doi.org/10.1038/s42004-022-00658-8
(204) Li, K.; Zhang, L.-Y.; Yan, C.; Wei, S.-C.; Pan, M.; Zhang, L.; Su, C.-Y. Stepwise Assembly of Pd6(RuL3)8 Nanoscale Rhombododecahedral Metal–Organic Cages via Metalloligand Strategy for Guest Trapping and Protection. *J. Am. Chem. Soc.* **2014**, *136* (12), 4456–4459. https://doi.org/10.1021/ja410044r
(205) Howlader, P.; Mondal, B.; Purba, P. C.; Zangrando, E.; Mukherjee, P. S. Self-Assembled Pd(II) Barrels as Containers for Transient Merocyanine Form and Reverse Thermochromism of Spiropyran. *J. Am. Chem. Soc.* **2018**, *140* (25), 7952–7960. https://doi.org/10.1021/jacs.8b03946
(206) Sun, Q.; Escobar, L.; Jong, J. de; Ballester, P. Self-Assembly of a Water-Soluble Endohedrally Functionalized Coordination Cage Including Polar Guests. *Chem. Sci.* **2021**, *12* (40), 13469–13476. https://doi.org/10.1039/D1SC03751J
(207) El Aroussi, B., Guénée, L., Pal, P., and Hamacek, J. Lanthanide-Mediated Supramolecular Cages and Host Guest Interactions. *Inorganic chemistry* **2011**, *50*(17), 8588-8597. https://doi.org/10.1021/ic201156q
(208) Liu, Y.; Wu, X.; He, C.; Jiao, Y.; Duan, C. Self-Assembly of Cerium-Based Metal–Organic Tetrahedrons for Size-Selectively Luminescent Sensing Natural Saccharides. *Chem. Commun.* **2009**, No. 48, 7554. https://doi.org/10.1039/b915358f
(209) Liu, C.-L.; Zhou, L.-P.; Tripathy, D.; Sun, Q.-F. Self-Assembly of Stable Luminescent Lanthanide Supramolecular M_4L_6 Cages with Sensing Properties toward Nitroaromatics. *Chem. Commun.* **2017**, *53* (16), 2459–2462. https://doi.org/10.1039/C7CC00189D
(210) Wang, Z.; Zhou, L.-P.; Zhao, T.-H.; Cai, L.-X.; Guo, X.-Q.; Duan, P.-F.; Sun, Q.-F. Hierarchical Self-Assembly and Chiroptical Studies of Luminescent 4d–4f Cages. *Inorg. Chem.* **2018**, *57* (13), 7982–7992. https://doi.org/10.1021/acs.inorgchem.8b01152
(211) Yao, Y.; Zhou, Y.; Zhu, T.; Gao, T.; Li, H.; Yan, P. Eu(III) Tetrahedron Cage as a Luminescent Chemosensor for Rapidly Reversible and Turn-On Detection of Volatile Amine/NH_3. *ACS Appl. Mater. Interfaces* **2020**, *12* (13), 15338–15347. https://doi.org/10.1021/acsami.9b21425
(212) Tang, X.; Chu, D.; Gong, W.; Cui, Y.; Liu, Y. Metal-Organic Cages with Missing Linker Defects. *Angewandte Chemie* **2021**, *133* (16), 9181–9187. https://doi.org/10.1002/ange.202017244
(213) Li, X.-Z.; Tian, C.-B.; Sun, Q.-F. Coordination-Directed Self-Assembly of Functional Polynuclear Lanthanide Supramolecular Architectures. *Chem. Rev.* **2022**, *122* (6), 6374–6458. https://doi.org/10.1021/acs.chemrev.1c00602
(214) Peters, J. A.; Djanashvili, K.; Geraldes, C. F. G. C.; Platas-Iglesias, C. The Chemical Consequences of the Gradual Decrease of the Ionic Radius along the Ln-Series. *Coordination Chemistry Reviews* **2020**, *406*, 213146. https://doi.org/10.1016/j.ccr.2019.213146

(215) Bünzli, J.-C. G. Review: Lanthanide Coordination Chemistry: From Old Concepts to Coordination Polymers. *Journal of Coordination Chemistry* **2014**, *67* (23–24), 3706–3733. https://doi.org/10.1080/00958972.2014.957201
(216) Barry, D. E.; Caffrey, D. F.; Gunnlaugsson, T. Lanthanide-Directed Synthesis of Luminescent Self-Assembly Supramolecular Structures and Mechanically Bonded Systems from Acyclic Coordinating Organic Ligands. *Chem. Soc. Rev.* **2016**, *45* (11), 3244–3274. https://doi.org/10.1039/C6CS00116E
(217) Bünzli, J.-C. G. Benefiting from the Unique Properties of Lanthanide Ions. *Acc. Chem. Res.* **2006**, *39* (1), 53–61. https://doi.org/10.1021/ar0400894
(218) Moore, E. G.; Samuel, A. P. S.; Raymond, K. N. From Antenna to Assay: Lessons Learned in Lanthanide Luminescence. *Acc. Chem. Res.* **2009**, *42* (4), 542–552. https://doi.org/10.1021/ar800211j
(219) Maas, H.; Currao, A.; Calzaferri, G. Encapsulated Lanthanides as Luminescent Materials. *Angewandte Chemie International Edition* **2002**, *41* (14), 2495–2497. https://doi.org/10.1002/1521-3773
(220) dos Santos, C. M. G.; Harte, A. J.; Quinn, S. J.; Gunnlaugsson, T. Recent Developments in the Field of Supramolecular Lanthanide Luminescent Sensors and Self-Assemblies. *Coordination Chemistry Reviews* **2008**, *252* (23), 2512–2527. https://doi.org/10.1016/j.ccr.2008.07.018
(221) Schmidt, A.; Casini, A.; Kühn, F. E. Self-Assembled M2L4 Coordination Cages: Synthesis and Potential Applications. *Coordination Chemistry Reviews* **2014**, *275*, 19–36. https://doi.org/10.1016/j.ccr.2014.03.037
(222) Chakrabarty, R.; Mukherjee, P. S.; Stang, P. J. Supramolecular Coordination: Self-Assembly of Finite Two- and Three-Dimensional Ensembles. *Chem. Rev.* **2011**, *111* (11), 6810–6918. https://doi.org/10.1021/cr200077m
(223) Pluth, M. D.; Raymond, K. N. Reversible Guest Exchange Mechanisms in Supramolecular Host–Guest Assemblies. *Chem. Soc. Rev.* **2007**, *36* (2), 161–171. https://doi.org/10.1039/B603168B
(224) Davis, A. V.; Raymond, K. N. The Big Squeeze: Guest Exchange in an M4L6 Supramolecular Host. *J. Am. Chem. Soc.* **2005**, *127* (21), 7912–7919. https://doi.org/10.1021/ja051037s
(225) Thordarson, P. Determining Association Constants from Titration Experiments in Supramolecular Chemistry. *Chem. Soc. Rev.* **2011**, *40* (3), 1305–1323. https://doi.org/10.1039/C0CS00062K
(226) Zimmermann, N.; Meggers, E.; Schultz, P. G. A Second-Generation Copper(II)-Mediated Metallo-DNA-Base Pair. *Bioorganic Chemistry* **2004**, *32* (1), 13–25. https://doi.org/10.1016/j.bioorg.2003.09.001
(227) Haino, T.; Matsumoto, Y.; Fukazawa, Y. Supramolecular Nano Networks Formed by Molecular-Recognition-Directed Self-Assembly of Ditopic Calix[5]Arene and Dumbbell [60]Fullerene. *J. Am. Chem. Soc.* **2005**, *127* (25), 8936–8937. https://doi.org/10.1021/ja0524088
(228) Crowley, J. D.; Bandeen, P. H. A Multicomponent CuAAC "Click" Approach to a Library of Hybrid Polydentate 2-Pyridyl-1,2,3-Triazole Ligands: New Building

Blocks for the Generation of Metallosupramolecular Architectures. *Dalton Trans.* **2009**, *39* (2), 612–623. https://doi.org/10.1039/B911276F
(229) Conde, N.; SanMartin, R.; Herrero, M. T.; Domínguez, E. Palladium NNC Pincer Complex as an Efficient Catalyst for the Cycloisomerization of Alkynoic Acids. *Advanced Synthesis and Catalysis* **2016**, *358* (20), 3283–3292. https://doi.org/10.1002/adsc.201600492
(230) Avram, L.; Cohen, Y. Diffusion NMR of Molecular Cages and Capsules. *Chem. Soc. Rev.* **2014**, *44* (2), 586–602. https://doi.org/10.1039/C4CS00197D
(231) Bolliger, J. L.; Ronson, T. K.; Ogawa, M.; Nitschke, J. R. Solvent Effects upon Guest Binding and Dynamics of a FeII4L4 Cage. *J. Am. Chem. Soc.* **2014**, *136* (41), 14545–14553. https://doi.org/10.1021/ja5077102
(232) Clever, G. H.; Kawamura, W.; Shionoya, M. Encapsulation versus Aggregation of Metal–Organic Cages Controlled by Guest Size Variation. *Inorg. Chem.* **2011**, *50* (11), 4689–4691. https://doi.org/10.1021/ic200517r
(233) Bañuelos, J. BODIPY Dye, the Most Versatile Fluorophore Ever? *The Chemical Record* **2016**, *16* (1), 335–348. https://doi.org/10.1002/tcr.201500238
(234) Tanaka, Y.; Wong, K. M.-C.; Yam, V. W.-W. Host–Guest Interactions of Phosphorescent Molecular Tweezers Based on an Alkynylplatinum(II) Terpyridine System with Polyaromatic Hydrocarbons. *Chemistry – A European Journal* **2013**, *19* (1), 390–399. https://doi.org/10.1002/chem.201201942

Appendix: Supplementary Materials

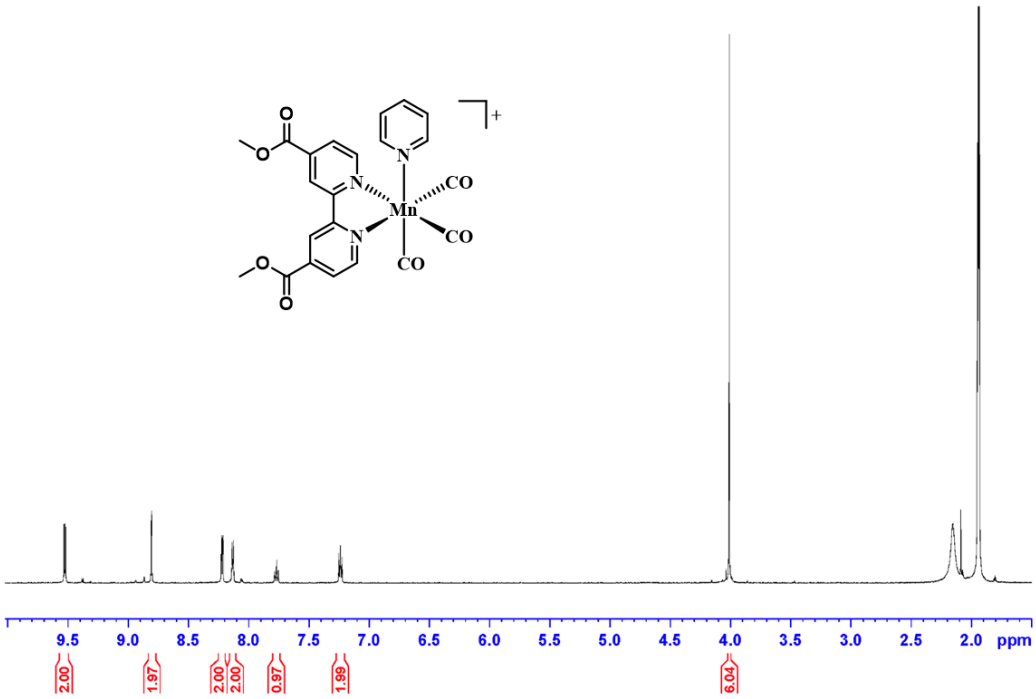

Figure A1. ^{1}H NMR spectrum of *fac*-[Mn(dmebpy)(CO)$_3$(py)](OTf) in CD_3CN.

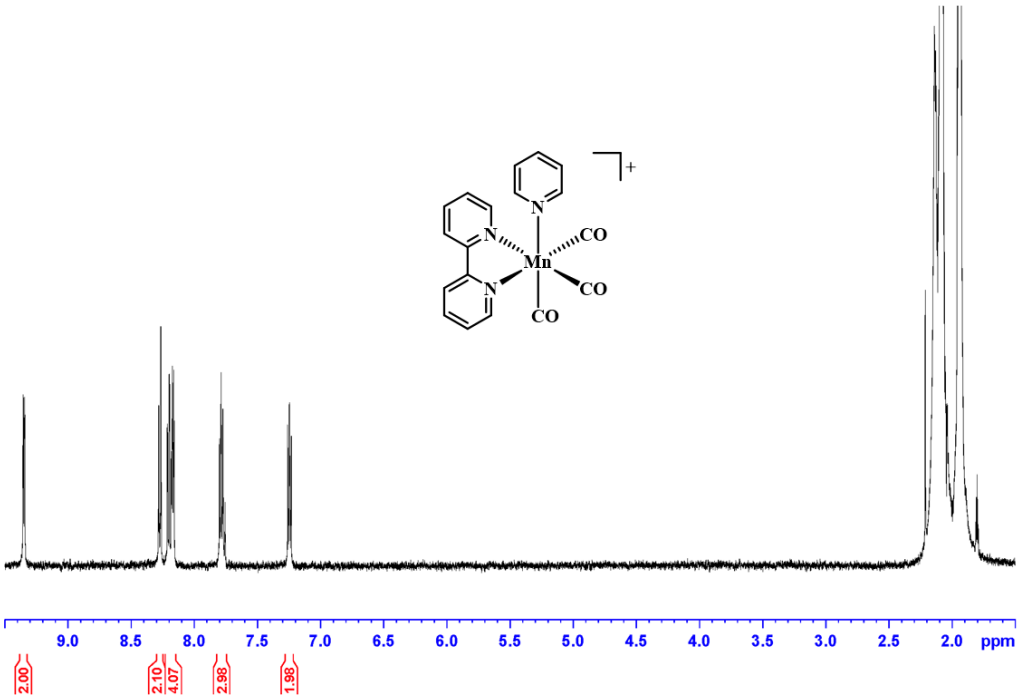

Figure A2. ^{1}H NMR spectrum of *fac*-[Mn(bpy)(CO)$_3$(py)](OTf) in CD_3CN.

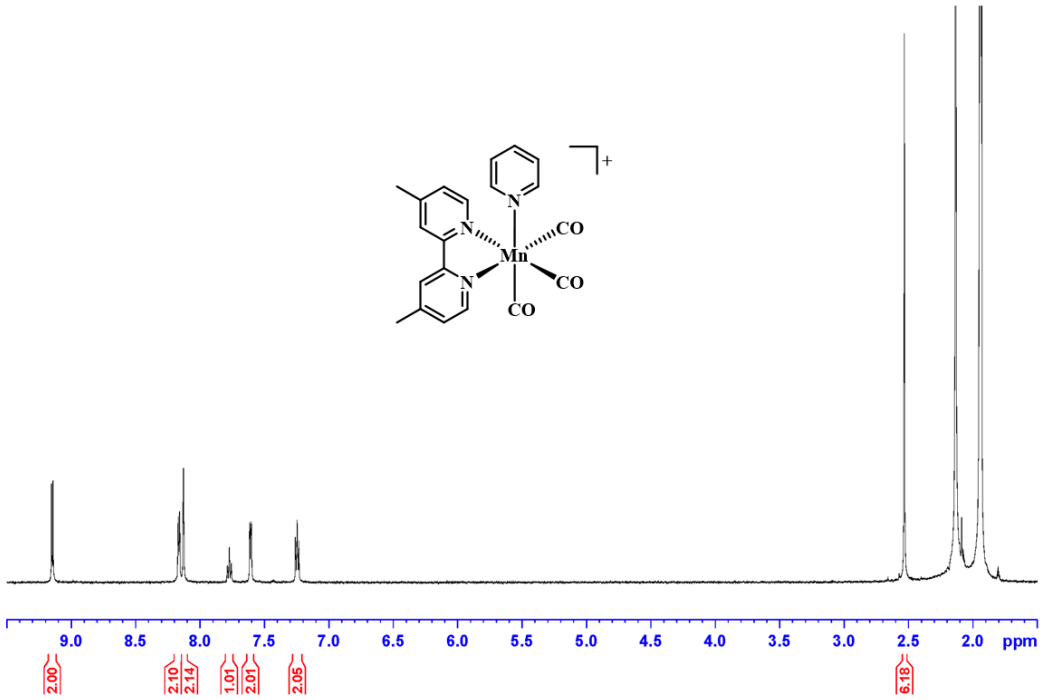

Figure A3. ^{1}H NMR spectrum of *fac*-[Mn(Me$_2$bpy)(CO)$_3$(py)](OTf) in CD_3CN.

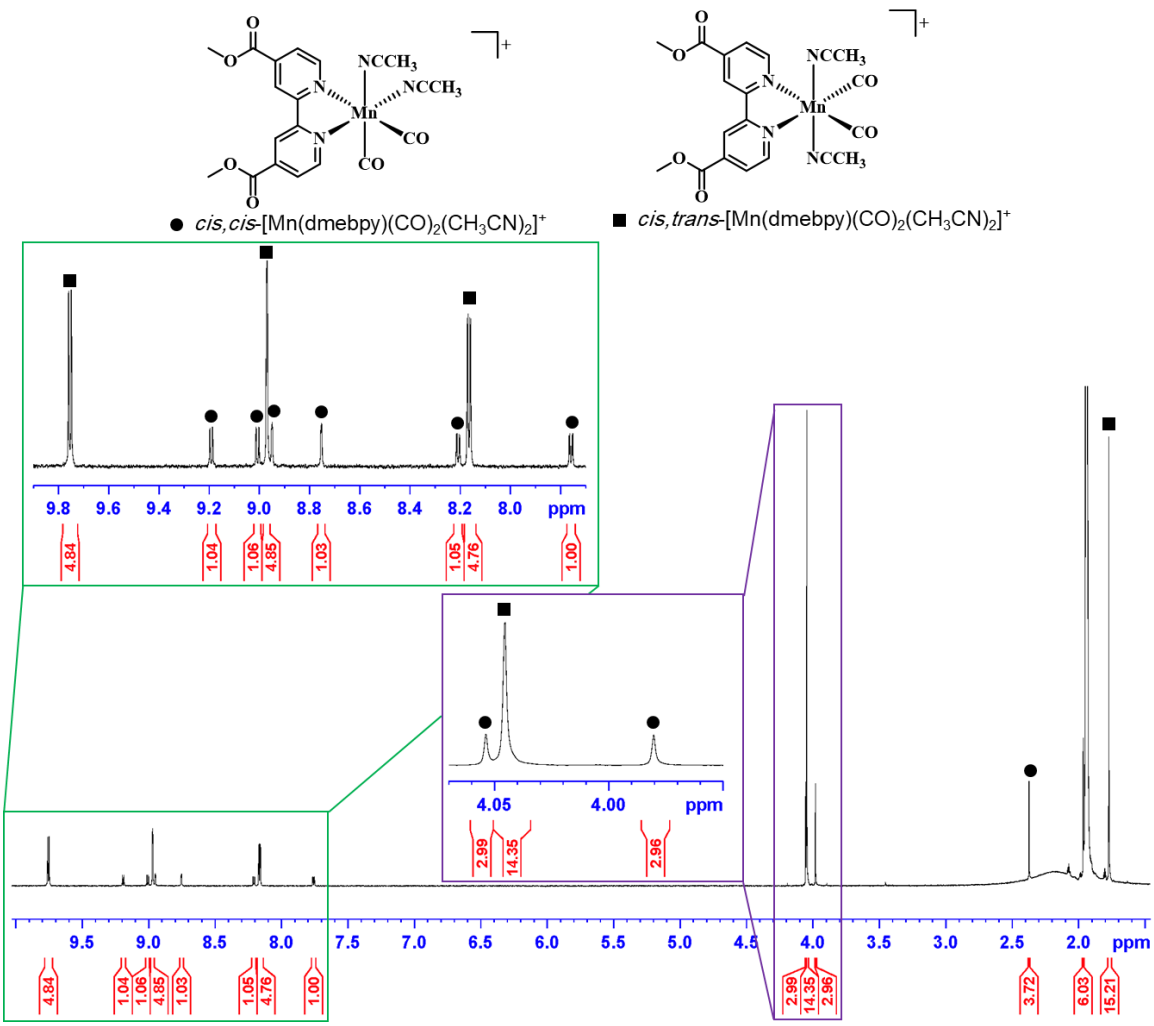

Figure A4. ^{1}H NMR spectrum of a mixture of *cis,cis*-[Mn(dmebpy)$(CO)_2(CH_3CN)_2]^+$ (circles, ~29%) and *cis,trans*-[Mn(dmebpy)$(CO)_2(CH_3CN)_2]^+$ (squares, ~71%) in CD_3CN.

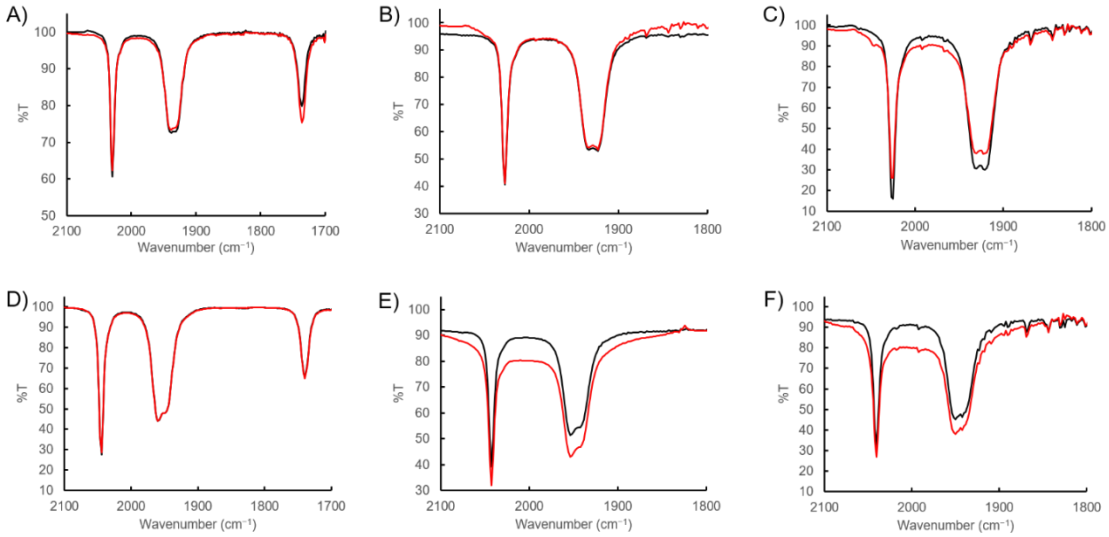

Figure A5. FTIR spectra for *fac*-[Mn(dmebpy)(CO)$_3$Br] (A), *fac*-[Mn(bpy)(CO)$_3$Br] (B), *fac*-[Mn(Me$_2$bpy)(CO)$_3$Br] (C), *fac*-[Mn(dmebpy)(CO)$_3$(py)]$^+$ (D), *fac*-[Mn(bpy)(CO)$_3$(py)]$^+$ (E), and *fac*-[Mn(Me$_2$bpy)(CO)$_3$(py)]$^+$ (F) in rt CH$_3$CN initially (black) and protected from light for 1 h (red).

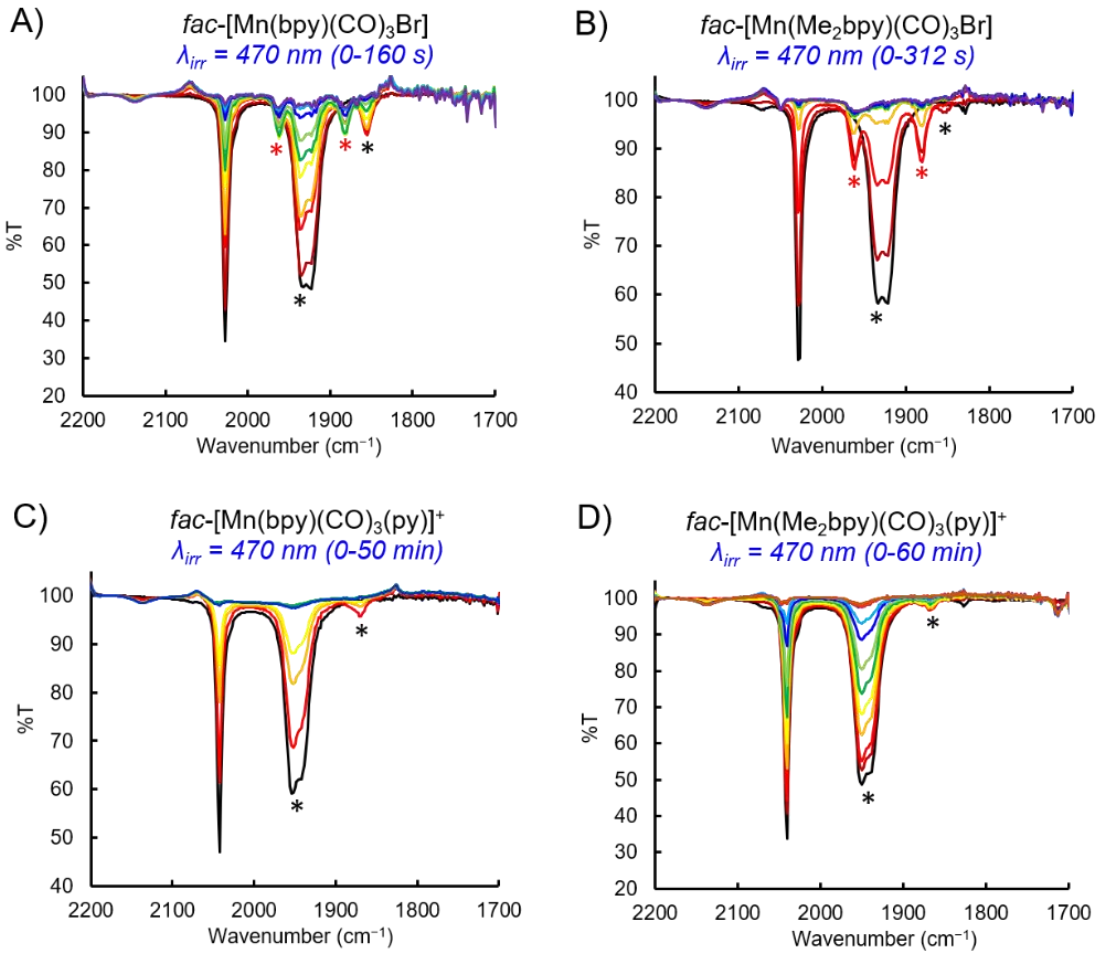

Figure A6. FTIR spectra for *fac*-[Mn(bpy)(CO)$_3$Br] (A), *fac*-[Mn(Me$_2$bpy)(CO)$_3$Br] (B), *fac*-[Mn(bpy)(CO)$_3$(py)]$^+$ (C), and *fac*-[Mn(Me$_2$bpy)(CO)$_3$(py)]$^+$ (D) in rt CH_3CN during photolysis with λ_{irr} = 470 nm. The first and second intermediate bands are denoted with black and red asterisks, respectively.

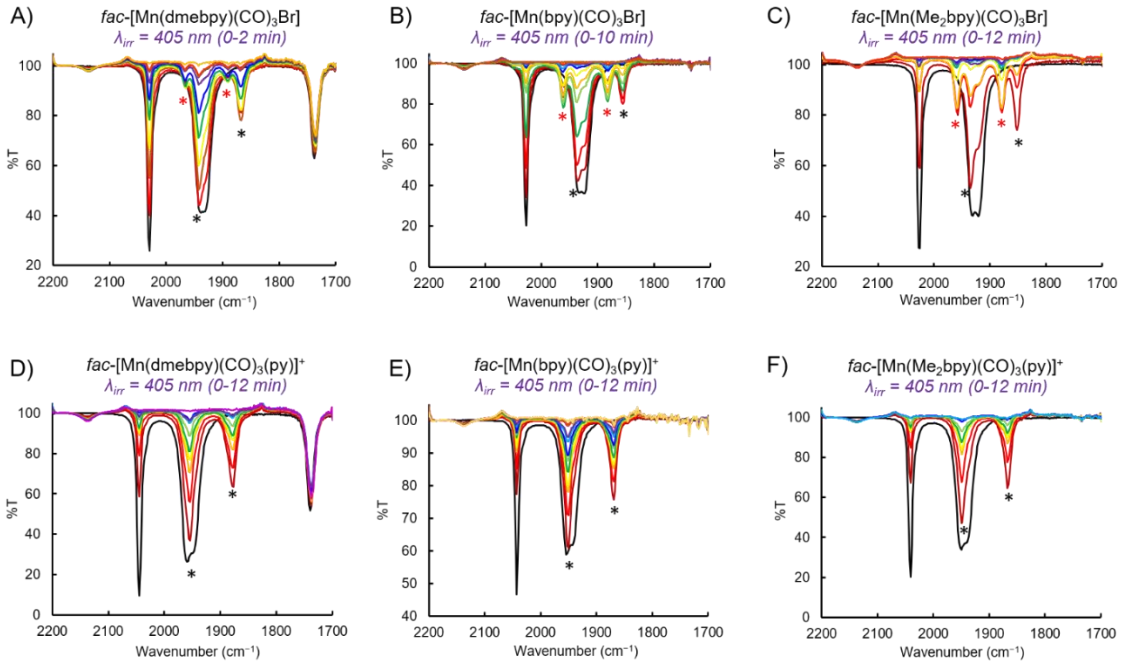

Figure A7. FTIR spectra for *fac*-[Mn(dmebpy)$(CO)_3$Br] (A), *fac*-[Mn(bpy)$(CO)_3$Br] (B), *fac*-[Mn(Me_2bpy)$(CO)_3$Br] (C), *fac*-[Mn(dmebpy)$(CO)_3$(py)]$^+$ (D), *fac*-[Mn(bpy)$(CO)_3$(py)]$^+$ (E), and *fac*-[Mn(Me_2bpy)$(CO)_3$(py)]$^+$ (F) in rt CH_3CN during photolysis with λ_{irr} = 405 nm. The first and second intermediate bands are denoted with black and red asterisks, respectively.

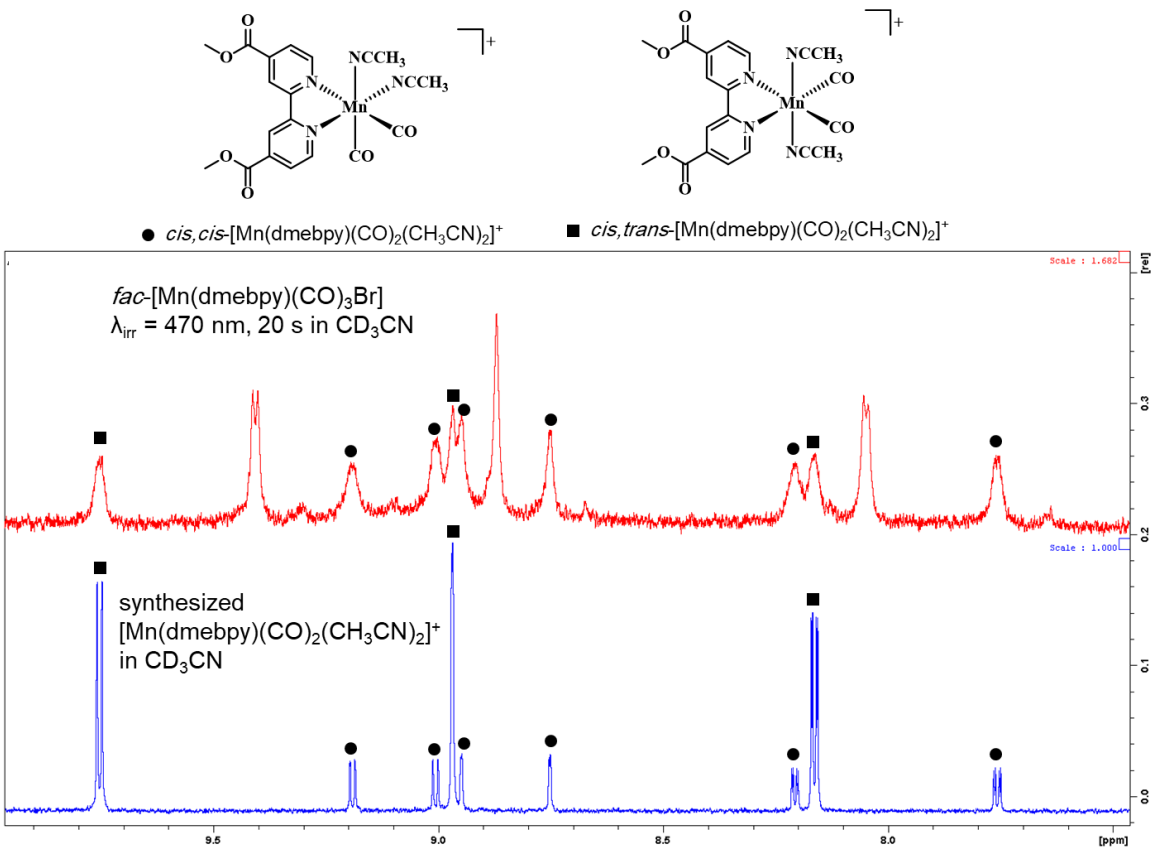

Figure A8. ^{1}H NMR spectra of a sample of *fac*-[Mn(dmebpy)(CO)$_3$Br] in CD_3CN following 470 nm irradiation for 20 s (red spectrum) and a mixture of synthesized *cis,cis*-[Mn(dmebpy)(CO)$_2$(CH$_3$CN)$_2$]$^+$ (circles) and *cis,trans*-[Mn(dmebpy)(CO)$_2$(CH$_3$CN)$_2$]$^+$ (squares) in CD_3CN (blue spectrum).

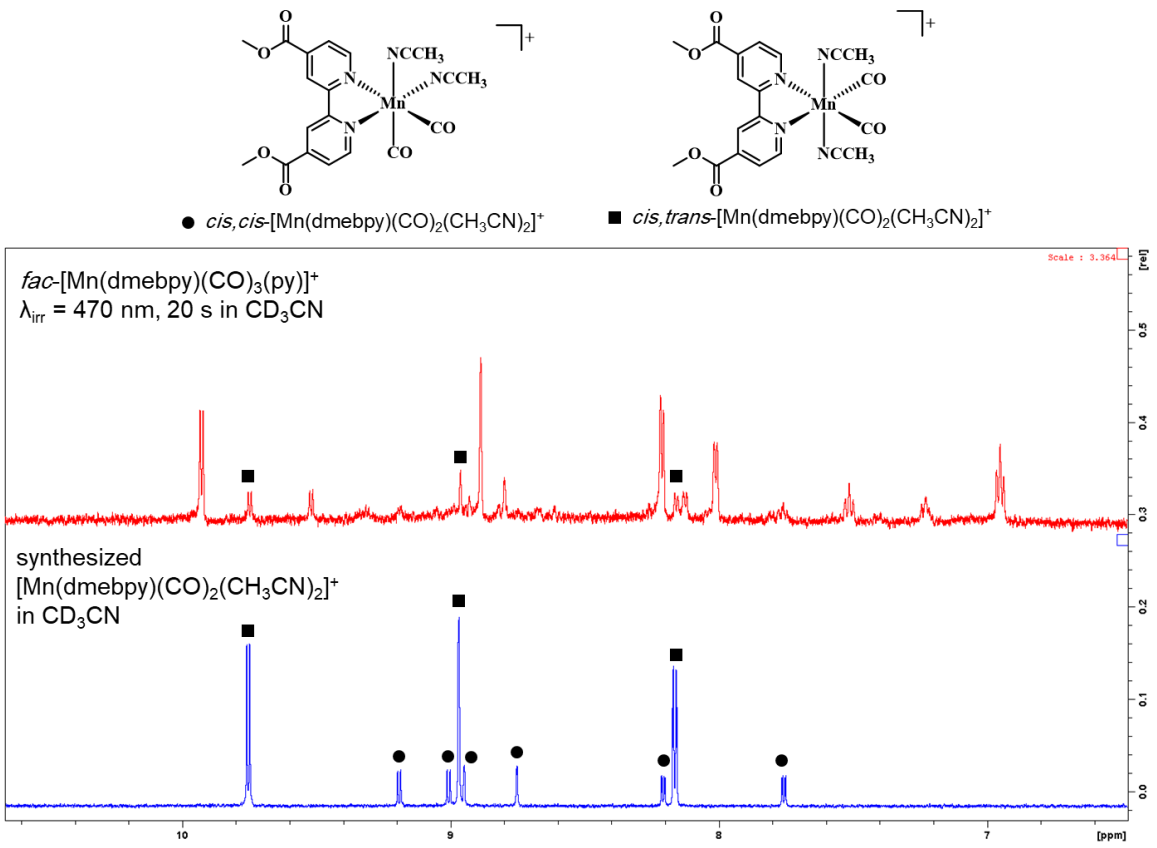

Figure A9. ^{1}H NMR spectra of a sample of *fac*-[Mn(dmebpy)(CO)$_3$(py)]$^+$ in CD_3CN following 470 nm irradiation for 20 s (red spectrum) and a mixture of synthesized *cis,cis*-[Mn(dmebpy)(CO)$_2$(CH$_3$CN)$_2$]$^+$ (circles) and *cis,trans*-[Mn(dmebpy)(CO)$_2$(CH$_3$CN)$_2$]$^+$ (squares) in CD_3CN (blue spectrum).

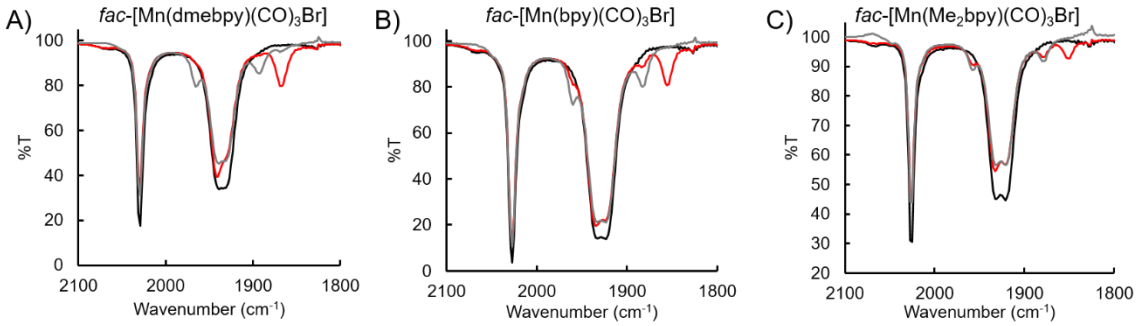

Figure A10. FTIR spectra for *fac*-[Mn(dmebpy)$(CO)_3$Br] (A), *fac*-[Mn(bpy)$(CO)_3$Br] (B), and *fac*-[Mn(Me_2bpy)$(CO)_3$Br] (C) in CH_3CN before irradiation (black), after irradiation for 10 s with 470 nm to form the first intermediate (red), and after storing the sample (containing the original species and first intermediate) in the dark in solution for 15 minutes (gray).

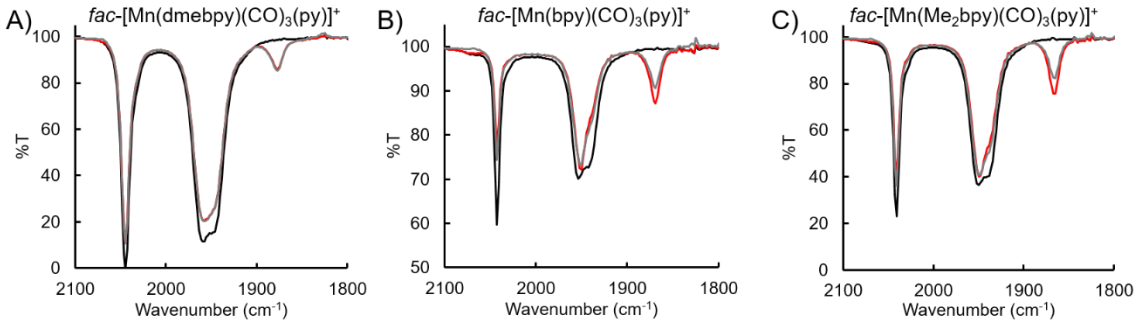

Figure A11. FTIR spectra for *fac*-$[Mn(dmebpy)(CO)_3(py)]^+$ (A), *fac*-$[Mn(bpy)(CO)_3(py)]^+$ (B), and *fac*-$[Mn(Me_2bpy)(CO)_3(py)]^+$ (C) in CH_3CN before irradiation (black), after irradiation for 10 s with 470 nm to form the first intermediate (red), and after storing the sample (containing the original species and first intermediate) in the dark in solution for 15 minutes (gray).

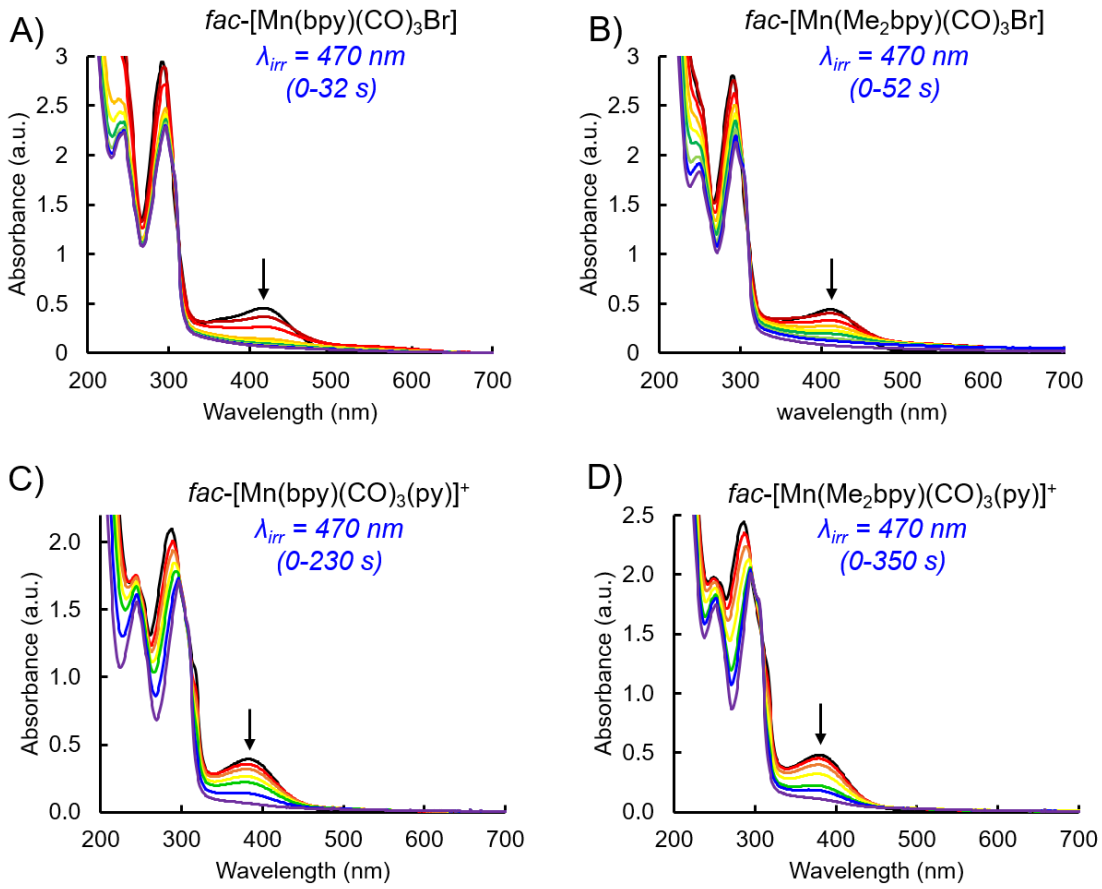

Figure A12. Electronic absorption spectra for *fac*-[Mn(bpy)(CO)$_3$Br] (A), *fac*-[Mn(Me$_2$bpy)(CO)$_3$Br] (B), *fac*-[Mn(bpy)(CO)$_3$(py)]$^+$ (C), and *fac*-[Mn(Me$_2$bpy)(CO)$_3$(py)]$^+$ (D) in rt CH_3CN during photolysis with λ_{irr} = 470 nm.

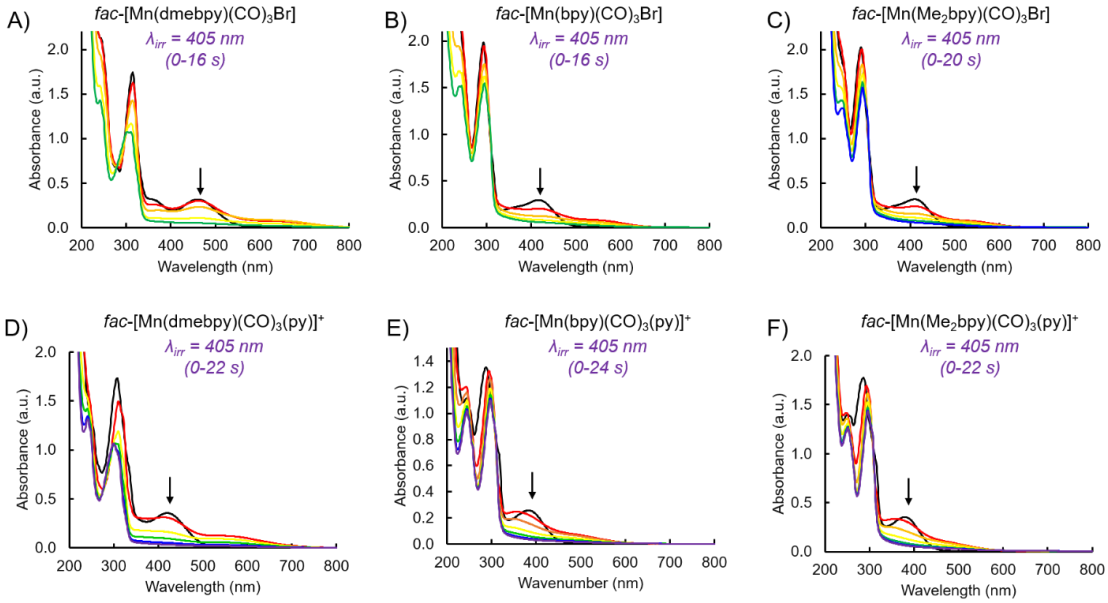

Figure A13. Electronic absorption spectra for *fac*-[Mn(dmebpy)$(CO)_3$Br] (A), *fac*-[Mn(bpy)$(CO)_3$Br] (B), *fac*-[Mn(Me_2bpy)$(CO)_3$Br] (C), *fac*-[Mn(dmebpy)$(CO)_3$(py)]$^+$ (D), *fac*-[Mn(bpy)$(CO)_3$(py)]$^+$ (E), and *fac*-[Mn(Me_2bpy)$(CO)_3$(py)]$^+$ (F) in rt CH_3CN during photolysis with λ_{irr} = 405 nm.

Summary of DFT coordinates:

(All coordinates are in units of Ångströms)

fac-[Mn(dmebpy)$(CO)_3$Br] energy-optimized geometry (0 charge, singlet multiplicity)

Atom	X	Y	Z
Br	0.00149	-2.08310	-2.13061
C	-3.68529	2.99931	-0.01537
C	3.68362	3.00102	-0.01591
O	4.99171	2.76575	0.02224
C	5.83335	3.91805	-0.09356
O	3.18509	4.09789	-0.14104
O	-3.18727	4.09658	-0.13897

O	-4.99328	2.76325	0.02125
C	-5.83547	3.91516	-0.09440
C	-3.46955	0.48859	0.25237
C	-2.63851	-0.61525	0.36602
N	-1.30370	-0.52246	0.35038
C	-0.73378	0.69640	0.22159
C	-1.50254	1.84793	0.10157
C	-2.88775	1.74492	0.11549
C	0.73320	0.69676	0.22167
N	1.30370	-0.52173	0.35127
C	1.50141	1.84858	0.10084
C	2.88667	1.74631	0.11547
C	2.63856	-0.61383	0.36745
C	3.46907	0.49039	0.25354
Mn	0.00041	-2.11153	0.43435
C	-0.00041	-2.12716	2.21192
O	-0.00083	-2.14336	3.37082
C	1.25558	-3.38712	0.34330
C	-1.25398	-3.38781	0.34208
O	2.05572	-4.21951	0.26400
O	-2.05355	-4.22066	0.26183
H	-4.54727	0.35809	0.27063
H	-3.06208	-1.61065	0.47498
H	-1.04592	2.82844	-0.00421

H	1.04433	2.82873	-0.00631
H	3.06261	-1.60895	0.47706
H	4.54685	0.36048	0.27241
H	6.85770	3.54453	-0.04565
H	5.65758	4.42476	-1.04821
H	5.64306	4.61355	0.73064
H	-6.85965	3.54106	-0.04737
H	-5.65937	4.42251	-1.04865
H	-5.64608	4.61029	0.73032

fac-[Mn(dmebpy)$(CO)_3$(py)]$^+$ energy-optimized geometry (+1 charge, singlet multiplicity)

Atom	X	Y	Z
N	-0.08450	-2.05832	1.34306
C	1.04835	-2.08620	2.06758
C	1.05537	-2.10927	3.45341
C	-0.15654	-2.10628	4.13276
C	-1.33184	-2.08292	3.39209
C	-1.25325	-2.06111	2.00862
C	3.75464	2.95291	0.06471
C	-3.60330	3.11380	0.02057
O	-4.91253	2.92687	-0.10528
C	-5.72952	4.07892	0.13422

O	-3.08049	4.16671	0.31131
O	3.27434	4.02845	0.34586
O	5.05510	2.71376	-0.06333
C	5.91737	3.83629	0.15645
C	3.49255	0.49195	-0.48555
C	2.64154	-0.58498	-0.68357
N	1.30953	-0.48185	-0.59460
C	0.76195	0.72633	-0.33093
C	1.55242	1.84647	-0.10807
C	2.93493	1.72868	-0.18052
C	-0.70508	0.76162	-0.35110
N	-1.30088	-0.41702	-0.64285
C	-1.44833	1.91499	-0.13317
C	-2.83304	1.85999	-0.23522
C	-2.63326	-0.45699	-0.76732
C	-3.43884	0.65480	-0.57236
Mn	-0.03198	-2.03541	-0.77157
C	0.01356	-1.90702	-2.56288
O	0.04163	-1.81036	-3.71273
C	-1.31048	-3.29448	-0.86699
C	1.18718	-3.35517	-0.79606
O	-2.11882	-4.11758	-0.93951
O	1.95810	-4.21611	-0.81413
H	1.98673	-2.08979	1.51650

H	2.00461	-2.13098	3.98212
H	-2.30726	-2.08381	3.87127
H	-2.16319	-2.04553	1.41179
H	4.56630	0.35377	-0.56802
H	3.04567	-1.56682	-0.91914
H	1.11338	2.81520	0.11425
H	-0.97282	2.86088	0.11299
H	-3.07610	-1.41585	-1.02635
H	-4.51563	0.56686	-0.68006
H	-0.18460	-2.12547	5.22009
H	-6.75984	3.74724	-0.00483
H	-5.58151	4.44417	1.15583
H	-5.48573	4.87373	-0.57832
H	6.93320	3.46285	0.01650
H	5.78952	4.22096	1.17361
H	5.70051	4.63018	-0.56583

cis,cis-[Mn(dmebpy)$(CO)_2(CH_3CN)$Br] energy-optimized geometry (0 charge, singlet multiplicity)

Atom	X	Y	Z
Br	-1.82705	-0.68496	-2.17111
C	-4.59270	0.89952	0.16715

C	-5.83829	1.61639	0.01561
O	4.21368	-4.09081	0.04615
O	4.85692	-1.93761	-0.07161
C	6.21661	-2.36884	-0.18274
O	1.45329	5.51189	0.07001
O	3.14263	4.03300	-0.07595
C	4.06331	5.12302	-0.18584
C	-0.39789	3.38526	0.28961
C	-1.22915	2.28191	0.39025
N	-0.76755	1.02712	0.36935
C	0.56140	0.81961	0.25176
C	1.45968	1.87790	0.14300
C	0.97244	3.17941	0.16056
C	0.96095	-0.59183	0.25174
N	-0.06139	-1.47268	0.36961
C	2.28253	-1.01346	0.14239
C	2.56579	-2.37351	0.15255
C	0.22307	-2.78404	0.38052
C	1.51229	-3.27476	0.27531
Mn	-1.91066	-0.69155	0.42896
C	-1.97456	-0.73991	2.18932
O	-2.01772	-0.79602	3.35333
C	-2.79092	-2.22891	0.32954
N	-3.59369	0.32546	0.28478

O	-3.37933	-3.23087	0.25845
H	-0.80679	4.39176	0.30939
H	-2.30519	2.40094	0.48956
H	2.52626	1.69853	0.04528
H	3.08854	-0.29208	0.04769
H	-0.61850	-3.46485	0.47710
H	1.69745	-4.34545	0.28746
C	1.86116	4.37134	0.04865
C	3.95123	-2.90792	0.03830
H	-6.65757	0.90996	-0.15943
H	-5.77486	2.30344	-0.83576
H	-6.05469	2.19212	0.92257
H	6.34970	-2.98872	-1.07567
H	6.81281	-1.45799	-0.26188
H	6.51074	-2.93887	0.70492
H	3.83932	5.72436	-1.07316
H	5.05237	4.67013	-0.27510
H	4.01439	5.75603	0.70647

cis,trans-[Mn(dmebpy)$(CO)_2(CH_3CN)$(py)]$^+$ energy-optimized geometry (+1 charge, singlet multiplicity)

Atom	X	Y	Z

N	2.18166	-0.00048	-1.57716
C	1.59241	-0.01137	3.58688
C	1.32287	-0.01037	5.00587
C	2.18723	-1.14771	-2.27965
C	2.20428	-1.18589	-3.66532
C	2.21956	0.01007	-4.37248
C	2.22071	1.20064	-3.65609
C	2.20296	1.15194	-2.27079
H	2.18122	-2.07293	-1.70675
H	2.20876	-2.14723	-4.17251
H	2.23843	2.16574	-4.15578
H	2.20939	2.07283	-1.69095
H	2.23565	0.01416	-5.46028
O	-2.85894	4.99281	0.06716
O	-2.88537	-4.97995	0.05386
O	-4.06423	-3.08646	-0.24620
O	-4.04653	3.10648	-0.24364
C	-5.23267	3.89528	-0.38912
C	-5.25471	-3.86882	-0.39107
C	-0.51554	-3.46656	0.33266
C	0.59302	-2.64375	0.44983
N	0.51772	-1.30989	0.36256
C	-0.69115	-0.73512	0.17673
C	-1.84776	-1.49655	0.03869

C	-1.75735	-2.88202	0.11236
C	-0.68717	0.73615	0.17941
N	0.52441	1.30392	0.36917
C	-1.83936	1.50418	0.04198
C	-1.74184	2.88890	0.12073
C	0.60656	2.63698	0.46180
C	-0.49746	3.46609	0.34577
Mn	2.12347	-0.00749	0.49841
C	3.39882	-1.24046	0.60574
O	4.24837	-2.03153	0.68031
C	3.40589	1.21740	0.61490
N	1.81451	-0.01142	2.45065
O	4.26026	2.00254	0.69662
H	-0.41482	-4.54567	0.40819
H	1.58063	-3.06943	0.61505
H	-2.81298	-1.02494	-0.11883
H	-2.80657	1.03811	-0.11940
H	1.59618	3.05670	0.63036
H	-0.39122	4.54438	0.42555
C	-2.94664	-3.77316	-0.02613
C	-2.92614	3.78666	-0.01761
H	1.85371	0.81913	5.48621
H	1.65865	-0.95357	5.45110
H	0.24765	0.10464	5.18282

H	-5.13314	4.58041	-1.23755
H	-6.04215	3.18538	-0.56766
H	-5.42371	4.46828	0.52430
H	-5.16042	-4.55258	-1.24120
H	-6.06090	-3.15437	-0.56630
H	-5.44678	-4.44288	0.52148

cis,cis-[Mn(dmebpy)$(CO)_2(CH_3CN)_2]^+$ energy-optimized geometry (+1 charge, singlet multiplicity)

Atom	X	Y	Z
N	1.86214	-0.77952	1.69730
C	4.74834	0.64040	-0.00339
C	6.02619	1.28975	0.17005
C	1.77198	-0.75126	2.85024
C	1.66171	-0.71984	4.28902
O	-4.27905	-3.95955	-0.07747
O	-4.82735	-1.78377	0.09747
C	-6.20622	-2.15595	0.19595
O	-1.11435	5.51805	-0.11123
O	-2.86690	4.11236	0.01735
C	-3.74554	5.24026	0.09375
C	0.64766	3.31608	-0.28294

C	1.43567	2.17840	-0.34881
N	0.92115	0.94554	-0.30210
C	-0.41662	0.79117	-0.19957
C	-1.27122	1.88693	-0.12312
C	-0.72972	3.16696	-0.16226
C	-0.87643	-0.60374	-0.19972
N	0.10528	-1.53003	-0.31918
C	-2.21553	-0.96770	-0.10294
C	-2.55712	-2.31445	-0.13533
C	-0.23423	-2.82661	-0.35408
C	-1.54605	-3.26004	-0.26733
Mn	1.99503	-0.82403	-0.33505
C	2.07437	-0.81275	-2.11378
O	2.12186	-0.81019	-3.27292
C	2.81962	-2.40422	-0.32141
N	3.72444	0.11867	-0.14484
O	3.37464	-3.42449	-0.32603
H	1.09651	4.30471	-0.32337
H	2.51628	2.25163	-0.44235
H	-2.34532	1.75317	-0.03666
H	-2.98935	-0.21232	-0.00409
H	0.57623	-3.54311	-0.45774
H	-1.77889	-4.32080	-0.29967
C	-1.57160	4.39700	-0.08424

C	-3.96717	-2.78987	-0.03749
H	6.76340	0.56824	0.53973
H	5.93509	2.10857	0.89250
H	6.37237	1.69480	-0.78735
H	2.54654	-1.18239	4.74003
H	0.76922	-1.27115	4.60523
H	1.58350	0.31677	4.63461
H	-6.36762	-2.79370	1.07137
H	-6.76030	-1.22143	0.30029
H	-6.52344	-2.68712	-0.70759
H	-3.51591	5.84329	0.97838
H	-4.75345	4.82814	0.16694
H	-3.65110	5.85833	-0.80516

cis,trans-[Mn(dmebpy)$(CO)_2(CH_3CN)_2]^+$ energy-optimized geometry (+1 charge, singlet multiplicity)

Atom	X	Y	Z
N	-2.14877	-0.07764	1.97448
C	-2.13049	0.11700	-3.10112
C	-2.01407	0.17563	-4.53922
C	-2.00131	-0.11909	3.12160
C	-1.82491	-0.16975	4.55391

O	2.67410	4.99400	0.03594
O	2.69067	-4.98534	-0.09756
O	3.90085	-3.08984	-0.01473
O	3.89114	3.10128	0.00235
C	5.08695	3.88904	0.00266
C	5.09894	-3.87410	-0.01209
C	0.30628	-3.46846	-0.10904
C	-0.80751	-2.64395	-0.10167
N	-0.71748	-1.30998	-0.05742
C	0.50489	-0.73520	-0.02471
C	1.66822	-1.49837	-0.01978
C	1.56676	-2.88442	-0.06255
C	0.50249	0.73618	0.00399
N	-0.72176	1.30729	0.02934
C	1.66338	1.50303	-0.00352
C	1.55730	2.88912	0.02265
C	-0.81638	2.64149	0.05107
C	0.29466	3.46970	0.05082
Mn	-2.32567	-0.00483	0.01516
C	-3.60471	-1.24916	-0.00359
O	-4.44919	-2.04565	-0.01308
C	-3.60909	1.23269	0.09318
N	-2.22995	0.07054	-1.94902
O	-4.45595	2.02487	0.14718

H	0.19560	-4.54863	-0.14610
H	-1.80800	-3.06880	-0.13110
H	2.64628	-1.02875	0.02077
H	2.64310	1.03616	-0.03412
H	-1.81841	3.06334	0.06884
H	0.18036	4.54994	0.07042
C	2.76302	-3.77714	-0.06081
C	2.75074	3.78560	0.02079
H	-2.54024	1.05815	-4.92015
H	-2.45408	-0.72260	-4.98656
H	-0.95870	0.23756	-4.82697
H	-2.68729	0.28742	5.05178
H	-0.91814	0.37556	4.83847
H	-1.73367	-1.21094	4.88281
H	5.13532	4.50769	0.90483
H	5.91338	3.17636	-0.01334
H	5.12092	4.53116	-0.88362
H	5.12279	-4.53112	0.86358
H	5.92285	-3.15943	0.02743
H	5.16141	-4.47716	-0.92391

fac-[Mn(bpy)$(CO)_3$Br] energy-optimized geometry (0 charge, singlet multiplicity)

Atom	X	Y	Z
Br	-1.04774	0.00019	2.09748
C	1.65808	-3.46869	-0.13240
C	0.56223	-2.63910	-0.31692
N	0.65341	-1.30371	-0.29781
C	1.86218	-0.73414	-0.09547
C	3.00546	-1.50533	0.09765
C	2.90207	-2.88881	0.08076
C	1.86209	0.73433	-0.09555
N	0.65326	1.30372	-0.29803
C	3.00525	1.50568	0.09759
C	2.90169	2.88914	0.08053
C	0.56191	2.63910	-0.31728
C	1.65765	3.46885	-0.13277
Mn	-0.93293	-0.00010	-0.47069
C	-0.84783	-0.00031	-2.24306
O	-0.79836	-0.00051	-3.40194
C	-2.21035	1.25356	-0.45054
C	-2.21023	-1.25388	-0.45018
O	-3.04621	2.05458	-0.41856
O	-3.04600	-2.05499	-0.41806
H	1.52657	-4.54699	-0.15638
H	-0.42611	-3.06044	-0.48698

H	3.97020	-1.03374	0.26244
H	3.97003	1.03422	0.26252
H	-0.42648	3.06030	-0.48745
H	1.52600	4.54713	-0.15688
H	3.78563	-3.50476	0.23168
H	3.78516	3.50522	0.23147

fac-[Mn(bpy)$(CO)_3$(py)]$^+$ energy-optimized geometry (+1 charge, singlet multiplicity)

Atom	X	Y	Z
N	1.41989	-0.00019	-0.87549
C	1.71529	-1.15096	-1.50581
C	2.29398	-1.19399	-2.76457
C	2.58903	-0.00010	-3.41085
C	2.29471	1.19373	-2.76415
C	1.71598	1.15062	-1.50541
C	-1.75494	-3.46431	-0.24256
C	-0.84213	-2.63731	0.39446
N	-0.85527	-1.30447	0.25772
C	-1.81658	-0.73408	-0.50413
C	-2.75542	-1.50456	-1.18361
C	-2.71969	-2.88619	-1.05673
C	-1.81622	0.73505	-0.50394

N	-0.85467	1.30479	0.25810
C	-2.75464	1.50616	-1.18328
C	-2.71826	2.88774	-1.05604
C	-0.84089	2.63758	0.39517
C	-1.75328	3.46519	-0.24167
Mn	0.53123	-0.00027	1.04917
C	-0.32295	-0.00036	2.62596
O	-0.88637	-0.00039	3.63422
C	1.68341	1.24685	1.63264
C	1.68289	-1.24806	1.63224
O	2.43704	2.03269	2.02303
O	2.43621	-2.03432	2.02241
H	1.48033	-2.07566	-0.98239
H	2.50784	-2.15673	-3.22140
H	2.50917	2.15651	-3.22063
H	1.48156	2.07527	-0.98168
H	-1.69849	-4.53950	-0.09763
H	-0.06832	-3.05712	1.03395
H	-3.51406	-1.03296	-1.80182
H	-3.44704	-3.50158	-1.58101
H	-3.51345	1.03507	-1.80167
H	-3.44529	3.50361	-1.58021
H	-0.06692	3.05685	1.03482
H	-1.69632	4.54031	-0.09646

H	3.04392	-0.00006	-4.39902

cis,cis-[Mn(bpy)$(CO)_2(CH_3CN)$Br] energy-optimized geometry (0 charge, singlet multiplicity)

Atom	X	Y	Z
Br	-0.57619	-0.62776	-2.14437
C	-3.57616	0.27039	0.26774
C	-4.97250	0.62146	0.14067
C	-0.20213	3.80237	0.11599
C	-0.70154	2.51978	0.29098
N	0.07749	1.43351	0.29018
C	1.40782	1.58471	0.11644
C	1.98137	2.84117	-0.06624
C	1.16588	3.96354	-0.06780
C	2.17606	0.33446	0.13663
N	1.44086	-0.78507	0.33283
C	3.55758	0.28119	-0.03472
C	4.20128	-0.94672	-0.00702
C	2.07303	-1.96684	0.36064
C	3.44369	-2.09386	0.19586
Mn	-0.55919	-0.53171	0.46452
C	-0.53032	-0.51137	2.22090
O	-0.50226	-0.52156	3.38836

C	-0.98790	-2.24974	0.46699
N	-2.45648	-0.01103	0.36376
O	-1.27979	-3.37813	0.46613
H	-0.87982	4.65207	0.12430
H	-1.76592	2.34908	0.43618
H	3.05379	2.94477	-0.20777
H	4.12605	1.19371	-0.19336
H	1.45216	-2.84544	0.52020
H	3.89882	-3.08027	0.22655
H	1.59617	4.95250	-0.20958
H	5.27890	-1.00527	-0.14205
H	-5.56226	-0.27060	-0.09927
H	-5.10292	1.35756	-0.66071
H	-5.34223	1.04868	1.07955

cis,trans-[Mn(bpy)$(CO)_2(CH_3CN)$(py)]$^+$ energy-optimized geometry (+1 charge, singlet multiplicity)

Atom	X	Y	Z
N	1.86146	-0.40275	0.07370
C	-3.20883	-1.52863	0.00619
C	-4.63904	-1.72955	-0.02250
C	2.56890	-0.29844	-1.06584

C	3.88094	0.14781	-1.10438
C	4.50741	0.50271	0.08376
C	3.78842	0.39107	1.26735
C	2.47950	-0.06291	1.21921
H	2.06288	-0.58809	-1.98476
H	4.39609	0.20852	-2.05956
H	4.22928	0.64719	2.22737
H	1.90191	-0.16317	2.13558
H	5.53688	0.85403	0.08793
C	-0.69863	1.30913	-3.57273
C	-0.49126	0.27094	-2.67609
N	-0.47445	0.44843	-1.34927
C	-0.69658	1.68716	-0.85553
C	-0.89908	2.77960	-1.69560
C	-0.89499	2.58851	-3.07048
C	-0.75174	1.77205	0.61309
N	-0.55946	0.60228	1.26208
C	-1.02912	2.94921	1.30381
C	-1.12926	2.91733	2.68768
C	-0.67526	0.57754	2.59563
C	-0.95968	1.70778	3.34813
Mn	-0.11631	-1.03480	0.06122
C	0.22167	-2.34993	-1.08075
O	0.43843	-3.22938	-1.81232

C	0.17037	-2.20352	1.36620
N	-2.06134	-1.37599	0.03002
O	0.36359	-2.98810	2.20427
H	-0.69996	1.10782	-4.64045
H	-0.32633	-0.74375	-3.03434
H	-1.06330	3.77273	-1.28691
H	-1.17634	3.88413	0.77096
H	-0.52652	-0.38581	3.08012
H	-1.04285	1.63013	4.42868
H	-1.05162	3.43167	-3.73926
H	-1.34623	3.82849	3.24040
H	-4.96320	-2.24361	0.88924
H	-4.91356	-2.33796	-0.89145
H	-5.15143	-0.76341	-0.08819

cis,cis-[Mn(bpy)$(CO)_2(CH_3CN)_2]^+$ energy-optimized geometry (+1 charge, singlet multiplicity)

Atom	X	Y	Z
N	0.54746	-0.50749	1.69353
C	3.63717	0.09832	-0.12579
C	5.04006	0.41950	-0.00596
C	0.51196	-0.41823	2.84643
C	0.47133	-0.30840	4.28528
C	0.34703	3.72003	-0.34359

C	0.81541	2.41601	-0.41659
N	0.00790	1.35450	-0.32646
C	-1.31989	1.54864	-0.17025
C	-1.85997	2.82911	-0.08338
C	-1.01519	3.92715	-0.16849
C	-2.12227	0.31879	-0.12181
N	-1.41786	-0.83126	-0.24929
C	-3.50667	0.31087	0.02690
C	-4.18398	-0.89979	0.04010
C	-2.08156	-1.99557	-0.24157
C	-3.45862	-2.07574	-0.10087
Mn	0.59644	-0.63563	-0.34152
C	0.60738	-0.68654	-2.11659
O	0.60538	-0.72557	-3.27736
C	0.98693	-2.37111	-0.30265
N	2.51224	-0.15806	-0.22536
O	1.25844	-3.50171	-0.29282
H	1.04442	4.54963	-0.42254
H	1.87432	2.20773	-0.55226
H	-2.92918	2.97214	0.04556
H	-4.05401	1.24351	0.13308
H	-1.48429	-2.89720	-0.35445
H	-3.94236	-3.04867	-0.10179
H	-1.42077	4.93422	-0.10312

H	-5.26499	-0.92147	0.15668
H	5.59646	-0.46029	0.33645
H	5.17785	1.23181	0.71637
H	5.43558	0.73507	-0.97788
H	0.92859	-1.19424	4.73969
H	-0.56760	-0.22855	4.62356
H	1.02148	0.58316	4.60605

cis,trans-[Mn(bpy)$(CO)_2(CH_3CN)_2]^+$ energy-optimized geometry (+1 charge, singlet multiplicity)

Atom	X	Y	Z
N	-0.90347	1.91982	-0.44485
C	-0.82292	-3.02527	0.70083
C	-0.68287	-4.42528	1.02667
C	-0.76119	3.03912	-0.70279
C	-0.59204	4.43700	-1.02398
C	1.57014	0.77361	3.38554
C	0.45618	0.59521	2.57763
N	0.54554	0.29113	1.27778
C	1.76898	0.15065	0.72080
C	2.93063	0.31530	1.47061
C	2.82941	0.63021	2.81871
C	1.76937	-0.18284	-0.71306
N	0.54622	-0.30141	-1.27584

C	2.93147	-0.36721	-1.45760
C	2.83091	-0.67914	-2.80647
C	0.45742	-0.60232	-2.57643
C	1.57189	-0.79958	-3.37933
Mn	-1.06410	0.00925	-0.00292
C	-2.34377	0.30029	1.20215
O	-3.19070	0.48811	1.97516
C	-2.34261	-0.25970	-1.21426
N	-0.94103	-1.90379	0.44013
O	-3.18886	-0.43324	-1.99133
H	1.44103	1.01966	4.43602
H	-0.54641	0.69957	2.98714
H	3.90841	0.19996	1.01141
H	3.90902	-0.26942	-0.99386
H	-0.54507	-0.68841	-2.99058
H	1.44336	-1.04225	-4.43067
H	3.72778	0.76165	3.41756
H	3.72959	-0.82588	-3.40130
H	-1.23968	-5.03405	0.30549
H	-1.07479	-4.61569	2.03211
H	0.37388	-4.71297	0.99536
H	-1.50305	4.82536	-1.49291
H	0.24738	4.56291	-1.71676
H	-0.38937	5.00872	-0.11141

fac-[Mn(Me_2bpy)($CO)_3$Br] energy-optimized geometry (0 charge, singlet multiplicity)

Atom	X	Y	Z
Br	-1.32611	-0.00024	2.11722
C	3.79115	-3.75091	0.14113
C	3.79091	3.75108	0.14167
C	1.31467	-3.46104	-0.19725
C	0.21350	-2.63836	-0.34995
N	0.29673	-1.30089	-0.33689
C	1.51145	-0.73467	-0.17134
C	2.65915	-1.50506	-0.01181
C	2.57920	-2.89514	-0.02104
C	1.51144	0.73469	-0.17129
N	0.29677	1.30086	-0.33722
C	2.65907	1.50511	-0.01127
C	2.57905	2.89520	-0.02057
C	0.21347	2.63833	-0.35027
C	1.31455	3.46104	-0.19723
Mn	-1.29480	-0.00006	-0.45692
C	-1.26738	0.00036	-2.22981
O	-1.25375	0.00072	-3.38999
C	-2.56894	1.25478	-0.39342
C	-2.56902	-1.25484	-0.39391

O	-3.40200	2.05754	-0.33347
O	-3.40223	-2.05748	-0.33433
H	1.18522	-4.54162	-0.21361
H	-0.77754	-3.06562	-0.48768
H	3.62820	-1.03005	0.12492
H	3.62810	1.03016	0.12585
H	-0.77757	3.06554	-0.48820
H	1.18507	4.54162	-0.21357
H	3.64125	-4.49442	0.93466
H	4.67779	-3.15465	0.38350
H	3.99543	-4.30863	-0.78311
H	3.64058	4.49525	0.93449
H	4.67741	3.15503	0.38495
H	3.99573	4.30804	-0.78294

fac-[Mn(Me_2bpy)($CO)_3$(py)]$^+$ energy-optimized geometry (+1 charge, singlet multiplicity)

Atom	X	Y	Z
N	-1.40351	-0.01332	1.24492
C	-1.44716	-1.14596	1.96828
C	-1.60312	-1.15495	3.34570
C	-1.72322	0.05538	4.01721
C	-1.68312	1.23067	3.27727
C	-1.52393	1.15325	1.90254

C	3.91721	-3.60995	0.48171
C	3.64199	3.88277	0.37333
C	1.53158	-3.41802	-0.28879
C	0.42958	-2.64201	-0.59668
N	0.43774	-1.30299	-0.51607
C	1.58236	-0.68740	-0.14504
C	2.72357	-1.41061	0.18464
C	2.71465	-2.80254	0.12532
C	1.52860	0.78143	-0.17032
N	0.34847	1.29920	-0.57848
C	2.60639	1.59672	0.15602
C	2.50011	2.98137	0.04390
C	0.24573	2.63047	-0.70656
C	1.28399	3.49463	-0.41096
Mn	-1.17016	-0.06269	-0.86044
C	-0.85192	-0.09912	-2.62345
O	-0.62939	-0.12132	-3.75691
C	-2.48362	1.13837	-1.09128
C	-2.39825	-1.36155	-1.01779
O	-3.33886	1.90033	-1.25476
O	-3.19956	-2.18858	-1.12933
H	-1.35265	-2.08332	1.42353
H	-1.63071	-2.10438	3.87388
H	-1.77567	2.20483	3.75021

H	-1.49041	2.06246	1.30543
H	1.46664	-4.50108	-0.37249
H	-0.49963	-3.10748	-0.91979
H	3.63483	-0.89718	0.48376
H	3.54198	1.16054	0.49827
H	-0.71079	3.01623	-1.05385
H	1.14159	4.56682	-0.53119
H	-1.84954	0.08215	5.09739
H	3.71283	-4.23418	1.36214
H	4.78124	-2.97437	0.70369
H	4.18395	-4.29188	-0.33618
H	3.31833	4.69978	1.03065
H	4.45904	3.34010	0.86104
H	4.03805	4.34690	-0.54041

cis,cis-[Mn(Me_2bpy)$(CO)_2$(CH_3CN)Br] energy-optimized geometry (0 charge, singlet multiplicity)

Atom	X	Y	Z
Br	-0.89673	-0.71917	-2.15156
C	-3.85956	0.37147	0.22291
C	-5.21996	0.83808	0.07723
C	-0.24543	3.64886	0.18531
C	-0.83716	2.40659	0.33207

N	-0.14068	1.26391	0.32703
C	1.19801	1.33014	0.17579
C	1.85863	2.54622	0.02341
C	1.13946	3.73837	0.02493
C	1.87969	0.02960	0.18590
N	1.06685	-1.03719	0.35651
C	3.25559	-0.11375	0.02877
C	3.83878	-1.37701	0.04441
C	1.62546	-2.25680	0.37154
C	2.98392	-2.46771	0.22194
Mn	-0.91507	-0.65416	0.46246
C	-0.91420	-0.65840	2.21763
O	-0.90589	-0.68527	3.38562
C	-1.45459	-2.33959	0.43609
N	-2.76785	0.00041	0.33535
O	-1.81571	-3.44805	0.41782
H	-0.86227	4.54597	0.19491
H	-1.91396	2.31426	0.45710
H	2.93948	2.57472	-0.09935
H	3.88388	0.76365	-0.11099
H	0.94882	-3.09759	0.50718
H	3.37490	-3.48356	0.24235
C	1.81310	5.06216	-0.12895
C	5.31113	-1.56773	-0.11417

H	-5.89396	-0.01185	-0.07860
H	-5.29530	1.51162	-0.78403
H	-5.53286	1.37750	0.97838
H	1.35943	5.63924	-0.94536
H	2.88354	4.95060	-0.33479
H	1.70075	5.66181	0.78470
H	5.52918	-2.26061	-0.93759
H	5.82321	-0.61968	-0.31338
H	5.74503	-2.00766	0.79419

cis,trans-[$Mn(Me_2bpy)(CO)_2(CH_3CN)(py)]^+$ energy-optimized geometry (+1 charge, singlet multiplicity)

Atom	X	Y	Z
N	-1.81472	0.00003	-1.03052
C	0.61172	0.00086	3.56366
C	1.38823	0.00110	4.78192
C	-2.07534	1.14933	-1.67905
C	-2.58330	1.19275	-2.96828
C	-2.84254	-0.00050	-3.63117
C	-2.58405	-1.19348	-2.96750
C	-2.07607	-1.14954	-1.67830
H	-1.87139	2.07212	-1.13989

H	-2.77238	2.15596	-3.43542
H	-2.77373	-2.15688	-3.43401
H	-1.87271	-2.07211	-1.13853
H	-3.24317	-0.00071	-4.64261
C	1.39619	3.46171	-0.22792
C	0.40661	2.64055	0.28956
N	0.43322	1.30718	0.18141
C	1.49047	0.73630	-0.44137
C	2.51048	1.50127	-0.99237
C	2.47785	2.89353	-0.89726
C	1.49020	-0.73703	-0.44103
N	0.43276	-1.30723	0.18205
C	2.50991	-1.50263	-0.99170
C	2.47680	-2.89483	-0.89588
C	0.40567	-2.64053	0.29086
C	1.39495	-3.46230	-0.22623
Mn	-1.01714	0.00040	0.88811
C	-2.16623	1.22848	1.45083
O	-2.93440	2.01871	1.82782
C	-2.16661	-1.22700	1.45152
N	-0.01566	0.00068	2.59045
O	-2.93500	-2.01678	1.82901
H	1.31767	4.54051	-0.10936
H	-0.44863	3.07062	0.80863

H	3.34862	1.02517	-1.49745
H	3.34820	-1.02710	-1.49707
H	-0.44972	-3.07003	0.81015
H	1.31605	-4.54101	-0.10713
C	3.57324	3.72241	-1.48115
C	3.57189	-3.72439	-1.47936
H	1.15392	-0.89008	5.37494
H	1.15560	0.89368	5.37350
H	2.45791	-0.00011	4.54476
H	3.36659	4.79331	-1.37893
H	3.71107	3.49336	-2.54603
H	4.52836	3.50715	-0.98308
H	3.36485	-4.79517	-1.37659
H	3.70979	-3.49594	-2.54435
H	4.52707	-3.50923	-0.98140

cis,cis-[Mn(Me_2bpy)(CO)$_2$(CH_3CN)$_2$]$^+$ energy-optimized geometry (+1 charge, singlet multiplicity)

Atom	X	Y	Z
N	0.89142	-0.70285	1.68714
C	3.95024	0.15689	-0.09463
C	5.32811	0.56802	0.04117
C	0.83718	-0.65564	2.84184

C	0.77122	-0.59762	4.28288
C	0.43579	3.57187	-0.24136
C	0.99042	2.30693	-0.32610
N	0.25523	1.18921	-0.28399
C	-1.08427	1.30191	-0.16079
C	-1.70602	2.54322	-0.06991
C	-0.94747	3.71072	-0.10820
C	-1.81164	0.02459	-0.14708
N	-1.03708	-1.07728	-0.28251
C	-3.19284	-0.06619	-0.01343
C	-3.82279	-1.30846	-0.02456
C	-1.63915	-2.27589	-0.29314
C	-3.00806	-2.43254	-0.16915
Mn	0.96357	-0.76147	-0.35185
C	0.98760	-0.75360	-2.12610
O	0.99398	-0.75390	-3.28789
C	1.44929	-2.47161	-0.36787
N	2.84508	-0.17063	-0.20688
O	1.77732	-3.58728	-0.39579
H	1.08095	4.44780	-0.27922
H	2.06501	2.17472	-0.43198
H	-2.78725	2.61352	0.02800
H	-3.79171	0.83455	0.10354
H	-0.99325	-3.14380	-0.40571

H	-3.43649	-3.43295	-0.18289
C	-1.58101	5.05963	-0.02456
C	-5.30545	-1.43427	0.09104
H	5.93442	-0.26983	0.40342
H	5.40302	1.39649	0.75451
H	5.71757	0.89624	-0.92900
H	1.22703	-1.49594	4.71364
H	-0.27386	-0.53663	4.60571
H	1.30939	0.28547	4.64480
H	-1.10635	5.66658	0.75729
H	-2.65355	4.99142	0.18829
H	-1.45347	5.60348	-0.97054
H	-5.58228	-2.28308	0.72833
H	-5.75748	-0.52277	0.49812
H	-5.75083	-1.61586	-0.89728

cis,trans-[Mn(Me_2bpy)(CO)$_2$(CH_3CN)$_2$]$^+$ energy-optimized geometry (+1 charge, singlet multiplicity)

N	1.27107	-0.00896	1.96284
C	1.14715	0.01396	-3.11224
C	0.99277	0.02167	-4.54827
C	1.13602	-0.01325	3.11239
C	0.97449	-0.01808	4.54768

C	-1.22826	3.46425	0.01569
C	-0.11363	2.64391	0.01044
N	-0.19344	1.30717	0.00433
C	-1.41766	0.73580	0.00358
C	-2.57843	1.50231	0.00758
C	-2.50192	2.89371	0.01193
C	-1.41786	-0.73733	-0.00042
N	-0.19295	-1.30890	-0.00646
C	-2.57794	-1.50353	0.00455
C	-2.50142	-2.89574	-0.00148
C	-0.11326	-2.64496	-0.00865
C	-1.22843	-3.46584	-0.00553
Mn	1.41739	-0.00059	0.00052
C	2.69443	1.24099	0.00748
O	3.53927	2.03922	0.01203
C	2.69485	-1.24177	-0.00293
N	1.27683	0.00818	-1.96208
O	3.53996	-2.03972	-0.00482
H	-1.10192	4.54520	0.02400
H	0.88629	3.07321	0.01343
H	-3.55658	1.02627	0.00833
H	-3.55610	-1.02748	0.01514
H	0.88653	-3.07463	-0.01012
H	-1.10169	-4.54666	-0.00366

C	-3.72930	3.74254	-0.00356
C	-3.73238	-3.73915	-0.02475
H	1.42002	-0.89243	-4.97537
H	1.50888	0.88899	-4.97491
H	-0.06975	0.07489	-4.81037
H	1.83875	-0.49901	5.01918
H	0.06736	-0.56880	4.82045
H	0.89250	1.00981	4.91818
H	-3.63679	4.58270	0.69586
H	-4.62384	3.16457	0.25416
H	-3.88282	4.17318	-1.00296
H	-3.57940	-4.68181	0.51387
H	-4.58856	-3.21306	0.41307
H	-3.99739	-3.99574	-1.06029

Table A1: X-ray crystal data and structure parameters for 4,4′-Me_2bpy-Br and 6,6′-Me_2bpy-Br.

Compound	4,4′-Me_2bpy-Br	6,6′-Me_2bpy-Br
Empirical formula	$C_{15}H_{12}BrMnN_2O_3$	$C_{15}H_{12}BrMnN_2O_3$
Formula weight	403.12	403.12
Crystal system	Monoclinic	Triclinic
Space group	$P2_1/c$	P-1
a/ Å	15.2930(12)	7.8133(8)
b/ Å	13.1490(10)	17.1490(15)
c/ Å	7.5014(6)	17.9215(18)
α(°)	90	73.446(4)
β(°)	95.145(3)	89.536(4)
γ(°)	90	79.143(4)
Volume ($Å^3$)	1502.4(2)	2257.9(4)
Z	4	6
Dc (Mg/m^3)	1.782	1.779
μ (mm^{-1})	3.551	3.544
F(000)	800	1200
reflns collected	37037	112390
indep. reflns	3751	11324
GOF on F^2	1.099	1.004
R1 (on F_o^2, $I > 2\sigma(I)$)	0.0481	0.0259
wR2 (on F_o^2, $I > 2\sigma(I)$)	0.1159	0.0614
R1 (all data)	0.0609	0.0350
wR2 (all data)	0.1204	0.0640

Table A2: X-ray crystal data and structure parameters for 4,4′-Me_2bpy-py and 6,6′-Me_2bpy-py.

Compound	4,4′-Me_2bpy-py	6,6′-Me_2bpy-py
Empirical formula	$C_{21}H_{17}F_3MnN_3O_6S$	$C_{21}H_{17}F_3MnN_3O_6S$
Formula weight	551.38	551.38
Crystal system	Monoclinic	Triclinic
Space group	$P2_1$	P-1
a/ Å	12.186(3)	8.725(5)

b/ Å	11.931(3)	11.379(6)
c/ Å	15.609(3)	11.891(7)
α(°)	90	105.02(2)
β(°)	94.620(6)	93.53(3)
γ(°)	90	97.11(2)
Volume ($Å^3$)	2261.8(8)	1126.1(12)
Z	4	2
Dc (Mg/m^3)	1.619	1.626
μ (mm^{-1})	0.745	0.748
F(000)	1120	560
reflns collected	52272	64224
indep. reflns	11373	5587
GOF on F^2	1.036	1.020
R1 (on F_o^2, I > 2σ(I))	0.1364	0.0248
wR2 (on F_o^2, I > 2σ(I))	0.3382	0.0666
R1 (all data)	0.2234	0.0265
wR2 (all data)	0.3836	0.0671

Table A3: Selected bond distances in Å for 4,4′-Me_2bpy-Br, 6,6′-Me_2bpy-Br, 4,4′-Me_2bpy-py, and 6,6′-Me_2bpy-py from X-ray crystallography.

Bond	4,4′-Me_2bpy-Br	6,6′-Me_2bpy-Br	4,4′-Me_2bpy-py	6,6′-Me_2bpy-py
Mn-$X_{(Br, N(py))}$	2.5327(7)	2.5423(4)	2.089(17)	2.1063(14)
		2.5270(4)	2.114(18)	
		2.5403(4)		
Mn−N(bpy)	2.023(3)	2.0787(16)	2.014(16)	2.0733(15)
	2.040(3)	2.0799(16)	2.065(16)	2.0670(16)
		2.0776(17)	2.040(19)	
		2.0843(16)	2.024(17)	
		2.0713(16)		
		2.0755(16)		
Mn−$C_{(C≡O)}$	1.822(4)	1.813(2)	1.79(3)	1.8130(17)
	1.828(4)	1.794(2)	1.796(19)	1.8185(16)
	1.809(4)	1.801(2)	1.81(2)	1.8088(16)
		1.799(2)	1.77(2)	
		1.815(2)	1.80(2)	
		1.804(2)	1.79(3)	

		1.806(2)		
		1.795(2)		
		1.806(2)		
C−$O_{(C\equiv O)}$	1.136(5)	1.145(2)	1.17(3)	1.1424(18)
	1.106(5)	1.151(3)	1.16(2)	1.1431(18)
	1.146(5)	1.149(2)	1.14(3)	1.1449(17)
		1.151(2)	1.20(3)	
		1.126(3)	1.18(3)	
		1.148(3)	1.19(3)	
		1.145(2)		
		1.145(2)		
		1.149(2)		

Table A4: Selected bond angles in degrees for 4,4′-Me_2bpy-Br, 6,6′-Me_2bpy-Br, 4,4′-Me_2bpy-py, and 6,6′-Me_2bpy-py from X-ray crystallography.

Angle	4,4′-Me_2bpy-Br	6,6′-Me_2bpy-Br	4,4′-Me_2bpy-py	6,6′-Me_2bpy-py
Br−Mn−N(bpy)	85.02(10)	87.61(5)	--	--
	86.80(9)	86.66(4)		
		87.68(4)		
		86.12(5)		
		87.30(5)		
		88.01(5)		
Br−Mn−$C_{(C\equiv O)}$	88.55(13)	82.48(7)	--	--
	88.19(12)	88.54(6)		
	179.07(13)	174.03(6)		
		86.43(7)		
		85.99(8)		
		175.34(6)		
		83.73(6)		
		88.52(7)		
		176.23(6)		
N(py)−Mn−N(bpy)	--	--	86.5(7)	85.07(6)
			85.4(6)	84.95(5)
			88.0(7)	
			85.4(7)	
N(py)−Mn−$C_{(C\equiv O)}$	--	--	90.8(8)	88.37(7)
			90.1(8)	88.73(6)
			179.3(8)	177.81(5)
			90.3(8)	
			94.0(9)	
			175.0(9)	
N(bpy)−Mn−$C_{(C\equiv O)}$	96.92(15)	97.00(8)	174.9(9)	98.90(6)
	94.48(15)	175.96(8)	93.5(8)	97.10(7)
	170.98(15)	96.53(8)	93.6(8)	172.10(5)
	94.79(15)	97.95(8)	95.7(8)	96.32(6)
	174.01(16)	100.01(7)	95.3(8)	95.78(6)

	93.88(15)	168.29(8) 99.69(8) 173.58(9) 95.37(8) 172.51(8) 99.27(8) 97.89(8) 96.40(7) 96.80(8) 175.82(8) 93.37(8) 170.91(8) 100.66(8)	172.1(8) 174.0(9) 95.6(9) 96.3(9) 96.9(8) 174.0(10) 87.7(9)	173.42(5)
$C_{(C\equiv O)}$−Mn−$C_{(C\equiv O)}$	88.82(17) 92.39(17) 90.74(17)	86.93(9) 93.19(9) 84.14(9) 81.00(9) 89.58(9) 91.01(10) 95.11(9) 87.78(9) 82.97(9)	89.2(9) 90.8(8) 89.2(9) 90.5(10) 87.7(10) 88.8(10)	85.33(7) 89.50(7) 90.60(6)
N(bpy)−Mn−N(bpy)	78.93(12)	78.58(6) 79.20(6) 78.96(6)	79.7(6) 78.9(7)	78.74(5)
Mn−$C_{(C\equiv O)}$−$O_{(C\equiv O)}$	177.8(4) 178.5(4) 179.2(4)	175.79(18) 174.45(17) 174.12(17) 171.95(19) 174.92(18) 172.42(19) 174.45(19) 175.87(17) 172.78(18)	178.2(19) 176.6(17) 177.0(19) 174.1(19) 176.7(19) 176(2)	175.60(12) 175.44(13) 176.80(12)

Table A5. Experimental and calculated C−O vibrational stretching frequencies for the photochemical intermediates during photolysis of 6,6′-Me_2bpy-Br and 6,6′-Me_2bpy-py

Photochemical intermediate	**Experimental ν(CO) (cm^{-1})** [a]	**Calculated ν(CO) (cm^{-1})** [b]
***cis,cis*-[Mn(6,6′-Me_2bpy)$(CO)_2$(CH_3CN)Br]**	*not observed*	1944, 1880
***cis,trans*-[Mn(6,6′-Me_2bpy)$(CO)_2$(CH_3CN)(py)]$^+$**	1948, 1863	1953, 1893

***cis,cis*-[Mn(6,6′-Me_2bpy)$(CO)_2(CH_3CN)_2]^+$**	*not observed*	1967, 1908
***cis,trans*-[Mn(6,6′-Me_2bpy)$(CO)_2(CH_3CN)_2]^+$**	1960, 1876 [c] (1958, 1875) [d]	1966, 1908

[a] Data collected in rt CH_3CN in a CaF_2 cell.
[b] Obtained from the energy optimized structures using the M06 level of DFT and the 6-31G* basis set for H, C, N, and O and the SDD basis set for Mn and Br.
[c] Obtained from intermediate bands observed during photolysis of 6,6′-Me_2bpy-Br.
[d] Approximate values obtained from the shoulders on the corresponding *cis,cis*-[Mn(6,6′-Me_2bpy)$(CO)_2(CH_3CN)(py)]^+$ intermediates bands during photolysis of 6,6′-Me_2bpy-py.

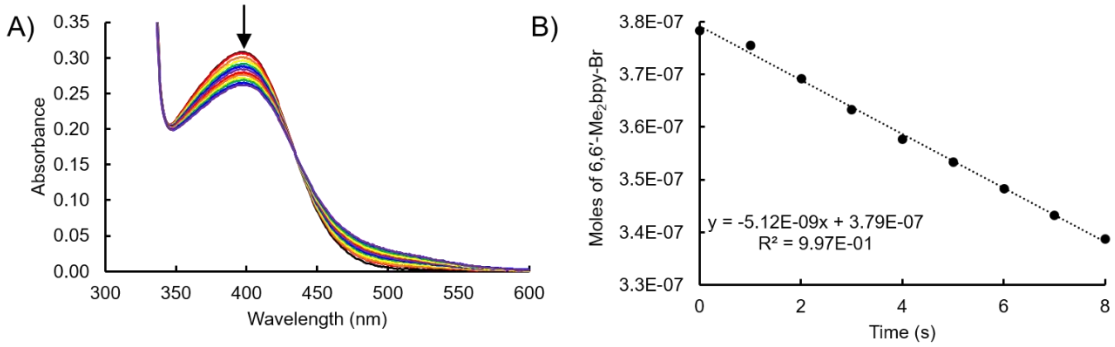

Figure A14. Change in absorbance as a function of 405 nm irradiation time for 110 μM 6,6′-Me_2bpy-Br in CH_3CN (A) and change in moles of 6,6′-Me_2bpy-Br vs irradiation time (B). Photon flux = 2.7×10^{-8} mol photons/s.

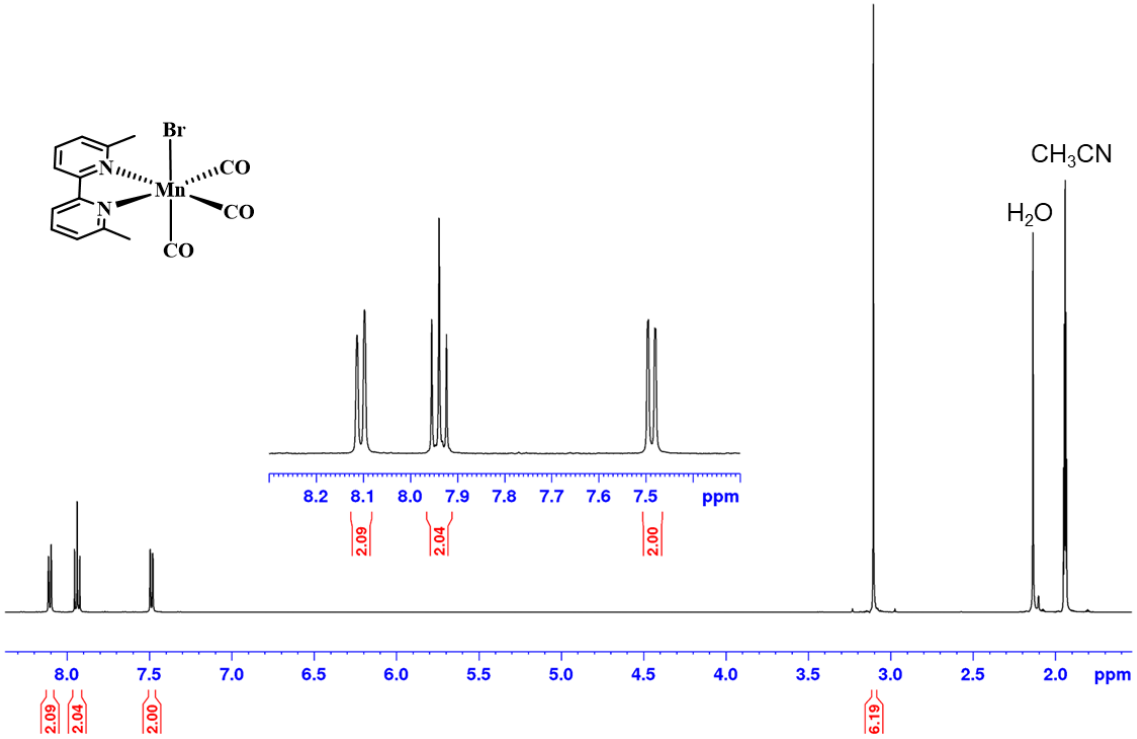

Figure A15. ^{1}H NMR of 6,6′-Me_2bpy-Br in CD_3CN.

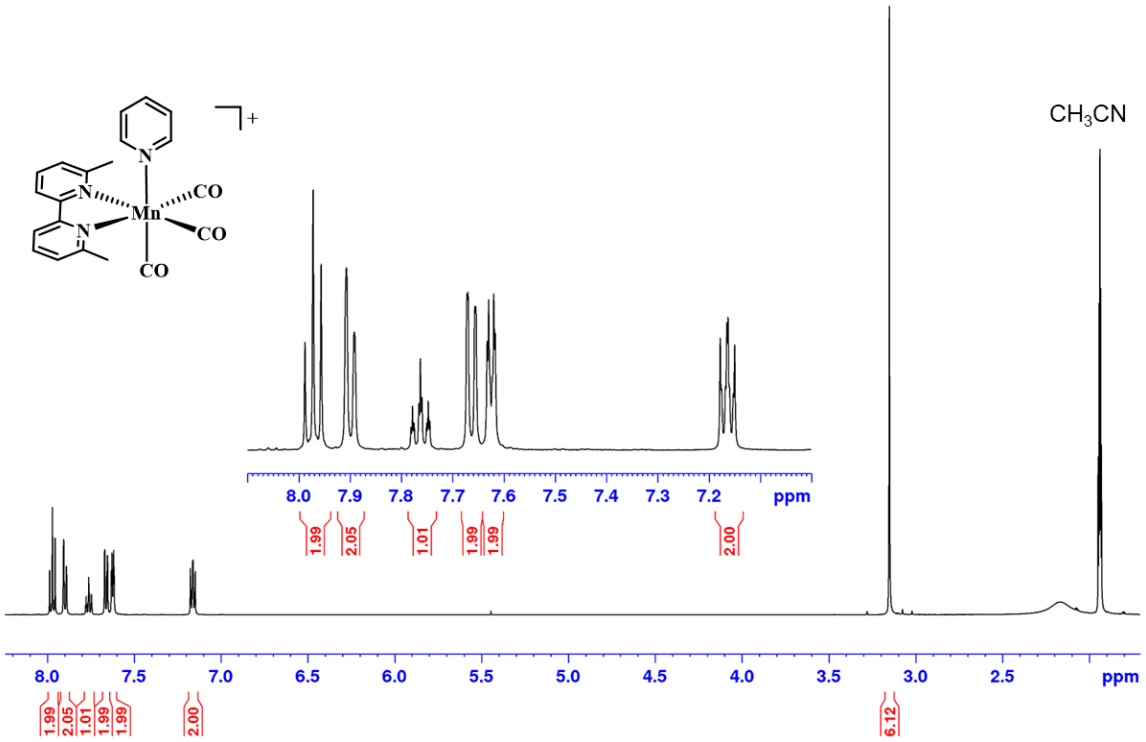

Figure A16. ^{1}H NMR of 6,6′-Me_2bpy-py in CD_3CN.

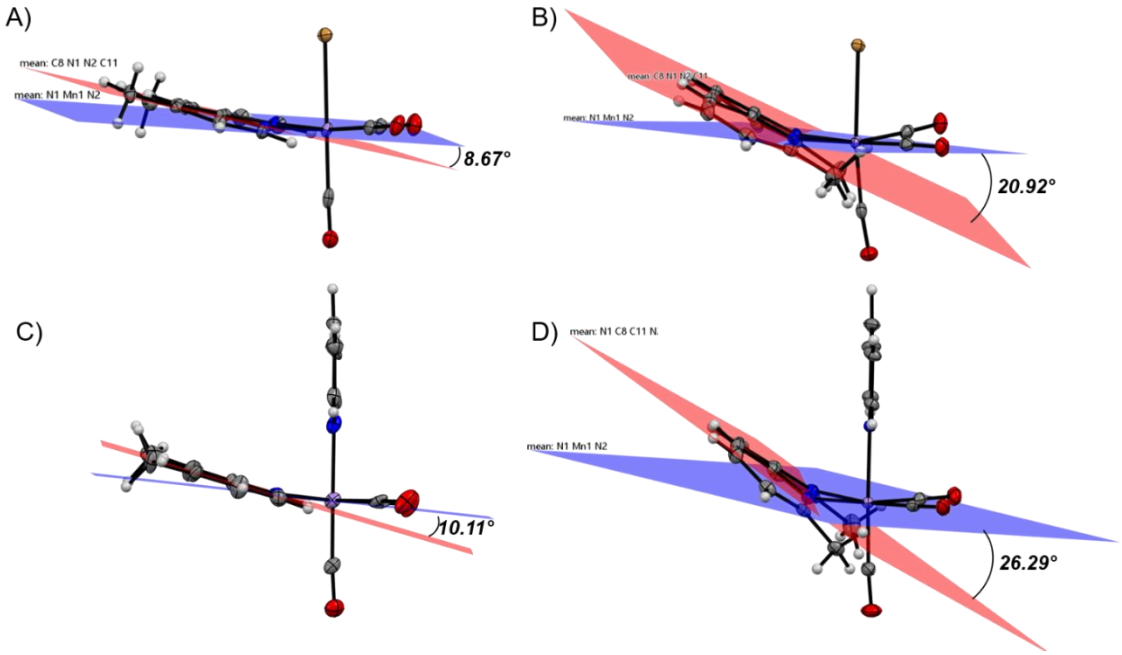

Figure A17. Crystal structures of 4,4′-Me_2bpy-Br (A), 6,6′-Me_2bpy-Br (B), 4,4′-Me_2bpy-py (C) and 6,6′-Me_2bpy-py (D) with the tilt angles between the plane defined by Mn(1), N(1), and N(2) (blue plane) and the plane defined by N(1), N(2), C(8), and C(11) (red plane).

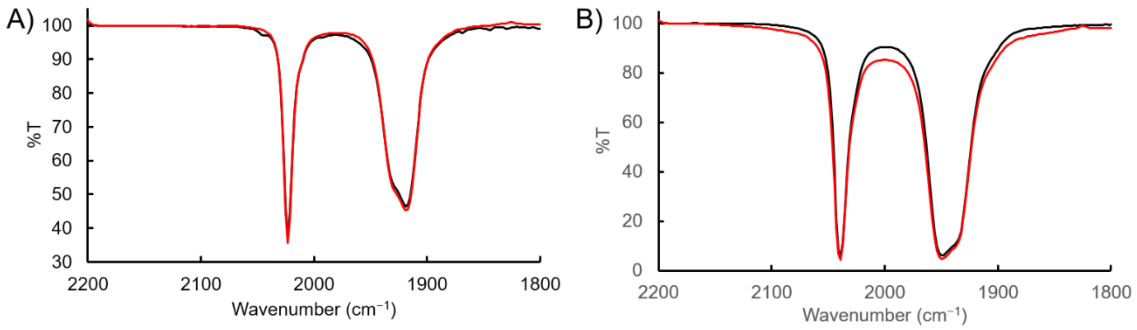

Figure A18. FTIR spectra for 6,6′-Me_2bpy-Br (A) and 6,6′-Me_2bpy-py (B) in CH_3CN in the dark at t = 0 (black) and 1 h (red).

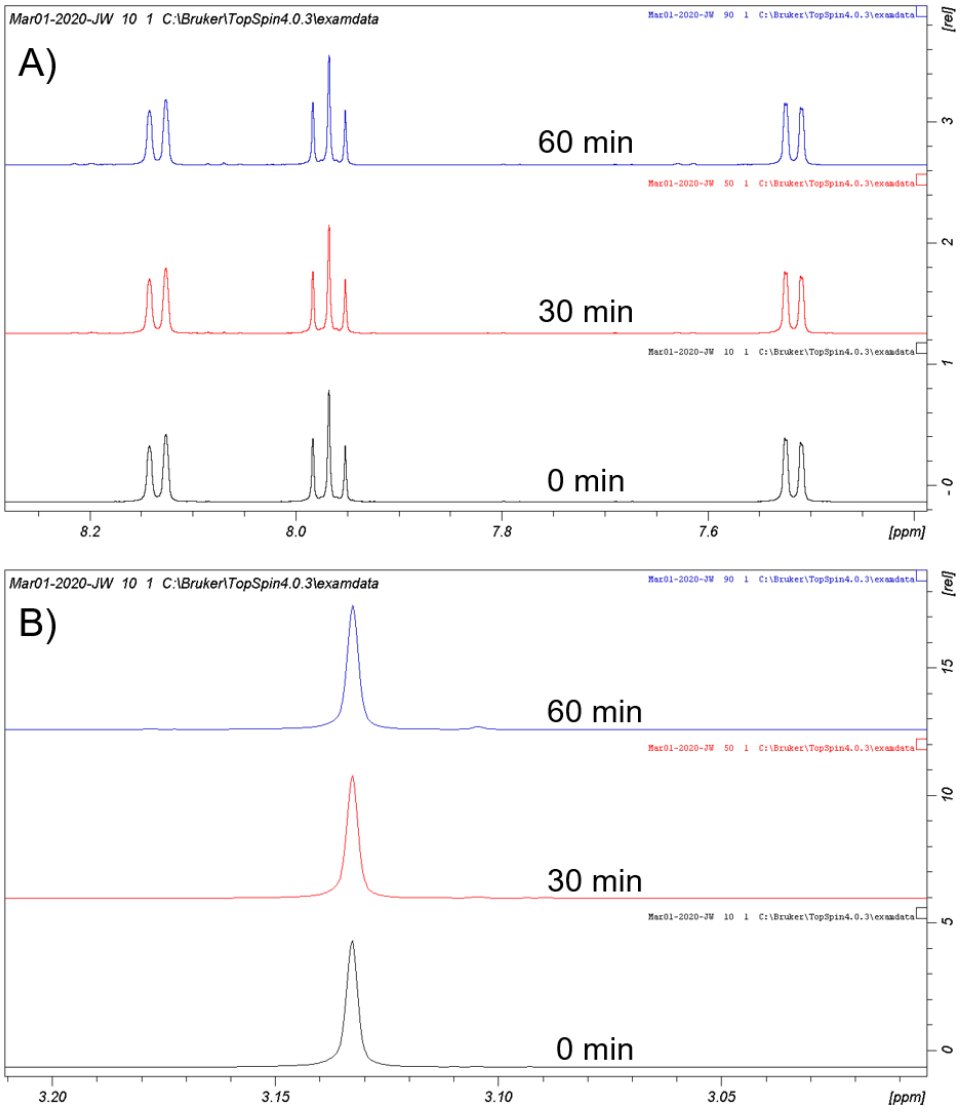

Figure A19. ^{1}H NMR spectra for 6,6′-Me_2bpy-Br in the aromatic region (A) and aliphatic region (B) in CD_3CN in the dark at t = 0 min (black), 30 min (red), and 60 min (blue).

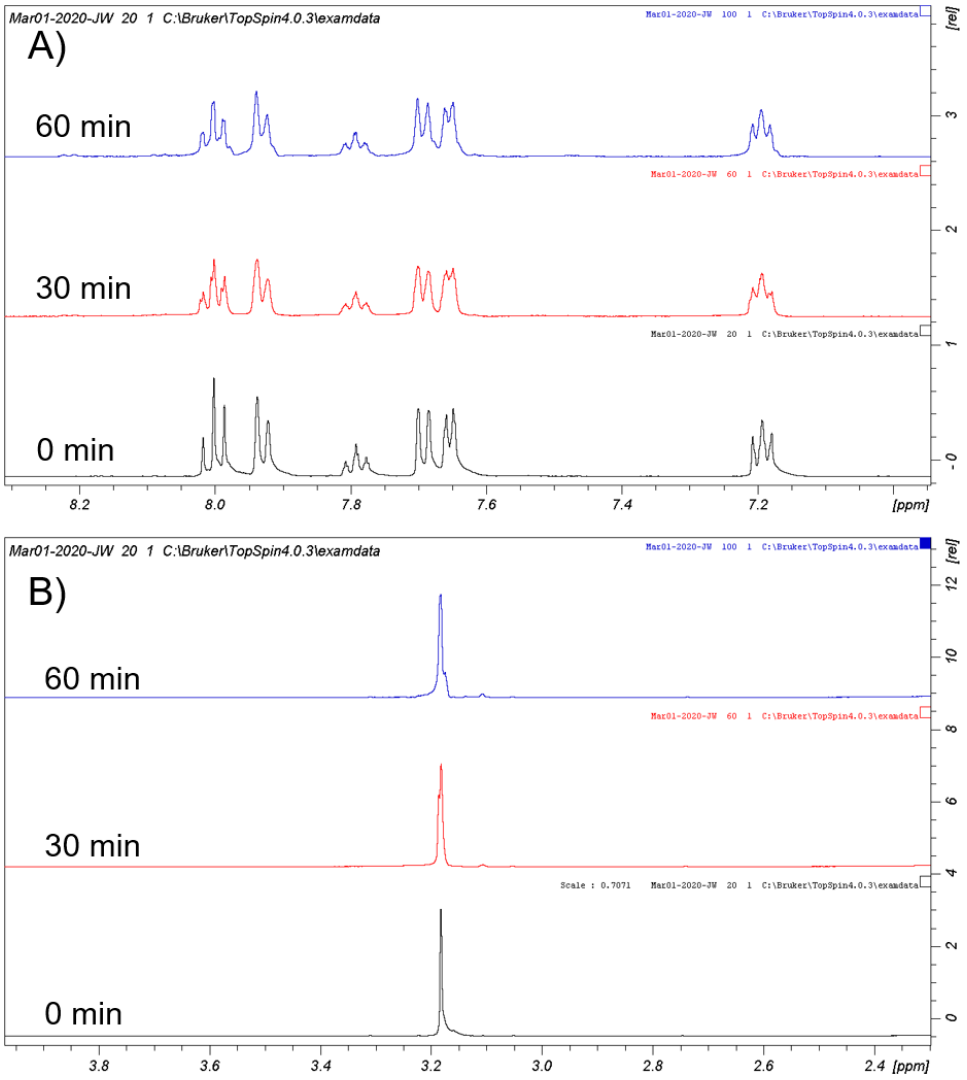

Figure A20. ^{1}H NMR spectra for 6,6′-Me_2bpy-py in the aromatic region (A) and aliphatic region (B) in CD_3CN in the dark at t = 0 min (black), 30 min (red), and 60 min (blue).

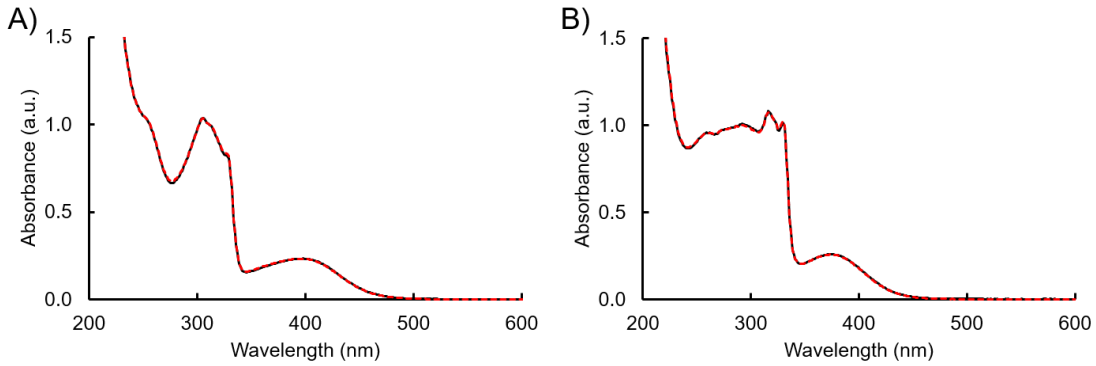

Figure A21. Electronic absorption spectra for 6,6′-Me_2bpy-Br (A) and 6,6′-Me_2bpy-py (B) in CH_3CN in the dark at t = 0 (black solid) and 1 h (red dashed).

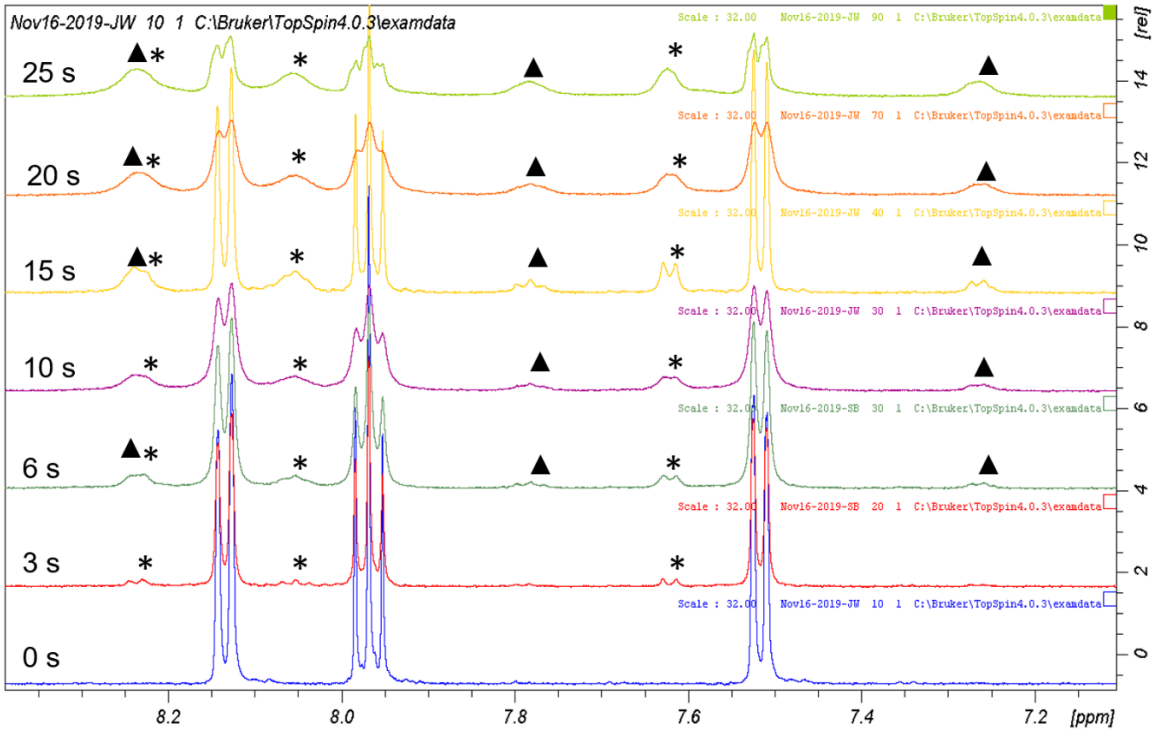

Figure A22. ^{1}H NMR spectrum of 6,6′-Me_2bpy-Br in CD_3CN irradiated with 405 nm light for 0, 3, 6, 10, 15, 20, and 25 s. Asterisks denote intermediate, and triangles denote free 6,6′-Me_2bpy ligand.

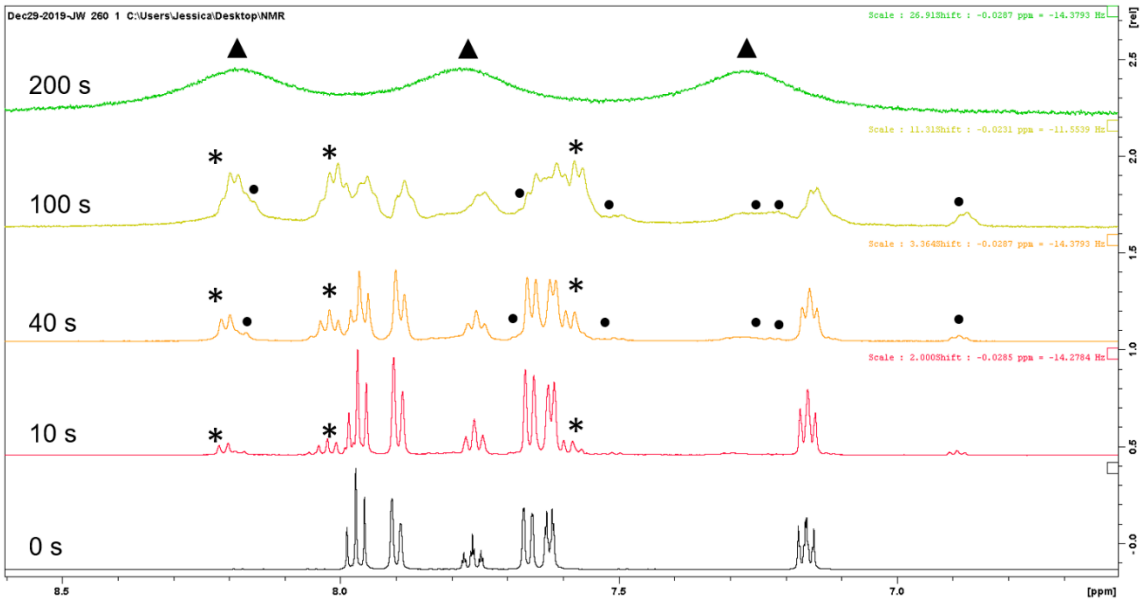

Figure A23. ^{1}H NMR spectrum of 6,6′-Me_2bpy-py in CD_3CN irradiated with 405 nm light for 0, 10, 40, 100, and 200 s. Asterisks denote *cis,trans*-[Mn(6,6′-Me_2bpy)$(CO)_2(CH_3CN)_2]^+$ intermediate, circles denote *cis,trans*-[Mn(6,6′-Me_2bpy)$(CO)_2(CH_3CN)$(py)]$^+$ and triangles denote free 6,6′-Me_2bpy ligand.

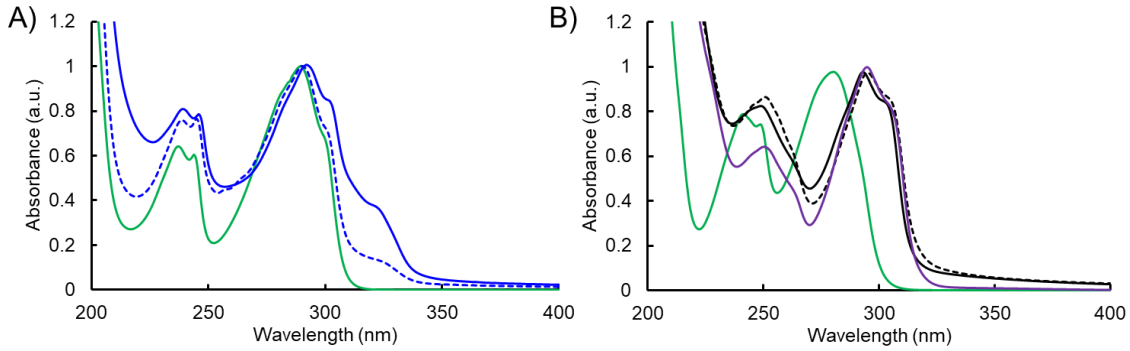

Figure A24. Electronic absorption spectra for the final photoproducts of 6,6′-Me_2bpy-Br (blue solid), 6,6′-Me_2bpy-py (blue dashed), and free 6,6′-Me_2bpy ligand (green) in CH_3CN (A), and final photoproducts of 4,4′-Me_2bpy-Br (black solid), 4,4′-Me_2bpy-py (black dashed), free 4,4′-Me_2bpy ligand (green), and [Mn(4,4′-Me_2bpy)$_3]^{2+}$ (purple) in CH_3CN (B).

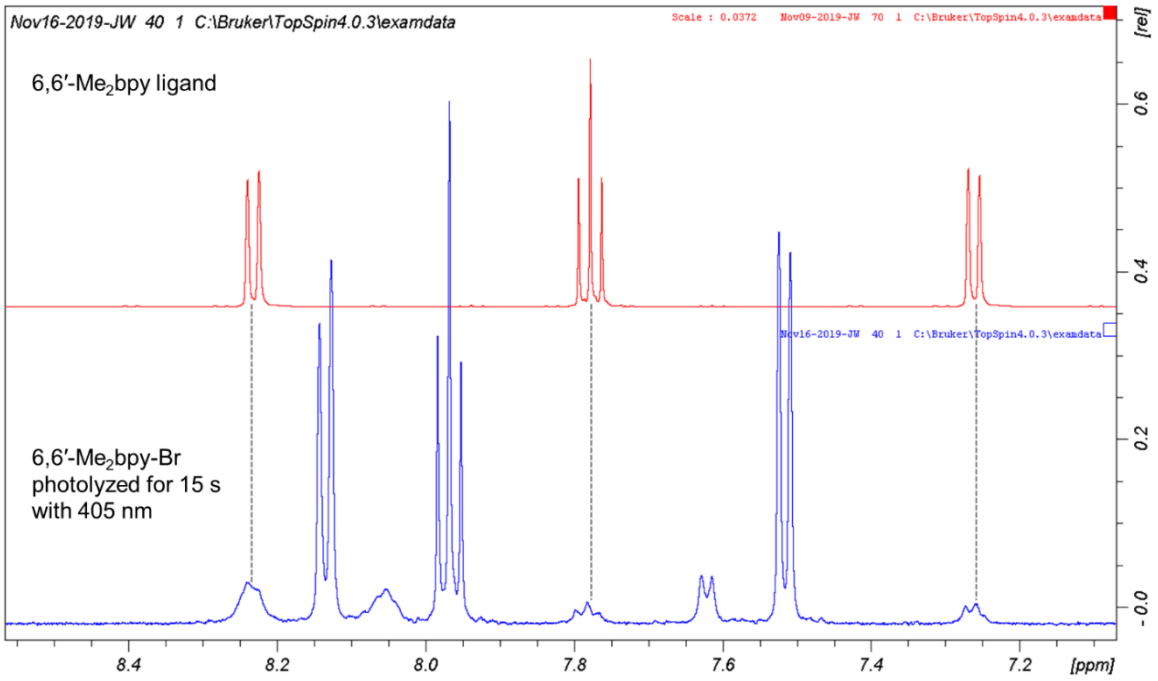

Figure A25. ^{1}H NMR spectrum of 6,6′-Me$_2$bpy in CD$_3$CN (red) and 6,6′-Me$_2$bpy-Br following irradiation with 405 nm light for 15 s.

Summary of DFT coordinates:

(All coordinates are in units of Ångströms)

6,6′-Me$_2$bpy-Br energy-optimized geometry (0 charge, singlet multiplicity)

Atom	X	Y	Z
Br	-0.08788	-0.56103	2.24707
C	3.49397	1.73120	-0.36029
C	2.69962	0.59852	-0.55164
N	1.35967	0.65455	-0.40284
C	0.78055	1.84912	-0.13015
C	1.52837	3.00423	0.07108
C	2.90948	2.93885	-0.02639
C	-0.69139	1.87026	-0.13158

N	-1.29985	0.70978	-0.47738
C	-1.41174	3.02602	0.14851
C	-2.79288	3.00439	0.02773
C	-2.63582	0.70325	-0.66102
C	-3.40271	1.84338	-0.41033
Mn	-0.00652	-0.93798	-0.30844
C	0.05240	-1.23052	-2.05770
O	0.09417	-1.43126	-3.19974
C	-1.22621	-2.21346	-0.02464
C	1.13113	-2.26511	0.06312
O	-1.92105	-3.11218	0.20455
O	1.76571	-3.19386	0.34206
C	-3.33235	-0.52425	-1.14734
C	3.37195	-0.67891	-0.93114
H	4.57092	1.64306	-0.48364
H	1.04540	3.95137	0.28871
H	3.51606	3.82765	0.13268
H	-0.90906	3.93731	0.45639
H	-3.37920	3.89358	0.24871
H	-4.47846	1.79562	-0.56386
H	-3.58305	-1.19608	-0.31615
H	-2.73031	-1.08233	-1.87276
H	-4.27699	-0.24594	-1.62831
H	3.51183	-1.32886	-0.05766

H	4.36791	-0.46711	-1.33579
H	2.80808	-1.23631	-1.68753

6,6′-Me_2bpy-py energy-optimized geometry (+1 charge, singlet multiplicity)

Atom	X	Y	Z
N	0.05196	0.30612	1.58356
C	1.22713	0.74784	2.06634
C	1.31644	1.68379	3.08467
C	0.14618	2.19046	3.63678
C	-1.07213	1.73751	3.14507
C	-1.07636	0.79990	2.12443
C	3.43307	1.09747	-1.48872
C	2.63222	0.00526	-1.14645
N	1.30466	0.15337	-0.95836
C	0.73337	1.35929	-1.20668
C	1.49067	2.47981	-1.52301
C	2.86680	2.34910	-1.64268
C	-0.73846	1.38536	-1.18710
N	-1.34519	0.20838	-0.89055

C	-1.46323	2.52223	-1.52234
C	-2.84618	2.44004	-1.59603
C	-2.68321	0.10578	-1.03020
C	-3.45374	1.21741	-1.37887
Mn	-0.02424	-1.12747	0.02924
C	-0.09798	-2.26501	-1.35732
O	-0.14709	-2.98582	-2.25894
C	-1.20400	-2.08264	0.98177
C	1.16236	-2.15348	0.89691
O	-1.87296	-2.74005	1.65982
O	1.83519	-2.86112	1.51836
C	-3.37458	-1.19797	-0.80856
C	3.28035	-1.32918	-0.98576
H	4.50078	0.94147	-1.62456
H	1.02160	3.44488	-1.68523
H	3.48190	3.21317	-1.88344
H	-0.96361	3.46029	-1.74262
H	-3.43602	3.31766	-1.85064
H	-4.53057	1.09899	-1.47441
H	-3.59330	-1.35763	0.25571
H	-2.78903	-2.04892	-1.17311
H	-4.33599	-1.19723	-1.33376
H	3.55152	-1.51724	0.06166
H	4.21078	-1.35602	-1.56372

H	2.64097	-2.14844	-1.33169
H	2.12941	0.33894	1.61371
H	2.29513	2.00311	3.43301
H	0.18291	2.92486	4.43863
H	-2.01652	2.10019	3.54208
H	-2.01733	0.43183	1.71750

cis,cis-[Mn(6,6′-Me_2bpy)$(CO)_2(CH_3CN)$Br] energy-optimized geometry (0 charge, singlet multiplicity)

Atom	X	Y	Z
Br	-0.13833	-0.40582	-2.23486
C	-3.39559	-0.97532	-0.27357
C	-4.78872	-1.11401	-0.63138
C	-1.36782	3.58918	0.49206
C	-1.43101	2.22937	0.80800
N	-0.39831	1.40700	0.54369
C	0.76059	1.93646	0.08311
C	0.87495	3.28015	-0.25597
C	-0.22067	4.11261	-0.07612
C	1.90796	1.01400	0.04973
N	1.65222	-0.26628	0.42139
C	3.18913	1.45065	-0.27061
C	4.24739	0.56018	-0.18274
C	2.69025	-1.11670	0.56965

C	3.99520	-0.72416	0.26595
Mn	-0.35237	-0.69780	0.38182
C	-0.49282	-0.99607	2.10415
O	-0.58155	-1.22311	3.24754
C	-0.29393	-2.43718	0.04850
N	-2.28516	-0.83052	0.01998
O	-0.37913	-3.57528	-0.18390
C	2.46558	-2.50521	1.06992
C	-2.65972	1.72028	1.49037
H	-2.22813	4.21934	0.70938
H	1.80299	3.68337	-0.64887
H	-0.16162	5.16540	-0.34420
H	3.36752	2.47677	-0.57660
H	5.25753	0.87526	-0.43527
H	4.80131	-1.44404	0.38991
H	2.13517	-3.17269	0.26379
H	1.71295	-2.53822	1.86558
H	3.40368	-2.91282	1.46386
H	-3.47316	1.54260	0.77466
H	-3.01803	2.47832	2.19793
H	-2.47419	0.79107	2.03593
H	-5.17532	-2.07909	-0.28531
H	-4.90587	-1.05492	-1.71946
H	-5.37460	-0.31124	-0.16759

cis,cis-[Mn(6,6′-Me_2bpy)$(CO)_2(CH_3CN)_2]^+$ energy-optimized geometry (+1 charge, singlet multiplicity)

Atom	X	Y	Z
N	0.21811	-0.25815	1.75337
C	3.42892	-0.97879	0.42467
C	4.82785	-1.08446	0.76625
C	0.15546	0.00866	2.87738
C	0.07655	0.33850	4.28046
C	1.34486	3.48912	-0.75707
C	1.42219	2.10583	-0.94448
N	0.39781	1.30376	-0.59863
C	-0.76569	1.86243	-0.18105
C	-0.88612	3.22830	0.04495
C	0.20027	4.05038	-0.22292
C	-1.91002	0.93967	-0.07264
N	-1.64528	-0.37200	-0.30956
C	-3.19952	1.40081	0.16803
C	-4.25540	0.50341	0.13001
C	-2.67803	-1.23705	-0.40501
C	-3.99145	-0.81693	-0.18514
Mn	0.36864	-0.77630	-0.22723
C	0.49703	-1.19701	-1.94506
O	0.57089	-1.48002	-3.07026

C	0.34171	-2.50409	0.19841
N	2.31542	-0.86489	0.12996
O	0.45795	-3.62577	0.47955
C	-2.43925	-2.66848	-0.75310
C	2.65620	1.54636	-1.57411
H	2.19616	4.10482	-1.04031
H	-1.81221	3.65718	0.41442
H	0.13446	5.12200	-0.04777
H	-3.38796	2.45174	0.36334
H	-5.27283	0.84004	0.31605
H	-4.79476	-1.54561	-0.26705
H	-2.11500	-3.24422	0.12323
H	-1.68138	-2.78231	-1.53610
H	-3.37083	-3.12201	-1.10939
H	3.46548	1.43715	-0.84022
H	3.01424	2.24312	-2.34179
H	2.48171	0.57285	-2.04006
H	5.21646	-2.06317	0.46367
H	4.96068	-0.96698	1.84754
H	5.39515	-0.30059	0.25019
H	0.52333	-0.46502	4.87639
H	-0.97139	0.46212	4.57513
H	0.61615	1.27182	4.47557

cis,trans-[Mn(6,6′-Me_2bpy)$(CO)_2(CH_3CN)_2]^+$ energy-optimized geometry (+1 charge, singlet multiplicity)

Atom	X	Y	Z
N	0.01334	0.44766	1.99934
O	1.78539	-2.64326	1.98254
C	-0.07043	-3.26396	-3.36095
C	0.02928	1.22267	2.85884
C	0.04984	2.18535	3.93506
C	3.47131	1.41022	-0.99566
C	2.67459	0.33409	-0.59700
N	1.34227	0.47172	-0.44608
C	0.76427	1.65614	-0.76315
C	1.51498	2.76283	-1.14556
C	2.89301	2.64088	-1.24480
C	-0.71178	1.68097	-0.76008
N	-1.32808	0.51747	-0.43770
C	-1.42626	2.81139	-1.14255
C	-2.80796	2.73564	-1.23638
C	-2.66496	0.42469	-0.58221
C	-3.42648	1.52595	-0.98111
Mn	-0.01283	-0.84795	0.51338
N	-0.03664	-1.92601	-1.12961
C	-0.05133	-2.51974	-2.12311

C	-1.19143	-1.86883	1.36551
C	1.13673	-1.90645	1.35894
O	-1.85936	-2.58612	1.99151
C	-3.36413	-0.86854	-0.32328
C	3.33062	-0.98324	-0.34698
H	4.54317	1.25947	-1.10277
H	1.03937	3.70997	-1.37890
H	3.50074	3.49371	-1.53927
H	-0.92010	3.74134	-1.38092
H	-3.38785	3.60752	-1.53124
H	-4.50320	1.41128	-1.08360
H	-3.55328	-1.00998	0.74881
H	-2.78712	-1.72594	-0.68603
H	-4.33828	-0.87016	-0.82501
H	3.52587	-1.13344	0.72280
H	4.29895	-1.01783	-0.85874
H	2.72023	-1.81930	-0.70493
H	-0.13571	1.67985	4.88945
H	-0.72640	2.94195	3.77558
H	1.02712	2.67902	3.97671
H	-0.22425	-4.32892	-3.15392
H	-0.88374	-2.90400	-4.00098
H	0.88145	-3.13705	-3.88868

cis,trans-[Mn(6,6′-Me_2bpy)$(CO)_2(CH_3CN)$(py)]$^+$ energy-optimized geometry (+1 charge, singlet multiplicity)

Atom	X	Y	Z
N	1.39111	-0.04835	-1.14653
C	2.13279	1.07104	-1.23369
C	3.50166	1.05467	-1.45226
C	4.14710	-0.16804	-1.59090
C	3.38935	-1.32981	-1.50658
C	2.02462	-1.22725	-1.28611
C	-4.96945	0.17693	0.73572
C	0.41008	3.42732	1.81561
C	-0.28716	2.67140	0.86991
N	-0.14998	1.33209	0.81217
C	0.60456	0.70746	1.74945
C	1.34228	1.41429	2.69215
C	1.25775	2.79941	2.70980
C	0.53478	-0.76627	1.75106
N	-0.25202	-1.32206	0.79711
C	1.17561	-1.53303	2.71765
C	0.97020	-2.90524	2.73168
C	-0.50560	-2.64479	0.84912
C	0.10026	-3.45824	1.80999
Mn	-0.65368	0.03157	-0.77735

N	-2.53042	0.09700	-0.16950
C	-3.61512	0.13235	0.23435
C	-0.96916	-1.10770	-2.09377
C	-0.87807	1.21087	-2.07779
O	-1.16185	-1.76197	-3.03881
O	-1.01710	1.89110	-3.01384
C	-1.43950	-3.26982	-0.13384
C	-1.18472	3.37719	-0.09190
H	0.27832	4.50702	1.82787
H	1.96913	0.90016	3.41405
H	1.82807	3.37550	3.43521
H	1.81456	-1.07307	3.46501
H	1.46383	-3.52757	3.47491
H	-0.12371	-4.52265	1.81511
H	-0.92148	-3.52053	-1.06937
H	-2.28057	-2.61176	-0.37565
H	-1.83547	-4.20647	0.27480
H	-0.65943	3.60490	-1.02934
H	-1.50726	4.33355	0.33535
H	-2.07379	2.78569	-0.33362
H	1.60440	2.01637	-1.12015
H	4.04422	1.99460	-1.51263
H	5.21993	-0.21454	-1.76541
H	3.84120	-2.31285	-1.61134

H	1.40911	-2.12264	-1.21628
H	-5.67654	0.21128	-0.10072
H	-5.17542	-0.71441	1.33891
H	-5.10985	1.06819	1.35751

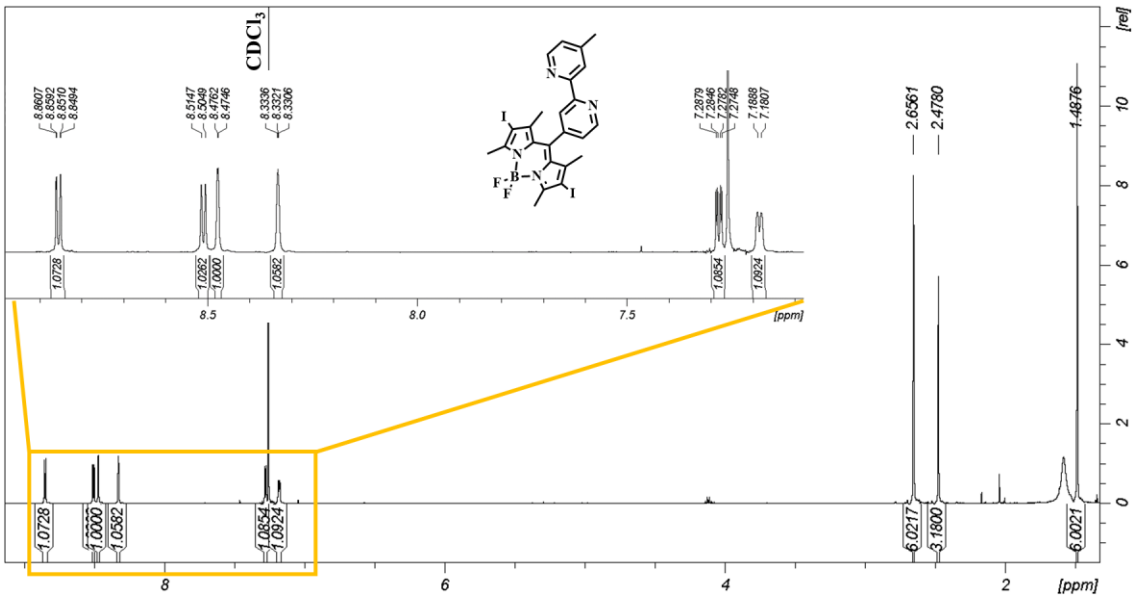

Figure A26. ^{1}H NMR spectrum of bpy-I-BDP in $CDCl_3$

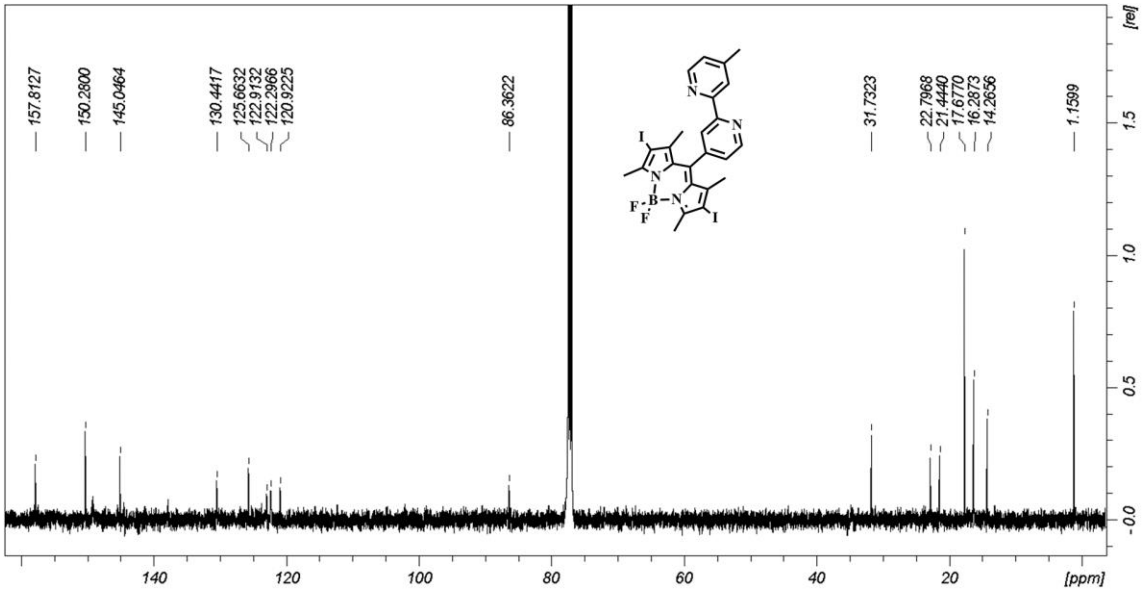

Figure A27. ^{13}C NMR spectrum of bpy-I-BDP in $CDCl_3$

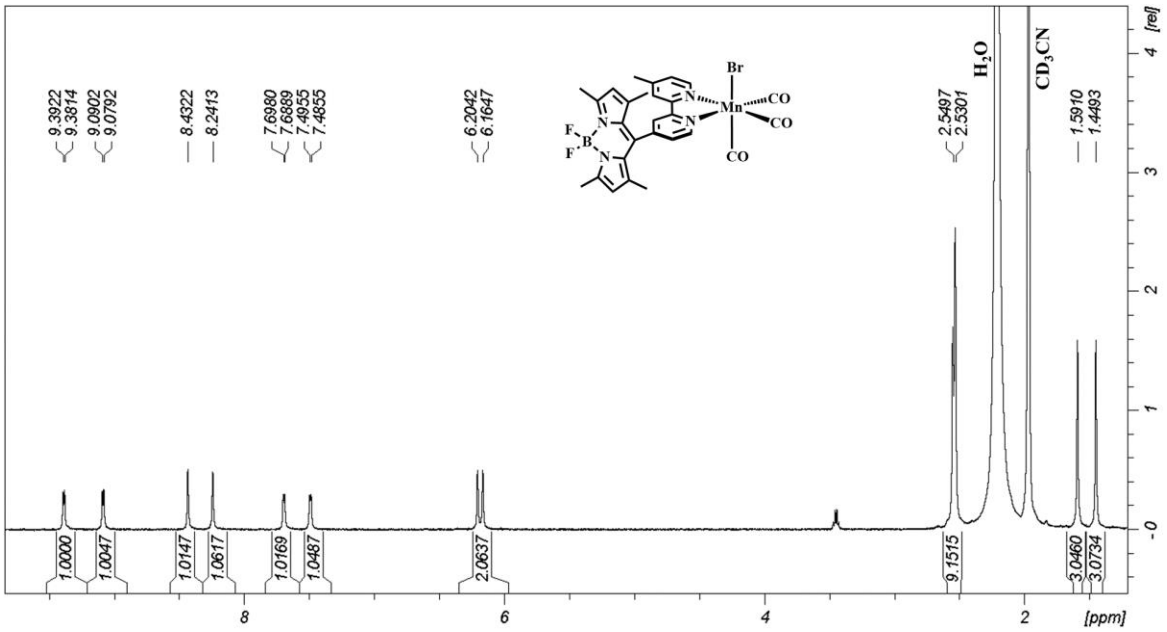

Figure A28. ^{1}H NMR spectrum of Mn-bpy-H-BDP in CD_3CN

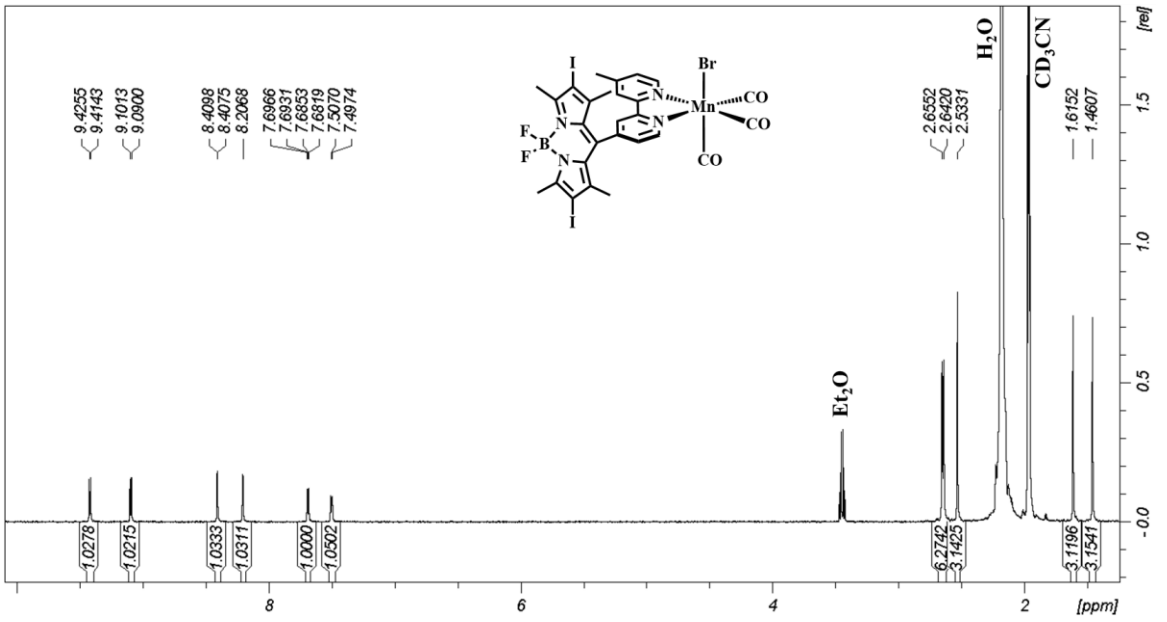

Figure A29. ^{1}H NMR spectrum of Mn-bpy-I-BDP in CD_3CN

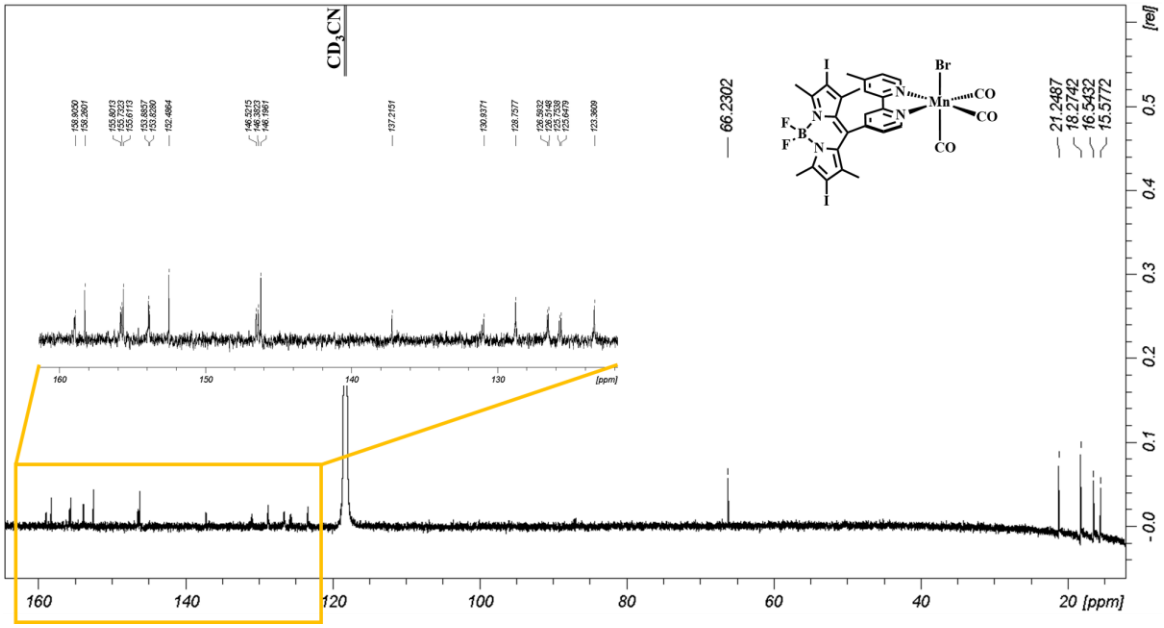

Figure A30. ^{13}C NMR spectrum of Mn-bpy-I-BDP in CD_3CN

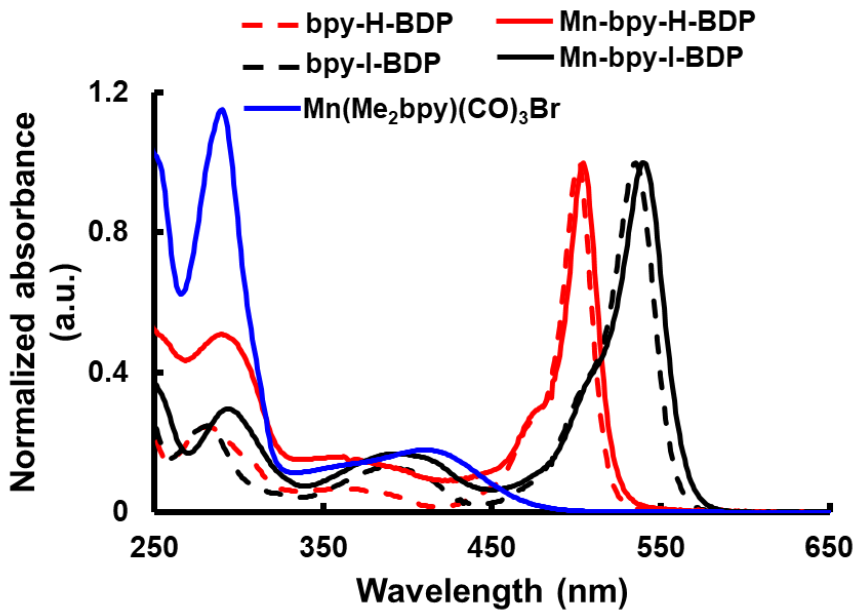

Figure A31. Overlaid electronic absorption spectra for bpy-H-BDP (red dashed), bpy-I-BDP (black dashed), Mn-bpy-H-BDP (red solid) and Mn-bpy-I-BDP (black solid) and $Mn(Me_2bpy)(CO)_3Br$ (blue solid) in room temperature CH_3CN

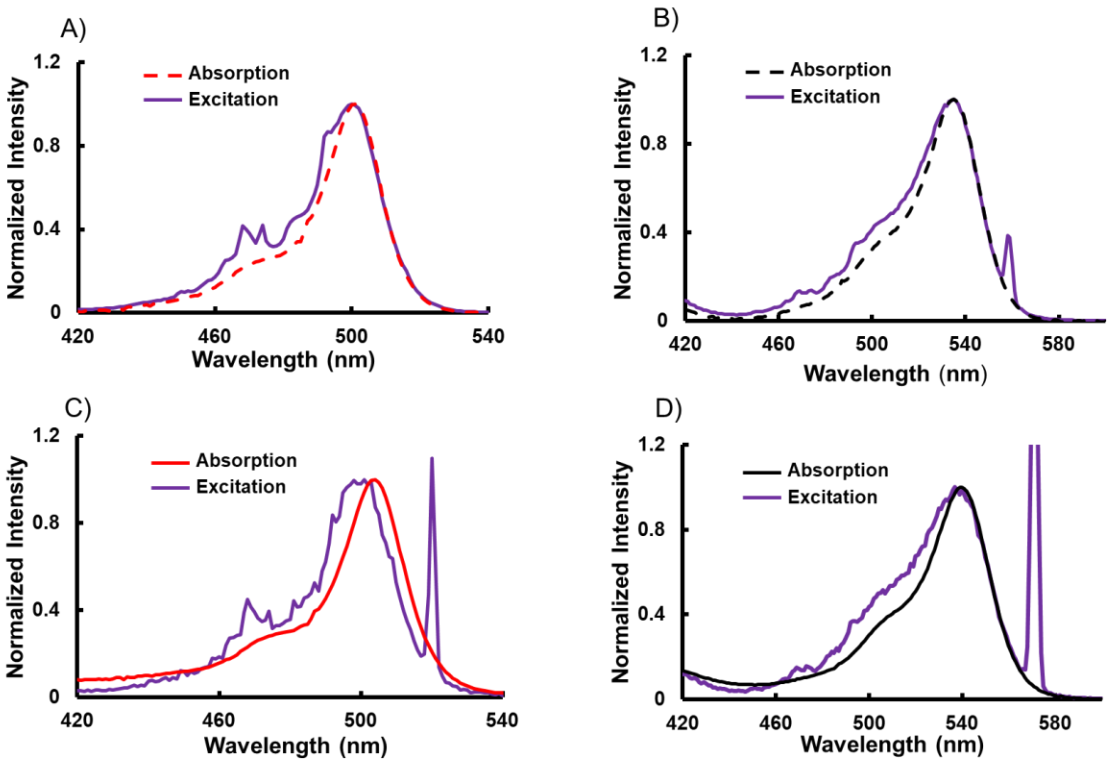

Figure A32. Overlaid absorption and excitation spectra of bpy-H-BDP (A) bpy-I-BDP (B) Mn-bpy-H-BDP (c) and Mn-bpy-I-BDP (D) in room temperature CH_3CN

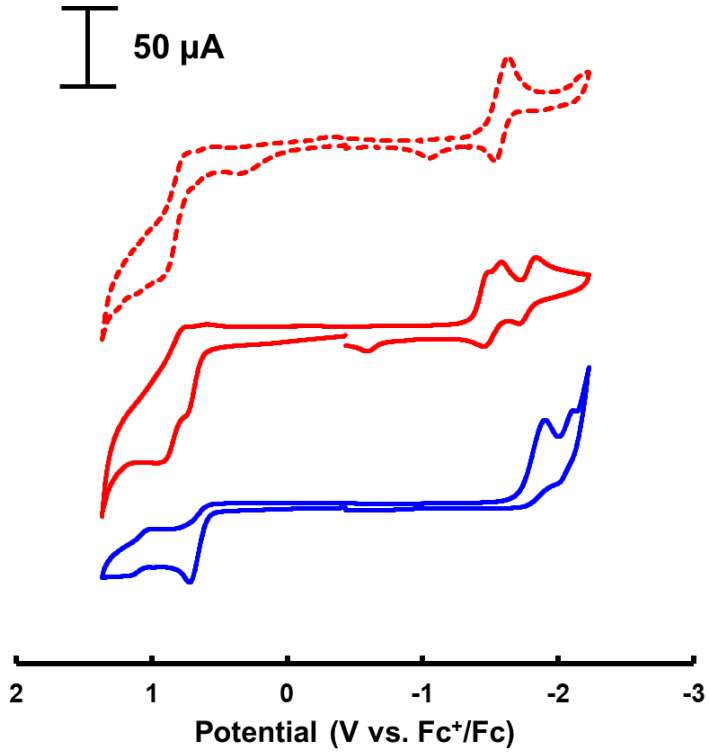

Figure A33. Cyclic voltammograms for 1 mM solutions of bpy-H-BDP (red dashed), Mn-bpy-H-BDP (red solid), and fac-[Mn(Me_2bpy)($CO)_3$Br] (blue solid), in room temperature DCM under a N_2 atmosphere with 0.1 M Bu_4NPF_6 as the supporting electrolyte, a glassy carbon working electrode, wire auxiliary electrode, Ag/AgCl reference electrode, and a scan rate of 200 mV/s. Potentials are referenced to the Fc^+/Fc couple (+0.43 V vs. Ag/AgCl)

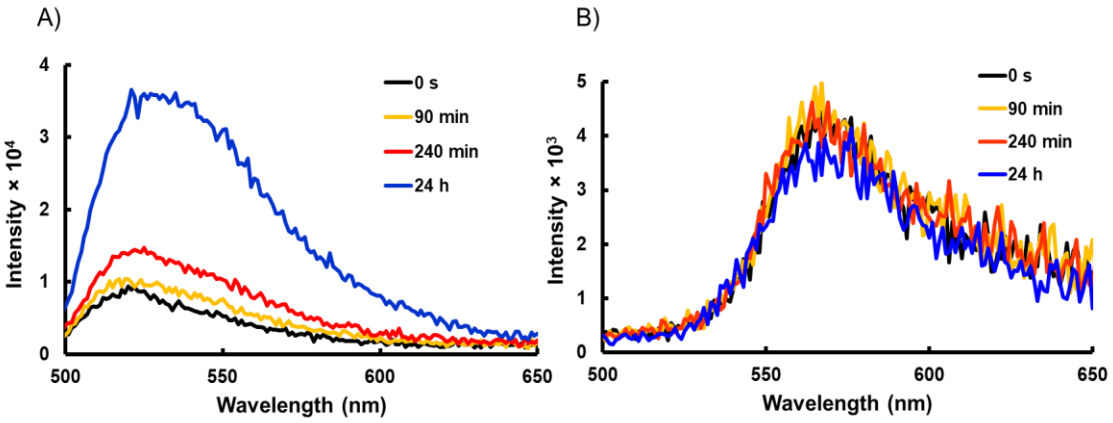

Figure A34. Emission spectra of Mn-bpy-H-BDP (A), and Mn-bpy-I-BDP (B) in room temperature CH_3CN in the dark at time intervals

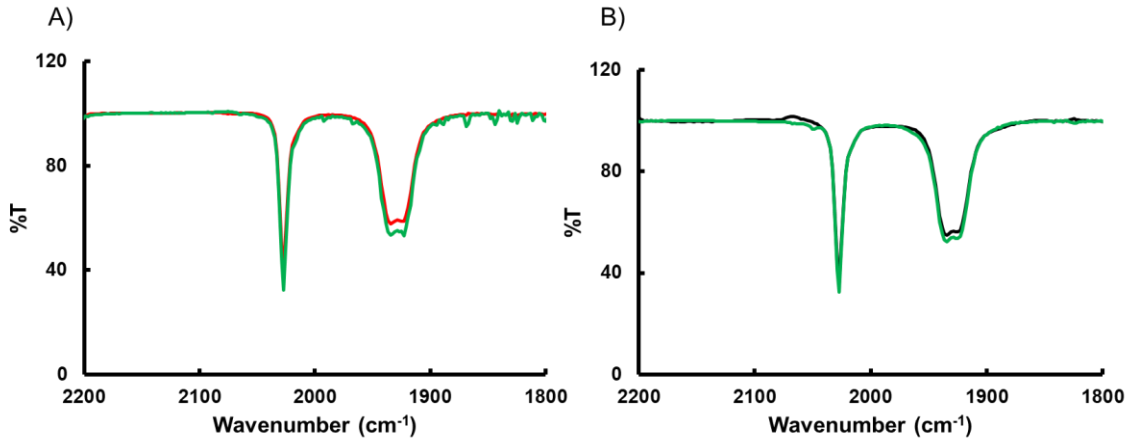

Figure A35. FTIR spectra for Mn-bpy-H-BDP initially (red solid) and kept in the dark for 1 h (green solid) (A) and Mn-bpy-I-BDP initially (black solid) and kept in the dark for 1 h (green solid) (B) in rt CH_3CN

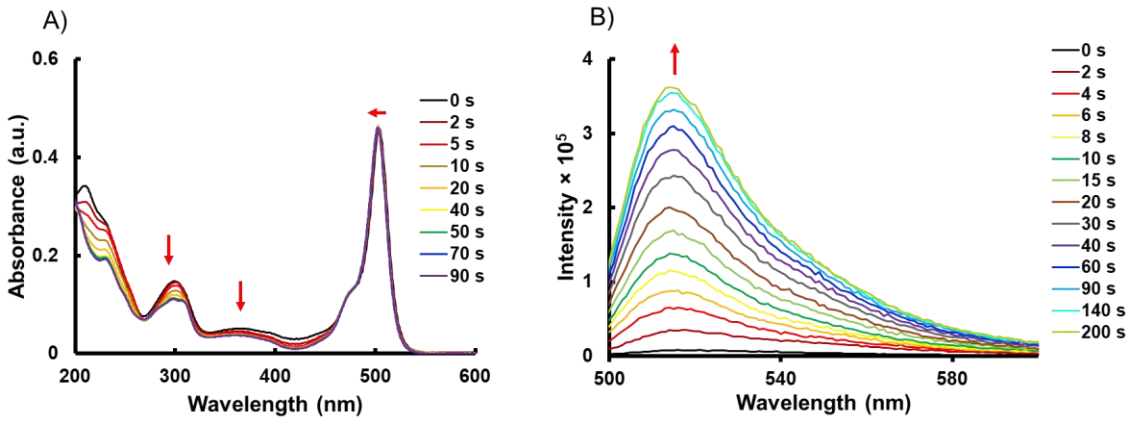

Figure A36. Absorption (A) and emission (B) spectra for the photolysis of Mn-bpy-H-BDP in rt CH_3CN with 535 nm LED

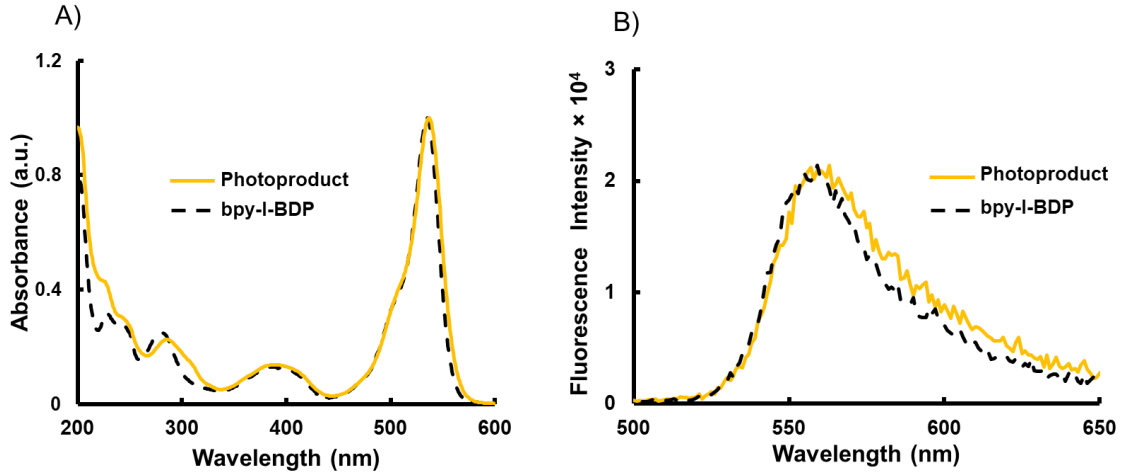

Figure A37. Overlaid Absorption (A) and emission spectra of Mn-bpy-I-BDP photoproduct (orange solid), and bpy-I-BDP (black dashed) in rt CH_3CN

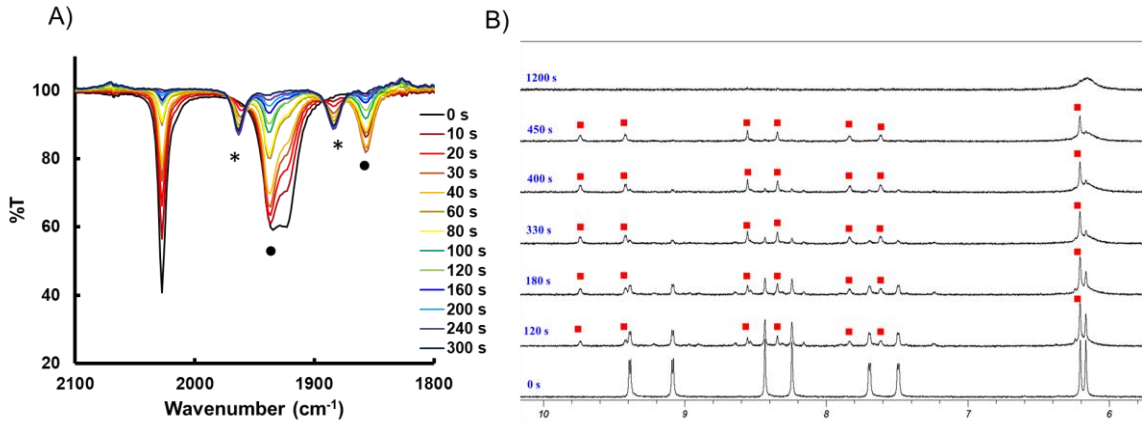

Figure A38. FTIR spectra (A) and ^{1}H NMR (B) photolysis of Mn-bpy-H-BDP in rt CH_3CN/CD_3CN, λ_{irr} = 535 nm

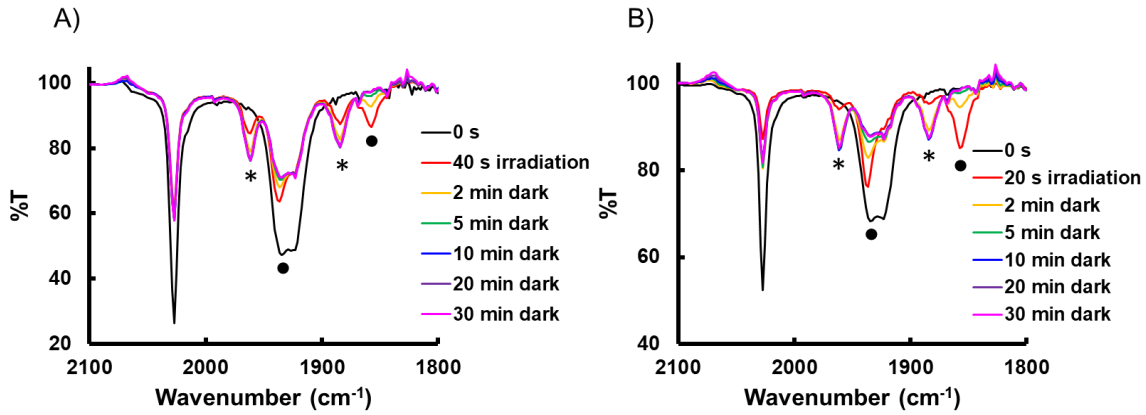

Figure A39. FTIR spectra for Mn-bpy-I-BDP after irradiation for 40 s with 590 nm LED and keeping in the dark up to 30 min (A) and Mn-bpy-H-BDP after irradiation for 20 s with 535 nm LED and keeping in the dark up to 30 min (B) in rt CH_3CN

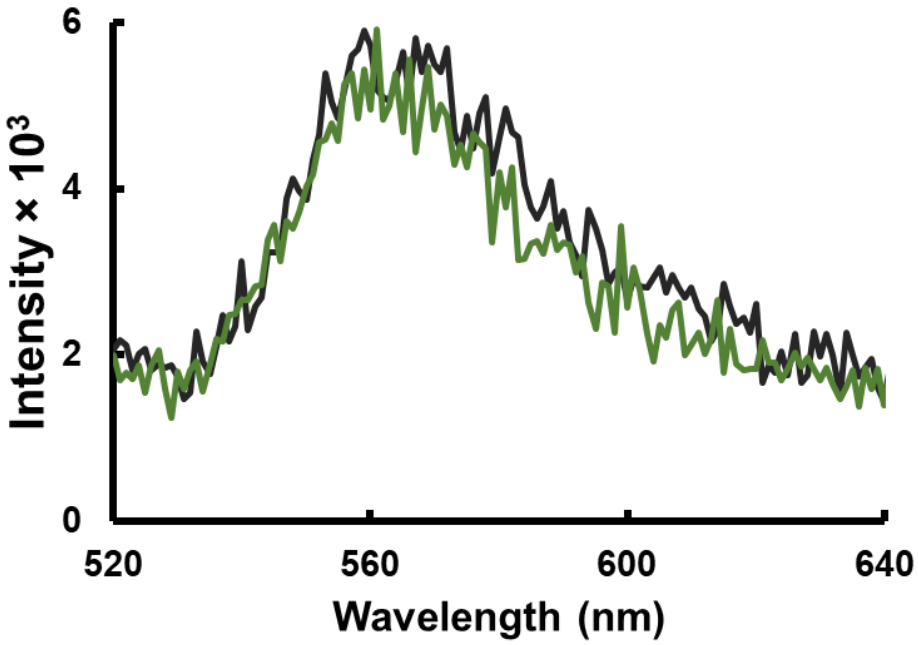

Figure A40. Emission spectra of Mn-bpy-I-BDP before the singlet oxygen detection experiment (black solid), and after the experiment (green solid), in rt CH_3CN, λ_{exc} = 490 nm, λ_{abs} at 490 nm: 0.1

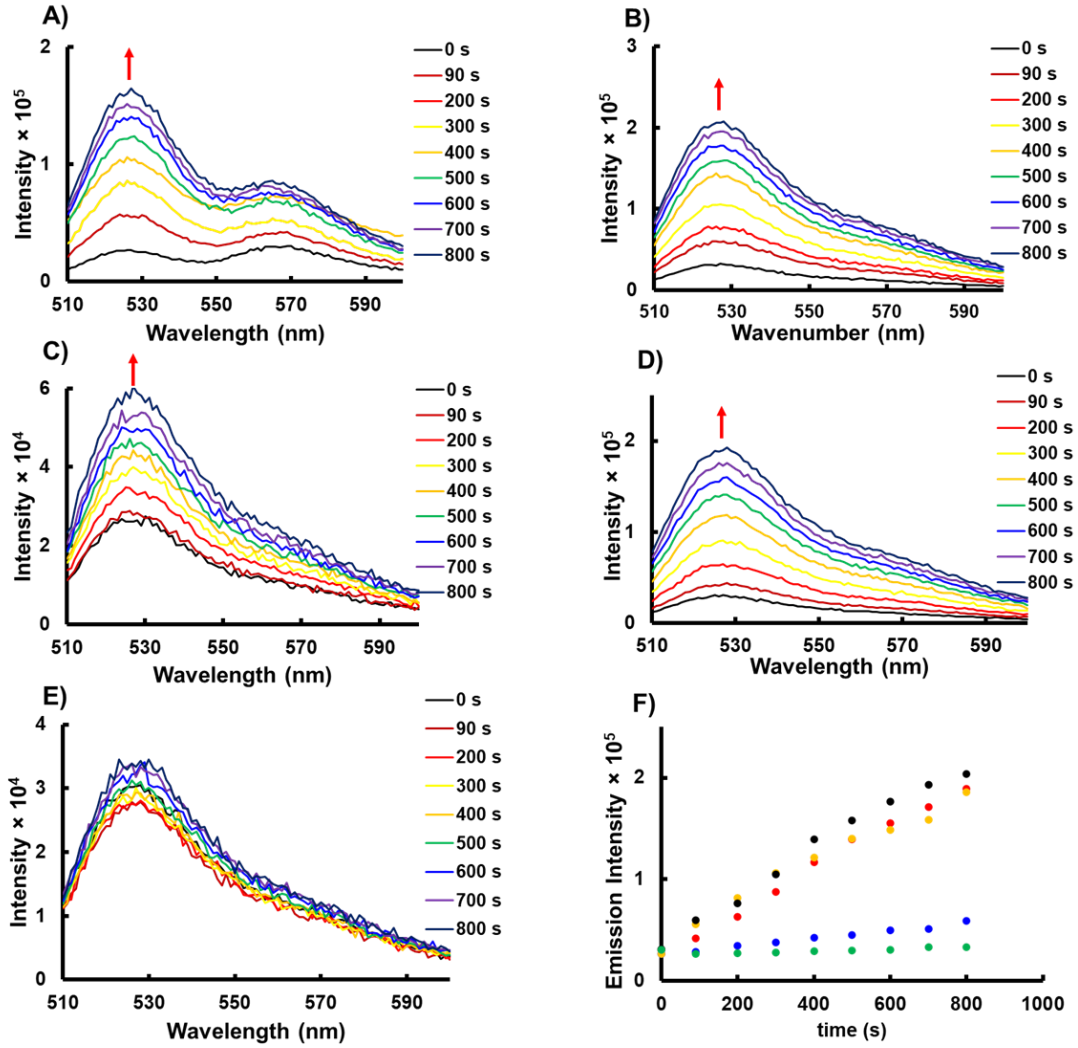

Figure A41. Increase in the emission intensity of SOSG during irradiation with 535 nm light in H_2O:MeOH (5%) in the presence of Rose Bengal (A), bpy-I-BDP (B), Mn-bpy-I-BDP (C), photoproducts of Mn-bpy-I-BDP (D), blank (SOSG+light) (E) and the change in the emission intensity of SOSG at 525 nm over time in the presence of Rose Bengal (orange circles), bpy-I-BDP (black circles), Mn-bpy-I-BDP (blue circles), photoproducts of Mn-bpy-I-BDP (red circles), and the blank (SOSG+light) (green circles) (F)

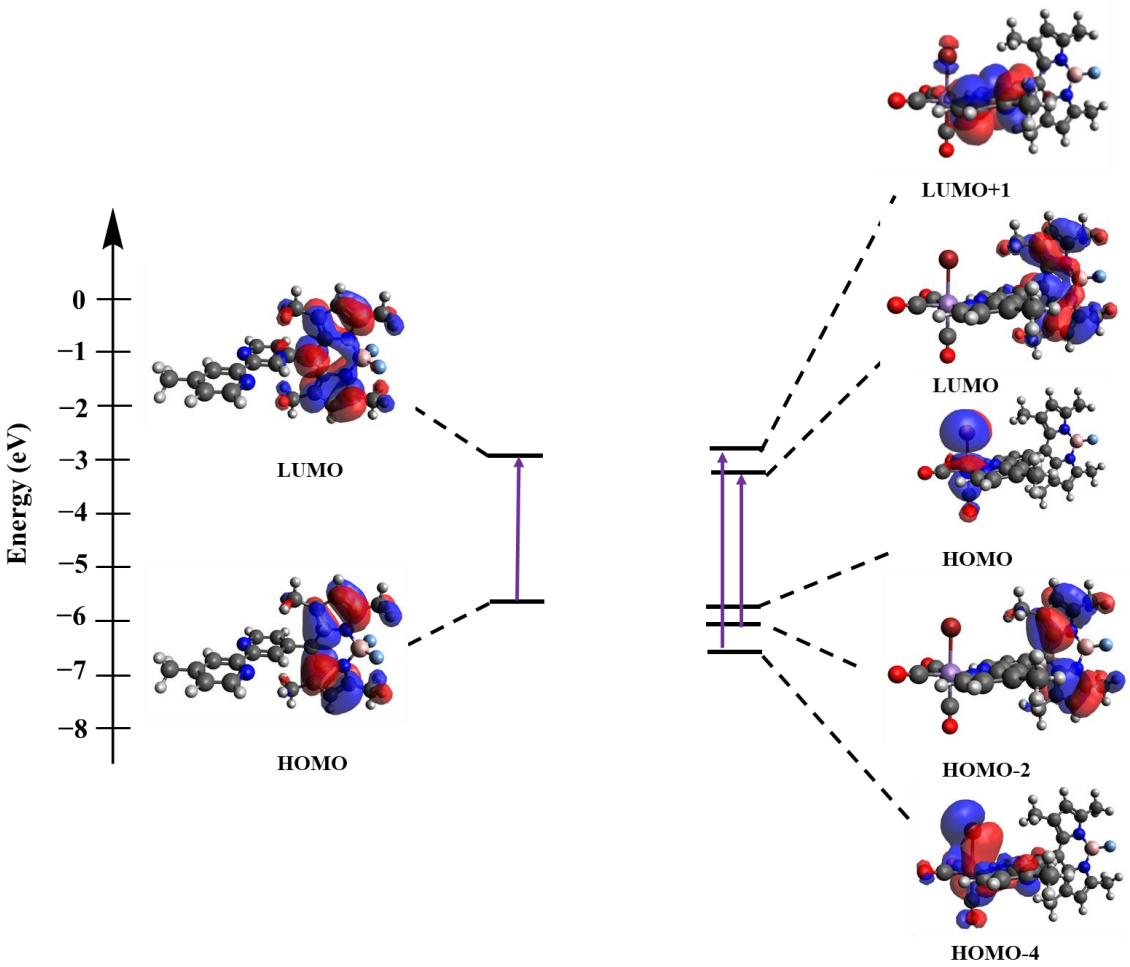

Figure A42. Frontier molecular orbitals, relative energies, and transitions of bpy-H-BDP (left) and Mn-bpy-H-BDP (right).

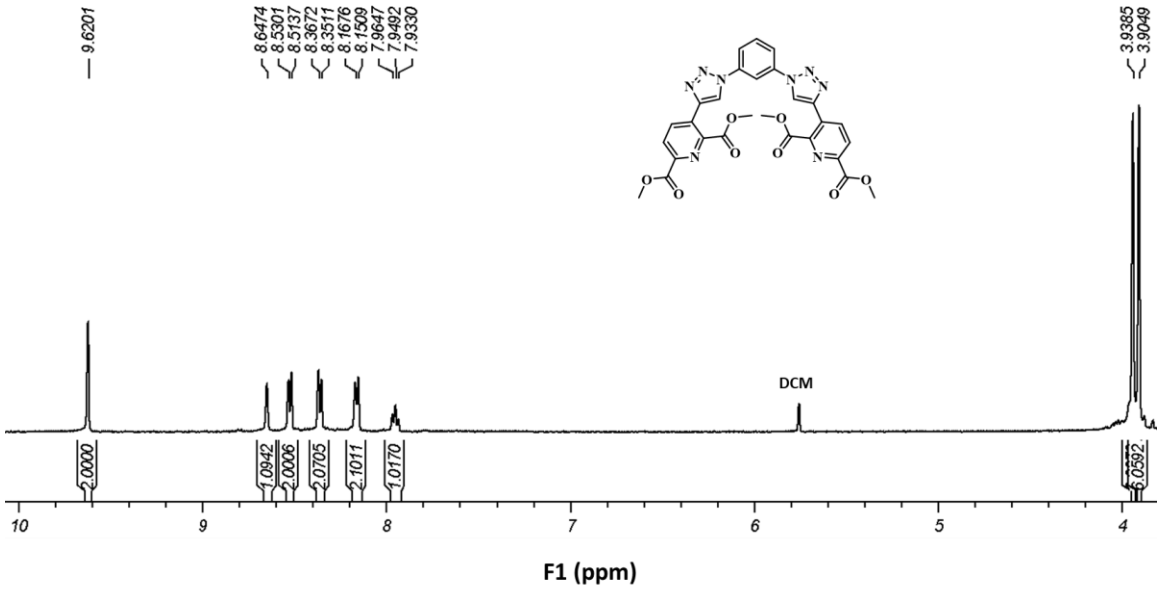

Figure A43. ^{1}H NMR spectrum of (5) in DMSO

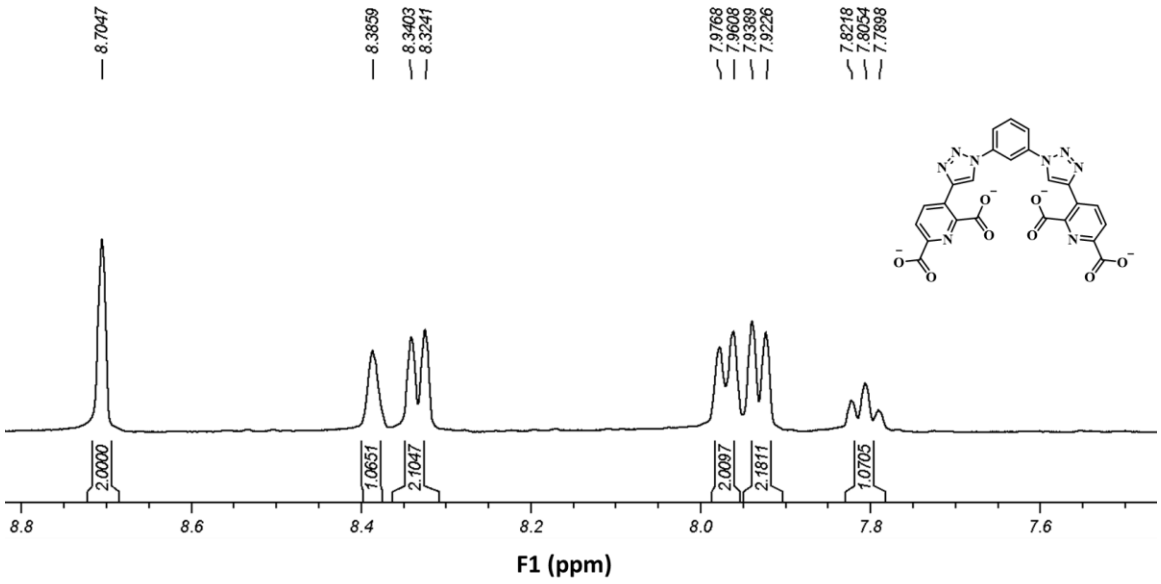

Figure A44. ^{1}H NMR spectrum of L in D_2O

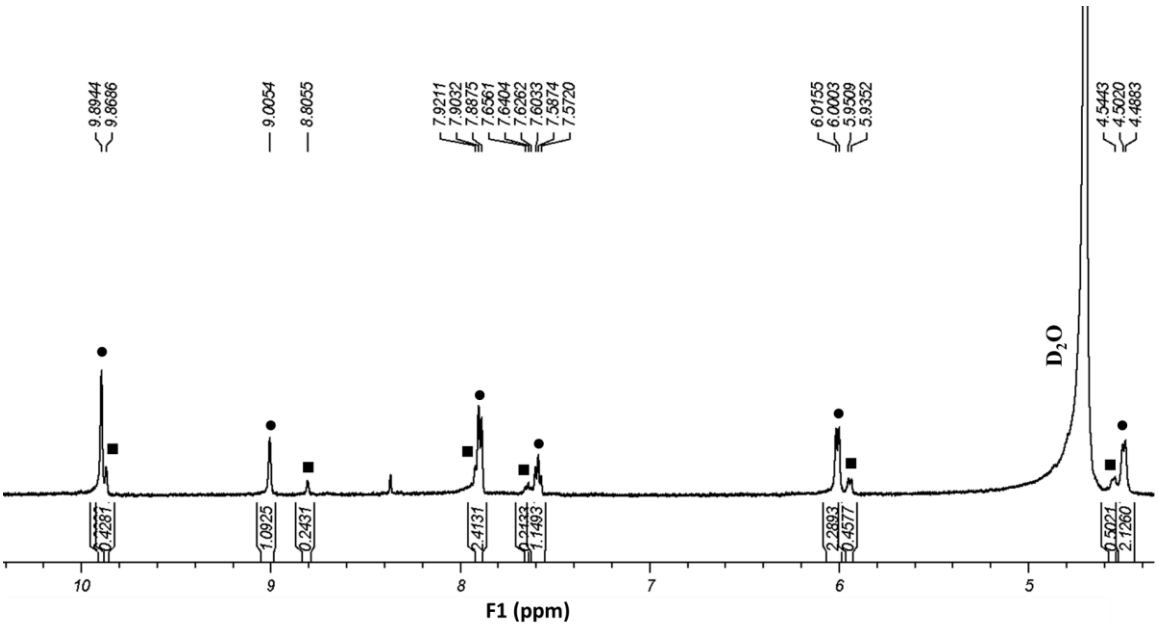

Figure A45. ^{1}H NMR spectrum of Eu_2L_3 assemblies in D_2O

Thesis and Dissertation Services